Atomic Scale Designing of Materials for Low-Temperature Fuel Cells

Ph.D. Thesis

by

ARUP MAHATA

DISCIPLINE OF CHEMISTRY

INDIAN INSTITUTE OF TECHNOLOGY INDORE

MARCH 2017

Atomic Scale Designing of Materials for Low-Temperature Fuel Cells

A THESIS

Submitted in partial fulfillment of the

requirements for the award of degree

of

DOCTOR OF PHILOSOPHY

by

ARUP MAHATA

DISCIPLINE OF CHEMISTRY

INDIAN INSTITUTE OF TECHNOLOGY INDORE

MARCH 2017

INDIAN INSTITUTE OF TECHNOLOGY INDORE

CANDIDATE'S DECLARATION

I hereby certify that the work which is being presented in the thesis entitled **Atomic Scale Designing of Materials for Low-Temperature Fuel Cells** in the partial fulfillment of the requirements for the award of the degree of **DOCTOR OF PHILOSOPHY** and submitted in the **DISCIPLINE OF CHEMISTRY, INDIAN INSTITUTE OF TECHNOLOGY INDORE**, is an authentic record of my own work carried out during the time period from AUGUST 2013 to MARCH 2017 under the supervision of **Dr. BISWARUP PATHAK**, Associate Professor, Discipline of Chemistry, IIT Indore.

The matter presented in this thesis has not been submitted by me for the award of any other degree of this or any other institute.

Signature of the student with date
(ARUP MAHATA)

This is to certify that the above statement made by the candidate is correct to the best of my knowledge.

Signature of Thesis Supervisor with date
(Dr. BISWARUP PATHAK)

ARUP MAHATA has successfully given his Ph.D. Oral Examination held on **……………….........**

Signature of Chairperson (OEB) Date:	Signature of External Examiner Date:	Signature(s) of Thesis Supervisor(s) Date:
Signature of PSPC Member #1 Date:	Signature of PSPC Member #2 Date:	Signature of Convener, DPGC Date:

Signature of Head of Discipline
Date:

Acknowledgements

It is my great pleasure to express my deepest respect and most sincere gratitude to my supervisor, Dr. Biswarup Pathak for his constant guidance and encouragement throughout my work. I am greatly indebted for his support, motivation and better understanding. His vision and dedication in presenting the projects has a remarkable influence on me.

I am thankful to my PSPC members, Dr. Sanjay Kr. Singh and Dr. Sudeshna Chattopadhyay for their valuable suggestions and guidance.

I would like to thank my experimental collaborators, Dr. Sanjay Kumar Singh, Dr. Tridib Kumar Sharma, Dr. Suman Mukhopadhyay, Dr. Bimlesh Lochab for their guidance and scientific discussion during the collaborative projects.

I wish to express my gratitude to Prof. Pradeep Mathur, Director, IIT Indore for his continuous support in every aspect.

I would like to thank IIT Indore for providing laboratory, computing facilities, and financial support.

I would also like to thank Dr. Satya S. Bulusu, Dr. Apurba Kr. Das, Dr. Tushar Kanti Mukherjee, Dr. Sampak Samanta, Dr. Shaikh M. Mobin, Dr. Rajneesh Misra, Dr. Chelvam Venkatesh, Dr. Anjan Chakraborty and Dr. Amrendra Kr. Singh for their guidance and help during various activities in the department.

I extend my deep thanks to my group members Ms. Indrani Choudhuri, Mr. Kuber Singh Rawat, Ms. Priyanka Garg, Mr. Sourabh Kumar, Ms. Preeti Bhauriyal, Ms. Gargee Bhattacharya, Mr. Chiranjit Mondal, Mr. Akhil S. Nair, Mr. Shyama Charan Mandal and Mr. Rameshwar Lal Kumawat for their selfless co-operation and help to make my work successful.

I would also like to thank Mr. Dhiraj Vijayvargiya, Mr. Yogendra Singh, Ms. Sarita Batra, Mr. Manish Kushwaha, Ms. Vinita Kothari and Mr. Rameshwar

Dauhare for their technical support. I would also like to thank Ms. Anjali Bandiwadekar, Mr. Rajesh Kumar, Mr. Lala Ram Ahirwar and other library staffs for their constant help, whenever required.

I would personally like to extend my sincere thanks to my all flat-mates during various times of my PhD period, Mr. Surajit Chatterjee, Mr. Arpan Bhattyacharya, Mr. Sagar Biswas and Mr. Mriganka Das who were always there whenever required and never let me down during these PhD days. Here, it is specially to be mentioned that, it has been a wonderful experience to work with many friends at IIT Indore during my PhD who really helped me in many aspects.

I would like to express my heartiest gratitude to my friends, Ms. Keya, Mr. Amit, Mr. Partha Pratim, Mr. Quazi, Mr. Krishnendu, and Mr. Jaydeb who were always there with me irrespective of my ups and downs.

I would like to take this opportunity to express my respect, love and gratitude to all the teachers from Rowtora Primary School, Garh Raipur High School, Vivekananda Mahavidyalaya, National Institute of Technology Durgapur and CSIR-Central Glass and Ceramic Research Institute for their kind love and leading me to the right path.

Most importantly, none of this would have been possible without the support of my family and I deeply express my love and gratitude to my lovable father Mr. Gurupada Mahata, mother Mrs. Namita Mahata, sister Mrs. Mithu Mahata, and brother in law Mr. Prabir Mahata for their unconditional love and support.

There are many more who have directly or indirectly contributed in making this journey successful, I wish I could thank them all, but time and space compel me to stop here.

ARUP MAHATA

Dedicated to
My Parents
and
All Well-Wishers

Abstract

There is a growing interest in the search for alternative energy resources due to the limited availability of fossil fuels and to reduce the emission of greenhouses gases (CO_2, CH_4, N_2O, ozone, chlorofluorocarbons and so on). Therefore, clean energy resources like fuel cells, lithium ion batteries, supercapacitors, and photovoltaics have emerged as alternative ways. A fuel cell is an energy-conversion device that converts the chemical energy from hydrogen or hydrogen-rich fuels into electrical power through electrochemical reactions. The fuel cells are categorized as low-temperature or high-temperature fuel cells. The category with operating temperature below 150 °C can be considered as low-temperature fuel cells. Oxygen reduction reaction (ORR) at the cathode is the most important reaction in low-temperature fuel cells, where Pt-black electrocatalyst with Pt(111) exposed surface is used as conventional cathode electrode.

Recently, metal nanoclusters (NCs) surrounded by multiple numbers of well-defined facets have shown its potential towards ORR in comparison to their bulk metal surfaces due to the presence of high surface unsaturation. These highly unsaturated sites possess higher d-band energies, which influences the overall activity of the NCs. Earlier theoretical studies are done either on small-sized metal NCs or bulk metal surfaces (slab model) to understand the catalytic activity of the experimentally synthesized NCs. However, the size of the NC is very important to its catalytic reactivity due to the finite-size effects. Moreover, the low-coordinated sites can’t be modelled in slab model study. Therefore, cluster model study with well-defined facet can only provide the real scenario about the experimental situation.

The contents of each chapter included in the thesis are discussed briefly as follows:

1. Introduction

In this chapter, a brief overview of the fuel cells and their working principle has been discussed, putting much emphasis on low-temperature fuel cells. The potential applicability of NC-based electrode in the low-temperature fuel cell has also been discussed here. The recent advances on hollow materials like metallic nanocage, nanoframes have been reviewed. Furthermore, the applicability of nanosheets based catalysts and their possible application in fuel cells has been discussed. In addition, the roles of the shape of NCs and composition of the core-metal in the core-shell NCs towards the catalytic activity have also been surveyed. Besides, the adsorption behavior and decomposition pathways of methanol at the anode of direct methanol fuel cell have also been discussed.

The last part of this chapter discusses the basis of the density functional theory which is used for the electronic structure calculations. The procedure for modelling the NCs, core-shell NC and nanosheets have also been discussed here. This chapter also covers the computational techniques which are used to explain the results of the computation.

2. Pt_3Ti ($Ti_{19}@Pt_{60}$)-based cuboctahedral core-shell nanocluster favors the direct oxygen reduction reaction pathway over the indirect pathway

In this chapter, the potential applicability of a cuboctahedral core-shell ($Ti_{19}@Pt_{60}$) NC towards ORR activity has been investigated and compared with that of a pure Pt NC (Pt_{79}). The energetic stability, thermal stability, and dissolution limit of $Ti_{19}@Pt_{60}$ NC has been investigated for its possible synthesis and practical usages. Thermodynamic and kinetic parameters are explored to find out the most favored ORR pathway and product selectivity on the $Ti_{19}@Pt_{60}$ NC. Rate-determining steps ($*O_2$ activation and *OH formation) are highly improved over the $Ti_{19}@Pt_{60}$ NC with respect to the cuboctahedral Pt NC (Pt_{79}), pure metal (Pt, Pd, and Ag), and alloy (Pt_3M; M = Ni, Co, Ti) based catalysts. The detailed investigation reveals that the $*O_2$-induced structural changes favor direct $*O_2$

dissociation on the $Ti_{19}@Pt_{60}$ NC surface. Further, it has been found that a dual mechanism (ligand effect and charge transfer) plays an important role to improve the ORR activity. The results obtained in this study provide fundamental insight into the role of a core-shell NC towards ORR activity.

3. Single-layered platinum nanocage as highly selective and efficient catalyst for fuel cells

In this chapter, the ORR pathways are systematically studied on the (111) facet of an octahedral single-layered platinum nanocage (Pt_{66}), enclosed by well-defined (111) facets. Energetic (cohesive energy), thermal (molecular dynamics simulation) and dynamic (phonon frequency) calculations are carried out to evaluate the stability of the nanocage. Thermodynamic (reaction free energies) and kinetic (free energy barriers, and temperature dependent reaction rates) parameters are investigated to find out the most favourable pathway for the ORR. The catalytic activity of the nanocage is investigated in greater detail toward its product selectivity (H_2O vs. H_2O_2). Previous theoretical and experimental reports on bulk Pt(111) show that direct O–O bond dissociation and OH formation are very much unlikely due to the high-energy barrier. However, it is found that the direct O–O bond dissociation and OH formation are thermodynamically and kinetically favourable when catalysed by an octahedral Pt-nanocage. The microkinetic analysis shows that the nanocage is a highly selective catalyst for the four-electron reduction ($*H_2O$ formation) over two-electron reduction ($*H_2O_2$ formation). The excellent catalytic activity of the nanocage is explained from the surface energy, compressive strain, Bader charge and density of states analysis.

4. Free-standing platinum monolayer as efficient and selective catalyst for oxygen reduction reaction

In this paper, a two-dimensional platinum monolayer (platene) sheet is reported for ORR activity using first-principle calculations. Unlike the previous reports of supported hexagonal planar monolayer, platene exhibits an orthorhombic buckled structure, where each Pt-atom is coordinated with six Pt-atoms. State-of-the-art calculation shows that the platene is energetically, thermally, dynamically and mechanically stable and thus can be synthesized. An orbital mixing between in-plane σ-orbital and out-of-plane π-orbital helps in stabilizing the buckling pattern. It has been found that the d_{z2} orbitals of the out-of-plane Pt atoms tilt themselves (by 30°) towards the d_{yz} orbital of the in-plane Pt atoms to gain the maximum overlap, which in turn stabilizes the buckled structure. The potential applicability of platene towards ORR activity has been investigated and it is found that the ORR rate determining step (OH formation) is significantly improved when catalyzed by the platene compared to any catalysts reported to date. The unique adsorption pattern of adsorbed oxygen-atom helps to lower the activation barrier of the rate determining step. The potential dependent study shows that the ORR is thermodynamically favourable at 0.38 V and thus lowers the overpotential for ORR. Besides, platene is very much selective towards H_2O formation over H_2O_2 formation.

5. Insights into the shape-dependent (cuboctahedral vs. octahedral) catalytic activity of platinum nanoclusters for fuel cell applications

In this chapter, the shape-dependent catalytic activities of two platinum NCs with cuboctahedral (Pt_{79}) and octahedral (Pt_{85}) shapes have been investigated toward ORR. The energetic stability, thermal stability, and dissolution limit of the NCs are investigated for their synthesis and practical usage. The four-electron (H_2O formation) vs. two-electron (H_2O_2 formation) ORR mechanisms are systematically studied on the (111) facet of the NCs to gain more insight into the shape-dependent ORR activity and product selectivity (H_2O vs. H_2O_2). Thermodynamic (reaction free energies) and kinetic (free energy barriers and temperature-dependent reaction rates) parameters are investigated to find out the most favored ORR pathway and product selectivity. The NC-based Pt catalysts are very efficient and selective with respect to the previously reported bulk metal (Pt, Pd, and Ag) based catalysts. The results show that the rate-determining step is no longer a rate-determining step when the reaction is catalyzed by the cuboctahedral NC. The excellent catalytic activity of the cuboctahedral NC is attributed to the surface energy, compressive strain and d-band center position of the catalyst. The results are very much consistent with experimental findings, and thereby such NC-based electrodes may serve as good candidates for fuel cell applications.

6. A cuboctahedral platinum (Pt_{79}) nanocluster favours di-sigma adsorption and improves the reaction kinetics for methanol fuel cells

In this chapter, the methanol dehydrogenation steps are studied very systematically on the (111) facet of a cuboctahedral platinum (Pt_{79}) NC enclosed by well-defined facets. The various intermediates formed during the methanol decompositions are adsorbed at the edge and bridge site of the facet either vertically (through C- and O-centres) or in parallel. The di-sigma adsorption (in parallel) on the (111) facet of the NC is the most stable structure for most of the intermediates and such binding improves the interaction between the substrate and the NC and thus the catalytic activity. The reaction thermodynamics, activation barrier, and temperature dependent reaction rates are calculated for all the successive methanol dehydrogenation steps to understand the methanol decomposition mechanism, and these values are compared with previous studies to understand the catalytic activity of the NC. It has been found that the catalytic activity of the NC is excellent while comparing with any previous reports and the methanol dehydrogenation thermodynamics and kinetics are best when the intermediates are adsorbed in a di-sigma manner.

7. Conclusions

The conclusions of research work described here are as follows:

i) The O_2-induced structural changes on $Ti_{19}@Pt_{60}$ NC make the NC as a very selective and efficient catalyst for H_2O over H_2O_2 formation and thus could be a promising catalyst for fuel cell applications.

ii) The rate determining steps of ORR (O–O bond dissociation and OH formation) are thermodynamically and kinetically favorable when catalyzed by an octahedral Pt-nanocage. The nanocage is a highly selective catalyst for the four-electron reduction (H_2O formation) over two-electron reduction (H_2O_2 formation).

iii) Free-standing orthorhombic platinum monolayer (platene) could be a very promising catalyst for the efficient and selective reduction of oxygen.

iv) The cuboctahedral NC improves the ORR activity and selectivity compared to the octahedral NC of similar size.

v) The methanol decomposition activity of the Pt_{79} NC is excellent while comparing with any previous reports and the methanol dehydrogenation thermodynamics and kinetics are best when the intermediates are adsorbed in a di-sigma manner.

List of Publications

1) **Mahata A.**, Garg P., Rawat K. S., Bhauriyal P., Pathak B. (2017) Free-standing Platinum Monolayer as Efficient and Selective Catalyst for Oxygen Reduction Reaction, J. Mater. Chem. A, 5, 5303-5313. (DOI: 10.1039/c7ta00685c)

2) **Mahata A.**, Pathak B. (2017) Bimetallic Core-Based Cuboctahedral Core-Shell Nanocluster for Hydrogen Peroxide ($2e^-$ reduction) over Water ($4e^-$ reduction) Formation: Role of Core Metals, Nanoscale, 9, 9537–9547. (DOI: 10.1039/c7nr03002a)

3) **Mahata A.**, Bhauriyal P., Rawat K. S., Pathak B. (2016), Pt_3Ti ($Ti_{19}@Pt_{60}$) Based Cuboctahedral Core-shell Nanocluster Favours Direct over Indirect Oxygen Reduction Reaction, ACS Energy Lett., 1, 797-805. (DOI: 10.1021/acsenergylett.6b00385)

4) **Mahata A.**, Rawat K. S., Choudhuri I., Pathak B. (2016), Single-layered Platinum Nanocage: A Highly Selective and Efficient Catalyst for Fuel Cell, J. Mater. Chem. A, 4, 12756-12767. (DOI: 10.1039/c6ta03245a)

5) **Mahata A.**, Rawat K. S., Choudhuri I., Pathak B. (2016), Cuboctahedral vs. Octahedral Platinum Nanoclusters: Insights into the Shape-dependent Catalytic Activity for Fuel Cell, Catal. Sci. Technol., 6, 7913-7923. (DOI: 10.1039/c6cy01709f)

6) **Mahata A.**, Rawat K. S., Choudhuri I., Pathak B. (2016), Octahedral Ni-nanocluster (Ni_{85}) for Efficient and Selective Reduction of Nitric Oxide (NO) to Nitrogen (N_2), Scientific Reports, 6, 25590. (DOI: 10.1038/srep25590)

7) **Mahata A.**, Choudhuri I., Pathak B. (2015), A Cuboctahedral Platinum (Pt_{79}) Nanocluster Enclosed by Well Defined Facets Favours Di-sigma Adsorption and Improves the Reaction Kinetics for Methanol Fuel Cell, Nanoscale, 7, 13438-13451. (DOI: 10.1039/c5nr01575h)

8) **Mahata A.**, Rai R. K., Choudhuri I., Singh S. K., Pathak B. (2014), Direct vs. Indirect Pathways for Nitrobenzene Reduction over Ni Catalyst Surface: A Density Functional Study, Phys. Chem. Chem. Phys., 16, 26365-26374. (DOI: 10.1039/c4cp04355c)

9) Rawat K. S., **Mahata A.**, Pathak B. (2017) Thermochemical and Electrochemical CO_2 Reduction on Octahedral Cu Nanocluster: Role of Solvent towards Product Selectivity, J Catal., 349, 118-127 (DOI: 10.1016/j.jcat.2017.03.011)

10) Bhauriyal P., **Mahata A.**, Pathak B. (2017), The Staging Mechanism of $AlCl_4$ Intercalation in Graphite Electrode for Aluminium-ion Battery, Phys. Chem. Chem. Phys., 19, 7980-7989. (DOI: 10.1039/c7cp00453b)

11) Bhauriyal P., **Mahata A.**, Pathak B. (2017), Hexagonal BC_3 Electrode for a High-Voltage Al-Ion Battery, J. Phys. Chem. C, 121, 9748–9756. (DOI: 10.1021/acs.jpcc.7b02290)

12) Bhauriyal P., **Mahata A.**, Pathak B. (2017), A Computational Study of Single-walled Carbon Nanotube Based Ultrafast High Capacity Al Battery, Chem. Asian J.,12, 1944–1951. (DOI: 10.1002/asia.201700570)

13) Garg P., Choudhuri I., **Mahata A.**, Pathak B. (2017), Band Gap Opening in Stanene Induced by Patterned B-N Doping, Phys. Chem. Chem. Phys., 19, 3660-3669. (DOI: 10.1039/c6cp07505c)

14) Bhattacharyya, G., **Mahata, A.**, Choudhuri, I. Pathak, B. (2017), Semiconducting Phase in Borophene: Role of Defect & Strain, J. Phys. D: Appl. Phys. (DOI: 10.1088/1361-6463/aa81b8)

15) Rawat K. S., **Mahata A.**, Pathak B. (2016), Catalytic Hydrogenation of CO_2 by Fe-Complexes Containing Pendant Amines: Role of Water and Base, J. Phys. Chem. C, 120, 26652-26662. (DOI: 10.1021/acs.jpcc.6b09333)

16) Rawat K. S., **Mahata A.**, Choudhuri I., Pathak B. (2016), Catalytic Hydrogenation of CO_2 by Manganese Complexes: Role of Pi-Acceptor Ligands, J. Phys. Chem. C, 120, 16478-16488. (DOI:10.1021/acs.jpcc.6b05065)

17) Rawat K. S., **Mahata A.,** Choudhuri I., Pathak B. (2016), N-heterocylic Carbene Based Mn-Electrocatalyst for Two Electron CO_2 Reduction over Proton Reduction: Role of Brønsted acids, J. Phys. Chem. C, 120, 8821-8831. (DOI: 10.1021/acs.jpcc.6b0220)

18) Choudhuri I., Sadhukhan D., Garg P., **Mahata A.**, Pathak B. (2016), Lewis Acid-Base Adducts for Improving the Selectivity and Sensitivity of Graphene based Gas Sensors, ACS Sensors, 1, 451.(DOI: 10.1021/acssensors.6b00031)

19) Choudhuri I., Kumar S., **Mahata A.**, Rawat K. S., Pathak B. (2016), Transition-Metal Embedded Carbon Nitride Monolayers: High-Temperature Ferromagnetism and Half-Metallicity, Nanoscale, 8, 14117-14126. (DOI: 10.1039/c6nr03282f)

20) Garg P., Kumar S., Choudhuri I., **Mahata A.**, Pathak B. (2016), Hexagonal Planar CdS Monolayer Sheet for Visible Light Photo-Catalysis, J. Phys. Chem. C, 120, 7052-7060. (DOI:10.1021/acs.jpcc.6b01622)

21) Choudhuri I., **Mahata A.**, Rawat K. S., Pathak B. (2016), Role of Ti doping and Al and B vacancies in the dehydrogenation of $Al(BH_4)_3$, J. Chem. Sci., 128, 1651. (DOI: 10.1007/s12039-016-1148-3)

22) Sharma B., **Mahata A.**, Mandani S., Sarma T. K., Pathak B. (2016), Coordination polymer hydrogels through Ag(I)-mediated spontaneous self-assembly of unsubstituted nucleobases and their antimicrobial activity, RSC Advances, 6, 62968-62973. (DOI: 10.1039/c6ra11137h)

23) Rai R. K., Gupta K., Tyagi D., **Mahata A.**, Behrens S., Yang X., Xu Q., Pathak B., Singh S. K. (2016), Access to highly active Ni-Pd bimetallic nanoparticle catalysts for C-C coupling reactions, Catal. Sci. Technol., 6, 5567-5579. (DOI: 10.1039/c6cy00037a)

24) Shukla S., Tripathi M., **Mahata A.**, Pathak B., Lochab B. (2016), Kinetics Behind a Strategy for Modulation of Sustainable Benzoxazines: Experimental Study and Its Theoretical Verification, Macromol. Chem. Phys., 217, 1342-1353. (DOI: 10.1002/macp.201600049)

25) Choudhuri I., Patra N., **Mahata A.**, Ahuja R., Pathak B. (2015), B-N@Graphene: Highly Sensitive and Selective Gas Sensor, J. Phys. Chem. C, 119, 24827-24836. (DOI: 10.1021/acs.jpcc.5b07359)

26) Shukla S., **Mahata A.**, Pathak B., Lochab B. (2015), Cardanol benzoxazines - Interplay of Oxazine Functionality (Mono to Tetra) and Properties, RSC Advances, 5, 78071-78080. (DOI:10.1039/c5ra14214h)

27) Choudhuri I., **Mahata A.**, Pathak B. (2014), Additives in Protic-Hydridic Hydrogen Storage Compounds: A Molecular Study, RSC Advances, 4, 52785-52795. (DOI: 10.1039/c4ra09778e)

28) Saha M., Nasani R., Das M., **Mahata A.**, Pathak B., Mobin S. M., Carrella L. M., Rentschler E., Mukhopadhyay S. (2014), Limiting Nuclearity in Formation of Polynuclear Metal Complexes through [2+3] Cycloaddition:Synthesis and Magnetic Properties of Tri- and Pentanuclear Metal Complexes Generated through Bridging Tetrazolate Moiety, Dalton Trans., 80, 8083-8093. (DOI: 10.1039/c4dt00378k)

29) Rai R. K., **Mahata A.**, Mukhopadhyay S., Gupta S., Li P., Nguyen K. T., Zhao Y., Pathak B., Singh S. K. (2014), Room-Temperature Chemoselective Reduction of Nitro Groups Using Non-noble Metal Nanocatalysts in Water, Inorg. Chem., 53, 2904-2909. (DOI:10.1021/ic402674z)

Table of Contents

Chapter 1: Introduction

Chapter 2: Pt_3Ti (Ti_{19}@Pt_{60}) Based Cuboctahedral Core-shell Nanocluster Favours Direct over Indirect Oxygen Reduction Reaction

Chapter 3: Single-layered Platinum Nanocage: A Highly Selective and Efficient Catalyst for Fuel Cell

Chapter 4: Free-standing Platinum Monolayer as Efficient and Selective Catalyst for Oxygen Reduction Reaction

Chapter 5: Cuboctahedral vs. Octahedral Platinum Nanoclusters: Insights into the Shape-dependent Catalytic Activity for Fuel Cell

Chapter 6: Cuboctahedral Platinum (Pt_{79}) Nanocluster Enclosed by Well Defined Facets Favours the Di-sigma Adsorption and Improves the Reaction Kinetics for Methanol Fuel Cell

Chapter 7: Scope for future work

List of Figures

Chapter 1

Chapter 2

Chapter 3

Chapter 4

Chapter 5

Chapter 6

List of Schemes

Chapter 1

Chapter 2

Chapter 3

Chapter 4

Chapter 5

Chapter 6

List of Tables

Chapter 1

Chapter 2

Chapter 3

Chapter 4

Chapter 5

Chapter 6

Acronyms

PEMFC	Polymer electrolyte membrane fuel cell
DMFC	Direct methanol fuel cell
AFC	Alkaline fuel cell
MCFC	Molten carbonate fuel cell
SOFC	Solid oxide fuel cell
HOR	Hydrogen oxidation reaction
MOR	Methanol oxidation reaction
ORR	Oxygen reduction reaction
NC	Nanocluster
ML	Monolayer
DFT	Density functional theory
LDA	Local density approximation
GGA	Generalized Gradient Approximation
PBE	Perdew-Burke-Ernzerhof
PAW	Projector augmented wave
VASP	Vienna Ab initio Simulation Package
AIMD	Ab initio molecular dynamics
CMD	Classical molecular dynamics
RMSD	Root mean square deviation
NEB	Nudged elastic Band
MEP	Minimum energy path
DFPT	Density functional perturbation theory
PDOS	Projected density of states
2D	Two-dimensional
ZPE	Zero-point energy

Chapter 1

Introduction

1.1 Clean energy resources

There is a growing interest in search for alternative energy resources due to the limited availability of fossil fuels and to reduce the emission of greenhouse gases *[1]*. In this scenario, fuel cell has emerged as one of the alternatives and promising sources of clean energies. The term “clean” arises due to the generation of water as the end product. The development of nanomaterials for clean energy applications is one of the major challenges in this century. In this aspect, computational study has been playing a major role toward the development of nanomaterials for clean energy applications. The focus of this doctoral thesis is to design nanocluster based electrodes for fuel cell applications.

1.2. Fuel cell

Fuel cell is a device that converts the chemical energy from hydrogen or hydrogen-rich fuels into electrical power through electrochemical reaction. Fuel cell mainly consists of an electrolyte and two electrodes. At the anode, the fuel is oxidized, whereas at the cathode, oxygen is reduced. The ions pass through the electrolyte from one side to the other. Simultaneously, electrons pass from the anode to the cathode through an external circuit and thus producing electricity. Fuel cells can produce electricity continuously for as long as fuel is provided.

Mainly six types of fuel cells are in the market. The basis working principles are almost similar in all cases. However, they are named based on the working principles and electrolytes used. The operating temperature of a fuel cell depends on the nature of the electrolyte. Depending on the operating temperature, different electrodes are chosen for oxidation and reduction reactions. A brief summary of various types of fuel cells based on the operating temperature and electrode reactions has been given in Table 1.1.

Table 1.1: Comparison of various kind of fuel cell

Types of fuel cell	Operating temperature (° C)	Fuel	Anode Reaction	Cathode Reaction
Polymer electrolyte membrane fuel cell (PEMFC)	40-90	H_2	$H_2 \rightarrow 2H^+ + 2e^-$	$½O_2 + 2H^+ + 2e^- \rightarrow H_2O$
Direct methanol fuel cell (DMFC)	60-130	CH_3OH	$CH_3OH + H_2O \rightarrow CO_2 + 6H^+ + 6e^-$	$3(½O_2) + 6H^+ + 6e^- \rightarrow 3H_2O$
Alkaline fuel cell (AFC)	40-200	H_2	$H_2 + 2OH^- \rightarrow 2H_2O + 2e^-$	$½O_2 + H_2O + 2e^- \rightarrow 2OH^-$
Phosphoric acid fuel cell (PAFC)	200	H_2	$H_2 \rightarrow 2H^+ + 2e^-$	$½O_2 + 2H^+ + 2e^- \rightarrow H_2O$
Molten carbonate fuel cell (MCFC)	650	H_2, CO, CH_4	$H_2 + CO_3^{2-} \rightarrow CO_2 + H_2O + 2e^-$	$½O_2 + CO_2 + 2e^- \rightarrow CO_3^{2-}$
Solid oxide fuel cell (SOFC)	600-950	H_2, CO, CH_4	$H_2 + O^{2-} \rightarrow H_2O + 2e^-$	$½O_2 + 2e^- \rightarrow O^{2-}$

1.3. Low-temperature fuel cell

The fuel cells are categorized as low-temperature or high-temperature on the basis of operation temperature. Low-temperature fuel cells are those which operate below 150 °C *[2]*. Both the PEMFC and DMFC fall in the range of low-temperature fuel cell. The working principle of DMFCs is the same as in the PEMFCs. Actually, DMFC is a special kind of PEMFC. In both the kinds of fuel cells, the porous carbon based materials are used as electrodes and both the electrodes are coated (one side) with platinum and thus named Pt/C electrode *[3]*. Basically, carbon materials act as a support to the platinum catalyst. Electrodes are separated by a proton exchange membrane electrolyte, which is a thin sheet that allows protons to pass through but forbid the passage of electrons and heavier gases.

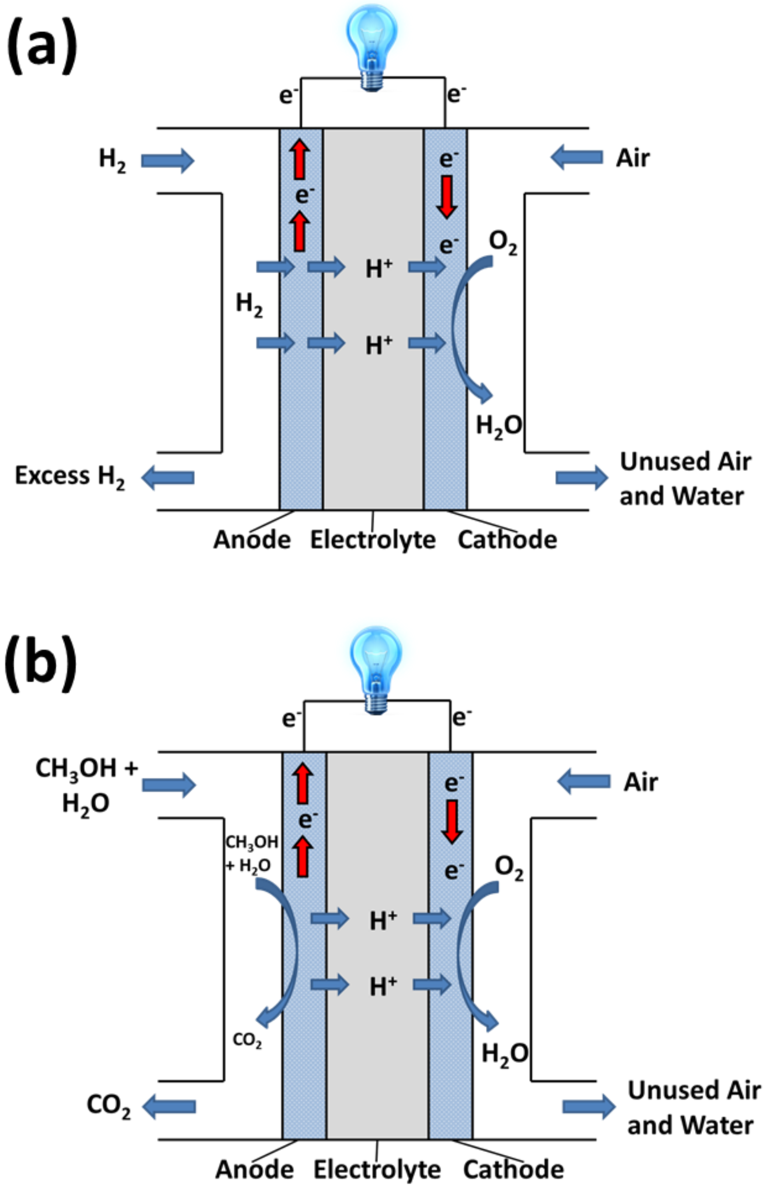

Figure 1.1: Schematic diagram of (a) PEMFC and (b) DMFC.

In the PEMFC, hydrogen gas is fed in the anode, where it dissociates into protons and electrons with the help of the catalyst (Figure 1.1a). However in DMFC, an aqueous methanol solution is feed at the anode as a fuel as shown in Figure 1.1b. In both the fuel cells, the positively charged protons pass through the electrolyte membrane and migrate toward the cathode. Meanwhile the electrons, with the help of carbon support, flow from the anode to the cathode via the external circuit. Therefore, the polymer electrolyte supports the ionic conductivity, whereas the carbon support improves the electric conductivity *[4]*. At the cathode, the protons, electrons (from the external circuit) and oxygen (from the air) combine to form water.

DMFC has some advantages over PEMFC as methanol is easy to store and handling liquid fuels is easier over gaseous hydrogen. Further, it is cheap compared to many other fuels. Besides, the hydrogen content per molecule is higher in methanol compared to that in hydrogen. However, there are certain advantages associated with PEMFC over DMFC also. As there are three different types of bond (C–H, O–H and C–O) present in methanol, the complexity of the dehydrogenation process arises whether the bond scission occurs via the C–H, O–H or C–O bonds. Moreover, the sequence of C-O, O–H and C–H bond activation depends on the catalyst *[5]* and therefore, the efficiency of the DMFC becomes crucial. Furthermore, due to presence of many reaction intermediates, the surface sites availability also becomes low, which thus lowers the efficiency of the fuel cell *[6]*. The CO poisoning is another major of concern in the case of DMFC *[7]*. In the following sections, we have discussed about the reaction mechanisms at the surface of Pt-nanocluster based electrodes. Further, we have given a brief overview about the conventional and nanomaterial based electrodes used for low-temperature fuel cells.

1.4. Electrode Reactions

1.4.1. Oxidation at Anode

Hydrogen and methanol oxidation reactions happen at the anode of PEMFC and DMFC, respectively.

1.4.1.1. Hydrogen oxidation reaction (HOR)

The gaseous hydrogen first adsorbs on the catalyst surface and undergoes for dissociation and followed by oxidation. The half-cell reaction for the oxidation process is:

$H_2 \rightarrow 2H^+ + 2e^- \quad E^0 = 0$ V

where E^0 is the standard half-cell potential based on a reversible hydrogen electrode (RHE). The reaction kinetics of the HOR on a Pt electrode is very fast *[8]*. Therefore, the main focus in PEMFC is to improve the reduction reaction at cathode to improve its performance.

1.4.1.2. Methanol oxidation reaction (MOR)

The electrochemical MOR is a 6-electron oxidation process. The liquid methanol is fed into the anode of the DMFC, where oxidation occurs. The half-cell reaction for this is as following:

$CH_3OH + H_2O \rightarrow CO_2 + 6H^+ + 6e^- \qquad E^0 = 0.02$ V/RHE

Although the thermodynamic potential for MOR is very close to HOR, the MOR is slower than HOR by several orders. This is because the MOR typically proceeds through a complicated reaction mechanism. Experimental identification of some stable surface products (CO), solution-phase product (CO_2), and surface intermediates (HCOO, HCHO and HCOH) have led to propose a dual-path mechanism for electrochemical methanol oxidation *[9-12]*:

- The direct path where methanol undergoes oxidation towards the direct formation of CO_2 (Scheme 1.1a).

- The indirect path where the oxidation reaction proceeds toward the formation of CO, which can undergo further oxidation for the formation of CO_2 (Scheme1.1b).

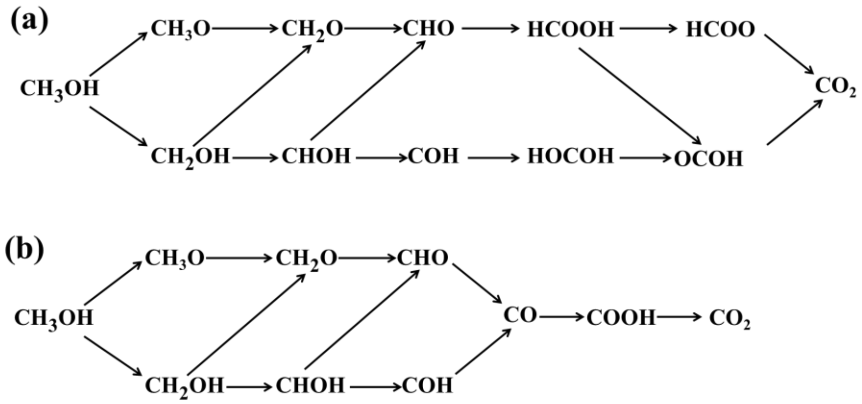

Scheme 1.1: Different proposed pathways for methanol oxidation: (a) direct and (b) indirect

Both the methanol oxidation pathways require the dissociation of C-H bond. So, a catalyst is important for the oxidation reaction. During the MOR, both the process may occur simultaneously. Although, the direct process is very much favored over the indirect one as the carbon monoxide strongly adsorbs on the surface of the Pt-catalyst. As a result, it reduces the number of available reaction sites, which subsequently affect the performance of DMFC.

Furthermore, the adsorption behavior of methanol on the surface of the catalyst is also very crucial for the overall process. It is widely expected that methanol tends to bind through its oxygen atom. However, due to the presence of π-electron cloud of >C=O bond, it influences the bonding of methanol on the catalyst surface. In this case, the unsaturation of the catalyst can play an important role. Some experimental studies *[13-14]* also reported that the >C=O group of methanol interacts parallel to the catalyst surface and the $–CH_3$ group is also inclined to the surface. Therefore, initial adsorption behavior of methanol can largely depend on the available adsorption sites of the catalyst. Due to the presence of many low-coordinated sites such as edge, terrace and vertex, there is a possibility that the π-cloud may interact with the catalysts surface, which might alter the reaction kinetics of the methanol decomposition. In the present thesis, the role of adsorption patterns of the reaction intermediates has been studied to understand the methanol dehydrogenation mechanism.

1.4.2. Reduction at Cathode

1.4.2.1. Oxygen reduction reaction (ORR)

ORR at cathode is the most important reaction in PEMFC. As the anodic process doesn't contain any overpotential, therefore ORR is the key reaction to improve the efficiency of the fuel cells. During the ORR, H_2O and H_2O_2 are the two end products, which are formed via four-electron ($4e^-$) and two-electron ($2e^-$) reduction reactions, respectively *[15]*.

$O_2 + 4H^+ + 4e^- = 2H_2O \quad E^0 = 1.23$ V/RHE

$O_2 + 2H^+ + 2e^- = H_2O_2 \quad E^0 = 0.69$ V/RHE

For the $4e^-$ reduction (H_2O formation), there are two mechanisms: i) associative and ii) dissociative *[16]*. In the associative mechanism, the reaction can precede via hydrogenation ($O_2 + H \rightarrow OOH$) followed by dissociation ($OOH \rightarrow O + OH$) and in the dissociative pathway, the adsorbed oxygen molecule (O_2) can undergo direct O-O bond dissociation ($O_2 \rightarrow O + O$). Then the end products are formed through subsequent hydrogenation and O-H bond formation steps. However, the associative pathway can happen via two pathways: (i) peroxyl and (ii) peroxide formations. In the peroxyl mechanism, the adsorbed oxygen molecule ($*O_2$) undergoes hydrogenation ($O_2 + H \rightarrow OOH$) followed by dissociation ($OOH \rightarrow O + OH$). Then the product (OH) can undergo subsequent hydrogenation for the formation of H_2O (major product). In the peroxide mechanism, OOH can undergo further hydrogenation for the formation of H_2O_2. This will be a two-electron reduction reaction if the end product is H_2O_2. However, H_2O_2 can further dissociate into OH, which can go for further protonation for the formation H_2O.

In fuel cells, four-electron reduction ($4e^-$) is preferred over a two-electron ($2e^-$) reduction in order to maximize the efficiency *[17]*. Furthermore, H_2O_2 formation affects the durability of the membrane of a PEM fuel cell by forming radical species *[1, 18]*. Thereby, the degree of the two different pathway reactions *i.e.* the product selectivity (H_2O vs. H_2O_2) is very important for the performance of a fuel

Cell and the development of the catalysts should be targeted towards the 4-electron reduction pathway. In this thesis, the attention has been devoted towards gaining the $4e^-$ pathway on different nanostructured based catalysts. In the following section, an overview of the catalysts used for ORR has been presented.

1.5. Catalysts

1.5.1. Bulk metal surface

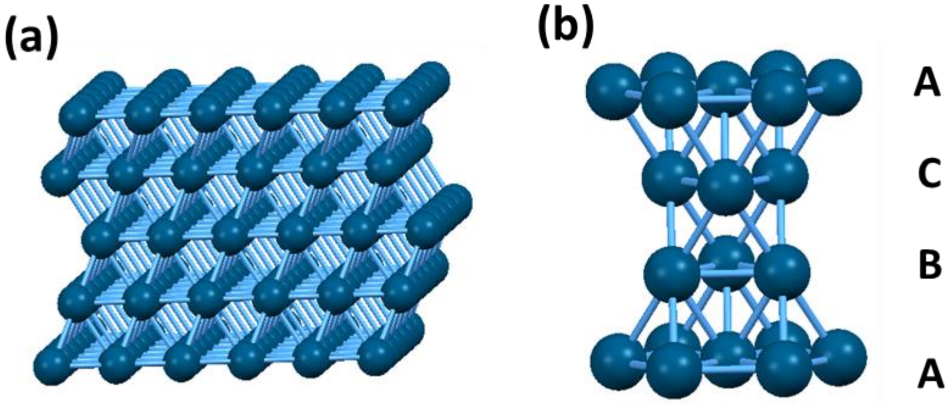

Figure 1.2: (a) Bulk Pt(111) surface and (b) face centered cubic arrangement of Pt(111) surface.

Bulk Pt(111) surface (Figure 1.2a) is the conventional catalyst for both the MOR and ORR *[1, 19]*. The (111) surface of platinum possess a face-centered cubic (fcc) structure. This exposes a surface with an atomic arrangement of 6-fold symmetry as has been shown in Figure 1.2b. The stacking pattern of fcc structure becomes in ABCABCA sequence.

1.5.2. Low-dimensional catalysts

1.5.2.1. Metal nanoclusters

Nanoclusters (NCs) are the aggregates of atoms or molecules having the size of 1-10 nanometers and consisting of up to a few hundred atoms. Though there are no clear cut separation between the definition of NC and nanoparticle, however the larger aggregates which contains 1000 or more atoms are generally called nanoparticles. Nano- and sub-nanoscale clusters are of huge interest because of their unusual properties and potential applications in next-generation devices like electronics *[20]*, magnetics *[21]* and catalysis *[22]*, which significantly differ from bulk materials. In this doctoral thesis, all the works are performed on Pt-based NCs due to the wide range of applications of Pt NCs in ORR, MOR and HOR. Further, mixed metal based NCs are promising for ORR. Such alloying with other metals leads to the formation of bimetallic catalysts like Pt skeleton *[23-24]*, Pt skin *[25]*, mixed alloy *[26-27]*, and core−shell structures *[28-30]*. Among them, core−shell-based (Figure 1.3) catalysts are very promising due to the easy tunability of the inside core and the presence of resistant shell layers for sustaining the harsh reaction conditions of fuel cells. It is widely accepted that mainly two mechanisms (ligand and strain effect) are responsible for the modification of the chemical properties of these surfaces *[31]*. In the ligand effect, the core atoms alter the chemical environment of the outside layer by modifying their electronic properties. In the strain effect, the chemical properties of the outside layer changes due to the modifications of the lattice parameters (bond length, bond angles) of outside layers. However, it is very difficult to separate the role of strain and ligand effects because most of the times the two effects occur together *[31]*. In the present thesis, the potential applicability of core-shell NC towards ORR has been investigated and the advantages of core-shell structure over conventional electrode have been studied in greater detail.

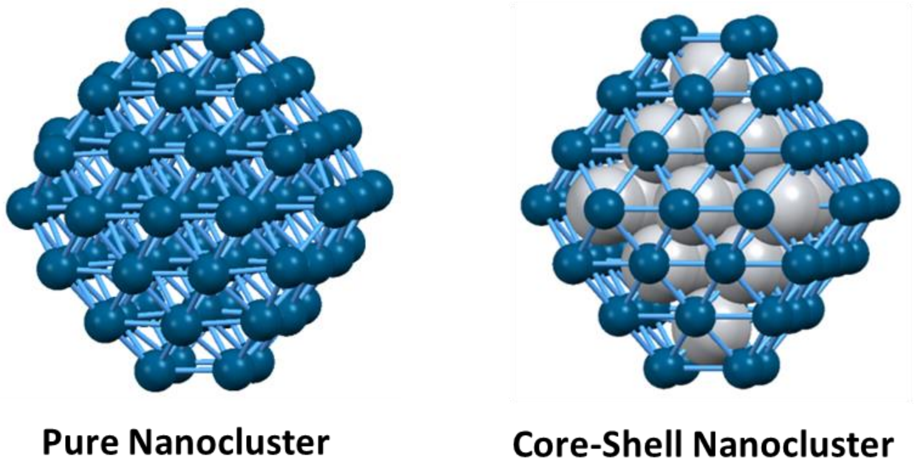

Figure 1.3: Cuboctahedral nanoclusters in the pure and core-shell form

Nanocages, nanoframes and nanoboxes have also attracted considerable attention due to their excellent catalytic activity with lower Pt-content. These structures have a void inside (Figure 1.4). Nanoframe consists of edge atoms only. The thickness of the edge is of around 1-5 nm *[32-34]*. High unsaturation in these structures makes them very reactive for catalytic reactions. Recently, experimental groups have synthesized Pt-based cubic, octahedral *[32]* and icosahedral nanocages *[33]* with well defined (111) and (100) facets. Other than Pt-based hollow nanoclusters, Pd-Rh nanoboxes *[34]* have been synthesized lately. Interestingly, such nanocages show superior ORR activity compared to the conventional Pt/C-based catalyst *[32-36]*. In the present thesis, a singled layered platinum-nanocage has been studied for ORR activity.

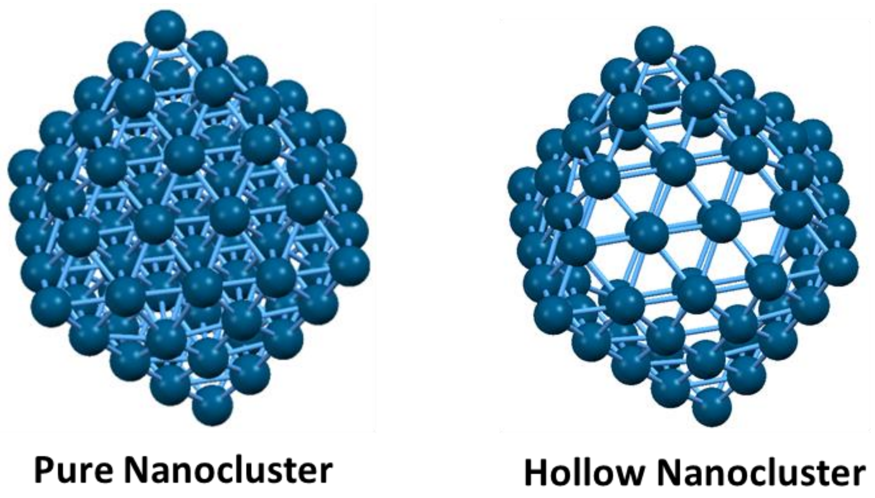

Pure Nanocluster

Hollow Nanocluster

Figure 1.4: Pure and hollow nanoclusters in octahedral geometry

Shape-dependent catalytic activity of NCs is another major area as the catalytic activity is very much selective to the shape of the catalyst. Transition metal NCs crystalizes in different shapes such as cubic, octahedral, cuboctahedral, truncated octahedral, icosahedral and so on. In case of cubic NCs, they are exposed with (100) facets only, whereas octahedral and icosahedral NCs are exposed with (111) facets. Cuboctahedral and truncated octahedral NCs contain both (100) and (111) facets (Figure 1.5). The stability of these catalysts is very much dependent on the exposed surface area, surface energy of the exposed facets, number of low-coordinated sites, and strain on the surface atoms. Apart from the stability, the catalytic activity is also very much shape dependent. The reactivity of the NCs depends on the type of the facets, and available low-coordinated reaction sites (edge, kink, vertex). El-Sayad and co-workers *[37]* have given the breakthrough by synthesizing a series of shape-controlled colloidal platinum nanoparticles in the shapes of tetrahedral, cubic, irregular-prismatic, icosahedral and cuboctahedral structures. Later on, extensive studies have been performed for the synthesis of shape-controlled well-defined Pt-nanocatalysts *[38-43]*. The shape of the catalyst is also very important for product selectivity such as benzene hydrogenation *[44]*, pyrrole hydrogenation *[45]*, butene isomerization *[46]*, glucose oxidation *[47]*, formic acid oxidation *[48]*, and CO oxidation *[49]* reactions. In this thesis, we have studied the shape-dependent ORR activity catalyzed by the cuboctahedral and octahedral NCs of similar size (Figure 1.5).

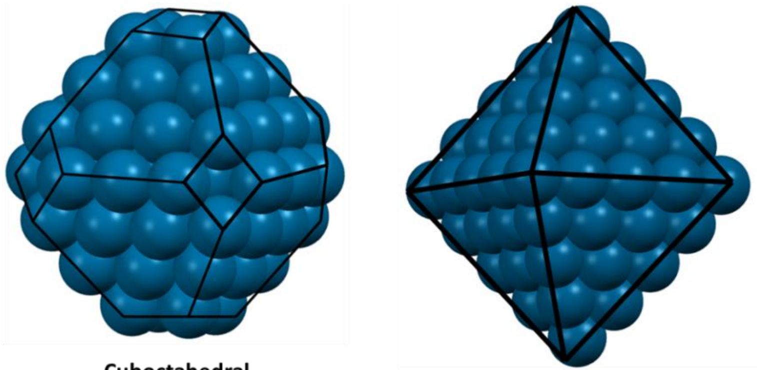

Cuboctahedral

Octahedral

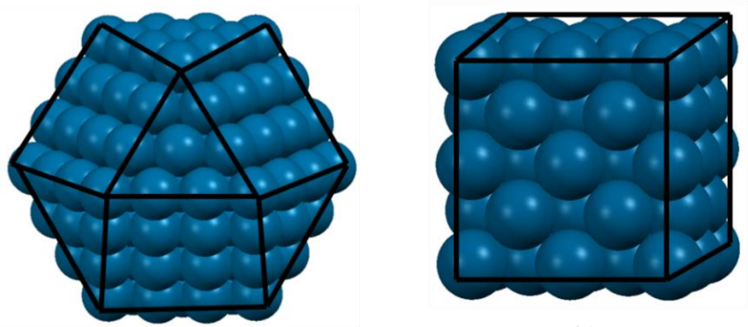

Turncated Octahedral

Cubic

Figure 1.5: Nanoclusters with different shapes

1.5.2.2. Metal nanosheets

Metallic nanosheet is another kind of active catalyst with lower Pt-content. Nanosheets are composed of few atomic layers to a thickness of 5 nm *[50]*. The nanosheets-based catalysts have been grown on a support material (generally over oxides or NCs surface) *[50-57]*. Free-standing nanosheets are also synthesized in the form of nanoplates *[55, 58]*. Interestingly, these ultrathin metallic layers are found be very active for ORR as well as for many oxidation-reduction reactions. Azdic and co-workers synthesized core-shell catalysts with a Pt monolayer shell and reported excellent ORR kinetics *[52]*. Wang and co-workers *[51]* synthesized free-standing ultrathin Pt−Cu alloy nanosheets of 4−6 atom thickness, which exhibits exhibit excellent electrocatalytic activities for the oxidation of ethanol in comparison to commercial Pt black and Pt/C catalysts. High energy Pt(110) surface based sheets have been synthesized lately. In fact, such high-energy based nanosheets are found to be very much active for catalytic reaction. Very recently, Bu et al. *[58]* synthesized (110) faceted core-shell based nanosheets with a low (0.8-1.2 Å) Pt-shell thickness. In the present thesis, we have shown that free-standing platinum monolayer improves ORR activity significantly.

1.6. Theory

This part of the chapter briefly describes about the fundamental theory and computational techniques used in all the works presented in the thesis.

1.6.1. The Many-Body Problem

Solid state materials are composed of multiple numbers of nuclei and electrons. In this kind of many-body systems, Schrödinger Equation is the basic tool for calculating their properties (electron-electron, electron-nucleus and nucleus-nucleus interactions). Hence, the Schrödinger equation of the many body system is the fundamental theory of the electronic structural calculations. Usually, the time independent Schrödinger Equation is used to evaluate these properties and can be expressed as follows

$$\mathrm{H}\Psi(\mathrm{r},\mathrm{R}) = \mathrm{E}\Psi(\mathrm{r},\mathrm{R}) \qquad (1.1)$$

where H is the Hamiltonian which describes all the interactions of the system, E is the total energy of the system and Ψ is the wave function which contains the information of the nuclei and electrons of the atoms. The Hamiltonian operator is expressed as follows

$$H = -\frac{h^2}{2m_e}\sum_i \nabla_i^2 - \sum_I \frac{h^2}{2M_I}\nabla_I^2 + \frac{1}{2}\sum_{i\neq j}\frac{e^2}{|\boldsymbol{r_i}-\boldsymbol{r_j}|} + \frac{1}{2}\sum_{I\neq J}\frac{Z_I Z_J e^2}{|\boldsymbol{R_I}-\boldsymbol{R_J}|} - \sum_{i,I}\frac{Z_I e^2}{|\boldsymbol{r_i}-\boldsymbol{R_I}|} \qquad (1.2)$$

where m_e and $\boldsymbol{r}_i$ are the mass and position of the electron, whereas M_I, R_I and Z_I are the masses of the nuclei, it's position and nuclear charges, respectively. The first and second term in this equation represents the kinetic energy of the electrons and the nuclei, respectively. The following terms are corresponding to the electron-electron repulsion, nuclei-nuclei repulsion and the electrons-nuclei attractive interaction, respectively.

However, to solve the Schrödinger Equation using the above Hamiltonian is practically impossible for the many-electron system. Therefore, it is very important to employ some approximations. The Born-Oppenheimer (BO) approximation *[59]* is most extensively used for this purpose.

According to the BO approximation, as the nuclei is 1836 times heavier than the electron, the speed of the nuclei is assumed to be stationary compared to the electron. Therefore, the kinetic energy of the nuclei can be neglected while comparing with the kinetic energy of electron. Therefore the Hamiltonian of the electron can be approximated as follows

$$H = -\frac{h^2}{2m_e}\sum_i \nabla_i^2 + \frac{1}{2}\sum_{i\neq j}\frac{e^2}{|\boldsymbol{r}_i-\boldsymbol{r_j}|} - \sum_{i,I}\frac{Z_I e^2}{|\boldsymbol{r}_i-\boldsymbol{R_I}|} \qquad (1.3)$$

Even after applying the BO approximation, the solution is computationally unaffordable for many electron systems. Therefore, the electron-electron interaction of the above equation requires further approximation. In this context, other approximation like density functional theory (DFT) is extremely useful and has been discussed in the following sections.

1.6.2. Density Functional Theory (DFT)

DFT is a quantum-mechanical method, which is used for investigating the electronics structure of many-body systems. DFT has been emerged as an indispensable tool in the wide research areas of computational material science. In the following, an overview of the basic principles of DFT is discussed.

1.6.2.1. The Hohenberg-Kohn theorems

DFT is based on the two theorems proposed by P. Hohenberg and W. Kohn *[60, 61]*.

Theorem 1: The first theorem states that the ground state properties of many electron systems can be evaluated by the electron density $n(\boldsymbol{r})$ of the interacting electrons moving under the external potential of $V_{ext}(\boldsymbol{r})$. Basically, the ground-state energy of Schrödinger's equation is a unique functional of the electron density $n_0(\boldsymbol{r})$.

Theorem 2: The second theorem talks about the universal total energy functional $E[n]$ in terms of particle density $n(\boldsymbol{r})$ under the external potential of $V_{ext}(\boldsymbol{r})$. The functional can be written as

$$E[\rho(\boldsymbol{r})] = E_{HK}[\rho(\boldsymbol{r})] + \int V_{ext}(\boldsymbol{r})\rho(\boldsymbol{r})d\boldsymbol{r} \tag{1.4}$$

where $E_{HK}[\rho(\boldsymbol{r})]$ represents the internal and kinetic energies of the all interacting particles of the system.

The ground state energy of a system can be obtained only if the functional of the electron density which actually minimizes the energy of the system, become the true ground state density $n_0(\boldsymbol{r})$. However, the exact form of the functional of the electron density was not clear from the theorems.

1.6.2.2. Kohn-Sham equations

Kohn and Sham derived a new set of equations to describe the Hohenberg-Kohn theorems. In the equations (Kohn-Sham equation), the complex many-body problem is replaced by the simple single particle non-interacting problems. These single particles are described by an effective potential $V(\boldsymbol{r}_i)$, called as Kohn-Sham potential. The total ground state energy can be written as

$$E[\rho(r)] = T_0[\rho(r)] + \frac{1}{2}\iint \frac{\rho(r)\rho(r)' dr dr'}{|r-r'|} + \int V_{ext}(r)\rho(r)dr + E_{xc}[\rho(r)dr] + E_{II}$$

(1.5)

in which the first term is the kinetic energy of the non-interacting electrons; the second term is the classical electron-electron Coulomb interaction (Hatree energy); the third term is the potential energy representing the interaction between valence electrons and the core electrons; the fourth one is the exchange-correlation interaction that considers all non-classical many-body effects between electrons. The last term stands for the nuclei-nuclei interaction. The above equation can be further reduced as

$$\left[-\frac{1}{2}\nabla^2 + V_{eff}(r)\right]\Psi_i(r) = E_i\Psi_i(r) \tag{1.6}$$

where $\Psi_i(r)$ stands for the Kohn-Sham orbitals instead of wave function, whereas V_{eff} can be represented as

$$V_{eff} = V_{Hartree} + V_{ext} + V_{xc} \tag{1.7}$$

It means that the effective potential can be represented in the forms of external potential, Coulomb interaction and the exchange correlation contribution. Therefore, the energy of many-body problem can be solved if the exchange correlation potential is known. However, the exchange correlation interaction is not easy to solve therefore different approximations are used to solve this problem. These approximations are extensively used for the simulation of molecular and solid state problems *[42]*.

1.6.2.3. Exchange-correlation functional

The unknown parameter in the above equation is the exchange-correlation functional term, which must be approximated for the practical use of Kohn-Sham equation. The exchange-correlation $E_{xc}\big(n(\boldsymbol{r})\big)$ part can be divided into exchange and correlations part, which are as follows

$$E_{xc}\big(n(\boldsymbol{r})\big) = E_x\big(n(\boldsymbol{r})\big) + E_c\big(n(\boldsymbol{r})\big) \tag{1.8}$$

Based on the electron density, the exchange correlation energy functional $E_{xc}(n(\boldsymbol{r}))$ can be approximated by some local functional. The main approximations for the exchange correlation are stated below.

1.6.2.4. Local Density Approximation (LDA)

In the LDA approximation *[62, 63]*, the exchange-correlation functional is derived from the homogeneous electron gas and can be defined as

$$E_{xc}^{LDA} = \int d^3r\, n(\boldsymbol{r})\, \mathcal{E}_{xc}^{hom}(n(\boldsymbol{r})) \tag{1.9}$$

where $\mathcal{E}_{xc}^{hom}(n(\boldsymbol{r}))$is the exchange-correlation energy per partical in a homogeneous gas with electron density $n(\boldsymbol{r})$.

LDA approximation is extensively used to determine the ground state properties of the solid state materials. The LDA works well in the system with a slowly varying density. It is found that LDA works well in the cases where even charge density varies quickly with some limitations while calculating some thermodynamic and electronic properties. It overestimates the cohesive energy, bond dissociation energy and adsorption energies in comparison to experimental values. Besides, it underestimates the experimental values significantly while calculating the band gap of semiconductor and insulator *[64]*.

1.6.2.5. Generalized Gradient Approximation (GGA)

In the GGA approximation, the gradient of electron density used to calculate the exact exchange energy. The exchange-correlation function based on generalized gradient approximation is expressed as follows:

$$E_{xc}^{GGA} = \int d^3r\, n(\boldsymbol{r})\, \mathcal{E}_{xc}^{GGA}\big(n(\boldsymbol{r}), \nabla n(\boldsymbol{r})\big) \tag{1.10}$$

The GGA approximation works nicely for the systems where the electron density electron density varies rapidly and has been found to provide accurate results while calculating the total energies, adsorption energies, lattice parameters etc. The most commonly used GGA approximation has been developed by Perdew, Burke and Ernzerhof (PBE). The exchange energy of PBE approximation in defined as follows.

$$E_x^{PBE} = \int d^3r\, n(\boldsymbol{r})\, \varepsilon_x^{PBE}\big(n(\boldsymbol{r}), s(\boldsymbol{r})\big) \tag{1.11}$$

The PBE exchange energy density is the product of LDA exchange and enhancement factor F_x^{PBE} which depends on $s(\boldsymbol{r})$.

$$\varepsilon_x^{PBE}\big(n(\boldsymbol{r}), s(\boldsymbol{r})\big) = \varepsilon_x^{LDA}\big(n(\boldsymbol{r})\big) * F_x^{PBE}\,\big(s(\boldsymbol{r})\big) \tag{1.12}$$

Apart from PBE, other GGA approximation like Perdew and Wang (PW91), revised PBE, PBEsol are also available *[65-67]*.

1.6.2.6. Projector Augmented Wave (PAW) Method

The electronic wave function behaves differently for the core and valance electrons because the positions of the electrons are different for core and valance electrons from the nuclei. The wave function oscillates rapidly for the core electrons where as smooth for the valance electrons. The valance electrons (outside the augmented region) are described by plane waves or other convenient basis set. However in the core region, it is computationally costly to describe the wave function using plane waves. Thus, the projector augmented-wave method (PAW) method *[68-71]* uses a partial wave expansion for describing the electrons in the augmented region.

The PAW technique transforms the oscillating wave function into a smother one. This is based upon a linear transformation operator(T), which transfers the all electron wave function, $\boldsymbol{\Psi_n}$ to a pseudo wave function, $\boldsymbol{\widetilde{\Psi}_n}$

$$|\boldsymbol{\Psi_n}\rangle = T|\boldsymbol{\widetilde{\Psi}_n}\rangle \tag{1.13}$$

Both $|\boldsymbol{\Psi_n}\rangle$ and $|\boldsymbol{\widetilde{\Psi}_n}\rangle$ can be represented as linear combination of partial waves for each augmentation regions,

$$|\mathbf{\Psi_n}\rangle = \sum_i c_i | \phi_i\rangle \tag{1.14}$$

$$|\widetilde{\mathbf{\Psi}}_\mathbf{n}\rangle = \sum_i c_i | \tilde{\phi}_i\rangle \tag{1.15}$$

The transformation operator, T is defined as

$$T = 1 + \sum_i (|\phi_n\rangle - |\tilde{\phi}_n\rangle) \langle \tilde{p}_i| \tag{1.16}$$

where $\langle \tilde{p}_i|$ is the projection function which can be initiated from different practical schemes. The pseudopotential simplifies the problems related to core and valance electrons. Therefore there are different types of pseudopotential available in order to transform the rapidly oscillating wave function into a smoother one *[68]*. The PAW method has combined the features of ultra-soft pseudopotentials *[71]* and linear augmented-plane-wave [69] methods. In this thesis work, the PAW method has been used as implemented in the Vienna *ab-initio* simulation package (VASP) *[72]*.

1.6.3. Other computational tools

1.6.3.1. *Ab initio* molecular dynamics

Ab Initio Molecular dynamics (AIMD) is a computational technique for investigating the effects of temperature on the dynamical behavior of the materials. Unlike with classical molecular dynamics (CMD), where the forces on the atoms are obtained from the generated model potentials following Newton's equation of motion, the AIMD uses the forces that are obtained from DFT calculations. Due to its huge computational cost, the application of AIMD is currently limited to a few hundreds of atoms.

In the doctoral thesis, the AIMD simulations are carried out using canonical ensemble (NVT) at different temperature with a time step of 1 femtosecond. Temperature control is achieved by Nosé thermostat model *[73]*. In addition, the root mean square deviation (RMSD) has helped to investigate the atomic displacements during the thermal treatment of the materials. The RMSD of the individual atom in the material system can be expressed in the following way:

$$RMSD = \sqrt{\frac{\sum_{i=1}^{N}[r_i(t_1)-r_i(t_2)]^2}{N}} \quad (1.17)$$

where N is the number of atoms in the simulation box whose positions are being compared and r_i is the position of i-th atom at time t.

1.6.3.2. Nudged Elastic Band (NEB) method

Finding the reaction rates of chemical reactions or diffusion events is a major concern in the area of theoretical chemistry and condensed matter physics. The NEB is a method for finding saddle point and minimum energy path (MEP) between the reactant and product of a reaction. NEB is widely accepted for estimating transition rates where a harmonic approximation of transition state theory (hTST) is used *[74]*. The rate constant for the transition around the saddle points can be defined as

$$k^{hTST} = \frac{\prod_i^{3N} v_i^{init}}{\prod_i^{3N-1} v_i^{\ddagger}} e^{-(E^{\ddagger}-E^{init})/k_B T} \quad (1.18)$$

where $E^{\ddagger}$ and E^{init} are the energies of the saddle point and initial state, respectively. v_i^{init} and $v_i^{\ddagger}$ are the normal mode frequencies for the initial and saddle point, respectively. The NEB method optimizes a number of intermediate images along the reaction path, where each image finds the possible lowest energy structure with maintaining an equal spacing to their neighboring images. This kind of local optimization (constrained) is done by adding spring forces along the band between images. In this thesis, the images are created using the program developed by Henkelmann *[75]*.

Unlike with other elastic band methods, the NEB method uses a force projection, which does not allow interfering the spring forces with the convergence of the elastic band to the MEP. Further, it also assures that that the true force does not affect the distribution of images along the MEP. For getting the saddle point, it is very important to decompose the true force and the spring force into components parallel and perpendicular to the path. This kind of force projection is referred as ‘‘nudging’’ and the spring forces only control the spacing of the images along the band.

1.6.3.3. Bader charge

Bader charge analysis is an intuitive way of dividing molecules into atoms for calculating the electronic charges on individual atoms in molecules or crystals, based on the Bader partitioning scheme *[76]*. The analysis is purely based on the electronic charge density. In this analysis, the partitioning of the density is determined according to its zero-flux surfaces (2-D surface on which the charge density is a minimum perpendicular to the surface). The charge distribution can be used to determine multipole moments of interacting atoms or molecules.

In the present thesis, we have used an algorithm developed by the Henkelman group *[77]*. This is a fast algorithm for doing Bader's analysis on a charge density grid. The algorithm is presented for carrying out the decomposition of electronic charge density into atomic contributions.

1.6.3.4. Phonon dispersion

The concept of lattice dynamics mainly deals with the collective vibration of atoms in the crystal, forming a wave of allowed wavelength and amplitude. The normal modes of vibration in a solid considered as quantum particle which is called as phonon. Lattice dynamics seeks to calculate the energies (or frequencies) of the phonons as a function of their wave vectors. The relationship between frequency of phonon and wave vectors is called phonon dispersion.

In this thesis work, the Phonopy code *[78]* is used to calculate phonon properties through the density functional perturbation theory (DFPT) *[79]*. Phonon frequency of a lattice is such a physical property which depends upon a system response to some form of perturbation. The external perturbations of the system may be calculated using DFT with the addition of some perturbing potential.

1.7. References

1. Jiao Y., Zheng Y., Jaroniec M, Qiao S. Z. (2015), Design of electrocatalysts for oxygen- and hydrogen-involving energy conversion reactions, Chem. Soc. Rev., 44, 2060-2086. (DOI: 10.1039/C4CS00470A)

2. Antolini E. (2009), Carbon supports for low-temperature fuel cell catalysts, Applied Catalysis B: Environmental, 88, 1–24, (DOI: 10.1016/j.apcatb.2008.09.030)

3. Litster S., McLean G. (2004), PEM fuel cell electrodes, J. Power Sources, 130, 61–76. (DOI: 10.1016/j.jpowsour.2003.12.055)

4. Gasteiger H. A., Panels J. E., Yan S. G. (2004), Dependence of PEM fuel cell performance on catalyst loading, 127, 162-171. (DOI: 10.1016/j.jpowsour.2003.09.013)

5. Moura A. S., Fajín J. L. C., Pinto A. S. S., Mandado M., Cordeiro M. N. D. S. (2015), Competitive Paths for Methanol Decomposition on Ruthenium: A DFT Study, J. Phys. Chem. C, 119, 27382–27391. (DOI: 10.1021/acs.jpcc.5b06671)

6. Batista E. A., Malpass G. R. P., Motheo A. J., Iwasita T. (2003) , New insight into the pathways of methanol oxidation, Electrochem. Commun., 5, 843–846. (DOI: 10.1016/j.elecom.2003.08.010)

7. Chung D. Y., Kim H., Chung Y., Lee M. J., Yoo S. J., Bokare A. D., Choi W., Sung Y. (2014), Inhibition of CO poisoning on Pt catalyst coupled with the reduction of toxic hexavalent chromium in a dual-functional fuel cell, Scientific Reports, 4, 7450. (DOI: 10.1038/srep07450)

8. Strmcnik1 D., Uchimura M., Wang C., Subbaraman R., Danilovic N., Vliet D., Paulikas A. P., Stamenkovic V. R., Markovic N. M. (2013), Improving the hydrogen oxidation reaction rate by promotion of hydroxyl adsorption, Nature Chemistry 5, 300–306. (DOI:B10.1038/nchem.1574)

9. Herrero E., Chrzanowski W., Wieckowski A. (1995), Dual Path Mechanism in Methanol Electrooxidation on a Platinum Electrode, J. Phys. Chem., 99, 10423-10424, (DOI: 10.1021/j100025a054)

10. Cao D., Lu G.-Q., Wieckowski A., Wasileski S. A., Neurock M. (2005), Mechanisms of Methanol Decomposition on Platinum: A Combined Experimental and ab Initio Approach, J. Phys. Chem. B, 109, 11622-11633, (DOI: 10.1021/jp0501188)

11. Iwasita T. (2002), Electrocatalysis of methanol oxidation, Electrochimica Acta, 47, 3663-3674. (DOI: 10.1016/S0013-4686(02)00336-5)

12. Breiter M. (1967), On the nature of reduced carbon dioxide, Electrochim. Acta, 12, 1213-1218. (DOI: 10.1016/0013-4686(67)80036-7)

13. Skoplyak O., Menning C. A., Barteau M. A., Chen J. G. (2007), Experimental and theoretical study of reactivity trends for methanol on Co/Pt(111)Co/Pt(111) and Ni/Pt(111)Ni/Pt(111) bimetallic surfaces, J. Chem. Phys., 127, 114707. (DOI: 10.1063/1.2768520)

14. Peremans A., Maseri J., Darville J., Gilles J. M. (1990), Interaction of methanol with a polycrystalline platinum surface studied by infrared reflection absorption spectroscopy, Sur. Sci., 227, 73-78. (DOI: 10.1016/0039-6028(90)90393-M)

15. Yeager E. (1986), Dioxygen electrocatalysis: mechanisms in relation to catalyst structure, J. Mol. Catal., 38, 5. (DOI: 10.1016/0304-5102(86)87045-6)

16. Noh S. H., Kwak D. H., Seo M. H., Ohsaka T., Han B. (2014), First principles study of oxygen reduction reaction mechanisms on N-doped graphene with a transition metal support, Electrochimica Acta, 140, 225–231, (DOI: 10.1016/j.electacta.2014.03.076)

17. de Bruijn F. A., Dam V. A. T., Janssen G. J. M. (2008), Review: durability and degradation issues of PEM fuel cell components, Fuel Cells, 8, 3-22. (DOI: 10.1002/fuce.200700053)

18. Sanchez-Sanchez C. M., Bard A., (2009), Hydrogen peroxide production in the oxygen reduction reaction at different electrocatalysts as quantified by scanning electrochemical microscopy, J. Anal. Chem., 81, 8094-8100. (DOI: 10.1021/ac901291v)

19. E.A. Batista, G.R.P. Malpass, A.J. Motheo, T. Iwasita, New mechanistic aspects of methanol oxidation, Journal of Electroanalytical Chemistry 571 (2004) 273–282, doi:10.1016/j.jelechem.2004.05.016

20. Osada M., Sasaki T. (2012), Two-Dimensional Dielectric Nanosheets: Novel Nanoelectronics From Nanocrystal Building Blocks, Adv. Mater., 24, 210-228. (DOI: 10.1002/adma.201103241)

21. Zhang X., Zhang J., Zhao J., Pan B., Kong M., Chen J., Xie Y. (2012), Half-metallic ferromagnetism in synthetic Co9Se8 nanosheets with atomic thickness, J. Am. Chem. Soc., 134, 11908-11911. (DOI: 10.1021/ja3046603)

22. Song F., Hu X. (2014), Exfoliation of layered double hydroxides for enhanced oxygen evolution catalysis, Nat. Commun., 5, 4477. (DOI: 10.1038/ncomms5477)

23. Stamenkovic V. R., Mun B. S., Mayrhofer K. J. J., Ross P. N., Markovic N. M. (2006), Effect of surface composition on electronic structure, stability, and electrocatalytic properties of Pt-transition metal alloys: Pt-skin versus Pt-skeleton surfaces. J. Am. Chem. Soc., 128, 8813–8819. (DOI: 10.1021/ja0600476)

24. Johansson T. P., Ulrikkeholm E. T., Hernandez-Fernandez P., Malacrida P., Hansen H. A., Bandarenka A. S., Nørskov J. K., Rossmeisl J., Stephens I. E. L., Chorkendorff I. (2014), Pt skin versus Pt skeleton structures of Pt_3Sc as electrocatalysts for oxygen reduction. Top Catal., 57, 245–254. (DOI: 10.1007/s11244-013-0179-y)

25. Wang C., Chi M., Li D., Strmcnik D., Vliet D., Wang G., Komanicky V., Chang K., Paulikas A. P., Tripkovic D., Pearson J., More K. L., Markovic N. M., Stamenkovic V. R. (2011), Design and synthesis of bimetallic electrocatalyst with multilayered Pt-skin surfaces. J. Am. Chem. Soc., 133, 14396–14403. (DOI: 10.1021/ja2047655)

26. Tang W. J., Zhang L., Henkelman G. (2011), Catalytic activity of Pd/Cu random alloy nanoparticles for oxygen reduction. J. Phys. Chem. Lett., 2, 1328–1331. (DOI: 10.1021/jz2004717)

27. Holewinski A., Idrobo J., Linic S. (2014), High-performance Ag–Co alloy catalysts for electrochemical oxygen reduction. Nat. Chem., 6, 828–834. (doi:10.1038/nchem.2032)

28. Wang J. X., Inada H., Wu L., Zhu Y., Choi Y., Liu P., Zhou W. P., Adzic R. R. (2009), Oxygen reduction on well-defined core - shell nanocatalysts: particle size, facet, and Pt shell thickness effects. J. Am. Chem. Soc., 131, 17298–17302. (DOI: 10.1021/ja9067645)

29. Oezaslan M., Hasché F., Strasser P. (2013), Pt-Based Core–Shell Catalyst Architectures for Oxygen Fuel Cell Electrodes, J. Phys. Chem. Lett., 4, 3273-3291. (DOI: 10.1021/jz4014135)

30. Mazumder V., Chi M., More K. L., Sun S. (2010), Core/shell Pd/FePt nanoparticles as an active and durable catalyst for the oxygen reduction reaction, J. Am. Chem. Soc., 132, 7848-7849. (DOI: 10.1021/ja1024436)

31. J. R. Kitchin, J. K. Nørskov, M. A. Barteau, and J. G. Chen, (2004) Role of Strain and Ligand Effects in the Modification of the Electronic and Chemical Properties of Bimetallic Surfaces, Phys. Rev. Lett. 93, 156801 (DOI: 10.1103/PhysRevLett.93.156801)

32. Zhang L., Roling L. T., Wang X., Vara M., Chi M., Liu J., Choi S., Park J., Herron J. A., Xie Z., Mavrikakis M., Xia Y. (2015), Platinum-based nanocages

with subnanometer-thick walls and well-defined, controllable facets, Science, 349, 412-416. (DOI: 10.1126/science.aab0801)

33. Wang X., Figueroa-Cosme L., Yang X., Luo M., Liu J., Xie Z., Xia Y. (2016), Pt-Based Icosahedral Nanocages: Using a Combination of {111} Facets, Twin Defects, and Ultrathin Walls to Greatly Enhance Their Activity toward Oxygen Reduction, Nano Lett., 16, 1467-1471. (DOI: 10.1021/acs.nanolett.5b05140)

34. Popa A., Samia A. C. S. (2014), Effect of metal precursor on the growth and electrochemical sensing properties of Pt–Ag nanoboxes, Chem. Commun., 50, 7295-7298. (DOI: 10.1039/C4CC01927J)

35. Mahmoud M. A., O'Neil D., El-Sayed M. A. (2014), Hollow and Solid Metallic Nanoparticles in Sensing and in Nanocatalysis, Chem. Mater., 26, 44-58. (DOI: 10.1021/cm4020892)

36. Fang Z., Wang Y., Liu C., Chen S., Sang W., Wang C., Zeng J. (2015), Rational Design of Metal Nanoframes for Catalysis and Plasmonics, Small, 11, 2593-2605. (DOI: 10.1002/smll.201402799)

37. Ahmadi T. S., Wang Z. L., Green T. C., Henglein A., El-Sayed M. A. (1996), Shape-controlled synthesis of colloidal platinum nanoparticles, Science., 272, 1924.

38. Wang C., Daimon H., Onodera T., Koda T., Sun S. (2008), A General Approach to the Size- and Shape-Controlled Synthesis of Platinum Nanoparticles and Their Catalytic Reduction of Oxygen, Angew. Chem. Int. Ed., 47, 3588-3591. (DOI: 10.1002/anie.200800073)

39. Sanchez C. M., Solla-Gullon J., Vidal-Iglesias F. J., Aldaz A., Montiel V., Herrero E. (2010), Imaging Structure Sensitive Catalysis on Different Shape-Controlled Platinum Nanoparticles, J. Am. Chem. Soc., 132, 5622-5624. (DOI: 10.1021/ja100922h)

40. Zhang J., Yang H., Fang J., Zou S. (2010), Synthesis and Oxygen Reduction Activity of Shape-Controlled Pt3Ni Nanopolyhedra, Nano Lett., 10, 638-644. (DOI: 10.1021/nl903717z)

41. Lim B., Jiang M., Tao J., Camargo P. H. C., Zhu Y., Xia Y. (2009), Shape-Controlled Synthesis of Pd Nanocrystals in Aqueous Solutions, Adv. Funct. Mater., 19, 189-200. (DOI: 10.1002/adfm.200801439)

42. Xia B. Y., Wu H. B., Wang X., Lou X. W. (2013), Index Facets and Enhanced Electrocatalytic Properties, Angew. Chem. Int. Ed., 52, 12337-12340. (DOI: 10.1002/anie.201307518)

43. Tang Y., Cheng W. (2013), Nanoparticle-Modified Electrode with Size- and Shape-Dependent Electrocatalytic Activities, Langmuir, 29, 3125-3132. (DOI: 10.1021/la304616k)

44. Bratlie K. M., Lee H., Komvopoulos K., Yang P., Somorjai G. A. (2007), Platinum Nanoparticle Shape Effects on Benzene Hydrogenation Selectivity, Nano Lett., 7, 3097-3101. (DOI: 10.1021/nl0716000)

45. Tsung C. K., Kuhn J. N., Huang W., Aliaga C., Hung L. I., Somorjai G. A., Yang P. (2009), Sub-10 nm Platinum Nanocrystals with Size and Shape Control: Catalytic Study for Ethylene and Pyrrole Hydrogenation, J. Am. Chem.Soc., 131, 5816-5822. (DOI: 10.1021/ja809936n)

46. Lee I., Delbecq F., Morales R., Albiter M. A., Zaera F. (2009), Tuning selectivity in catalysis by controlling particle shape, Nat.Mater., 8, 132-138. (DOI: 10.1038/nmat2371)

47. Wang J., Gong J., Xiong Y., Yang J., Y Gao., Liu Y., Lu X., Tang Z. (2011), Shape-dependent electrocatalytic activity of monodispersed gold nanocrystals toward glucose oxidation, Chem. Commun, 47, 6894-6896. (DOI: 10.1039/C1CC11784J)

48. Zhang X., Yin H., Wang J., Chang L., Gao Y., Liu W., Tang Z. (2013), Shape-dependent electrocatalytic activity of monodispersed palladium nanocrystals toward formic acid oxidation, Nanoscale., 5, 8392-8397. (DOI: 10.1039/C3NR03100D)

49. Wang R., He H., Liu L. C., Dai H. X., Zhao Z. (2012), Shape-dependent catalytic activity of palladium nanocrystals for the oxidation of carbon monoxide, Catal. Sci. Technol., 2, 575-580. (DOI: 10.1039/C2CY00417H)

50. Duan H., Yan N., Yu R., Chang C., Zhou G., Hu H., Rong H., Niu Z., Mao J., Asakura H., Tanaka T., Dyson P. J., Li J., Li Y. (2014), Ultrathin rhodium nanosheets, Nat. Commun., 5, 3093. (DOI: 0.1038/ncomms4093)

51. Saleem F., Zhang Z., Xu B., Xu X., He P., Wang X. (2013), Ultrathin Pt–Cu nanosheets and nanocones, J. Am. Chem. Soc., 135, 18304-18307. (DOI: 10.1021/ja4101968)

52. Chen G., Kuttiyiel K. A., Su D., Li M., Wang C., Buceta D., Du C., Gao Y., Yin G., Sasaki K., Vukmirovic M. B., Adzic R. R. (2016), Oxygen reduction kinetics on Pt monolayer shell highly affected by the structure of bimetallic AuNi cores, Chem. Mater., 28, 5274-5281. (DOI: 10.1021/acs.chemmater.6b00500)

53. Kuttiyiel K. A., Sasaki K., Choi Y., Su D., Liu P., Adzic R. R. (2012), Bimetallic IrNi core platinum monolayer shell electrocatalysts for the oxygen reduction reaction, Energy Environ. Sci., 5, 5297-5304. (DOI: 10.1039/C1EE02067F)

54. Zhang H. (2015), Ultrathin Two-Dimensional Nanomaterials, ACS Nano., 9, 9451-9469. (DOI: 10.1021/acsnano.5b05040)

55. Ling T., Wang J., Zhang H., Song S., Zhou Y., Zhao J., Du X. (2015), Freestanding ultrathin metallic nanosheets: materials, synthesis, and applications, Adv. Mater., 27, 5396-5402. (DOI: 10.1002/adma.201501403)

56. Zhang X., Lu Z., Yang Z. (2016), A comparison study of oxygen reduction on the supported Pt, Pd, Au monolayer on WC (0001), J. Power Sources., 321, 163-173. (DOI: 0.1016/j.jpowsour.2016.04.135)

57. Zhang Y., Hsieh Y., Volkov V., Su D., An W., Si R., Zhu Y., Liu P., Wang J. X., Adzic R. R. (2014), High Performance Pt Monolayer Catalysts Produced via Core-Catalyzed Coating in Ethanol, ACS Catal., 4,738-742. (DOI: 10.1021/cs401091u)

58. L. Bu, N. Zhang, S. Guo, X. Zhang, J. Li, J. Yao, T. Wu, G Lu, J. Ma, D. Su, X. Huang, Biaxially strained PtPb/Pt core/shell nanoplate boosts oxygen reduction catalysis, Science 354, 1410-1414. (DOI: 10.1126/science.aah6133)

59. Born M., Oppenheimer J. (1927), Zur Quantentheorie der Molekeln, J. Ann. Physik, 84, 457. (DOI: 10.1002/andp.19273892002)

60. Hohenberg P., Kohn W. (1964), Inhomogeneous electron gas, Phys. Rev. B, 136, B864. (DOI: 10.1103/PhysRev.136.B864)

61. Kohn W., Sham L. J. (1965), Self-Consistent Equations Including Exchange and Correlation Effects, Phys. Rev.., 140, 1133. (DOI: 10.1103/PhysRev.140.A1133)

62. Martin, R. M. (2004), Electronic structure: basic theory and practical methods, Cambridge University press.

63. Ceperley D. M., Alder B. (1980), Ground State of the Electron Gas by a Stochastic Method, J. Phys. Rev. Lett. 45, 566. (DOI: 10.1103/PhysRevLett.45.566)

64. van de Walle A., Ceder G. (1999), Correcting overbinding in local-density-approximation calculations, Phys. Rev. B 59, 14992. (DOI: 10.1103/PhysRevB.59.14992)

65. J. P. Perdew, Wang Y. (1992), Accurate and simple analytic representation of the electron-gas correlation energy, Phys. Rev. B 45: 13244-13249. (DOI: 10.1103/PhysRevB.45.13244)

66. Perdew J. P., Burke K., Ernzerhof M. (1996), Generalized gradient approximation made simple, Phys. Rev. Lett., 77, 3865-3868. (DOI: 10.1103/PhysRevLett.77.3865)

67. Perdew J. P., Ruzsinszky A., Csonka G. I., Vydrov O. A., Scuseria G. E., Constantin L. A., Zhou X., Burke K. (2008), Restoring the density-gradient expansion for exchange in solids and surfaces, Phys. Rev. Lett., 100, 136406. (DOI: 10.1103/PhysRevLett.100.136406)

68. Vanderbilt D. **(**1990), Soft self-consistent pseudopotentials in a generalized eigenvalue formalism, Phys. Rev. B, 41, 7892-7895. (DOI: 10.1103/PhysRevB.41.7892)

69. Andersen, O.K. (1975), Linear methods in band theory, Phys. Rev. B., 12, 3060-3083. (DOI: 10.1103/PhysRevB.12.3060)

70. Blochl P. E. (1994), Projector augmented-wave method, Phy. Rev. B, 50, 17953. (DOI : 10.1103/PhysRevB.50.17953)

71. Hamann D. R., Schlüter M., Chiang C. (1979), Norm-Conserving Pseudopotentials, Physical Review Letters., 43(20), 1494-1497. (DOI: 10.1103/PhysRevLett.43.1494)

72. Kresse G., Joubert D. (1999), From ultrasoft pseudopotentials to the projector augmented-wave method, Phy. Rev. B, 59, 1758. (DOI: 10.1103/PhysRevB.59.17580)

73. Nosé S. (1984), A unified formulation of the constant temperature molecular dynamics methods. J. Chem. Phys., 81, 511-519. (DOI: 10.1063/1.447334)

74. G. Mills and H. Jónsson, (1994) Quantum and thermal effects in H2 dissociative adsorption: Evaluation of free energy barriers in multidimensional

quantum systems, Phys. Rev. Lett. 72, 1124. (DOI: 10.1103/PhysRevLett.72.1124)

75. Henkelman G., Jonsson H. (2000) A climbing image nudged elastic band method for finding saddle points and minimum energy paths, J. Chem. Phys., 113, 9978-9985. (DOI: 10.1063/1.1329672)

76. Bader, R. F. W. (1994), Atoms in Molecules: A Quantum Theory; Oxford University Press: USA.

77. Henkelman G., Arnaldsson A., Jonsson H. (2006), A fast and robust algorithm for Bader decomposition of charge density. Comput. Mater. Sci., 36, 354-360. (DOI: 10.1016/j.commatsci.2005.04.010)

78. Togo A., Oba F., Tanaka I. (2008), First-principles calculations of the ferroelastic transition between rutile-type and $CaCl_2$-type SiO_2 at high pressures, Phys. Rev. B: Condens. Matter., 78, 134106. (DOI: 10.1103/PhysRevB.78.134106)

79. Baroni S., Giannozzi P., Testa A. (1987), Green's-function approach to linear response in solids, Phys. Rev. Lett., 58, 1861. (DOI: 10.1103/PhysRevLett.58.1861)

Chapter 2

Pt_3Ti (Ti_{19}@Pt_{60}) Based Cuboctahedral Core-shell Nanocluster Favours Direct over Indirect Oxygen Reduction Reaction

2.1. Introduction

Proton exchange membrane (PEM) fuel cell has attracted considerable interest in the area of clean energy sources due to its high efficiency, low operating temperature, stationary/portable power supply and zero carbon emission *[1-4]*. The performance of a fuel cell depends mainly on the performance of oxygen reduction reaction (ORR) at the cathode. However, the slow reaction kinetics of ORR and the use of Pt-metal as electrodes (Pt/C) prevent the commercialization of PEM fuel cells *[5-7]*. Therefore, the lowering of Pt loading without compromising the performance of a fuel cell is highly sought after. In order to lower the Pt-loading, alloying Pt with other transition metals appeared to be a promising approach for improving the efficiency and stability of catalyst. Such alloying with other metals leads to the formation of bi-metallic catalysts like Pt-skeleton *[8-9]*, Pt-skin *[10]*, mixed alloy *[11-12]* and core-shell structures *[13-15]*. Among them, core-shell based catalysts are very promising due to the easy tunability of inside core and the presence of resistant shell layers for sustaining the harsh reaction conditions of fuel cells.

Using computational approach, Nørskov and co-workers *[9,16-18]* studied $Pt_3M(111)$ (M= Ti, Zr, Ni, Co, Fe, Y, V, Sc, Rh) catalysts for ORR and developed a volcano-type catalytic trend. They credited to low binding energy of the intermediate species (O and OH) on the $Pt_3M(111)$ surfaces relative to bulk Pt(111) for the superior catalytic activities of $Pt_3M(111)$ (M= Co, Ni, Sc, Y). In this way, they established an optimal range of binding energy (of *O), which is 0.2 eV lower from the bulk Pt(111) as a suitable catalyst for ORR *[16]*. The conclusion was drawn on the basis of the change in d-band center position of the surface atoms due to the influence of subsurface layer. In contrast, Goddard and co-workers *[19]* reported that the universal correlation (as proposed by Nørskov and co-workers) between d-band center and catalytic activity is valid only when the d-band center is linearly related with binding energy. Xin *et al*. *[20]* also argued that the d-band model is not valid when adsorbates have almost completely filled valence shell (like OH, F and Cl) and the substrates have fully occupied d-band (i.e d^9 or d^{10} substrate). Therefore, the underlying reason behind the ORR catalytic activity of different kinds of catalytic systems is still not clear and requires further investigations.

However, in all the previous theoretical studies, the core-shell nanoparticles have been often modelled by considering the slab models, where the underneath layers are represented as core layers for the simplicity of calculations *[21-23]*. However, the twin boundaries, edge and facet atoms can't be modelled considering the slab model. In fact, these low-coordinated sites are most active sites and affect the overall activity of the few nanometer-sized nanoparticles *[24-26]*. These highly unsaturated sites possess higher d-band energies, which influences the overall activity of the nanoparticles. Basically, slab model resembles a larger nanoparticle. Therefore, cluster model study with well-defined facet can only provide the real scenario about the experimental situation. Using small sized cluster (Pt_4-Pt_{28}), several theoretical groups studied the ORR and mainly stressed on the adsorption behaviours of the reaction intermediates *[27-29]*. However, there are limited reports of ORR on a well-defined nanocluster (NC) *[30-38]*. Henkelmann and co-workers *[30-31]* studied ORR activity on the Pd/Cu@Pd, M-Au@Pt and M-Ag@Pt [M= Pd, Ir, Rh, Ru, and Cu] and provided a linear relationship between the ORR activity and alloy-core composition. However, their conclusion was on the basis of oxygen binding energy on the NC's facet. Shin *et al*. *[32]* studied the $M_{13}@Pt_{42}$ core-shell [M= Fe, Co, Ni, Cu, Ru, Rh, Pd, Ag, Os, Ir, and Au] structure for ORR activity with different core metals and established a relation between core metal and ORR activity based on the binding energy of intermediate species and reaction free energies. Yang *et al. [33]* screened the ORR activity of binary $Pt_{42}M_{13}$ (M= Fe, Co, Ni, Cu) systems considering the adsorption strength of O-atom and reported that the $Pt_{42}Fe_{13}$ is the best ORR catalyst. Jennings *et al*. *[34-36]* studied only the O_2-dissociation (very first step of ORR) reaction on the various possible sites of the Pt_{79} NC's facets and proposed that the core-metal, which interacts weakly with the Pt-shell will be beneficial for O_2 dissociation reaction. However, to the best of our knowledge, the complete ORR pathways have not been investigated in any of these studies.

Apart from the theoretical studies, bimetallic Pt_3TM (TM = Ti, V, Fe, Co, and Ni) alloy based catalysts have been experimentally reported for improved ORR activity *[39,40]*. Among them, Pt_3Ti alloy has attracted considerable attention due to the strong segregation of Pt to the outermost layer *[41]*. It has been experimentally reported that carbon-supported $Pt_{75}Ti_{25}$ nanoparticles display a two-fold improvement in ORR activity while compared to a Pt/C catalyst *[42]*. Ting *et al.* reported that PtTi–based ternary alloys (PtTi@M; M=Ni, Cu, and V) improve the ORR activity by 6-10 times compared to the Pt electrocatalyst *[43]*. Moreover, the catalyst poisoning (CO poisoning) reduces significantly due to the weak binding of CO on the Pt_3Ti alloy surface. Furthermore, Ti is about 350 times cost-effective than Pt *[34]*. Therefore, Pt-Ti-based alloys have been emerged as promising candidates for ORR. Therefore, we have modelled a ~1.5 nm size of Ti-core cuboctahedral platinum NC ($Ti_{19}@Pt_{60}$) to understand the role of core atoms towards ORR activity through a systematic ORR mechanism study.

ORR can proceed either via the four-electron reduction reaction for the formation of H_2O or via the two-electron reduction for the formation of H_2O_2 *[44]*. However, the four-electron reduction ($4e^-$) is preferred over the two-electron ($2e^-$) reduction for the catalytic efficiency as well as durability of fuel cells *[45]*. Thereby, the product selectivity (H_2O vs. H_2O_2) is very important for the performance of a fuel cell. For the first time, a systematic study (Scheme 1) based on the reaction free energies and activation barriers for all possible ORR elementary steps is done on the Pt(111) facet of $Ti_{19}@Pt_{60}$ core-shell NC. For comparisons, our results are compared with the available theoretical and experimental data on the bulk Pt(111) surfaces. Kinetic analysis is performed to gain more insights into the rate of reaction and product selectivity (H_2O vs. H_2O_2). Moreover, the dissolution limit, thermal and energetic studies are performed to check the stability of the $Ti_{19}@Pt_{60}$. A detailed investigation based on the structural changes, electronic properties and charge transfer is performed to gain more insights into their roles towards ORR activity. This study will certainly provide a significant insight into the designing of an efficient catalyst for fuel cell applications.

2.2. Model and computational details

Pt_3M (M=Co, Fe, Ni, Ti) based surfaces are well known for excellent ORR activity *[39,40]*. However, here we have designed a core-shell NC (~1.5 nm) keeping the same ratio of Pt and Ti (3:1). Therefore, we have modelled the $Ti_{19}@Pt_{60}$ NC of ~1.5 nm in the shape of cuboctahedral geometry, where the core and shell structures contain 19 and 60 atoms, respectively. The $Ti_{19}@Pt_{60}$ NC (Figure 2.1a & b) is modelled with eight (111) and six (001) facets. The reaction mechanism has been studied on the Pt(111) facet of the NC. It is well-justified in the previous literature (theoretically as well as experimentally) that (111) is the mostly exposed and active facet of the catalyst for ORR *[46-53]*. The periodic Ti@Pt(111) is modelled through replacing one of the sub-surfaces by a Ti layer as shown in Figure 2.1c.

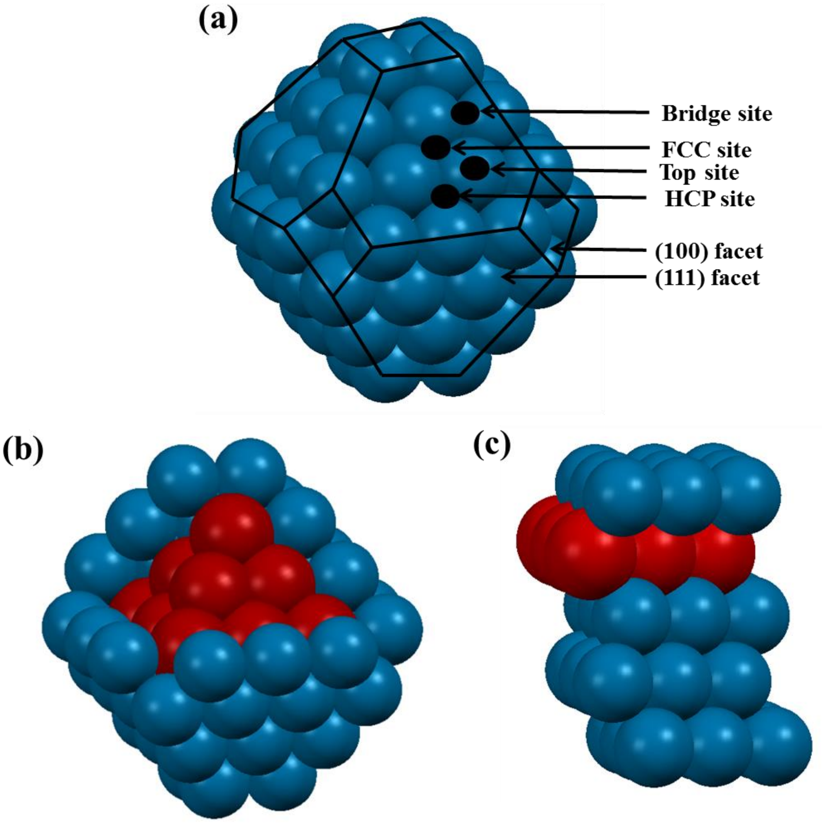

Figure 2.1: (a-b) Cuboctahedral core-shell ($Ti_{19}@Pt_{60}$) NC with eight (111) and six (001) facets and (c) the periodic Ti@Pt(111) surface. Here, red and blue colour balls represent titanium and platinum atoms, respectively.

The first-principles calculations are performed using a projector augmented wave (PAW) *[54]* method as implemented in the Vienna Ab initio Simulation Package (VASP) *[55-57]*. The exchange-correlation potential is described by using the generalized gradient approximation of Perdew-Burke-Ernzerhof (GGA-PBE) *[58]*. Plane wave with a kinetic energy cut off of 470 eV is used to expand the electronic wave functions. A 22 × 22 × 22 Å^3 cubic supercell is used to optimize the metal clusters to rule out the possibility of interactions between the periodically repeated metal clusters. The Brillouin zone is sampled with a Gamma point (1×1×1) for clusters. The total energy of the $Ti_{19}@Pt_{60}$ is improved by 0.001 eV if the k-point mesh set to 2 × 2 × 2. Therefore, we have used Gamma point for all the calculations to save the computational cost. All the atoms are full relaxed during the structural relaxation. A (3 × 3) supercell of Ti@Pt(111) is modelled [Figure 2.1c] to minimize the lateral interactions between the repeating images. The bulk Ti@Pt(111) slab is composed of five atomic layers, where the bottom three layers are fixed and the top two layers are relaxed. A 12 Å of vacuum is used along the z-direction to avoid any periodic interactions. The Brillouin zone is sampled using a 3 × 3 × 1 k-point grid for the surface calculations. All the structures are fully optimized, where the convergence criteria for total energy and forces are set at 10^{-4} eV and <0.02 eV/Å, respectively. Spin-polarized calculations are performed for all the calculations. We have included Grimme's D3-type *[59]* of semiempirical method to include the dispersion energy corrections for van der Waals interactions. The climbing nudged elastic band (CI-NEB) method *[60]* is used to locate the transition state. Six intermediate images are used in each CI-NEB pathway. Vibrational frequencies for the initial, transition and final states of the reactions are calculated and the transition states are confirmed by the presence of one imaginary frequency. Zero-point energy (ZPE) is calculated using the following equation:

$$\text{ZPE} = \sum_i 1/2 h\upsilon_i \qquad (2.1)$$

where h is the Planck constant and υ_i is the frequency of the i^{th} vibrational mode. The reaction free energies (ΔG) are calculated using the following equation:

$$\Delta G = \Delta E + \Delta ZPE - T\Delta S \qquad (2.2)$$

where ΔE, ΔZPE and ΔS are the difference in total energies, zero-point energies and entropy between the product/TS and reactant. The adsorption energies (E_{ad}) for all possible adsorbates are calculated using the following equation:

$$E_{ad} = E_{*\text{-adsorbate}} - (E_{*} + E_{adsorbate}) \tag{2.3}$$

where $E_{*\text{-adsorbate}}$ is the total energies of the surface-adsorbate, E_{*} and $E_{adsorbate}$ are the single point energies of the surface and adsorbate in the optimized geometry of surface-adsorbate, respectively. The adsorbed intermediate (R) is denoted with an asterisk (*) sign.

2.3. Results and Discussion:

We have divided this section into three parts. In the first part, we have investigated the energetic stability, thermal stability and dissolution nature of the NC. Then, the adsorption behaviours of the ORR intermediates on the (111) facet of the NC are studied and compared with the adsorption behaviours on the bulk Ti@Pt(111) for a vis-à-vis assessment between slab and cluster model. The catalytic activities are compared with previous reports on the bulk Pt(111) and Pt_3Ti(111) surfaces. This is because; there are no reports on full ORR mechanism on a well-defined core-shell model. Furthermore, all possible ORR mechanisms are investigated followed by an attempt to find out the underlying reason behind the excellent catalytic activity of the $Ti_{19}@Pt_{60}$. Subsequently, kinetic analysis is performed to explore the efficiency and selectivity of the NCs toward four-electron vs. two-electron reduction.

2.3.1 Stability of the NCs

The energetic stability of the NCs has been performed using formation energy calculations. For comparisons, we have calculated formation energies of bulk Pt(111) surface. Formation energy (E_f) of Pt(111) surface, Pt_{79} and $Ti_{19}@Pt_{60}$ NC has been calculated using the following equation.

$$E_f = [E_{Pt(111)} - 45 \times \mu_{Pt}]/45 \tag{2.4}$$

$$E_f = [E_{Pt79} - 19 \times \mu_{Pt}]/79 \tag{2.5}$$

$$E_f = [(E_{Pt79} - E_{Ti19@Pt60}) - 19 \times (\mu_{Pt} - \mu_{Ti})]/79 \tag{2.6}$$

where $E_{Pt(111)}$, E_{Pt79} and $E_{Ti19@Pt60}$ are the total energies of the Pt(111) surface, Pt_{79} and $Ti_{19}@Pt_{60}$ NC, respectively. μ_{Pt} and μ_{Ti} are the chemical potentials of the bulk fcc-Pt and hcp-Ti, respectively. Our calculated formation energies *[61]* are 0.82, 0.72 and 0.23 eV/atom for the Pt_{79} *[62]*, $Ti_{19}@Pt_{60}$, bulk Pt(111), respectively. The formation energy values reveal that the formation of core shell NC ($Ti_{19}@Pt_{60}$) is energetically more favourable than the pure Pt-nanocluster (Pt_{79}). Further, we have calculated the average binding energies (E_b) of the NCs using the following formula:

$$E_b = [E_{Ti19@Pt60} - (19\times E_{Ti} + 60\times E_{Pt})]/79 \qquad (2.7)$$

where $E_{Ti19@Pt60}$, E_{Ti} and E_{Pt} represent the total energies of $Ti_{19}@Pt_{60}$ NC, Ti atom and Pt atom, respectively. Our calculated average binding energies for bulk Pt fcc, bulk Pt(111), Pt_{79} and $Ti_{19}@Pt_{60}$ are -5.69, -5.47, -4.87 and -5.64 eV/atom, respectively. Therefore, atoms of $Ti_{19}@Pt_{60}$ NC are more strongly bonded than in Pt_{79} and bulk Pt(111).

The thermal stability of the NCs is verified by carrying out Ab Initio Molecular Dynamics Simulations (AIMD) using canonical ensemble at 300-600 K. This temperature range is considered for our study as most of the fuel cells operate in this temperate range. Temperature control is achieved by Nosé thermostat model *[63]*. The structure is heated with a time step of 1 femtosecond (fs) for 20 picoseconds (ps). No structure reconstruction is found after the simulation. The fluctuation of the total energy is smooth throughout the AIMD simulation (Figure 2.2a). Hence, the structure remains stable up to 600 K. We have plotted the root mean square displacement (RMSD) as a function of time step (Figure 2.2b) for all the cases. Our RMSD plots show that atomic displacements are negligible in the whole temperature range. The snapshots of atomic configuration of the $Ti_{19}@Pt_{60}$ at the end of MD simulations are shown in the Figure 2.3. Therefore, we can predict that the $Ti_{19}@Pt_{60}$ can withstand temperature as high as 600 K. These results demonstrate that high-energy barriers from other local minima structures separate the $Ti_{19}@Pt_{60}$ NC.

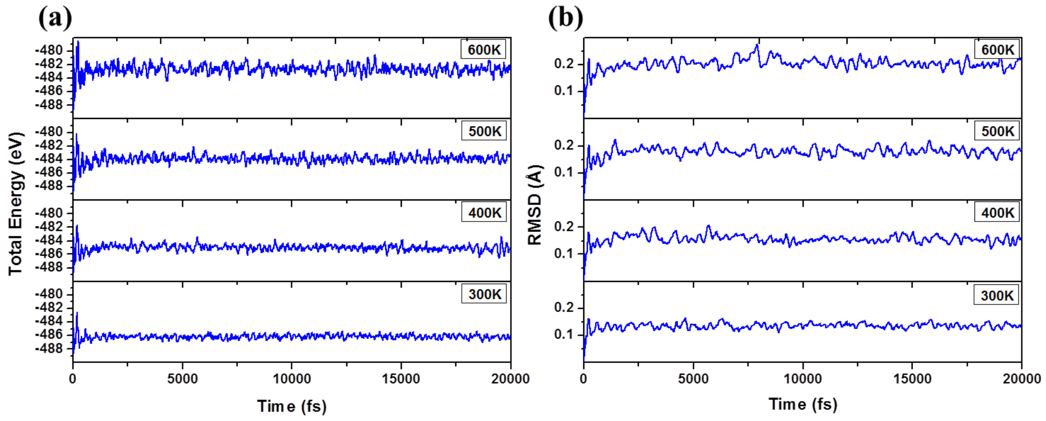

Figure 2.2: Molecular dynamics simulation analysis at different temperatures as a function of time step: (a) total energy and (b) RMSD.

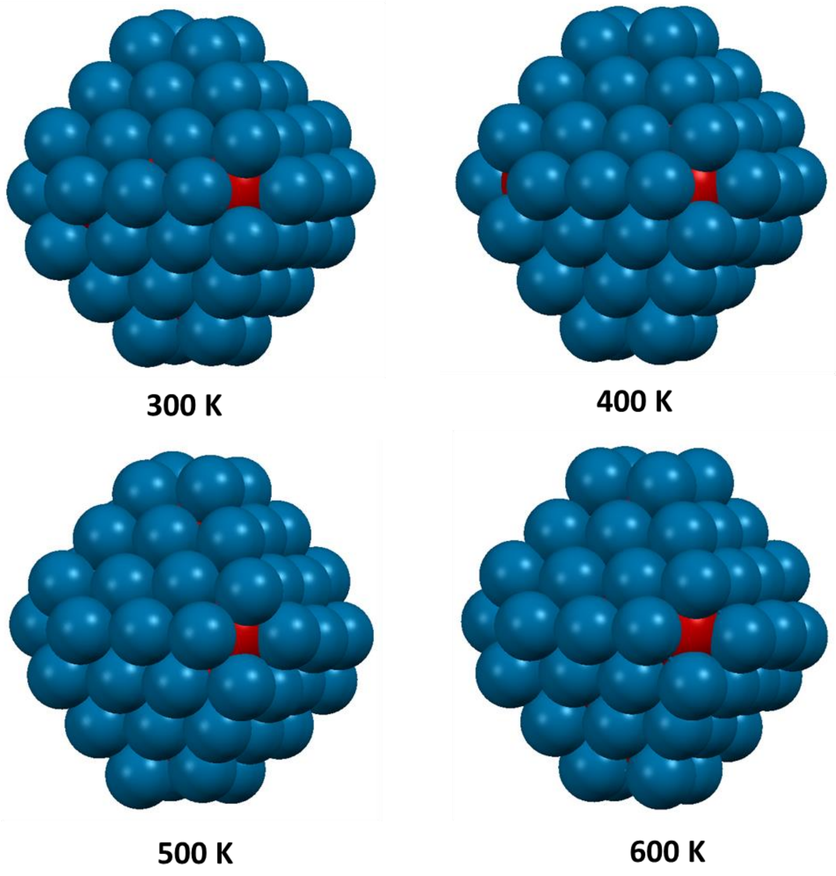

Figure 2.3: Snapshots of the NCs after the simulation at different temperatures

The electrochemical stability of the nanoparticles is a major concern in the acidic media of fuel cell. There are different computational models, which have been proposed for the dissolution behaviour of nanoparticle *[64-69]*. However, the shell-by-shell layer dissolution is a very well-accepted mechanism regarding the degradation issue *[69-71]*. Therefore, we have calculated the dissolution potential of the outermost shell layer of the $Ti_{19}@Pt_{60}$ and compared with that of Pt_{79} to understand the potential applicability in the harsh reaction conditions of fuel cell. The dissolution potential of the outermost layer is calculated using the following equation:

$$U = U_{Bulk} + \frac{1}{2me} [E_{Core} + mE_{Shell} – E_{Core\text{-}Shell}] \qquad (2.8)$$

where U and U_{Bulk} are the dissolution potentials of Pt(111) facet in the $Ti_{19}@Pt_{60}$ and bulk Pt (fcc), respectively. E_{core} represents the total energy of the core structure. $E_{core\text{-}shell}$ is the total energy of the core-shell structure and E_{shell} is the energy of the surface Pt atoms within the bulk (fcc) geometry. The details of the formalism of the dissolution model have been performed as follows.

Dissolution of Pt into the solution proceeds through the following equation

$$Pt \rightarrow Pt^{2+} +2e^{-} \qquad (2.9)$$

Therefore, the dissolution potentials (U) of the NCs with respect to the standard hydrogen electrode (SHE) have been calculated using the following equation

$$U = \frac{1}{2me} [E_{Core}- E_{Core\text{-}Shell}] + \frac{1}{2e} [\mu^{0} (Pt^{2+}, aq) + kT\log_{e} (a_{Pt^{2+}})] \qquad (2.10)$$

where E_{core} represents the total energy of the core structure. $E_{core\text{-}shell}$ is the total energy of the core-shell structure. μ^{0}, k, T and $a_{Pt^{2+}}$ are the chemical potential of the Pt^{+2} ion at standard conditions, the Boltzmann constant, the absolute temperature and the activity of Pt^{+2} ion, respectively. Similarly, the dissolution potential of the bulk Pt (U_{Bulk}) has been given by

$$U_{Bulk} = \frac{1}{2e} [\mu^{0} (Pt^{2+}, aq) + kT\log_{e} (a_{Pt^{2+}}) – E_{bulk}] \qquad (2.11)$$

where the value of U_{Bulk} relative to the SHE is 1.011 V if the concentration of Pt^{2+} is 10^{-6} M *[72]*. Our calculation shows that the energy per atom of the bulk fcc Pt (E_{Bulk}) is -6.03 eV. Therefore, combining the equation (2.10) and (2.11), we can get

$$U = U_{Bulk} + \frac{1}{2me} [E_{Core} + mE_{Bulk} - E_{Core\text{-}Shell}] \qquad (2.12)$$

The above equation can be written for simplicity as

$$U = U_{Bulk} + \frac{1}{2me} [E_{Core} + mE_{Shell} - E_{Core\text{-}Shell}] \qquad (2.13)$$

where E_{shell} is the energy of the surface Pt atoms within the bulk (fcc) geometry.

Our calculated results show that the dissolution potentials of outer shell layer are 0.73 and 1.17 V for Pt_{79} and $Ti_{19}@Pt_{60}$, respectively. Therefore, we find that $Ti_{19}@Pt_{60}$ is more resistant to the experimental operation potential (0.9 V) of ORR than the pure Pt_{79} NC. This is may be due to the strong bonding between the Ti and Pt atoms. In fact, this strong bonding is also reflected from our calculated average binding energy values. Earlier, Kattel *et al. [73]* also reported that $Pt_3Ti(111)$ surface has better stability against Pt dissolution compared to Pt(111) surface. Moreover, some previous experimental studies also suggested that the Pt-Ti bimetallic nanoparticles show better chemical stability in acid medium than Pt-M (M= Co, Ni, Zn, and Cu) bimetallic nanoparticles *[74-76]*.

2.3.2 ORR Mechanism

2.3.2.1 Adsorption

All the ORR intermediates species are adsorbed over the four possible catalytic sites (Figure 2.1a) on the (111) facet of the $Ti_{19}@Pt_{60}$ NC: (i) top, (ii) bridge, (iii) face centered cubic (fcc) and (iv) hexagonal close packed (hcp). The most stable intermediate species and their preferred binding sites along with their respective binding energies are given in Table 2.1. For comparisons, we have calculated adsorption energies of the intermediate species on the pure Pt NC (Pt_{79}) facet and on the bulk Ti@Pt(111), and Pt(111) surfaces. We find that the preferred binding sites are same for all the adsorbates on all these surfaces. It is interesting to find out that most of the intermediates are adsorbed weakly on the Pt(111) facet of the Ti_{19}@Pt_{60} NC compared to platinum NC (Pt_{79}) nanocluster. Further, the adsorption energies of the intermediates on Ti_{19}@Pt_{60} are either lower or comparable while comparing with the periodic Pt(111) surface. However, while comparing with the periodic Ti@Pt(111) surface, we find that the adsorption energies are either higher or comparable. Therefore, Ti_{19}@Pt_{60} shows interesting behaviour compared to other surfaces. Moreover, CO adsorbs weakly on the Ti_{19}@Pt_{60} NC compared to Pt_{79}, and thus lessening the probability of catalyst poisoning. The adsorption behaviours of the intermediates have been shown in Figure 2.4.

Table 2.1: Preferred binding sites, binding energies (eV) of the most stable ORR intermediate species on the bulk Pt(111) *[52]*, bulk Ti@Pt(111) surfaces and Pt(111) facet of the Pt_{79} *[62]* and Ti_{19}@Pt_{60} NCs. Here t, b, and f denote top, bridge, and fcc sites, respectively.

Adsorbed Species	**Ti_{19}@Pt_{60}**	**Pt_{79}**	**Bulk Pt(111)**	**Bulk Ti@Pt(111)**
*O_2 (superoxo)	-0.43 (b)	-1.56 (b)	-0.67 (b)	-0.05 (b)
*O_2 (tilted)	-0.12 (t)	-0.60 (t)	-0.17 (t)	-0.08 (t)
*O	-3.15 (f)	-5.19 (f)	-4.42 (f)	-3.33 (f)
*OH	-2.15 (t)	-2.49 (t)	-2.37 (t)	-2.14 (t)
*OOH	-1.12 (b)	-1.40 (b)	-1.15 (b)	-0.85 (b)
*H_2O_2	-0.15 (b)	-0.34 (b)	-0.30 (b)	-0.15 (b)
*H_2O	-0.21 (t)	-0.23 (t)	-0.26 (t)	-0.13 (t)
*H	-2.22 (f)	-2.80 (f)	-2.77 (f)	-2.05 (f)
*CO	-1.28 (f)	-2.46 (f)	-1.88 (f)	-0.29 (f)

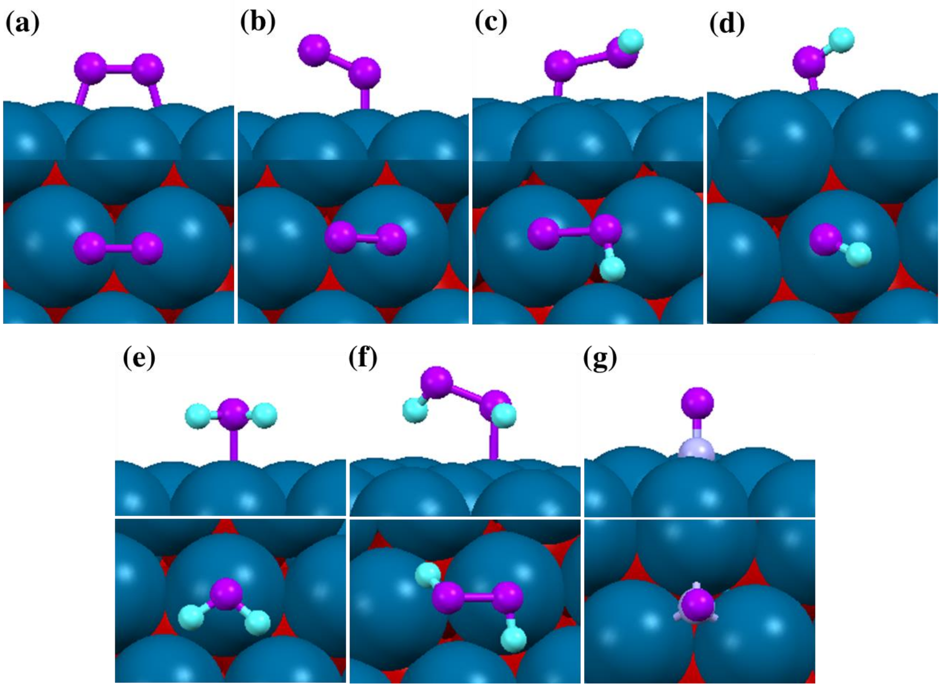

Figure 2.4: Adsorption sites of the most stable adsorbates on the (111) facet of the $Ti_{19}@Pt_{60}$ NC: (a) $*O_2$ (superoxo), (b) $*O_2$ (tilted), (c) *OOH, (d) *OH, (e) $*H_2O$, (f) $*H_2O_2$, and (g) *CO.

2.3.2.2 Reaction Mechanism

During ORR, H_2O and H_2O_2 are the two end products, which are formed via the four-electron ($4e^-$) and two-electron ($2e^-$) reduction reactions, respectively. We have proposed two pathways for O_2 dissociation: (i) direct and (ii) indirect pathways. In case of direct pathway, O-O bond dissociation is favoured over hydrogenation, whereas in case of indirect pathway, hydrogenation is preferred over O-O bond dissociation. Consequently, the product selectivity (H_2O vs. H_2O_2) can be related to the direct vs. indirect mechanism. In a fuel cell, the four electron reduction is preferred over two electron reduction for the product selectivity (towards $*H_2O$ formation) and the three most important steps for the $4e^-$ reduction ORR are (i) $*O_2$ activation, (ii) *OH, and (iii) $*H_2O$ formation. We have studied all the elementary reactions (Scheme 2.1) considering the Langmuir–Hinschelwood mechanism, where two reaction species adsorb close to each other on their preferred sites and the adsorbed species undergo a bi-molecular reaction.

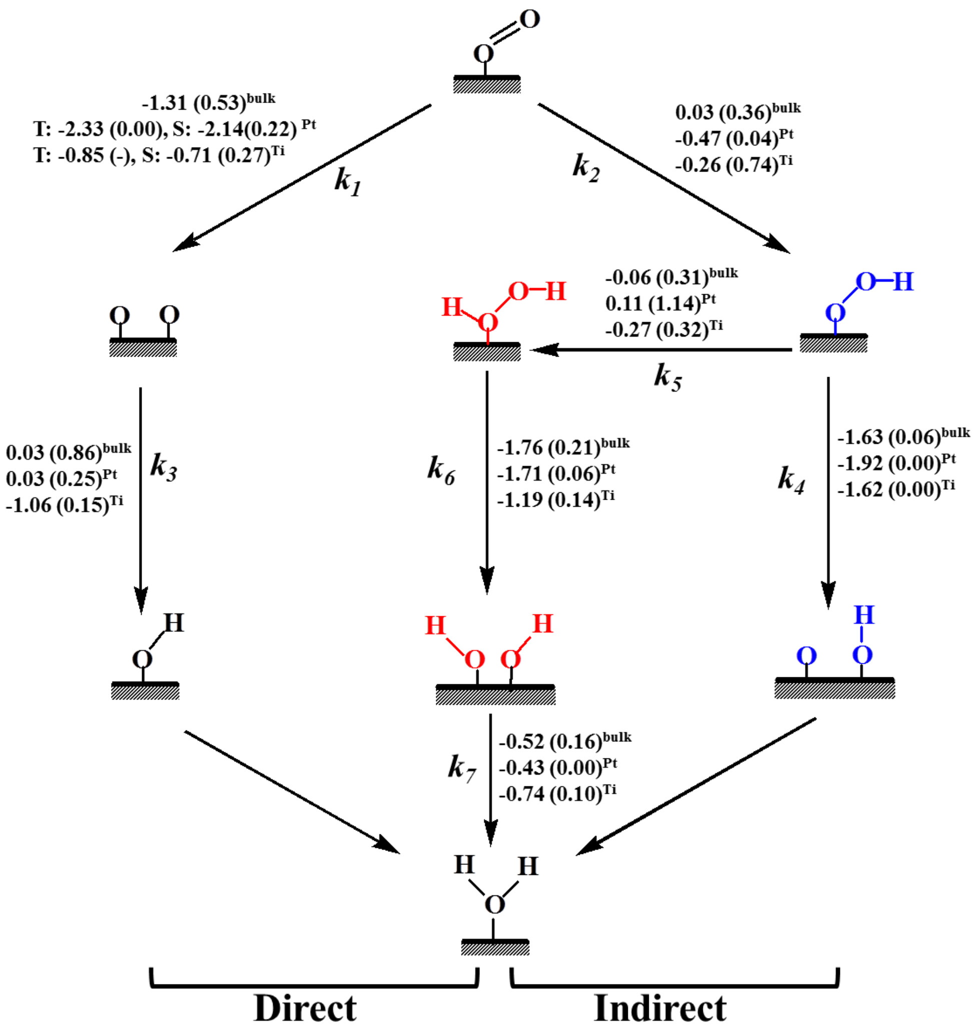

Scheme 2.1: Reaction free energies (eV) and activation barriers (eV, in parenthesis) are presented for all the possible elementary steps of ORR over (111) facet of the $Ti_{19}@Pt_{60}$ NC. Our calculated values are compared with the previous reports on ORR over Pt_{79} *[62]* NC and bulk Pt(111) *[77]*. For the direct *O_2 dissociation step, S and T represent the superoxo and tilted adsorption of *O_2, respectively.

O_2 activation:

There are two competing pathways for *O_2 activation. Either the adsorbed O_2 will dissociate into atomic oxygen (*O) via direct pathway or it will be hydrogenated to *OOH via indirect pathway. Previous studies show that hydrogenation process (*OOH formation) is kinetically favoured over dissociation process (*O formation) on the bulk (Pt, Pd, Ag) and alloy (Pt_3Ti, Pt_3Cu, Pt_3Ni) periodic Pt(111) surfaces *[23,73,77,78-80]*. Therefore, it will be very interesting to know whether core-shell based NC prefers direct over indirect mechanism or not?

As shown in Table 2.1, O_2 can be adsorbed via two ways: i) tilted, and ii) superoxo. We have calculated the activation barriers of direct O-O dissociation (step 2.1) for both the adsorption modes (tilted and superoxo) on the (111) facet of NCs. On the Pt_{79} NC, the step is a barrier less process while adsorbed in a tilted way, whereas the activation barrier is 0.22 eV when adsorbed in a superoxo way. Therefore, $*O_2$ may rearrange itself from superoxo to tilted form, followed by dissociation into atomic oxygen. The calculated rearrangement barrier is found to be very low (0.01 eV) on the (111) facet of Pt_{79}. In earlier studies, similar kind of rearrangements reported for $*O_2$ over the periodic Pt(111) and Pt_{66} nanocage *[52,81]*. Here, on the $Ti_{19}@Pt_{60}$ core-shell NC, the activation barrier for $*O_2$ dissociation is 0.27 eV while adsorbed in a superoxo way. Interestingly, we find a high activation barrier of 1.20 eV, while $*O_2$ rearranges from superoxo to titled form on the core-shell NC. This barrier was very low (0.01) on the pure Pt NC surface. Therefore, we can say that O_2 dissociation on the $Ti_{19}@Pt_{60}$ core-shell NC favoured while adsorbed in a superoxo way. Further, we could not locate the transition state for $*O_2$ dissociation while adsorbed in a tilted manner. Based on these findings, we find that $*O_2$ (superoxo) does not undergo rearrangement like previously reported on the periodic Pt (111) and nanocage facet.

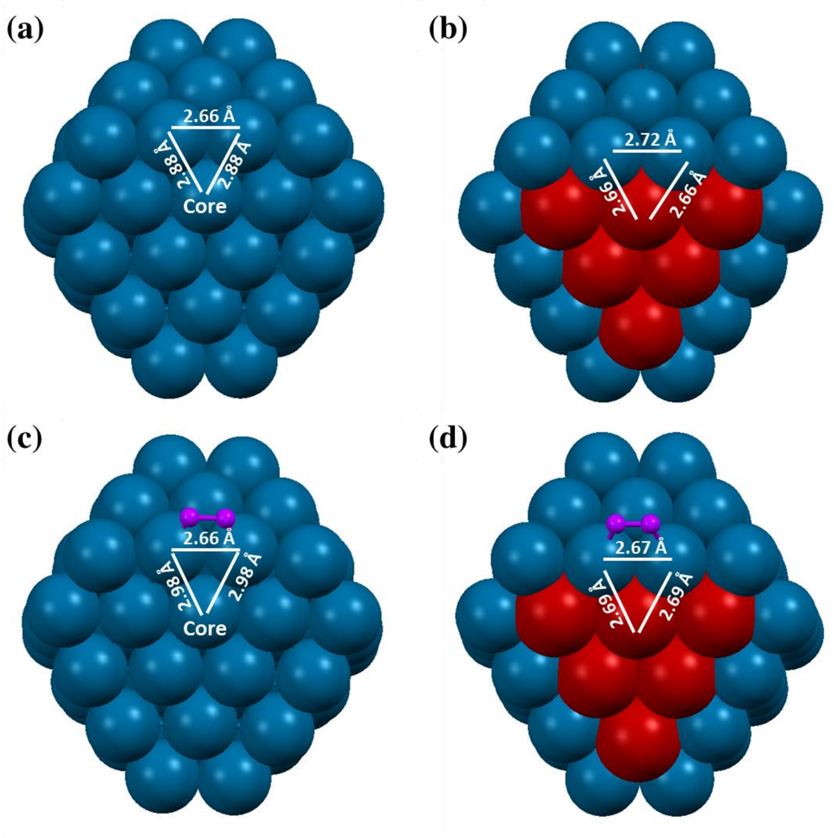

Figure 2.5: Illustration of the O_2-induced surface reconstruction. Here, red and blue balls represent Ti and Pt atoms, respectively; (a) Pt_{79}, (b) $Ti_{19}@Pt_{60}$, (c) $Pt_{79}O_2$ and (d) $Ti_{19}@Pt_{60}O_2$

Previous reports show that $*O_2$ has to bind strongly so that it can dissociate into atomic oxygen easily *[82]*. We have found that the adsorption energy of $*O_2$ (superoxo) are -1.56 and -0.43 eV on the Pt_{79} and $Ti_{19}@Pt_{60}$, respectively. Therefore, the $*O_2$ dissociation should be more kinetically favorable on the Pt_{79} facet than that of the $Ti_{19}@Pt_{60}$. However, the activation barriers are very much comparable on the Pt_{79} (0.22 eV) and $Ti_{19}@Pt_{60}$ (0.27 eV) while adsorbed in superoxo pattern. Therefore, we wonder what could be the driving force for direct $*O_2$ dissociation, which lowers the activation barrier on the $Ti_{19}@Pt_{60}$ NC in spite of the lower adsorption energy of $*O_2$ (superoxo). We have calculated the O_2-induced strain of the NCs. The strain is calculated by the energy difference between the optimized NC and the single point energy of the NC within the optimized geometry of O_2 adsorbed NC. Our calculated strain energies are 0.07 and 0.23 eV for the Pt_{79} and $Ti_{19}@Pt_{60}$ NCs, respectively. Therefore, it appears to be quite ambiguous that the O_2-induced strain is less on the Pt_{79} than on the $Ti_{19}@Pt_{60}$ NC in spite of the strong adsorption of $*O_2$ on the Pt_{79} NC. Thereby, we have carefully investigated the structural parameters to find out the underlying reason behind this (Figure 2.5). The Pt-Pt bond distances are 2.66 and 2.72 Å in the Pt_{79} and $Ti_{19}@Pt_{60}$ NCs, respectively. Interestingly, the Pt-Pt bond distance does not change after $*O_2$ adsorption on the Pt_{79}, whereas it changes from 2.72 Å to 2.67 Å in the $Ti_{19}@Pt_{60}$ NC after $*O_2$ adsorption. However, in the Pt_{79}, the Pt-Pt (between core-Pt and shell-Pt atoms) bond distance changes from 2.88 to 2.98 Å in the core shell due to $*O_2$ adsorption. In contrast, the change in Pt-Ti bond distance in $Ti_{19}@Pt_{60}$ NC, (between core-Pt and shell-Ti atoms) is less (by 0.03 Å) than in the Pt_{79} NC (0.10 Å).

Due to the difference in electronegativities, the charge transfer is maximum in the $Ti_{19}@Pt_{60}$ core shell NC. As a result, a significant amount of charge transfer occurs from Ti to Pt anti-bonding orbitals. This could be the reason for the long Pt-Pt bond distances in the $Ti_{19}@Pt_{60}$ core shell NC. However, such a high bond distances in the core-shell NC facilitates the O_2 activation process. More importantly, due to the strong electronegative nature of the Pt surface, the adsorbents are weakly adsorbed on the surface. Nørskov and co-workers demonstrated earlier that the binding energy of the adsorbents should be optimum for improved ORR activity *[16]*. It indicates that such a core-shell NC model might be very helpful to reach the optimal binding energy of the adsorbents, which in turn might be very helpful for improved ORR activity. On the other hand, as soon as O_2 comes near to the surface, there is a charge transfer from Pt to O_2 molecule and the bonding nature of the surface Pt-atoms changes. Thus, the Pt-Pt bond shortens and induces a localized strain, which in turn facilitates the activation of O_2 molecule. Therefore, we believe that such a core-structure model will be very promising than a pure Pt NC for improved ORR activity.

Interestingly, it has been experimentally found that adsorbed O_2 can oxidize the gold nanoparticle by altering the morphology of the particle *[83-84]*. Further, the catalytic process on bimetallic surface depends on the adsorbate-induced structural changes where a strong interaction (like O_2 adsorption) is present between the metal and adsorbates *[85-86]*. In fact, such O_2-induced surface strain has been reported in the literatures *[87-88]*. Besides, it is very interesting to find out that $*O_2$ induces the surface reconstruction process even at very low coverage (one oxygen molecule per facet), which is in well agreement with experimental reports that O_2-induced surface reconstruction can occur on $Cu_3Pt(110)$ alloy even at very low oxygen pressure (10^{-7} to 10^{-09} Torr) *[89-90]*. Apart from the O_2 activation, there are experimental reports, where the CO, hydrogen, chloride-induced structural reconstructions have been reported for improved catalytic activity *[91-93]*.

Table 2.2: O_2 dissociation barriers and the bond distances (Pt-Pt and Pt-Ti) on the (111) facet of $*O_2$ adsorbed Pt_{79} and $Ti_{19}@Pt_{60}$ NCs.

System	**Barrier (eV)**			**Bond distance (Å)**			
				Between shell Pt atoms		**Between core and shell atoms**	
	O_2 rearrangement	O_2 Dissociation (tilted)	O_2 dissociation (superoxo)	Optimized NC	$*O_2$ adsorbed (superoxo) NC	Optimized NC	$*O_2$ adsorbed (superoxo) NC
Pt_{79}	0.01	0.00	0.22	2.66	2.66	2.88	2.98
$Ti_{19}@Pt_{60}$	1.20	-	0.27	2.72	2.67	2.66	2.69

Now, the superoxo to tilted rearrangement barrier can be understood from the adsorption energies of tilted $*O_2$. The adsorption energies of $*O_2$ are -0.12 (tilted) and -0.43 eV (superoxo) on the $Ti_{19}@Pt_{60}$ NC. Due to the lower binding energy of tilted $*O_2$, the core shell NC doesn't favour the $*O_2$ rearrangement from superoxo to tilted and thus the barrier is high. In contrast, the Pt_{79} allows the superoxo $*O_2$ to rearrange in the tilted configuration due to its strong adsorption in both the configurations (-0.60 eV for tilted and -1.56 eV for superoxo). Therefore, on Pt_{79} NC, the adsorbed (superoxo) $*O_2$ tends to dissociate into atomic oxygen via the tilted configuration in a two-step process, whereas the superoxo $*O_2$ directly dissociates into *O on the $Ti_{19}@Pt_{60}$ NC. So, the rearrangement process (rearrangement followed by dissociation) facilitates the direct $*O_2$ dissociation on the Pt_{79} NC, whereas the O_2–induced structural changes facilitates the direct dissociation on the

Ti_{19}@Pt_{60} NC. This behaviour is completely opposite from the ‘Strain Effect’ *[94-95]*, which typically arises due to the size mismatch of the core atoms, which in turn generates either compressive or tensile strain at the surface layers. The compressive strain down-shifts the d-band center, resulting the weak adsorption of reaction intermediates, which subsequently improves the catalytic efficiency *[94-95]*. In fact, it is theoretically reported that $^*O_2$ dissociation barrier becomes lower on the compressively strained surface *[96]*. However, our results show that the $^*O_2$ dissociation is favoured due to the tensile strain present on the Ti_{19}@Pt_{60} NC surface, and the atoms rearrange significantly as soon as $^*O_2$ is adsorbed. Though the surface is under tensile strain (with respect to bulk Pt(111)), the Pt atoms release some of their strain during O_2 adsorption and such changes (from tensile to compressive) in strain facilitate the O_2 dissociation. However, we don’t find any such changes (Table 2.2) on the Pt_{79} NC and thus the tensile strain is important for the $^*O_2$ dissociation. Therefore, the tensile strain does not influence the $^*O_2$ activation step, rather the $^*O_2$ induced structural changes is the underlying reason for excellent activity towards direct O_2 dissociation.

Table 2.3: Reaction free energies (ΔG in eV) and activation barriers ($\Delta G^{\ddagger}$ in eV) for the all-possible elementary reactions on the (111) facet of the Pt_{79} *[62]* and Ti_{19}@ Pt_{60} NCs.

Steps	**Elementary Reactions**	**Ti_{19}@ Pt_{60}**		**Pt_{79}**	
		ΔG	**$\Delta G^{\ddagger}$**	**ΔG**	**$\Delta G^{\ddagger}$**
2.1	$^*O_2 \rightarrow {}^*O + {}^*O$ (tilted)	-0.85	-	-2.33	0.00
	$^*O_2 \rightarrow {}^*O + {}^*O$ (superoxo)	-0.71	0.27	-2.14	0.22
2.2	$^*O_2 + {}^*H \rightarrow {}^*OOH$	-0.26	0.74	-0.47	0.04
2.3	$^*O + {}^*H \rightarrow {}^*OH$	-1.06	0.15	0.03	0.25
2.4	$^*OOH \rightarrow {}^*O + {}^*OH$	-1.62	0.00	-1.92	0.00
2.5	$^*OOH + {}^*H \rightarrow {}^*H_2O_2$	-0.27	0.32	0.11	1.14
2.6	$^*H_2O_2 \rightarrow {}^*OH + {}^*OH$	-1.19	0.14	-1.71	0.06
2.7	$^*OH + {}^*H \rightarrow {}^*H_2O$	-0.74	0.10	-0.43	0.00

Similarly, O_2 hydrogenation (step 2.2) is exergonic on the Pt_{79} and $Ti_{19}@Pt_{60}$ NCs. Our calculated barriers for the O_2 hydrogenation process are 0.04 and 0.74 eV on the Pt_{79}, $Ti_{19}@Pt_{60}$, respectively. The previous reported barriers for O_2 hydrogenation (step 2.2) are 0.25 *[23]*, 0.36 *[77]* and 0.30 eV *[78]* on the periodic Pt(111). Kattel *et al. [63]* reported an activation barrier of 0.20 eV over the periodic Pt_3Ti (111). Therefore, the *OOH formation barrier is high over the $Ti_{19}@Pt_{60}$ NC. So the $Ti_{19}@Pt_{60}$ NC is very selective for O_2 dissociation over O_2 hydrogenation, whereas the Pt_{79} NC favours O_2 activation as well as O_2 hydrogenation.

***OH formation:**

The *OH formation is another important step for ORR and previous studies on bulk (111) surfaces (Pt, Pd, Ag, Pt_3Ti, Pt_3Cu and Pt_3Ni) show *[23,73,77-80]* that this is one of the rate determining steps of ORR. The direct O-O bond dissociation followed by hydrogenation leads to the formation of *OH (step 2.3). The *OH formation step (step 2.3) is little endergonic (0.03 eV) over the Pt_{79} NC, whereas it is exergonic process (-1.06 eV) over the $Ti_{19}@Pt_{60}$ NC surface. The activation barriers for *OH formation are 0.25 and 0.15 eV over Pt_{79}, and $Ti_{19}@Pt_{60}$, respectively. Previous studies reported activation barriers of 0.74 *[72]* and 0.86 eV *[68]* on the periodic Pt(111); 0.80 eV on the Pt_3Ti *[73]*; 0.81 eV on the Pt/Cu *[77]* and 0.72 eV on the Pd(111) *[79]* surfaces. Therefore, the *OH formation is very much favourable on the $Ti_{19}@Pt_{60}$ NC surface than on the Pt_{79} and other periodic (111) surfaces.

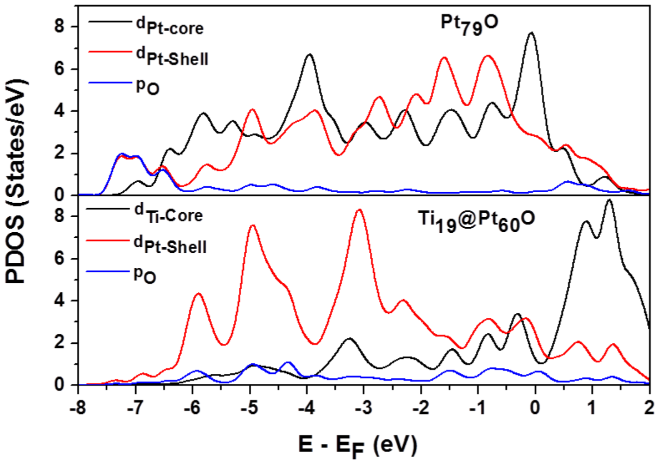

Figure 2.6: Projected density of states (PDOS) of *O adsorbed Pt_{79} and $Ti_{19}@Pt_{60}$ structures.

We have calculated the d-band center position of the (111) facet atoms of the NCs. The calculated d-band centers are -2.50 and -2.73 eV for Pt_{79} and $Ti_{19}@Pt_{60}$, respectively. The downshift of d-band center of $Ti_{19}@Pt_{60}$ weakens the binding energy of the intermediates. Furthermore, our DOS analysis (Figure 2.6) shows that the overlap of O-p and Pt-d states is less in $Ti_{19}@Pt_{60}$ compared to Pt_{79}, resulting the weak adsorption of oxygen atom. Such weak adsorption of the intermediates improves the desorption process and reduces the possibility of surface poisoning. This phenomenon is in good agreement with the 'ligand effect' proposed by Nørskov and co-workers *[94-95]*.

In general, a downward shift in the d-states relative to the Fermi level results in a downward shift in the anti-bonding states. This leads to the filling of the anti-bonding states, which in turn weakens the bond strength. In this way, Nørskov and co-workers developed a linear relationship between electronic structure and adsorption energies. Such core-shell structure has a lower binding energy for *O due to the ligand effect but improves (by weakening the binding strength of *O) the *OH formation step (*O + *H → *OH). As a result, the OH formation step is very much favourable over the core-shell nanostructure compared to bulk and other metal-based catalysts. Previously, Henkelmann and co-workers also demonstrated that the O-binding energy could be tuned by changing the core composition of the core-shell (M@Pd where M=Pd, Cu) nanoparticles *[31]*.

On the other hand, Nørskov and co-workers evaluated the ligand effect towards ORR activity mainly from their reaction free energy data.[16] However, we feel that the kinetic factor should be taken into account along with the reaction free energy to understand the excellent catalytic activity of core-shell NC toward ORR activity. Further such findings can be explained from the Bader charge analysis. Subsequently, we have plotted electrostatic potential (Figure 2.7) over the NC surface to understand the role of charge toward OH formation. The lower activation barrier for *OH formation over the $Ti_{19}@Pt_{60}$ NC can be explained from the charge analysis. Our calculated Bader charge *[81]* (using Henkelman programme *[98-100]*) shows that the charges on *O atoms are 0.67 |e| and 0.70 |e| while adsorbed on Pt_{79} and $Ti_{19}@Pt_{60}$, respectively. This is due to the electronegativity difference between the Ti and

Pt atoms. As Pt is more electronegative than Ti, thus O is more electronegative in the core-shell structure. In fact, we have calculated the binding energy of surface Pt atoms for both the NCs. We find that the binding energies of surface Pt atoms are -6.84 and -7.91 eV for Pt_{79} and $Ti_{19}@Pt_{60}$, respectively. Furthermore, the electrostatic potential is plotted (Figure 2.7) on the total electron density surface to show a more qualitative and illustrative analysis of the charge distribution. The plot shows that oxygen atom accumulates more negative charge when adsorbs on the $Ti_{19}@Pt_{60}$ NC than Pt_{79} NC. The accumulation of more negative charge at the *O atom on $Ti_{19}@Pt_{60}$ facilitates the protonation and thus the OH formation. Therefore, our results reveals that a dual mechanism (ligand effect and charge transfer) is responsible for the excellent catalytic improvement of the *OH formation step, which is one of the rate determining steps for ORR. The ligand effect makes the reaction thermodynamically favourable and the charge accumulation at the *O atom improves the kinetics of the step. Therefore, we propose that early transition metal (as a core atoms) with strong electrostatic interaction with Pt-shell layer can further improve the ORR activity by lowering the binding strength of *O and increasing the charge on *O atom.

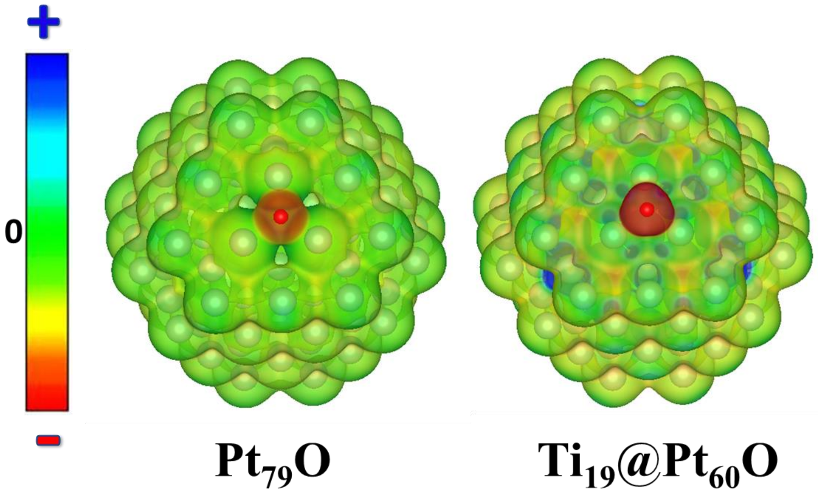

Figure 2.7: Electrostatic potential (ESP) surface (isosurface value: 0.04 e·Å^{-3}) of O-adsorbed (a) Pt_{79} and (b) $Ti_{19}@Pt_{60}$ NCs. The blue and red colors denote less and more electron density in the electrostatic potential surface.

Furthermore, *OH formation is also possible via indirect pathways (step 2.4) too; such as via peroxyl formation followed by O-O bond dissociation (step

2.4). This step is a barrierless and downhill process on both the NCs with reaction free energies of -1.92 (Pt_{79}) and -1.62 (Ti_{19}@Pt_{60}) eV. Yao *et al. [78]* and Kai *et al. [77]* reported activation barriers of 0.12 eV and 0.06 eV, respectively for the *OOH dissociation (step 2.4) step over the periodic Pt(111).

It is very interesting to note that free energy for *OOH dissociation (step 2.4) is more exergonic on the Pt_{79} NC (-1.92 eV) than on the Ti_{19}@Pt_{60} NC (-1.62 eV). Therefore, the compressive strain on the Pt_{79} NC favours the reaction thermodynamics of *OOH dissociation. Such observation is very much agreement with the previous report on periodic Pt(111), where they have reported that *OOH dissociation becomes more exergonic over the compressively strained surface *[96]*.

Formation/Decomposition of *H_2O_2:

The two-electron reduction process leads to the formation of H_2O_2. H_2O_2 can be formed (step 2.5) via two successive hydrogenations on O_2 (*O_2 + *H → *OOH, *OOH + *H → *H_2O_2). Our calculated activation barriers for H_2O_2 formation (step 2.5) are 1.14 and 0.32 eV over the Pt_{79}, and Ti_{19}@Pt_{60} NCs surface, respectively. However the *OOH formation barrier (0.74 eV) is very high compared to *OOH hydrogenation (0.32 eV) on the Ti_{19}@Pt_{60} NC. Therefore, H_2O_2 formation is very much unlikely on the Ti_{19}@Pt_{60} surface. Wang and co-workers *[73]* reported an activation barrier of 0.19 and 0.07 eV for the H_2O_2 formation (step 2.5) on the periodic Pt(111) and Pt_3Ti(111), respectively. Therefore, previous report also showed that the Ti alloying lowers the activation barrier for H_2O_2 formation. The *H_2O_2 dissociation barrier (step 2.6) into *OH is low on the core-shell structure and very much comparable on the Pt_{79}. The dissociation behaviour of *H_2O_2 on the NCs follows similar trend as on the periodic surfaces *[73]*.

***H_2O formation:**

The adsorbed *OH can undergo hydrogenation (step 2.7) for the formation of *H_2O. This is calculated to be a barrierless process on the Pt_{79} NC surface. The activation barrier for *H_2O formation on the Ti_{19}@Pt_{60} NCs is 0.10 eV.

The previous studies reported H_2O formation barriers of 0.16 eV *[70]*, 0.09 *[69]* and 0.14 eV *[72]* on the periodic Pt(111). The periodic $Pt_3Ti(111)$ shows an activation barrier of 0.12 eV. Therefore, the previous calculated barriers are very much in good agreement with our calculated barrier of 0.10 eV on the core-shell surface. Our calculation shows that the $*H_2O$ formation is more exergonic on the $Ti_{19}@Pt_{60}$ NC, whereas the activation barrier is lower on the Pt_{79} NC. This interesting observation can be understood from the adsorption behaviour of the *OH and$*H_2O$. The binding energies of *OH are similar on both the NCs, whereas $*H_2O$ is more stabilized on the $Ti_{19}@Pt_{60}$. Thus, the reaction is more exergonic on the core-shell surface. However, the $*H_2O$ formation is more favourable over *OH formation on the surface of the NCs. This suggests that the $*H_2O$ formation will not influence the reaction kinetics on the NCs.

Therefore, after careful investigation, we find that *OH formation step is the rate determining step on the Pt_{79} NC, whereas the direct $*O_2$ dissociation is the rate determining step on $Ti_{19}@Pt_{60}$ NC. We find that the $*O_2$ induced structural changes favours the direct $*O_2$ dissociation over the $Ti_{19}@Pt_{60}$ NC. Moreover, the *OH formation step ($*O + *H \rightarrow *OH$) is significantly improved (lowered by 0.10 eV) when catalysed by the $Ti_{19}@Pt_{60}$ NC than the Pt_{79} NC. Our detailed investigation reveals that a dual mechanism (ligand effect and charge transfer) plays important role to improve the ORR activity over the core-shell structure.

2.3.3 Solvation and Kinetic Study:

In order to model the realistic electrochemical conditions of ORR, it is necessary to consider the influence of water environment on the ORR process. We have included the solvation effects using the VASPsol code *[101-102]* to calculate the reaction free energies for all the elementary steps. This kind of implicit solvation model has been successfully implemented in previous studies and shows excellent consistency with experiment *[103-104]*. The dielectric constant of water solvent is set to 78.4. The calculated reaction free energies in the gas and solvation mediums have been given in Table 2.4. The results indicate that the elementary steps become more thermodynamically favourable in the water medium. Therefore, the reaction kinetics will be further improved in the presence of water.

Table 2.4: Reaction free energies of the elementary steps on $Ti_{19}@Pt_{60}$ for (a) gas and (b) solvation medium.

Steps	**Elementary Reactions**	**$Ti_{19}@Pt_{60}$**	
		ΔG(gas phase)	**ΔG(solvation)**
2.1	$*O_2 \rightarrow *O + *O$ (tilted)	-0.87	-1.03
	$*O_2 \rightarrow *O + *O$ (superoxo)	-0.67	-0.81
2.2	$*O_2 + *H \rightarrow *OOH$	-0.26	-0.39
2.3	$*O + *H \rightarrow *OH$	-1.06	-1.06
2.4	$*OOH \rightarrow *O + *OH$	-1.62	-1.70
2.5	$*OOH + *H \rightarrow *H_2O_2$	-0.27	-0.30
2.6	$*H_2O_2 \rightarrow *OH + *OH$	-1.19	-1.25
2.7	$*OH + *H \rightarrow *H_2O$	-0.74	-0.88

Furthermore, we have done a detailed kinetic analysis based on our preliminary DFT results to understand the product selectivity that is four-electron (H_2O formation) vs. two-electron (H_2O_2 formation) reduction reactions. The forward (k_i) rate constants for all the elementary steps are calculated using the following equation:

$$k_i = \left(\frac{k_B T}{h}\right)\left(\frac{q_{TS}}{q_R}\right) e^{-\Delta G^{\ddagger}/k_B T} \qquad (2.14)$$

where k_B is the Boltzmann constant, T is the temperature, h is the Plank constant. Here, q_{TS} and q_R are the vibrational partition functions for the transition state and reactant structures, respectively and $\Delta G^{\ddagger}$ is the Gibbs free energy barrier for the initial and final state of the elementary reaction.

Table 2.5: Rate constants (s^{-1}) of the elementary reactions at different temperatures on the Pt_{79} and $Ti_{19}@Pt_{60}$ NC. Here k_i stands for the forward rate constant of the ith step.

Steps	**Elemen-tary reactions**	**300 K**		**500 K**	
		Pt_{79}	**$Ti_{19}@Pt_{60}$**	**Pt_{79}**	**$Ti_{19}@Pt_{60}$**
2.1	$*O_2 \xrightarrow{k_1} *O+*O$ (tilted)	8.66×10^{12}	-	1.24×10^{13}	-
	$*O_2 \xrightarrow{k_1} *O+*O$ (superoxo)	2.10×10^{09}	3.03×10^{08}	1.05×10^{11}	3.30×10^{10}
2.2	$*O_2+*H \xrightarrow{k_2} *OOH$	1.36×10^{12}	3.47×10^{00}	4.31×10^{12}	5.88×10^{05}
2.3	$*O+*H \xrightarrow{k_3} *OH$	1.32×10^{08}	1.25×10^{10}	1.15×10^{10}	2.21×10^{11}
2.4	$*OOH \xrightarrow{k_4} *O+*OH$	7.92×10^{12}	1.51×10^{13}	1.22×10^{13}	1.72×10^{13}
2.5	$*H+*OOH \xrightarrow{k_5} *H_2O_2$	5.39×10^{-07}	3.52×10^{07}	3.82×10^{01}	7.63×10^{09}
2.6	$*H_2O_2 \xrightarrow{k_6} *OH + *OH$	8.73×10^{11}	3.60×10^{10}	3.62×10^{12}	5.01×10^{11}
2.7	$*H+*OH \xrightarrow{k_7} *H_2O$	1.67×10^{13}	1.38×10^{11}	2.06×10^{13}	7.66×10^{11}

The rate constants (Table 2.5) are calculated in the temperature range of 300 K to 500 K as the fuel cell operates in this temperate range *[52, 105]*. The rate constants improve significantly as we increase the temperature. At 300 K, the ratio of direct and indirect O_2 activation rate constants (k_1/k_2) * is 8.73×10^{07} on the $Ti_{19}@Pt_{60}$ NC. Hence, the formation of *O is very much unlikely via indirect pathway on the $Ti_{19}@Pt_{60}$ NC, which improves the product selectivity and reduces the formation of unwanted by-products (such as $*H_2O_2$ formation). Hence, our kinetic analysis suggests that $Ti_{19}@Pt_{60}$ NC is highly selective and efficient towards four-electron reduction (H_2O formation) over two-electron reduction (H_2O_2 formation) reaction. Furthermore, the $Ti_{19}@Pt_{60}$ NC can improve the rate determining *OH formation step by ~10^2 times compared to the Pt_{79} NC.

We have done spin-polarized calculations in all the calculations. We find that the adsorbed *O_2 shows a total magnetic moment of 0.84 μB, whereas adsorbed *O is a nonmagnetic one. Our findings are in good agreement with the previous reported magnetic calculations *[106]*. However, we have not considered the potential energy crossing of the two states. We understand that the calculated TS crossing the potential energy surface of the two states may be higher or lower than the adiabatic TS. We have calculated the reaction free energies of *O_2 activation steps (step 2.1 & 2.2) using different functionals (PBEsol, rPBE and PW91) and our results show that the trend is same irrespective of the functionals used (Table 2.6).

Table 2.6: Accuracy of the level of calculation

Functionals	**Reaction free energies (eV)**		**Bond distances (Å)**			**Adsorption Energy (eV)**	
	k_1	**k_2**	**Pt-Pt**		**O-O (adsorbed)**	***O_2**	***OOH**
			Pure NC	**After O_2 adsorption**			
PBE	-0.71	-0.26	2.72	2.67	1.31	-0.43	-1.12
PBEsol	-0.82	-0.25	2.68	2.63	1.31	-0.76	-1.43
rPBE	-0.54	-0.26	2.74	2.67	1.32	-0.08	-0.82
PW91	-0.74	-0.33	2.72	2.67	1.32	-0.55	-1.24

2.4. Conclusion

First-principles calculations are performed to understand the ORR activity on (111) facet of the well-defined cuboctahedral $Ti_{19}@Pt_{60}$ NC. Energetic, thermal and electrochemical stabilities of the NC are evaluated from the total energy, AIMD simulation and dissolution potential, respectively. The calculated results suggest that $Ti_{19}@Pt_{60}$ NC is thermodynamically more stable than Pt_{79} NC. Molecular dynamics simulations suggest that the $Ti_{19}@Pt_{60}$ can withstand temperatures as high as 600 K without any structural reconstruction. Dissolution potential shows that the $Ti_{19}@Pt_{60}$ NC is electrochemically more stable compared to the Pt_{79} NC. Reaction free energies and activation barriers are calculated for all the possible elementary steps of ORR on the (111) facet of the $Ti_{19}@Pt_{60}$ and compared with Pt_{79} NC and previously reported pure (Pt, Pd, and Ag) and alloyed (Pt_3M; M= Ni, Co, Ti) based metal catalysts. Our detailed investigation finds that the O_2-induced surface strain facilitates the direct $*O_2$ dissociation on the $Ti_{19}@Pt_{60}$ NC surface. This is completely opposite to the previous reports on alloy based catalysts, where the compressive strain generated at the surface layer due to the alloying (Strain effect) was credited for their superior catalytic activity. Here, the $*O_2$ induced structural changes favours the direct $*O_2$ dissociation over the $Ti_{19}@Pt_{60}$ NC in spite of the presence of tensile strain on the surface atoms. After careful investigation on density of states, d-band center, electrostatic potential and Bader charge, we find that a dual mechanism (ligand effect and charge transfer) plays important role to improve the ORR over the $Ti_{19}@Pt_{60}$ NC. The ligand effect favours reaction thermodynamics, whereas the charge accumulation on the *O atom improves the reaction kinetics. Our kinetics analysis shows that the $Ti_{19}@Pt_{60}$ NC is a very selective and efficient catalyst for H_2O formation over H_2O_2, and thus a promising catalyst for the fuel cell applications. Moreover, our solvation calculation shows that the reaction becomes thermodynamically more favorable in water medium and thus the reaction kinetics may further improve in the presence of water.

2.5. References

1. Jiao Y., Zheng Y., Jaroniecb M., Qiao S. Z. (2015), Design of electrocatalysts for oxygen-and hydrogen-involving energy conversion reactions. Chem. Soc. Rev., 44, 2060–2086. (DOI: 10.1039/C4CS00470A)

2. Bruijn F. A. de., Dam V. A. T., Janssen G. J. M. (2008), Review: durability and degradation issues of PEM fuel cell components. Fuel Cells, 8, 3–22. (DOI: 10.1002/fuce.200700053)

3. Vinayan B. P., Nagar R., Rajalakshmi N., Ramaprabhu S. (2012), Novel platinum–cobalt alloy nanoparticles dispersed on nitrogen- doped graphene as a cathode electrocatalyst for PEMFC applications. Adv. Funct. Mater., 22, 3519–3526. (DOI: 10.1002/adfm.201102544)

4. Lubitz W., Tumas W. (2007), Hydrogen: an overview. Chem. Rev., 107, 3900–3903. (DOI: 10.1021/cr050200z)

5. Watanabe M., Tryk D. A., Wakisaka M., Yano H., Uchida H. (2012), Overview of recent developments in oxygen reduction electrocatalysis, Electrochim. Acta, 84, 187–201. (DOI: 10.1016/j.electacta.2012.04.035)

6. Wang X. X., Tan Z. H., Zeng M., Wang J. N. (2014), Carbon nanocages: A new support material for Pt catalyst with remarkably high durability. Sci. Rep., 4, 4437. (doi: 10.1038/srep04437)

7. Calle-Vallejo F., Koper M. T. M., Bandarenka A. S. (2013), Tailoring the catalytic activity of electrodes with monolayer amounts of foreign metals, Chem. Soc. Rev., 42, 5210–5230. (DOI: 10.1039/C3CS60026B)

8. Stamenkovic V. R., Mun B. S., Mayrhofer K. J. J., Ross P. N., Markovic N. M. (2006), Effect of surface composition on electronic structure, stability, and electrocatalytic properties of Pt-transition metal alloys: Pt-skin versus Pt-skeleton surfaces. J. Am. Chem. Soc., 128, 8813–8819. (DOI: 10.1021/ja0600476)

9. Johansson T. P., Ulrikkeholm E. T., Hernandez-Fernandez P., Malacrida P., Hansen H. A., Bandarenka A. S., Nørskov J. K., Rossmeisl J., Stephens I. E. L., Chorkendorff I. (2014), Pt skin versus Pt skeleton structures of Pt_3Sc as electrocatalysts for oxygen reduction. Top Catal., 57, 245–254. (DOI: 10.1007/s11244-013-0179-y)

10. Wang C., Chi M., Li D., Strmcnik D., Vliet D., Wang G., Komanicky V., Chang K., Paulikas A. P., Tripkovic D., Pearson J., More K. L., Markovic N. M., Stamenkovic V. R. (2011), Design and synthesis of bimetallic electrocatalyst with multilayered Pt-skin surfaces. J. Am. Chem. Soc., 133, 14396–14403. (DOI: 10.1021/ja2047655)

11. Tang W. J., Zhang L., Henkelman G. (2011), Catalytic activity of Pd/Cu random alloy nanoparticles for oxygen reduction. J. Phys. Chem. Lett., 2, 1328–1331. (DOI: 10.1021/jz2004717)

12. Holewinski A., Idrobo J., Linic S. (2014), High-performance Ag–Co alloy catalysts for electrochemical oxygen reduction. Nat. Chem., 6, 828–834. (doi:10.1038/nchem.2032)

13. Wang J. X., Inada H., Wu L., Zhu Y., Choi Y., Liu P., Zhou W. P., Adzic R. R. (2009), Oxygen reduction on well-defined core - shell nanocatalysts: particle size, facet, and Pt shell thickness effects. J. Am. Chem. Soc., 131, 17298–17302. (DOI: 10.1021/ja9067645)

14. Oezaslan M., Hasché F., Strasser P. (2013), Pt-Based Core–Shell Catalyst Architectures for Oxygen Fuel Cell Electrodes, J. Phys. Chem. Lett., 4, 3273-3291. (DOI: 10.1021/jz4014135)

15. Mazumder V., Chi M., More K. L., Sun S. (2010), Core/shell Pd/FePt nanoparticles as an active and durable catalyst for the oxygen reduction reaction, J. Am. Chem. Soc., 132, 7848-7849. (DOI: 10.1021/ja1024436)

16. Greeley J., Stephens I. E. L., Bondarenko A. S., Johansson T. P., Hansen H. A., Jaramillo T. F., Rossmeisl J., Chorkendorff I., Nørskov J. K. (2009), Alloys of platinum and early transition metals as oxygen reduction electrocatalysts. Nat. Chem., 1, 552–556. (DOI: 10.1038/nchem.367)

17. Stamenkovic V., Mun B. S., Mayrhofer K. J. J., Ross P. N., Markovic N. M., Rossmeisl J., Greeley J., Nørskov J. K. (2006), Changing the activity of electrocatalysts for oxygen reduction by tuning the surface electronic structure. Angew. Chem. Int. Ed., 45, 2897–2901. (DOI: 10.1002/ange.200504386)

18. Jackson A., Viswanathan V., Forman, A. J., Larsen A. H., Nørskov J. K., Jaramillo T. F. (2014), Climbing the activity volcano: core–shell Ru@ Pt electrocatalysts for oxygen reduction. ChemElectroChem, 1, 67–71. (DOI: 10.1002/celc.201300117)

19. Hofmann T., Yu, T. H., Folse M., Weinhardt L., Bär M., Zhang Y., Merinov B. V., Myers D. J., Goddard W. A., Heske, C. (2012), Using photoelectron spectroscopy and quantum mechanics to determine d-band energies of metals for catalytic applications. J. Phys. Chem. C, 116, 24016–24026. (DOI: 10.1021/jp303276z)

20. Xin H., Linic S. (2010), Communications: Exceptions to the d-band model of chemisorption on metal surfaces: The dominant role of repulsion between adsorbate states and metal d-states. J. Chem. Phys., 132, 221101. (DOI: 10.1063/1.3437609)

21. Greeley J., Mavrikakis M. (2004), Alloy catalysts designed from first principles. *Nat. Mater., 3,* 810–815. (DOI:10.1038/nmat1223)

22. Nilekar A. U., Mavrikakis M. (2008), Improved oxygen reduction reactivity of platinum monolayers on transition metal surfaces. Surf. Sci., 602, L89-L94. (DOI: 10.1016/j.susc.2008.05.036)

23. Duan Z., Wang G. (2011), A first principles study of oxygen reduction reaction on a Pt(111) surface modified by a subsurface transition metal M (M = Ni, Co, or Fe), Phys. Chem. Chem. Phys., 13, 20178-20187. (DOI: 10.1039/C1CP21687B)

24. Greeley J., Nørskov J. K., Mavrikakis M. (2002), Electronic structure and catalysis on metal surfaces. Annu. Rev. Phys. Chem., 53, 319–348. (DOI: 10.1146/annurev.physchem.53.100301.131630)

25. Mahata A., Choudhuri I., Pathak B. (2015), A cuboctahedral platinum (Pt79) nanocluster enclosed by well defined facets favours di-sigma adsorption and improves the reaction kinetics for methanol fuel cells, Nanoscale, 7, 13438-13451. (DOI: 10.1039/C5NR01575H)

26. Hammer B., Nørskov J. K. (1995), Electronic factors determining the reactivity of metal surfaces. Surf. Sci., 343, 211-220. (DOI: 10.1016/0039-6028(96)80007-0)

27. Yang Z., Zhang Y., Wu R. (2012), High stability and reactivity of Pt-based core–shell nanoparticles for oxygen reduction reaction. J. Phys. Chem. C, 116, 13774-13780. (DOI: 10.1021/jp300971e)

28. Jin N., Han J., Wang H., Zhu X., Ge Q. (2015), A DFT study of oxygen reduction reaction mechanism over O-doped graphene-supported Pt_4, Pt_3Fe and Pt_3V alloy catalysts. Int. J. Hydrogen Energy, 40, 5126-5135. (DOI: 10.1016/j.ijhydene.2015.02.101)

29. Wang Y., Balbuena P. B. (2005), Potential energy surface profile of the oxygen reduction reaction on a Pt cluster: adsorption and decomposition of OOH and H_2O_2. J. Chem. Theory Comput., 1, 935-943. (DOI: 10.1021/ct0500794)

30. Zhang L., Iyyamperumal R., Yancey D. F., Crooks R. M., Henkelman G. (2013), Design of Pt-shell nanoparticles with alloy cores for the oxygen reduction reaction. ACS Nano, 7, 9168-9172. (DOI: 10.1021/nn403788a)

31. Zhang L., Henkelman G. (2012), Tuning the oxygen reduction activity of Pd shell nanoparticles with random alloy cores. J. Phys. Chem. C, 116, 20860-20865. (DOI: 10.1021/jp305367z)

32. Shin J., Choi J., Cha P., Kim S. K., Kim I., Lee S., Jeong D. S. (2015), Catalytic activity for oxygen reduction reaction on platinum-based core–shell nanoparticles: all-electron density functional theory. Nanoscale, 7, 15830-15839. (DOI: 10.1039/C5NR04706D)

33. Yang Y., Dai C., Shen Y., Fisher A., Cheng D. (2016), Design of binary and ternary platinum shelled electrocatalysts with inexpensive metals for the oxygen reduction reaction. Int. J. Hydrogen Energy, 41, 13014. (DOI: 10.1016/j.ijhydene.2016.05.036)

34. Jennings P. C., Polleta B. G., Johnston R. L. (2012), Theoretical studies of Pt–Ti nanoparticles for potential use as PEMFC electrocatalysts. Phys. Chem. Chem. Phys., 14, 3134–3139. (DOI: 10.1039/C2CP23430K)

35. Jennings P. C., Aleksandrov H. A., Neyman K. M., Johnston R. L. (2014), DFT studies of oxygen dissociation on the 116-atom platinum truncated

octahedron particle. Phys. Chem. Chem. Phys., 16, 26539–26545. (DOI: 10.1039/C4CP02147A)

36. Jennings P. C., Aleksandrov H. A., Neyman K. M., Johnston R. L. (2014), A DFT study of oxygen dissociation on platinum based nanoparticles. Nanoscale, 6, 1153–1165. (DOI: 10.1039/C3NR04750D)

37. Kettner M., Schneider W. B., Auer A. A. (2012), Computational study of Pt/Co core–shell nanoparticles: Segregation, adsorbates and catalyst activity. J. Phys. Chem. C, 116, 15432–15438. (DOI: 10.1021/jp303773y)

38. Wei G., Liu Z. (2013), Optimum nanoparticles for electrocatalytic oxygen reduction: the size, shape and new design. Phys. Chem. Chem. Phys., 15, 18555–18561. (DOI: 10.1039/C3CP53758G)

39. Stamenkovic V. R., Fowler B., Mun B. S., Wang G., Ross P. N., Lucas C. A., Marković N. M. (2007), Improved oxygen reduction activity on Pt_3Ni (111) via increased surface site availability. Science, 315, 493-497. (DOI: 10.1126/science.1135941)

40. Stamenkovic V., Mun B. S., Mayrhofer K. J. J., Ross P. N., Markovic N. M., Rossmeisl J., Greeley J., Nørskov J. K. (2006), Changing the activity of electrocatalysts for oxygen reduction by tuning the surface electronic structure. Angew. Chem., 118, 2963-2967. (DOI: 10.1002/ange.200504386)

41. Paßens M., Caciuc V., Atodiresei N., Moors M., Blügel S., Wasera R., Karthäuser S. (2016), Tuning the surface electronic structure of a Pt_3Ti (111) electro catalyst. Nanoscale, 8, 13924. (DOI: 10.1039/C5NR08420B)

42. Ding E., More K. L., He T. (2008), Preparation and characterization of carbon-supported PtTi alloy electrocatalysts. J. Power Sources, 175, 794-799. (DOI: 10.1016/j.jpowsour.2007.10.010)

43. He T., Kreidlera E. (2008), Combinatorial screening of PtTiMe ternary alloys for oxygen electroreduction. Phys. Chem. Chem. Phys., 10, 3731-3738. (DOI: 10.1039/B802818B)

44. Yeager E. (1986), Dioxygen electrocatalysis: mechanisms in relation to catalyst structure. J. Mol. Catal., 38, 5-25. (DOI: 10.1016/0304-5102(86)87045-6)

45. Sanchez-Sanchez C. M., Bard A. J. (2009), Hydrogen peroxide production in the oxygen reduction reaction at different electrocatalysts as quantified by scanning electrochemical microscopy. Anal. Chem., **81**, 8094-8100. (DOI: 10.1021/ac901291v)

46. Markovic N. M., Gasteiger H. A., Ross P. N. (1996), Oxygen reduction on platinum low-index single-crystal surfaces in alkaline solution: rotating ring disk Pt (hkl) studies. J. Phys. Chem., 100, 6715-6721. (DOI: 10.1021/jp9533382)

47. Tian N., Zhou Z. Y., Sun S. G., Ding Y., Wang Z. L. (2007), Synthesis of tetrahexahedral platinum nanocrystals with high-index facets and high electro-oxidation activity. Science, 316, 732-735. (DOI: 10.1126/science.1140484)

48. Susut C., Chapman G. B., Samjeske G., Osawa M. Y., Tong Y. J. (2008), An unexpected enhancement in methanol electro-oxidation on an ensemble of Pt(111) nanofacets: a case of nanoscale single crystal ensemble electrocatalysis. Phys. Chem. Chem. Phys, 10, 3712-3721. (DOI: 10.1039/B802708K)

49. Solla-Gullon J., Vidal-Iglesias F. J., Lopez-Cudero A., Garnier E., Feliu J. M., Aldaz A. (2008), Shape-dependent electrocatalysis: methanol and formic acid electrooxidation on preferentially oriented Pt nanoparticles. Phys. Chem. Chem. Phys., 10, 3689-3698. (DOI: 10.1039/B802703J)

50. Duan Z., Wang G. (2013), Comparison of reaction energetics for oxygen reduction reactions on Pt(100), Pt(111), Pt/Ni(100), and Pt/Ni(111) surfaces: A first-principles study. *J. Phys. Chem. C,* **117**, 6284-6292. (DOI: 10.1021/jp400388v)

51. Han B., Viswanathan V., Pitsch H. (2012), First-principles based analysis of the electrocatalytic activity of the unreconstructed Pt(100) surface for

oxygen reduction reaction. J. Phys. Chem. C, 116, 6174-6183. (DOI: 10.1021/jp2075379)

52. Mahata A., Rawat K. S., Choudhuri I., Pathak B. (2016), Single-layered platinum nanocage: a highly selective and efficient catalyst for fuel cells. J. Mater. Chem. A, **4**, 12756-12767. (DOI: 10.1039/C6TA03245A)

53. Mahata A., Rawat K. S., Choudhuri I., Pathak B. (2016), Octahedral Ni-nanocluster (Ni_{85}) for efficient and selective reduction of nitric oxide (NO) to nitrogen (N_2) Scientific Reports, 6, 25590. (doi: 10.1038/srep25590)

54. Blochl P. E. (1994), Projector augmented-wave method, Phy. Rev. B, 50, 17953. (DOI : 10.1103/PhysRevB.50.17953)

55. Kresse G., Hafner J. (1993), Ab initio molecular dynamics for liquid metals, Phy. Rev. B, 47, 558. (DOI: 10.1103/PhysRevB.47.558)

56. G Kresse., Hafner J. (1994), Ab initio molecular-dynamics simulation of the liquid-metal–amorphous-semiconductor transition in germanium, Phy. Rev. B, 49, 14251-14269. (DOI: 10.1103/PhysRevB.49.14251)

57. Kresse G., Joubert D. (1999), From ultrasoft pseudopotentials to the projector augmented-wave method, Phy. Rev. B, 59, 1758. (DOI: 10.1103/PhysRevB.59.17580)

58. Perdew J. P., Chevary J. A., Vosko S. H., Jackson K. A., Pederson M. R., Singh D. J., Fiolhais C. (1992), Atoms, molecules, solids, and surfaces: Applications of the generalized gradient approximation for exchange and correlation, Phy. Rev. B, 46, 6671. (DOI: 10.1103/PhysRevB.46.6671)

59. Grimme S., Antony J., Ehrlich S., Krieg S. (2010), A consistent and accurate ab initio parametrization of density functional dispersion correction (DFT-D) for the 94 elements H-Pu, J. Chem. Phys., 132, 154104. (DOI: 10.1063/1.3382344)

60. Henkelman G., Jonsson H. **(**2000) A climbing image nudged elastic band method for finding saddle points and minimum energy paths, J. Chem. Phys., 113, 9978-9985. (DOI: 10.1063/1.1329672)

61. Choudhuri I., Patra N., Mahata A., Ahuja R., Pathak B. (2015), B–N@Graphene: highly sensitive and selective gas sensor. J. Phys. Chem. C, 119, 24827-24836. (DOI: 10.1021/acs.jpcc.5b07359)

62. Mahata A., Rawat K. S., Choudhuri I., Pathak B. (2016), Cuboctahedral vs. octahedral platinum nanoclusters: Insights into the shape-dependent catalytic activity for fuel cell applications. Catal. Sci. Technol., 6, 7913-7923. (DOI: 10.1039/C6CY01709F)

63. Nosé S. (1984), A unified formulation of the constant temperature molecular dynamics methods. J. Chem. Phys., 81, 511-519. (DOI: 10.1063/1.447334)

64. Escano, M. C. S. (2015), First-principles calculations of the dissolution and coalescence properties of Pt nanoparticle ORR catalysts: The effect of nanoparticle shape. Nano Res., 8, 1689-1697. (DOI 10.1007/s12274-014-0670-1)

65. Greeley J., Nørskov J. K. (2007), Electrochemical dissolution of surface alloys in acids: Thermodynamic trends from first-principles calculations. Electrochimica Acta, 52, 5829-5836. (DOI: 10.1016/j.electacta.2007.02.082)

66. Caballero G., Balbuena P. B. (2010), Dissolution-resistant core−shell materials for acid medium oxygen reduction electrocatalysts. J. Phys. Chem. Lett., 1, 724–728. (DOI: 10.1021/jz1000165)

67. Seo J. K., Khetan A., Seo M. H., Kim H., Han B. (2013), First-principles thermodynamic study of the electrochemical stability of Pt nanoparticles in fuel cell applications. *J.* Power Sources, 238, 137-143. (DOI: 10.1016/j.jpowsour.2013.03.077)

68. Noh S. H., Han B., Ohsaka T. (2015), First-principles computational study of highly stable and active ternary PtCuNi nanocatalyst for oxygen reduction reaction. Nano Research, 8, 3394–3403. (DOI: 10.1007/s12274-015-0839-2)

69. Noh S. H., Seo M. H., Seo J. K., Fischerc P., Han B. (2013), First principles computational study on the electrochemical stability of Pt–Co nanocatalysts. Nanoscale, 5, 8625-8633. (DOI: 10.1039/C3NR02611F)

70. Komanicky V., Chang K. C., Menzel A., Markovic N. M., You H., Wang X., Myers D. (2006), Stability and Dissolution of Platinum Surfaces in Perchloric Acid. J.Electrochem. Soc., 153, B446-B451. (DOI: 10.1149/1.2229284)

71. Chen X., Chen S., Wang J. (2016), Screening of catalytic oxygen reduction reaction activity of metal-doped graphene by density functional theory. App. Sur. Sci., 379, 291-295. (DOI: 10.1016/j.apsusc.2016.04.076)

72. Tang L., Han B., Persson K., Friesen C., He T., Sieradzki K., Ceder G. (2010), Electrochemical stability of nanometer-scale Pt particles in acidic environments. J. Am. Chem. Soc., 132, 596-600. (DOI: 10.1021/ja9071496)

73. Kattel S., Duan Z., Wang G. (2013), Density functional theory study of an oxygen reduction reaction on a Pt_3Ti alloy electrocatalyst. J. Phys. Chem. C, 117, 7107-7113. (DOI: 10.1021/jp400158r)

74. Duan H., Hao Q., Xu C. (2015), Hierarchical nanoporous PtTi alloy as highly active and durable electrocatalyst toward oxygen reduction reaction. J. Power Sources, 280, 483–490. (DOI: 10.1016/j.jpowsour.2015.01.136)

75. He T., Kreidler E., Xiong L., Luo J., Zhongb C. J. (2006), Alloy electrocatalysts combinatorial discovery and nanosynthesis. J. Electrochem. Soc., 153, A1637-A1643. (DOI: 10.1149/1.2213387)

76. He T., Kreidler E., Xiong L., Ding E. (2007), Combinatorial screening and nano-synthesis of platinum binary alloys for oxygen electroreduction. J. Power Sources, 165, 87-91. (DOI: 10.1016/j.jpowsour.2006.12.030)

77. Li K., Li Y., Wang Y., He F., Jiao M., Tang H., Wu Z. (2015), The oxygen reduction reaction on Pt(111) and Pt(100) surfaces substituted by subsurface Cu: a theoretical perspective. J. Mater. Chem. A, 3, 11444-11452. (DOI: 10.1039/C5TA01017A)

78. Sha Y., Yu T. H., Merinov B. V., Shirvanian P., Goddard W. A. (2011), Oxygen hydration mechanism for the oxygen reduction reaction at Pt and Pd fuel cell catalysts. J. Phys. Chem. Lett., 2, 572-576. (DOI: 10.1021/jz101753e)

79. Farberow C. A., Godinez-Garcia A., Peng G. W., Perez-Robles J. F., Solorza-Feria O., Mavrikakis M. (2013), Mechanistic studies of oxygen reduction by hydrogen on PdAg(110). ACS Catal., 3, 1622-1632. (DOI: 10.1021/cs4002699)

80. Sha Y., Yu T. H., Liu Y., Merinov B. V., Goddard III W. A. (2010), Theoretical study of solvent effects on the platinum-catalyzed oxygen reduction reaction. J. Phys. Chem. Lett., 1, 856-861. (DOI: 10.1021/jz9003153)

81. Keith J. A., Jerkiewicz G., Jacob T. (2010), Theoretical investigations of the oxygen reduction reaction on Pt(111). ChemPhysChem, 11, 2779-2794. (DOI: 10.1002/cphc.201000286)

82. Jennings P. C., Aleksandrov H. A., Neyman K. M., Johnston R. L. (2015), O_2 Dissociation on M@Pt Core–Shell Particles for 3d, 4d, and 5d Transition Metals. J. Phys. Chem. C, 119, 11031–11041. (DOI: 10.1021/jp511598e)

83. Weiher N., Beesley A. M., Tsapatsaris N., Delannoy L., Louis C., van Bokhoven J. A., Schroeder S. L. M. (2007), Activation of oxygen by metallic gold in Au/TiO_2 catalysts. J. Am. Chem. Soc., 129, 2240–2241. (DOI: 10.1021/ja067316c)

84. Boronata M., Corma A. (2010), Oxygen activation on gold nanoparticles: separating the influence of particle size, particle shape and support interaction. Dalton Trans., 39, 8538-8546. (DOI: 10.1039/C002280B)

85. Galhenage R. P., Ammal S. C., Yan H., Duke A. S., Tenney S. A., Heyden A., Chen D. A. (2012), Nucleation, Growth, and Adsorbate-Induced Changes in Composition for Co–Au Bimetallic Clusters on TiO_2. J. Phys. Chem. C, 116, 24616–24629. (DOI: 10.1021/jp307888p)

86. Menning C. A., Chen J. G. (2009), General trend for adsorbate-induced segregation of subsurface metal atoms in bimetallic surfaces. J. Chem. Phys., 130, 174709. (DOI: 10.1063/1.3125926)

87. Murphy S., Manai G., Shvets I. V. (2005), Oxygen-induced p(3 × 1) reconstruction of the W(1 0 0) surface. Sur. Sci., 579, 65-72. (DOI: 10.1016/j.susc.2005.01.048)

88. Oemry F., Nakanishi H., Kasai H., Maekawa H., Osumi K., Sato K. (2014), Adsorbed oxygen-induced cluster reconstruction on core–shell Ni@Pt and Pt clusters. J. Alloys and Compounds, 594, 93-101. (DOI: 10.1016/j.jallcom.2014.01.084)

89. Shen Y. G., O'Connor D. J., Wandelt K. (1998), The surface composition, structure and oxygen-induced (2×1) reconstruction of $Cu_3Pt(110)$. Surface Science, 10, 1-14. (DOI :10.1016/S0039-6028(98)00262-3)

90. Tenney S. A., Ratliff J. S., Roberts C. C., He W., Ammal S. C., Heyden A., Chen D. A. (2010), Adsorbate-induced changes in the surface composition of bimetallic clusters: Pt−Au on $TiO_2(110)$. J. Phys. Chem. C, 114, 21652–21663. (DOI: 10.1021/jp108939h)

91. Xie R., Chen D., Wang X., He T., Liu F. (2002), Adsorbate-induced surface stress of chloride monolayer on Au(111) electrode. J. Phys. Chem. B, 106, 12948–12956. (DOI: 10.1021/jp0210982)

92. Lei Y., Zhao H., Rivas R. D., Lee S., Liu B., Lu J., Stach E., Winans R. E., Chapman K. W., Greeley J. P., Miller J. T., Chupas P. J., Elam J. W. (20014), Adsorbate-induced structural changes in 1–3 nm platinum nanoparticles. J. Am. Chem. Soc, 136, 9320–9326. (DOI: 10.1021/ja4126998)

93. Yancey D. F., Chill S. T., Zhang L., Frenkel A. I., Henkelman G., Crooks R. M. (2013), A theoretical and experimental examination of systematic ligand-induced disorder in Au dendrimer-encapsulated nanoparticles. Chem. Sci., 4, 2912-2921. (DOI: 10.1039/C3SC50614B)

94. Kitchin J. R., Nørskov J. K., Barteau M. A., Chen J.G. (2004), Role of strain and ligand effects in the modification of the electronic and chemical properties of nimetallic surfaces. Phys. Rev. Lett., 93, 156801. (DOI: 10.1103/PhysRevLett.93.156801)

95. Kitchin J. R., Nørskov J. K., Barteau M. A., Chen, J. G.(2004), Modification of the surface electronic and chemical properties of Pt(111) by subsurface 3d3d transition metals. J. Chem. Phys., 120, 10240. (DOI: 10.1063/1.1737365)

96. Kattel S., Wang G. (2014), Beneficial compressive strain for oxygen reduction reaction on Pt (111) surface. J. Chem. Phys., 141, 124713. (DOI: 10.1063/1.4896604)

97. Bader, R. F. W. Atoms in Molecules: A Quantum Theory; Oxford University Press: USA, **1994.**

98. Henkelman G., Arnaldsson A., Jonsson H.(2006), A fast and robust algorithm for Bader decomposition of charge density. Comput. Mater. Sci., 36, 354-360. (DOI: 10.1016/j.commatsci.2005.04.010)

99. Sanville E., Kenny S. D., Smith R., Henkelman G. (2007), Improved grid-based algorithm for Bader charge allocation. J. Comput. Chem., 28, 899. (DOI: 10.1002/jcc.20575)

100. Tang W., Sanville E., Henkelman G. (2009), A grid-based Bader analysis algorithm without lattice bias. J. Phys.: Condens. Matter., 21, 084204. (DOI: 10.1088/0953-8984/21/8/084204)

101. Mathew K., Sundararaman R., Letchworth-Weaver K., Arias T. A., Hennig R. G. (2014), Implicit solvation model for density-functional study of nanocrystal surfaces and reaction pathways J. Chem. Phys., 140, 084106. (DOI: 10.1063/1.4865107)

102. Fishman M., Zhuang H. L., Mathew K., Dirschka W., Hennig R. G. (2013), Accuracy of exchange-correlation functionals and effect of solvation on the surface energy of copper. Phys. Rev. B: Condens. Matter Mater. Phys. 87, 245402. (DOI: 10.1103/PhysRevB.87.245402)

103. Mahata A., Rai R. K., Choudhuri I., Singh S. K., Pathak B. (2014), Direct vs. indirect pathway for nitrobenzene reduction reaction on a Ni catalyst surface: a density functional study. Phys. Chem. Chem. Phys., 16, 26365-26374. (DOI: 10.1039/C4CP04355C)

104. Goodpaster J. D., Bell A. T., Head-Gordon M. (2016), Identification of possible pathways for C–C bond formation during electrochemical reduction of CO_2: New theoretical insights from an improved electrochemical model. J. Phys. Chem. Lett., 7, 1471–1477. (DOI: 10.1021/acs.jpclett.6b00358)

105. Mahata A., Choudhuri I., Pathak B. (2015), A cuboctahedral platinum (Pt_{79}) nanocluster enclosed by well defined facets favours di-sigma adsorption and improves the reaction kinetics for methanol fuel cells. Nanoscale, 7, 13438-13451. (DOI: 10.1039/C5NR01575H)

106. Qi L., Qian X., Li J. (2008), Near neutrality of an oxygen molecule adsorbed on a Pt(111) surface. Phys. Rev. Lett., 101, 146101. (DOI: 10.1103/PhysRevLett.101.146101)

Chapter 3

Single-layered Platinum Nanocage: A Highly Selective and Efficient Catalyst for Fuel Cell

3.1 Introduction

Proton exchange membrane (PEM) fuel cell is one of the most promising devices for clean energy due to their high efficiency, low operating temperature and zero emission *[1-4]*. Oxygen reduction reaction (ORR) is the key reaction at the cathode and controls the performance of a fuel cell. However, Pt-based electrodes limit the performance of a fuel cell due to the sluggish ORR reaction rate and high overpotential *[5-6]*. As a result, the efficiency remains low, while the costs are very high for Pt-based electrodes. In the past few decades, considerable efforts (experimental and theoretical) have been made to improve the ORR activity. Pd and Ir based electrodes have been emerged as potential electrodes to sustain the harsh reaction conditions of the fuel cells *[7-10]*. However, due to their low abundances, the main challenge remains to lessen the cost of the catalyst. So, it is very important to design a highly active and cheap electrode for ORR. However, the limited choice of such catalysts has made this a difficult task for the scientific community. Pt has been reported to be the most suitable catalyst among all for ORR. Thus, the key challenge is to reduce the Pt loading without compromising the performance of a fuel cell. In this context, alloying Pt with other transition metals has been emerged as a good alternative for efficiency and stability of the catalyst. Such alloying with other metals leads to the formation of bi-metallic *[11-13]*, mixed alloy *[14-15]* and core-shell structures *[16-18]*. These bi-metallic catalysts, not only reduce the Pt-content, but also increase the specific activity which in turns increases the efficiency of ORR activity. Norskov and co-workers *[19-21]* studied a series of Pt_3M alloy-based (M= Ti, V, Ni, Co, Fe, Y, Sc, Rh) catalysts for ORR activity and the low binding energy of the intermediate species (O and OH) on the alloy surfaces relative to Pt(111) bulk surface is the reason for their (Pt_3M, M = Co, Ni, Sc, Y) superior catalytic activities.

The discovery of fullerene *[22]* gave a new direction in the area of hollow materials. Later on, many fullerene like structures such as B-fullerene *[23]*, BN-fullerenes *[24-25]* and inorganic fullerenes *[26]* have been synthesized for various applications. Similarly, metal-based hollow nanoclusters have been recently synthesized, which not only lower the Pt-content, but also improve the electro catalytic activity significantly. Recently, Pd-Rh nanoboxes *[27]* demonstrated excellent catalytic activity towards ORR. Xie and co-workers used an effective strategy for reducing the Pt-content by synthesizing atomic layer-by-layer deposition of Pt on Pd-nanocubes *[28]*. Besides, they have synthesized a series of octahedral-based nano-clusters *[29]*, by deposition of a few atomic layers (1-6 layers) of platinum on the Pd octahedral structure. Similarly, Pt-based cubic, octahedral *[30]* and icosahedral nanocages *[31]* have been synthesized with well defined (111) and (100) facets by depositing a few atomic layers of Pt on Pd nanocrystals and then etching away the Pd template. Considerable progresses have been made on the noble metal based nanocages, nanoframes and nanoboxes for ORR activity *[32-36]*. Recently, Adzic and co-workers synthesized a highly stable Pt monolayer on different substrate for ORR reactivity *[37-39]*. Interestingly, such nanocages show superior catalytic activity (towards ORR) compared to a Pt/C-based catalyst *[29-31]*. The developments in the field of single-layered materials inspired us to model a singled layered platinum-nanocage for ORR activity.

We report here for the first time that a single layered octahedral platinum nanocage (Pt_{66}) enclosed by eight (111) facets can improve the ORR activity significantly. Besides, the Pt- loading (lowers the Pt-content by 22%) of the nanocage for ORR is considerably lower than that of a similar size nanocluster (Pt_{85}).

Despite extensive experimental reports on ORR activity over a hollow nanocluster (such as nanocage, nanoframe, nanobox and so on), the underlying reason behind their excellent catalytic behaviour is yet to be understood. Thereby, the superior catalytic activity of the nanocage is investigated through a systemic study. The energetic, dynamic and thermal stability of this nanocage is verified by cohesive energy, phonon, and molecular dynamics calculations, respectively. ORR involves many-electron reduction and it can proceed either through a more efficient four-step, four-electron reduction with the formation of H_2O or via a two-step, two-electron reduction for the formation of H_2O_2 *[40]*. In fuel cells, four-electron reduction ($4e^-$) is preferred over a two-electron ($2e^-$) reduction in order to maximize the efficiency. Furthermore, H_2O_2 formation affects the durability of the membrane of a PEM fuel cell *[1,41]*. Thereby, the product selectivity (H_2O vs. H_2O_2) is very important for the performance of a fuel cell. The formations of *OH (*O + H^+ + e^- $\rightarrow$ *OH) and *H_2O (*OH + H^+ + e^- $\rightarrow$ *H_2O) are the two most important steps for a platinum electrode-based fuel cell *[42-45]*. Therefore, the stability of the intermediate species (*O and *OH) is one of the governing factors for the selective four-electron ($4e^-$) reduction reaction. The adsorption behaviour of all the possible ORR intermediates and the complete O_2 reduction pathways are studied on Pt(111) facet of the nanocage surfaces. For comparisons, our results are compared with the available experimental and theoretical data on bulk Pt(111) surfaces. Microkinetic analysis is performed to gain more insights into the surface coverage, rate of reaction and product selectivity (H_2O vs. H_2O_2). The product selectivity (H_2O vs. H_2O_2) and exceptional catalytic activity of the nanocage are discussed at the end.

3.2 Model and Computational Details

An octahedral shape of ~1.5 nm diameter of Pt_{85} nanocluster is modelled by cutting along all (111) planes of the bulk face cantered cubic Pt structure. All the core atoms (19 atoms) of the Pt_{85} nanocluster are removed to create a void inside. Thus, the single layer nanocage (Figure 3.1a) structure consists of 66 platinum atoms. Pt-nanocages with icosahedral *[31]* and octahedral *[30]* geometries have been synthesized lately. Moreover, Pt(111) facet is the majorly exposed facet observed in the XRD pattern of experimentally synthesized Pt nanoclusters *[46-48]*. Previous experimental and theoretical reports show that Pt(111) surface shows better ORR activity than Pt(100) or any other Pt-surfaces *[12,44,49-52]*. Stamenkovic et al. *[12]* demonstrated through their experimental study that the Pt(111) surface shows two times higher ORR activity than the Pt(100) surface. Similarly, Zhang et al. *[49]* reported that Pt_3Ni nanoctahedra terminated with (111) facets improves the ORR activity by five-fold compared to the similar sized Pt_3Ni nanocube terminated with (100) facets. Carlos et al. *[50]* reported that the octahedral platinum nanoparticle with (111) facets exhibits an enhanced ORR activity while comparing with the cubic nanoparticles. Moreover, Markovic et al. *[51]* reported that the sequence of ORR activity on Pt(hkl) is (100) < (110) < (111).

Similarly, Duan et al. *[44]* reported from their theoretical study that Pt(111) surface shows better ORR activity compared to the Pt(100) surface. Moreover, Han et al. *[52]* stressed on the significant role of the square-symmetry of Pt(100) surface and reported that Pt(111) surface shows better catalytic activity compared to Pt(100) surface at the fuel cell operating voltage of around 0.7-0.8 V. Therefore, inspired by these findings, we have designed an octahedral nanocage enclosed by (111) facets to improve the ORR activity.

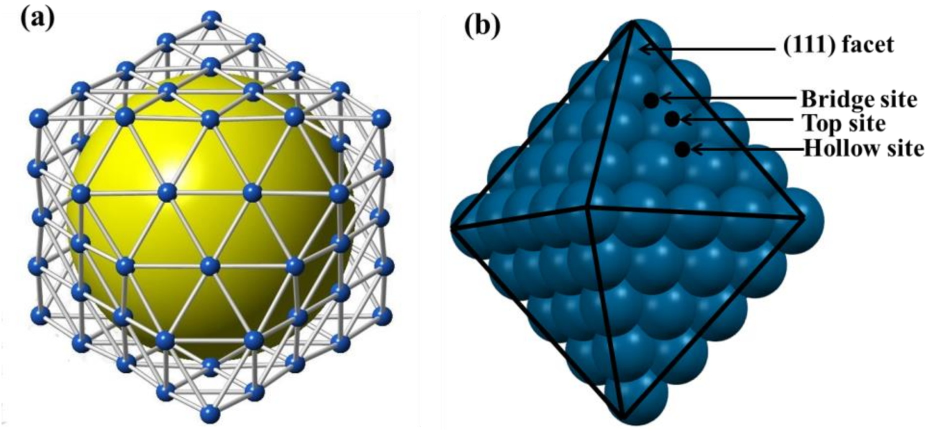

Figure 3.1: Octahedral nanocage with eight (111) facets: (a) yellow sphere represents the inside void of the nanocage and (b) different adsorption sites on (111) facet of the nanocage.

The first-principles calculations are performed using a projected augmented wave (PAW) *[53]* method as implemented in the Vienna Ab initio Simulation Package (VASP) *[54-56]*. The exchange-correlation potential is described by using the generalized gradient approximation of Perdew-Burke-Ernzerhof (GGA-PBE) *[57]*. Plane wave with a kinetic energy cut off of 470 eV is used to expand the electronic wave functions. A 25 × 25 × 25 $Å^3$ cubic supercell is used to optimize the metal nanocage to rule out the possibility of interactions between the periodically repeated metal clusters. The nanocage is placed at the center of the box. During structural relaxation, all the atomic coordinates are optimized whereas the cell volume and cell shape are kept fixed. The Brillouin zone is sampled with a Gamma point (1×1×1) for clusters. The total energy of the nanocage cluster (Pt_{66}) is improved by 0.00003 eV if the k-point mesh set to 2 × 2 × 2. Therefore, we have used Gamma point for all the calculations to save the computational cost. All the atoms are relaxed for the full structural relaxation. The bulk Pt(111) surface is modelled with a (3 × 3) supercell to minimize the lateral interactions between the repeating images. The metal slab is composed of five atomic layers, where the bottom three layers are fixed and top two layers are relaxed. A 12 Å of vacuum is used along the z-direction to avoid periodic interactions. The Brillouin zone is sampled using a 3 × 3 × 1 k-point grid for the surface calculations. All the systems are fully optimized, where the convergence criteria for total energy and forces are set at 10^{-4} eV and <0.02 eV/Å, respectively. For electronic structure calculations, a 2 × 2 × 2 k-point mesh is used for the nanocage, whereas a 9 × 9 × 1 k-point mesh is used for bulk Pt(111) surface. Spin-polarized calculations are performed for all the molecular species and oxygen adsorbed intermediates. We have included Grimme's D3-type *[58]* of semiempirical method to include the dispersion energy corrections for van der Waals interactions. Phonon frequency of the nanocage is calculated using density functional perturbation theory *[59]*. The climbing nudged elastic band (CI-NEB) method *[60]* is used to locate the transition state. Six intermediate images are used in each CI-NEB pathway. Vibrational frequencies for the initial, transition and final states of the reactions are calculated and the transition states are confirmed by the presence of one imaginary frequency. Zero-point energy (ZPE) is calculated using the following equation:

$$\mathrm{ZPE} = \sum_i 1/2 h\upsilon_i \tag{3.1}$$

where h is the Planck constant and υ_i is the frequency of the i^{th} vibrational mode. The adsorption energies (E_{ad}) for all possible adsorbates are calculated using the following equation:

$$E_{ad} = E_{*\text{-adsorbate}} - (E_{*} + E_{adsorbate}) \tag{3.2}$$

where $E_{*\text{-adsorbate}}$ is the total energies of the surface-adsorbate, E_{*} and $E_{adsorbate}$ are the single point energies of the surface and adsorbate in the optimized geometry of surface-adsorbate, respectively. We have used this convention for better comparisons, as the extent of deformation is different for different surfaces. The reaction free energy is calculated using the total energy difference between the products and the reactants. Thus, negative free energy suggests the exergonic nature of the reaction, whereas positive reaction energy suggests the endergonic nature of the reaction. Activation barriers are calculated by the energy differences between the transition and initial states. The reaction free energies(ΔG) and activation barriers ($\Delta G^{\ddagger}$) are calculated using zero point energy (ZPE) and entropy corrections. The adsorbed intermediate (R) is denoted with an asterisk (*) sign.

3.3 Results and Discussion

We have divided this section into three parts. In the first part, we have discussed about energetic, thermal and dynamical stability of the Pt-nanocage. Then, the adsorption behaviour of ORR intermediates on the nanocage surface is studied and compared with previous theoretical and experimental reports on Pt(111) bulk surfaces. Furthermore, all possible elementary steps are subsequently studied for ORR followed by an attempt is made to find out the underlying reason behind the excellent catalytic behaviour of the nanocage and its catalytic activity is compared with previously reported bulk Pt(111) surface based catalysts. Finally, the effect of applied voltage on the free energy diagram has been discussed and a detailed microkinetic analysis has been performed to explore the selectivity of four-electron vs. two-electron reduction reaction.

3.3.1 Nanocage Stability

Energetic Stability:

Total energy calculations are performed to evaluate the thermodynamic stability of the nanocage. Cohesive energy is calculated for the nanocage (Pt_{66}) to find out the possibility of synthesizing such a nanocage structure. The cohesive energy (E_{coh}) is calculated as follows

$$E_{coh} = (E_{Nanocage} - nE_{Pt})/n \tag{3.3}$$

where $E_{Nanocage}$ is the optimized energy of the NCs, n is the number of platinum atoms in the NCs and E_{Pt} is the energy of one isolated platinum atom. For comparisons, we have calculated cohesive energies for bulk and Pt(111) surface. The calculated cohesive energies are -4.71, -5.47 and -5.71 eV/atom for the nanocage, bulk Pt(111) surface and bulk platinum, respectively. The cohesive energy indicates that the nanocage structure is less stable with respect to the bulk Pt(111). Our calculated cohesive energy value of bulk platinum is very much in agreement with the experimental value of -5.84 eV/atom *[61]*.

Thermal Stability

Low-temperature fuel cells (DMFC, PEMFC and AFC) are operated in the temperature range from 300 to 600 K *[5,16]*. Thus, the thermal stability of the nanocage is verified by carrying out Ab Initio Molecular Dynamics Simulations (AIMD) using canonical ensemble at 300-600 K with a time step of 1 femtosecond. Temperature control is achieved by nóse thermostat model *[62]*. First, the structure is heated at 300 K with a time step of 1 femtosecond (fs) for 20 picoseconds (ps), but no structure reconstruction is found. The fluctuation of the total energy is smooth throughout the AIMD simulation (Figure 3.2).

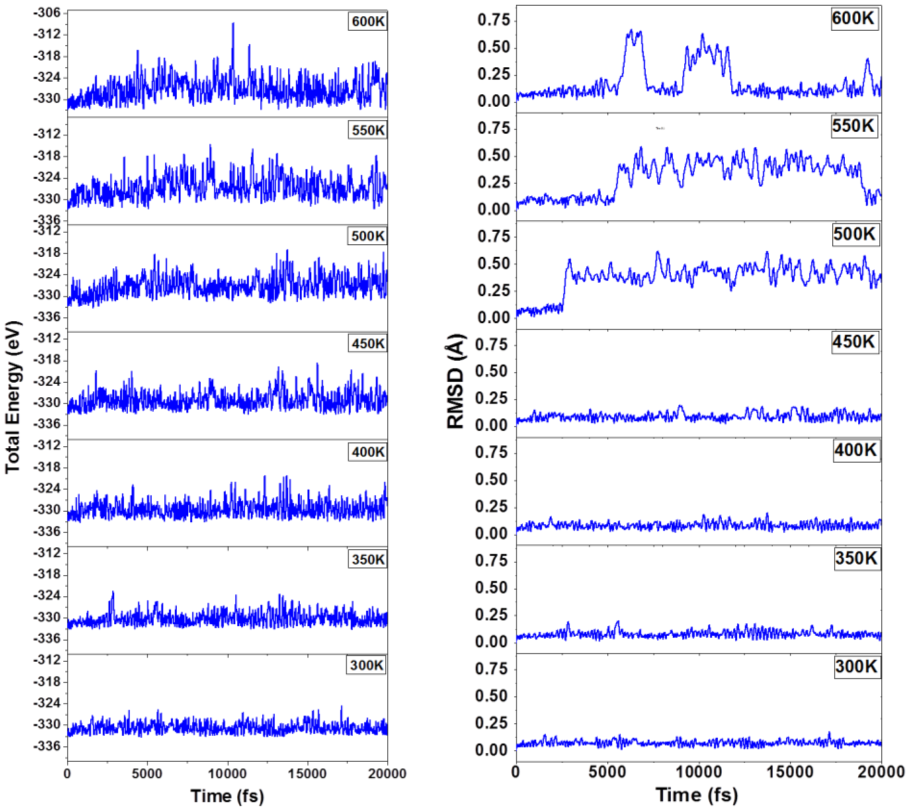

Figure 3.2: Molecular dynamics simulation analysis at different temperatures as a function of time step: (a) total energy and (b) RMSD.

Hence, the structure remains stable at room temperature. Furthermore, simulations using an NVT ensemble at 350, 400, 450, 550, and 600 K with a time step of 1 fs were carried for 20 ps. We have plotted the root mean square displacement (RMSD) as a function of time step (Figure 3.2b) for all the cases. Our RMSD plots show that atomic displacements are negligible at lower temperatures (300-450 K) but significant at higher temperatures (500-600 K). The snapshots of atomic configurations of Pt_{66}-nanocage at the end of MD simulations are shown in Figure 3.3.

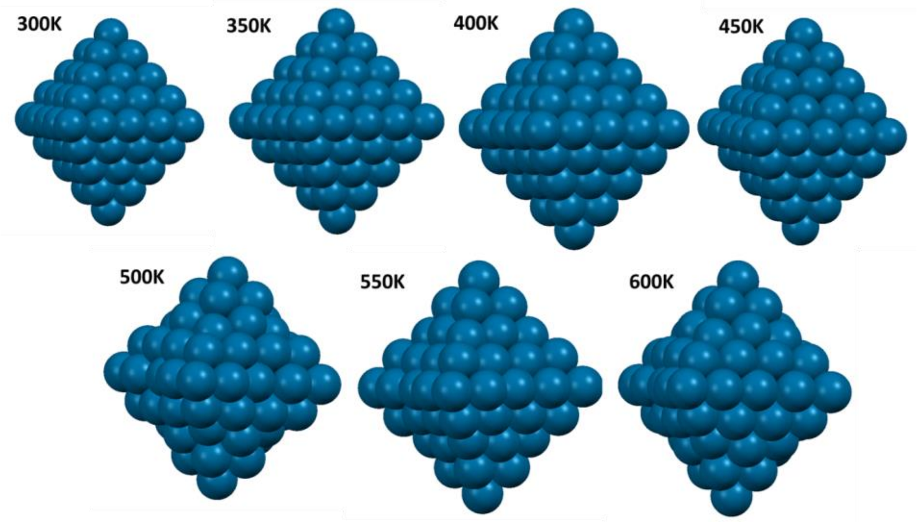

Figure 3.3: Snapshots of the nanocage after the simulation at different temperatures.

We did not find any structural reconstruction even after heating at 600 K for 20 ps. We have carefully investigated the structure of the nanocage during the AIMD simulation at higher temperatures (500-600 K). At 500 K, our RMSD vs. time step plot shows that RMSD value is significantly high around 2600 fs. We find that the diameter of the nanocage (14.69 Å) increases to 14.75 Å (Figure 3.4a) at 2600 fs. Similarly the diameter of the nanocage increases to 14.97 Å (Figure 3.4b) at 550 K. Interestingly at 600K, our plot shows that maximum atomic displacements occur in two stages. During the first maxima (around 5650- 7150 fs), the surface atoms are moving inwards and the cluster size reduces to 14.42 Å (Figure 3.4c). The second hump (9120-11880 fs), shows that the surface atoms are moving outwards and the average diameter of the nanocage increases to 15.04 Å (Figure 3.4d). However, the structure returns back to the minimum energy structure at the end of the simulation. Thus, at higher temperatures, atomic displacements are maximum and at 600 K, atomic displacements are occurring in both ways (inwards and outwards). However, even at 600 K, inter-conversion is not possible to any other structures.

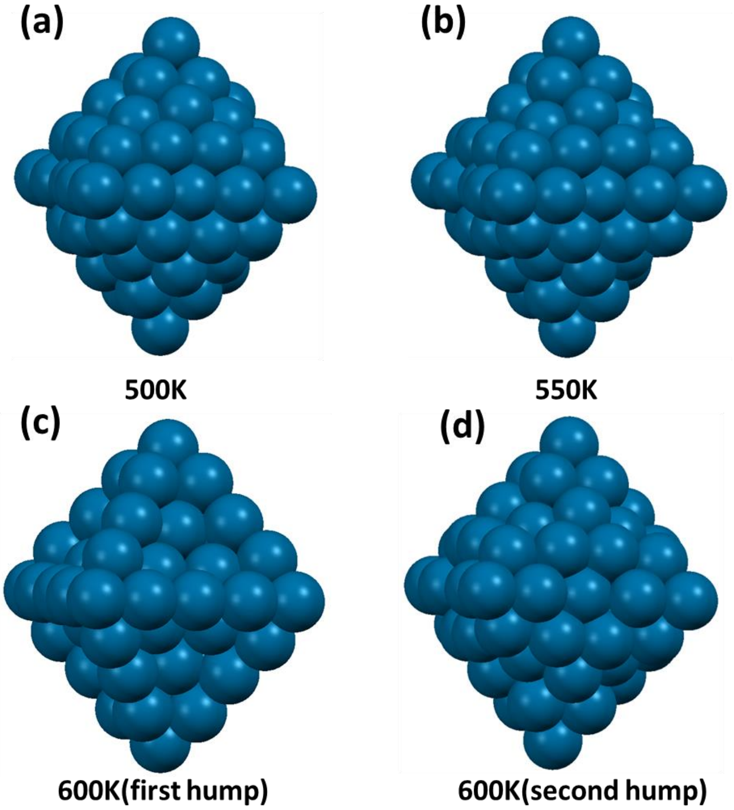

Figure 3.4: Snapshots of the nanocage after the simulation at different temperatures.

Thereby, we predict that the nanocage can withstand temperatures as high as 600 K. These results demonstrate that the single layered nanocage is separated by high-energy barriers from other local minima structures.

Dynamic Stability:

The dynamic stability of the nanocage is evaluated from the phonon calculation by using Density Functional Perturbation Theory (DFPT) as implemented in VASP. Our phonon calculation on Pt_{66}-nanocage shows small imaginary frequencies in the order of <35i cm^{-1} (Supporting Information for details). Therefore, the nanocage could be a dynamically stable cluster.

Generally, nanocages are synthesized on a support material *[32]* and in that case, they might show exceptional stability on a support material.

3.3.2 ORR Mechanism

3.3.2.1 Adsorption

Three different catalytic sites (Figure 3.1b) are present on Pt(111) facet of the nanocage: (i) top, (ii) bridge, and (iii) hollow. Here, fcc and hcp sites are equivalent and represented as a hollow site. We have checked the relative stabilities of the intermediate species ($*O_2$, $*O$, $*OH$, $*OOH$, $*H_2O$ and $*H_2O_2$) adsorbed on all the three possible sites and then the most stable conformers are considered for detailed study. The most preferred binding sites of the intermediate species and their respective binding energies are calculated and given in Table 3.1. For comparison, we have calculated adsorption energy of the intermediate species on a bulk Pt(111) surface. Furthermore, all these values are compared (Table 3.1) with previous reported values on bulk Pt(111) surface to estimate the accuracy of our calculations.

Table 3.1: Preferred sites, binding energies (eV) of the most stable ORR intermediate species on Pt(111) facet of the nanocage and bulk Pt(111) surface. Here t, b, h and f denote top, bridge, hollow and fcc sites respectively. Values of previous report on Pt(111) surfaces are taken from the references *[63, 64]*.

Adsorbed species	**Nanocage (Pt_{66})**	**Pt(111) surface**	**Previous report of Pt(111) surface**
$*O_2$	-1.82 (b)	-0.67 (b)	-0.69(b)*[63]*, -0.62(b)*[64]*
$*O$	-5.32 (h)	-4.42 (f)	-3.96(f) *[63]*, -4.30(f) *[64]*
$*OH$	-3.03 (b)	-2.37 (t)	-2.22(t) *[63]*, -2.21(t) *[64]*
$*OOH$	-1.39 (b)	-1.15 (b)	-1.15(b) *[63]*, -0.94(b) *[64]*
$*H_2O_2$	-0.22 (b)	-0.30 (b)	-0.37(b) *[63]*, -0.27(b) *[64]*
$*H_2O$	-0.09 (t)	-0.26 (t)	-0.25(t) *[63]*, -0.20(t) *[64]*
$*H$	-2.74 (h)	-2.77 (f)	-2.74(f) *[63]*, -2.62(t) *[64]*

*O_2

*O_2 prefers to be adsorbed in a superoxo way on the bridge site of the nanocage with adsorption energy of -1.82 eV. However, the adsorption energy (for superoxo structure) is -0.67 eV while adsorbed on bulk Pt(111) surface. Thereby, O_2 is strongly adsorbed on the Pt_{66} nanocage surface compared to bulk Pt(111) surface. Furthermore, the adsorbed *O-O bond distances are 1.39, and 1.37 Å while adsorbed on nanocage and bulk Pt(111), respectively. Similarly, *O_2 can be adsorbed (via one of the O atoms) in a tilted way at the top site of Pt(111) facet of the nanocage with an adsorption energy -0.51 eV. The respective binding energy is -0.17 eV when adsorbed on bulk Pt(111) surface. This indicates that the nanocage is highly active for O_2 activation in relative to bulk Pt(111) surface.

Our calculated O_2 adsorption energy (-0.67 eV) while adsorbed in a superoxo fashion on bulk Pt(111) surface is very much in consistent with the previous calculated values of -0.41, *[65]* -0.49, *[66]* -0.62 *[64]* and -0.69 eV *[63]* on bulk Pt(111) surface. The adsorption energy (-0.17 eV) calculated for the tilted conformer is also very much comparable with the previous calculated value of -0.06 eV *[66]*. In superoxo form, our calculated *O-O bond distance and vibrational frequency of O_2 bond while adsorbed on bulk Pt(111) surface are 1.37 Å and 879 cm^{-1}, which are also very much comparable with the experimental bond distance and vibrational frequency of 1.37 Å *[67]* and 870 cm^{-1}, *[68]* respectively. The *O_2 superoxo form (-0.67 eV) is characterized experimentally through the temperature-programmed desorption technique and the experimentally reported binding energy of -0.38 eV *[69]* matches with our calculated binding energy of -0.67 eV. Using electron energy loss spectroscopy, Steininger *et al.* *[70]* reported the *O_2 binding energy of ≈ 0.5 eV, which is again very much in consistent with our calculated adsorption energy of -0.67 eV. Thereby, we find that our results are in very much agreement with previously reported (theoretical and experimental) values.

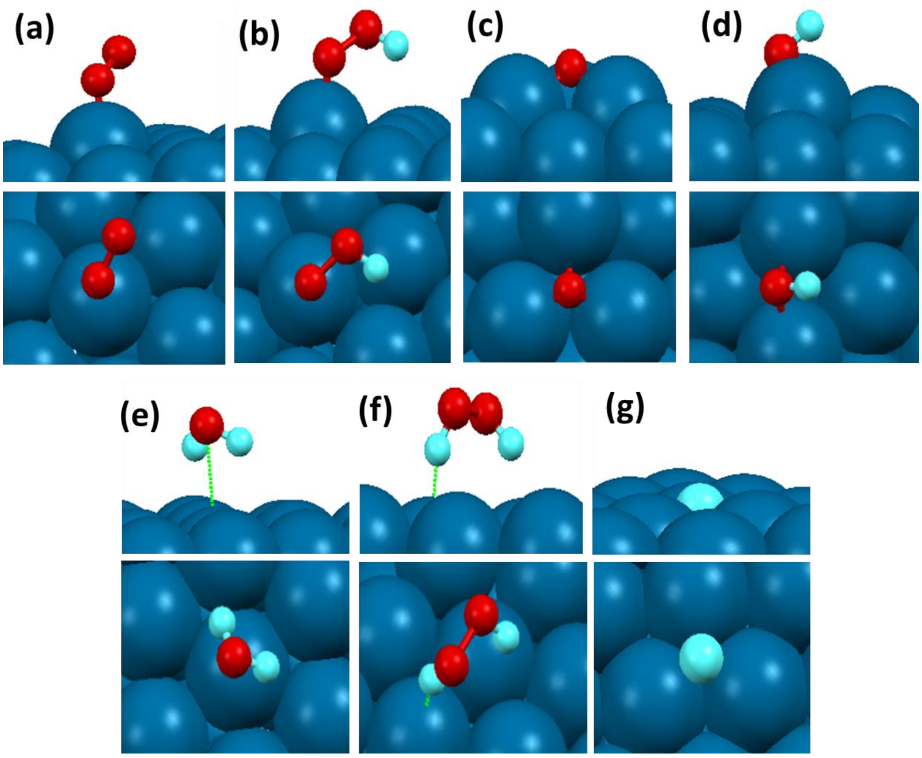

Figure 3.5: Adsorption pattern of the reaction intermediates.

*O

*O is found to be more stable at the hollow site of the nanocage with adsorption energy of -5.32 eV. However, *O prefers fcc site of the bulk Pt(111) with a binding energy of -4.42 eV. Thereby, the nanocage is more reactive for *O binding. Previous surface model studies reported adsorption energies of -4.30 *[64]*, -4.51 eV *[71]*, and -4.46 eV *[72]* for *O binding at the fcc site of bulk Pt(111). Furthermore, our result is very much in agreement with experimental oxygen atom binding energy of 4.32 eV over a clean Pt(111) surface *[73]*.

*OH

*OH prefers to be adsorbed at the bridge site of Pt(111) facet of the nanocage with an adsorption energy of -3.03 eV, which is higher than the adsorption energies (-2.37 eV) on bulk Pt(111) surface. Previous studies on bulk Pt(111) surfaces reported the adsorption energies of -2.21 *[64]* and -2.45 eV *[71]* at the top position. Our calculated adsorption energy value on bulk Pt(111) is very much consistent with the experimental heat of formation of -2.14 eV over bulk Pt(111) surface *[74]*.

Interestingly, we find *O and *OH are strongly adsorbed over the nanocage surface compared to bulk Pt(111), which is far from optimal binding energy range of *O and *OH on Pt_3M alloy surfaces as proposed by Norskov and co-workers *[19-21]*.

*H_2O and *H_2O_2

*H_2O adsorbs very weakly at the top site of (111) facet of the nanocage with an adsorption energy of -0.09 eV. In the bulk Pt(111) surface, *H_2O is calculated to be most stable at the top site with an adsorption energy of -0.26 eV, which is very much consistent with the previous theoretical adsorption energies of -0.20 *[64]* and -0.22 eV *[65]*. The experimental binding energy of *H_2O is -0.52 eV *[75]*. Gland *et al. [76]* reported the experimental adsorption energy of *H_2O to be within -0.43-0.62 eV using the thermal desorption spectroscopy (TDS) and X-ray photoemmision spectroscopy (XPS). Our calculated adsorption energies of *H_2O_2 are -0.22 and -0.30 eV over the nanocage and bulk Pt(111), respectively. Previous theoretical studies reported the adsorption energies of -0.37 *[63]* and -0.27 eV *[64]* over bulk Pt(111). The weak adsorption energy of *H_2O and *H_2O_2 over the nanocage surface compared to Pt(111) suggests that the easy desorption of water from the catalyst surface. Therefore, reduces the possibility of surface poisoning.

Moreover, we have studied the adsorption behaviour of some important intermediates (O_2, O and OH) at the low-coordinated edge site to compare the catalytic activity of the edge site with respect to the Pt(111) surface of the nanocage. At the edge site, the calculated binding energies are -2.02, -4.72 and -3.02 eV for *O_2, *O and *OH, respectively. However, the respective binding energies are -1.82, -5.32 and -3.03 eV on the Pt(111) facet of the nanocage. We find that *O_2 adsorbs only in a superoxo way at the edge site of the nanocage with binding energy of -2.02 eV. However, at the edge site, we could not locate a minimum energy structure where *O_2 adsorbs in a titled way as observed on the Pt(111) surface. Thus, *O_2 has a higher binding energy (by 0.20 eV) at the edge site than on the Pt(111) facet of the nanocage.

On the other hand, *O has a lower binding energy (by 0.60 eV), and *OH has a comparable binding energy at the edge site of the nanocage.

3.3.2.2 Reaction Mechanism

During the ORR, H_2O and H_2O_2 are the two end products, which are formed via four-electron ($4e^-$) and two-electron ($2e^-$) reduction reactions, respectively. For the $4e^-$ reduction (H_2O formation), we propose two possible pathways: i) direct and ii) indirect (Scheme 3.1). In the direct pathway, the adsorbed oxygen molecule ($*O_2$) can undergo direct O-O bond dissociation ($*O_2 \rightarrow *O + *O$) and in the indirect mechanism, the reaction can precede via hydrogenation ($*O_2 + *H \rightarrow *OOH$) followed by dissociation ($*OOH \rightarrow *O + *OH$). Then the end products are formed through subsequent hydrogenation and O-H bond formation steps. However, the indirect bond dissociation can happen via two pathways: (i) peroxyl and (ii) peroxide formations. In the peroxyl mechanism, the adsorbed oxygen molecule ($*O_2$) undergoes hydrogenation ($*O_2 + *H \rightarrow *OOH$) followed by dissociation ($*OOH \rightarrow *O + *OH$). Then the product (*OH) can undergo subsequent hydrogenation for the formation of H_2O (major product). In the peroxide mechanism, *OOH can undergo further hydrogenation for the formation of $*H_2O_2$. This will be a two-electron reduction reaction if the end product is H_2O_2. However, $*H_2O_2$ can further dissociate into *OH, which can go for further protonation for the formation H_2O. Therefore, it is clear from the above three mechanisms that there are three important steps for four-electron ORR: (i) *O, (ii) *OH and (iii) $*H_2O$ formation steps.

The reaction free energies and activation barriers are calculated for all the possible elementary steps of ORR on the nanocage surface and then compared with previous reports on bulk Pt(111). Such comparison gives us an idea about the distinct nature of the nanocage-catalyst towards ORR activity.

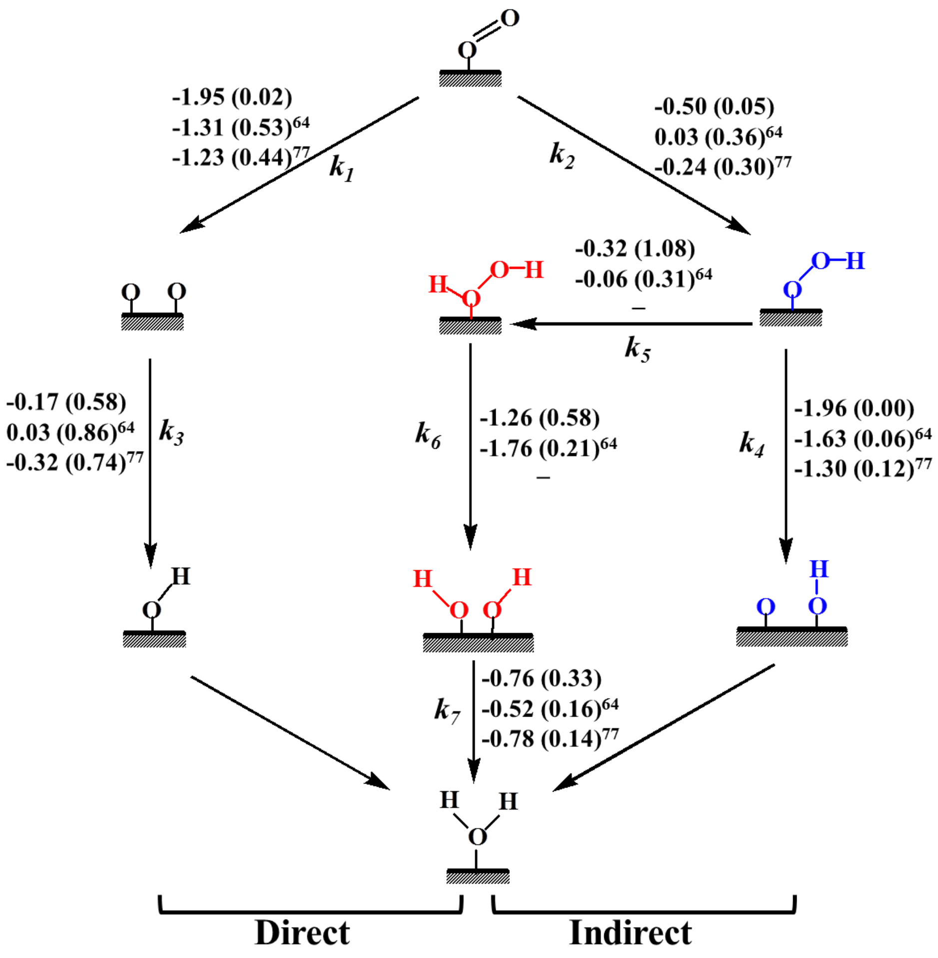

Scheme 3.1: Reaction free energies (eV) and activation barriers (eV, in parenthesis) are presented for all the possible elementary steps of ORR over (111) facet of the Pt_{66} nanocage. Our calculated respective values are compared with previous reports on oxygen reduction over Pt(111) *[64,77]* bulk surfaces.

O_2 activation:

Direct O-O bond dissociation is one of the very important steps for fuel cell application as it leads to the formation of H_2O, which reduces the formation of unwanted by-products. Thereby, direct dissociation favours $4e^-$ reduction over $2e^-$ reduction. Earlier studies show direct O-O bond dissociation (Step 3.1) is not kinetically favoured over O_2 hydrogenation (Step 3.2) on bulk Pt, Pd, Ag surfaces *[77-78]*. Thus, there are two competing pathways for $*O_2$ while adsorb on the catalyst surface. Either the adsorbed O_2 will dissociate into atomic oxygen *O or hydrogenated to *OOH.

$*O_2 \rightarrow *O + *O \quad \Delta G = -1.95, \Delta G^{\ddagger} = 0.02$ eV (Step 3.1)

$*O_2 + *H \rightarrow *OOH \quad \Delta G = -0.50, \Delta G^{\ddagger} = 0.05$ eV (Step 3.2)

As discussed, $*O_2$ can be adsorbed via two conformers: (i) suproxo and (ii) titled *[66]*. The calculated O_2 dissociation (Step 3.1) barriers on the nanocage surface are 0.35 and 0.02 eV for superoxo and tilted conformers, respectively. Thus, during the activation process, the adsorbed $*O_2$ may rearrange itself from the superoxo to tilted conformer. In fact, the barrier (0.06 eV) is very low for such conformational rearrangement. Similar kind of observation reported on bulk Pt(111) surface *[66]*. The very low barrier for conformational rearrangement certainly favours the O_2 dissociation from the tilted conformer. The previously calculated O-O bond dissociation barriers are 0.53 eV *[64]* and 0.44 eV *[77]* on bulk Pt(111) and 0.72 eV and 1.22 eV on bulk Pd(111) *[77]* and Ag(111) *[78]* surfaces, respectively.

Similarly, O_2 hydrogenation (Step 3.2) on the nanocage surface is also exergonic (-0.50 eV) with an activation barrier of 0.05 eV. The barriers for the same step (Step 3.2) reported to be 0.25 *[63]*, 0.36 *[64]* and 0.30 eV *[77]* on Pt(111) bulk surfaces. Therefore, the nanocage is highly reactive towards O_2 dissociation and favours direct O_2 bond dissociation over hydrogenation. This is opposite to other highly active catalysts such as Pt(111), Pd(111) and Ag(111), which favour hydrogenation over direct O_2 bond dissociation.

***OH formation**

The *OH formation is another important step for ORR and previous studies on bulk Pt(111) surfaces show *[63-65,77]* that this is one of the rate determining steps of ORR.

$*O + *H \rightarrow *OH \quad \Delta G = -0.17, \Delta G^{\ddagger} = 0.58$ eV (Step 3.3)

$*OOH \rightarrow *O + *OH \quad \Delta G = -1.96, \Delta G^{\ddagger} = 0.00$ eV (Step 3.4)

The direct O-O bond dissociation followed by hydrogenation leads to the formation of *OH (Step 3.3). The direct formation of *OH (Step 3.3) on the nanocage surface is exergonic (-0.17 eV) with an activation barrier of 0.58 eV.

Previous studies reported activation barriers of 0.74 *[77]* and 0.86 eV *[64]* on bulk Pt(111) and 0.72 eV on Pd(111) *[78]*.

Furthermore, *OH formation is possible via indirect pathways (Step 3.4) too; such as via peroxyl formation followed by O-O bond dissociation (Step 3.4). This step is a barrierless process on the nanocage surface with a reaction energy of -1.96 eV. Yao *et al. [77]* and Kai *et al. [64]* reported activation barriers of 0.12 eV and 0.06 eV for the *OOH dissociation (Step 3.4) step over bulk Pt(111) surfaces.

Though direct O-O bond dissociation (barrier 0.02 eV) is slightly favoured over O_2 hydrogenation (barrier 0.05 eV) but the OH formation (barrier 0.58 eV) is not favoured. On the other hand, indirect *OH formation (Step 3.4) is highly favourable on the nanocage surface. This suggests that *OOH will dissociate into *OH even if *OOH is formed on the nanocage surface. Thereby, the *OH formation is highly favoured via indirect pathway ($*O_2 + *H \rightarrow *OOH \rightarrow *OH$) than direct pathway ($*O_2 \rightarrow *O \rightarrow *OH$) on the nanocage surface.

Bader atomic charges [79] are calculated using Henkelman programme *[80-82]* to find out the net amount of charge transfer from the surface to intermediate species. Our Bader charge analysis shows that the charges on *O atoms are -0.70 |e| and -0.66 |e| while adsorbed on nanocage and bulk Pt(111) surfaces, respectively. The lower barrier for the *OH formation step (*O + *H → *OH) can be understood form the net negative charge gained at the O-atom from the surface Pt-atoms of the nanocage. We find that the adsorbed O-atom gains more negative charge when adsorbed on the nanocage than on the bulk Pt(111) surface, owing to the strong adsorption of O-atom on the nanocage surface. The accumulation of more negative charge at the O-atom facilitates the protonation and thus the OH formation. As a result, the nanocage offers a different ORR pathways compared to the earlier reports.

*H_2O_2 formation and decomposition

The two-electron reduction process leads to the formation of H_2O_2. H_2O_2 can be formed via two successive hydrogenations on O_2 (*O_2 + *H → *OOH, *OOH + *H → *H_2O_2).

*OOH + *H → *H_2O_2 $\Delta G = -0.32$, $\Delta G^{\ddagger} = 1.08$ eV   (Step 3.5)

*H_2O_2 → *OH + *OH $\Delta G = -1.26$, $\Delta G^{\ddagger} = 0.58$ eV   (Step 3.6)

Thus, *OOH can undergo further hydrogenation for the formation of *H_2O_2 (Step 3.5). Our calculated activation barrier and free energy for this process are 1.08 and -0.32 eV respectively. Zhiyao *et al. [63]* reported activation barriers of 0.19 eV for H_2O_2 (Step 3.5) formation on bulk Pt(111) surface. This suggests that H_2O_2 formation is favoured on bulk Pt(111) surface. In contrary, the nanocage does not favour H_2O_2 formation. It indicates that the nanocage is highly selective for four-electron reduction over two-electron reduction. The *H_2O_2 can again dissociate into *OH (Step 3.6). The activation barrier for this step is 0.58 eV on the nanocage surface. Therefore, we predict that such nanocage could be a very selective catalyst for water formation and therefore could be a promising catalyst for fuel cell applications.

*H_2O formation

*OH + *H → *H_2O $\Delta G = -0.76$, $\Delta G^{\ddagger} = 0.33$ eV   (Step 3.7)

The adsorbed *OH undergoes protonation for the formation of *H_2O. On the nanocage surface, the activation barrier for this process is 0.33 eV with a reaction free energy of -0.76 eV. Previous studies reported H_2O formation barriers of 0.16 eV *[64]*, 0.09 *[63]* and 0.14 eV *[77]* on bulk Pt(111) surfaces, which are lower than our calculated barrier of 0.33 eV on the nanocage surface. However, the *H_2O formation barrier (0.33 eV) is lower than *OH formation (0.58 eV) barrier on the nanocage surface. This suggests that *OH formation is the rate determining step on the nanocage surface. It indicates that the *H_2O formation will not influence the reaction kinetics on the nanocage surface. On the other hand, *OH formation barrier (0.58 eV) is significantly higher (0.74-0.86 eV) on bulk surface than the nanocage surface. Therefore, in spite of the high activation barrier for *H_2O formation (Step 3.7), the nanocage catalyst is more efficient for ORR than any other catalysts reported so far. Moreover, *H_2O adsorption energy is very low on the nanocage surface (-0.09 eV) compared to bulk Pt(111) surface (-0.26 eV), lessening the possibility of surface poisoning.

Therefore, our results show excellent catalytic activity of the nanocage towards ORR. This includes excellent catalytic activity towards rate-determining steps as well as for other important steps. We find that *O_2 activation processes (*O_2 → *O + *O and *O_2 + *H → *OOH) and *OH formation (*O + *H → *OH) are significantly improved over the nanocage surface.

In addition, we have also calculated the activation barriers for *O_2 dissociation (*O_2 → *O + *O) and *OH formation (*O + *H → *OH) steps at the low-coordinated edge site to compare the ORR activity at the edge site with respect to the Pt(111) surface of the nanocage. The activation barrier for the *O_2 dissociation is 0.21 eV at the edge site compared to 0.02 eV on the Pt(111) surface. This indicates *O_2 activation is easier on the surface than at the edge site. Similarly, the calculated activation barrier for the *OH formation is 0.77 eV at the edge site compared to 0.58 eV on the Pt(111) surface. Thereby, *OH formation is favourable on the Pt(111) surface than at the edge site. The high barriers for *O_2 dissociation and *OH formation could be due to the low adsorption energy of *O at the edge site.

It has been previously reported that compressive strain at the shell layer of core-shell structure could be the reason for enhancement of ORR performance *[83-84]*. Hence, the compressive/tensile strain energy (E_{strain}) is calculated using the following equation:

$$E_{strain} = E_{unrelaxed} - E_{relaxed} \qquad (3.4)$$

where $E_{relaxed}$ is the total energy of the optimized cluster/surface and $E_{unrelaxed}$ is the total energy (single point energy) of the cluster in the bulk geometry. The strain (ε) is calculated using the following equation:

$$\varepsilon = \Delta d/d \qquad (3.5)$$

where d is the diameter of the cluster/surface in its optimized structure and Δd is the change in the diameter from their bulk position.

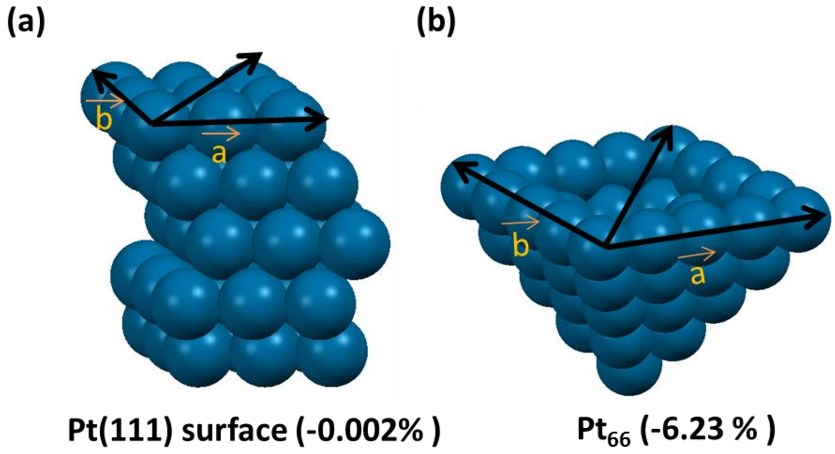

Figure 3.6: The compressive surface strain on: (a) bulk Pt (111) and (b) nanocage.

The calculated (Figure 3.6) strain energies (compressive strain) for nanocage and bulk Pt(111) are 16.12 (-6.23 %) and 0.32 eV (-0.002 %), respectively.

Furthermore, we have calculated the surface energy of the nanocage to check its reactivity with respect to the bulk Pt(111) surface. The surface energy (E_{sur}) is calculated using the following equation:

$$E_{sur} = (E_{nanocage/surface} - E_{bulk})/ A_{nanocage/surface} \qquad (3.6)$$

where, $E_{nanocage/surface}$ is the total energy of the nanocage/surface, E_{bulk} is the total energy of a bulk system containing the same number of atoms and $A_{nanocage/surface}$ is the total surface area of the nanocage/surface. The calculated surface energy for the Pt(111) surface and nanocage are 0.11 and 0.17 eV/atom, respectively. The higher surface energy of the nanocage is reflected by the strong adsorption of the reaction intermediates also. Thus, our adsorption, surface and strain energy analysis confirm that nanocage is highly reactive compared to the bulk Pt(111) surface.

The stronger adsorption of *O and *OH and weaker adsorption of *H_2O can be further explained from their projected density of states (PDOS) analysis. Figure 3.7 shows that the Pt 3d orbitals of the nanocage are more stabilized while interacting with the O 2p orbitals of O/OH (Figure 3.7a-b). In contrary, the extent of stabilization (Figure 3.7a-b) is low while interacting with bulk Pt(111). The extent of orbital overlap is also high for *O and *OH adsorption, whereas low for *H_2O adsorption (Figure 3.7c) on the nanocage surface.

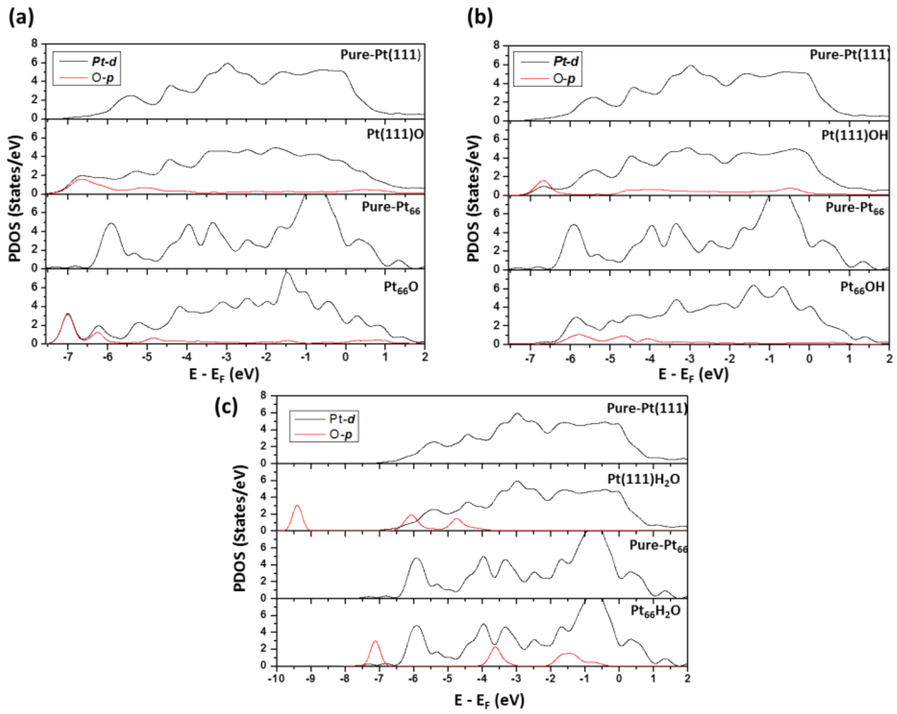

Figure 3.7: Projected density of states (PDOS) of (a) *O, (b) *OH and (c) *H_2O adsorbed Pt(111) and nanocage structures. PDOS of pure Pt(111) and nanocage (Pt_{66}) shown for comparison.

Therefore, our detailed investigation concludes that the void inside the nanocage induces a compressive strain in the system, which in turn improves the activity; thus the adsorption of the intermediates. The strong adsorption of the intermediates facilitates the charge transfer process (from the nanocage to adsorbed intermediates), which in turn improves the O-O dissociation and subsequent hydrogenation steps. As a result, it proceeds through a different mechanism (O-O dissociation followed by hydrogenation) than reported earlier (O-O hydrogenation followed by dissociation). This is in contrary to other bulk metal-based catalysts and therefore we believe that such nanocage-based catalysts can improve the ORR activity significantly.

3.3.3 Effect of Applied Potential

Catalysts are exposed to electrical potential during the course of the reaction. Therefore, the effects of electrode potential on free energy and reduction mechanisms have been investigated as proposed by Norskov and co-workers *[42]*. The free energy change (ΔG) is calculated as follows:

$$\Delta G = \Delta E + \Delta ZPE - T\Delta S - eU \qquad (3.7)$$

where ΔE is the total energy change obtained from the DFT calculations, ΔZPE is the change in zero-point energy, T is the room temperature (300 K), ΔS is the entropy change, e is the transferred charge for the elementary step and U is the electrode potential with respect to the standard hydrogen electrode.

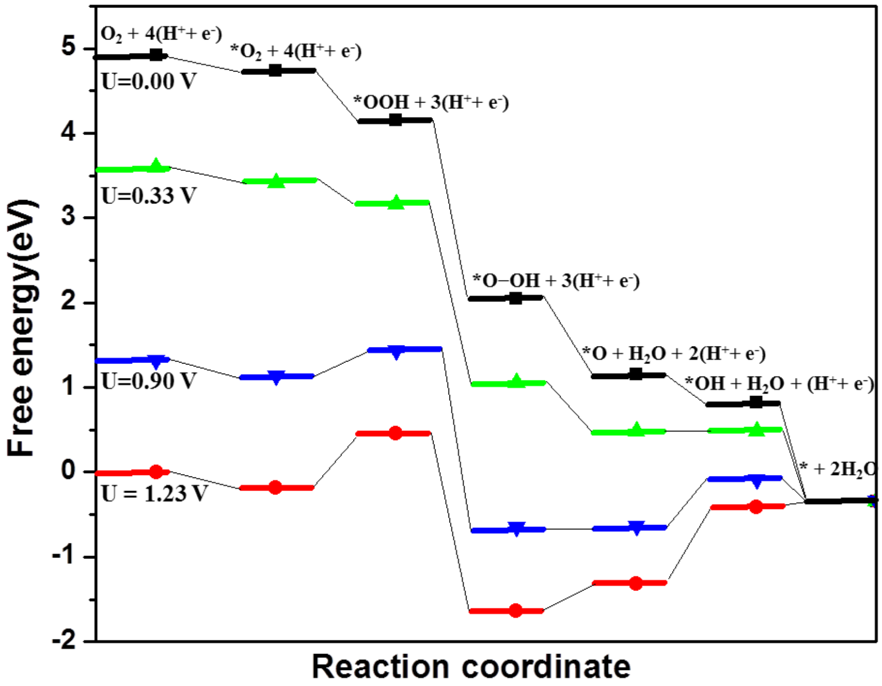

Figure 3.8: Free energy diagrams for ORR mechanism at different potentials.

Figure 3.8 shows that all the elementary steps are downhill process at U = 0 V. However, the proton transfer steps are thermodynamically not favourable as we increase the potential. Our calculated free energies show that the highest electrode potential under which all the elementary reactions are exergonic is 0.33 V. Thus, the working potential for the nanocage is 0.33 V and above this potential, some of the elementary reactions are endergonic. The *OH formation (*O + *H → *OH) step is not thermodynamically favourable at higher potentials. This suggests that the *OH formation is the rate determining step for ORR process, which is again very much in consistent with our kinetic study. However, *OOH and $*H_2O$ formations are less sensitive to applied potential. We have also studied the free energy diagram at 0.9 V (experimental operating potential) and we find that the $*H_2O$ formation is exergonic, whereas *OH formation is endergonic. It again indicates that *OH formation is the rate determining steps on the nanocage surface.

3.3.4 Kinetic Analysis

From the elementary pathways, we discover that many pathways are possible for O-O bond dissociation reaction. The reaction free energy versus reaction coordinate gives an overall idea to locate the minimum energy pathway from several possibilities. The roles of surface coverage, partial pressures (of reactant and product) and reaction temperature cannot be fully understood from the Gibbs free energy calculations. These experimental parameters can provide further insights into O_2 reduction reaction. Thus, we have done a detailed mickrokinetic analysis based on our preliminary DFT results to understand the roles of surface coverage, and reaction temperature toward the reaction kinetics. The forward $(\mathrm{k_i})$ rate constants for all the elementary steps are calculated using the following equation:

$$\mathrm{k_i} = \left(\frac{k_B T}{h}\right)\left(\frac{q_F}{q_I}\right) e^{-\Delta \mathrm{G}^{\ddagger}/k_B T} \tag{3.8}$$

where k_B is the Boltzmann constant, T is the temperature, h is the Planck's constant. Here q_I and q_F are the vibrational partition functions for the initial and final state structures and $\Delta G^{\ddagger}$ is the Gibbs free energy barrier for the initial and final state of the elementary reaction. The vibrational partition functions (q) are calculated using the following equation:

$$q = \sum_i \frac{1}{1-e^{-h v_i/k_B T}} \tag{3.9}$$

where, υ_i are the vibrational frequencies. All the exergonic reactions are assumed to be irreversible, hence only forward steps are considered for developing the microkinetic model.

Table 3.2: Rate constants (s^{-1}) of the elementary reactions at different temperatures and here k_i stands for the forward step of i-th step.

Elementary reactions	300 K	400 K	500 K
$*O_2 \rightarrow *O + *O$ (k_1)	2.71×10^{12}	4.45×10^{12}	6.31×10^{12}
$*O_2 + *H \rightarrow *OOH$ (k_2)	1.11×10^{12}	2.34×10^{12}	3.84×10^{12}
$*O + *H \rightarrow *OH$ (k_3)	9.35×10^{02}	3.25×10^{05}	1.14×10^{07}
$*OOH \rightarrow *O + *OH$ (k_4)	3.64×10^{13}	3.24×10^{13}	3.19×10^{13}
$*H + *OOH \rightarrow *H_2O_2$ (k_5)	5.38×10^{-06}	2.41×10^{-01}	1.57×10^{02}
$*H_2O_2 \rightarrow *OH + *OH$ (k_6)	1.08×10^{03}	4.04×10^{05}	1.18×10^{07}
$*H + *OH \rightarrow *H_2O$ (k_7)	2.29×10^{07}	7.15×10^{08}	5.93×10^{09}

As the oxygen reduction temperature in the low-temperature fuel cell ranges from 300 K to 500 K *[85-86]*, the rate constants (Table 3.2) are calculated in the same temperature range (300 K to 500 K). The rate constants improve significantly as we increase the temperature. At 300 K, the rate constants ratio between $*O_2$ dissociation and $*O_2$ hydrogenation (k_1/k_2) is 2.44. Hence, *O formation is highly favourable over *OOH formation ($*O_2 \rightarrow *O + *O$ and $*O_2 + *H \rightarrow *OOH$). Thus, we predict that the reaction might be proceeding through *OOH intermediate as the k_1/k_2 ratio is low. Therefore, it is important to examine the extent of possibility for proceeding the reaction further from the *OOH intermediate. The ratio of rate constants (k_4/k_5) for $*OOH \overset{k_4}{\rightarrow} *O + *OH$ and $*OOH + *H \overset{k_5}{\rightarrow} *H_2O_2$ is 6.76×10^{18}, implying that the *OOH dissociation is favourable over *OOH hydrogenation. Therefore, even if the reaction proceeds through *OOH intermediate, it will dissociate into *O and *OH ($*OOH \rightarrow *O + *OH$). Hence, our kinetic analysis suggests that the ORR favours four-electron reduction (H_2O formation) over two-electron reduction (H_2O_2 formation) on the nanocage surface.

The lesser possibility of two-electron reduction can be further confirmed from the microkinetic analysis. The ratio for the rate of formation of $*H_2O$ and $*H_2O_2$ formations is 5.23×10^{44} under 1:1 partial pressure ratio of oxygen and hydrogen. Hence, the two-electron reduction is not favourable for the formation of hydrogen peroxide. This is very much in consistent with our activation barrier study, where we find that hydrogenation is favoured at *OH over *OOH. Therefore, the temperature dependant rate constant and mikrokinetic analysis show that single layered platinum nanocage is highly selective and efficient toward four-electron oxygen reduction reaction.

3.4 Conclusion

First-principles calculations are performed to understand the ORR activity on (111) facet of the octahedral nanocage (Pt_{66}) enclosed by well-defined facets. Energetic, thermal and dynamic stability of the nanocage evaluated from the total energy, AIMD simulation and phonon calculations, respectively. Molecular dynamics simulation suggests that the nanocage can withstand temperatures as high as 600 K without any structural reconstruction. During the ORR, H_2O and H_2O_2 are the two end products, which are formed via four-electron ($4e^-$) and two-electron ($2e^-$) reduction reactions, respectively. The reaction free energies and activation barriers are calculated for all the possible elementary steps of ORR on the nanocage surface and then compared with previous reports on bulk Pt(111). Our detailed investigation suggests that the nanocage induces a compressive strain in the system, which in turn improves the activity of the nanocage and thus improves the adsorption of the intermediates. Our results show that the *O and *OH adsorb strongly on the nanocage surface compared to bulk Pt(111) surface, which facilitates the charge transfer process (from the nanocage to adsorbed intermediates), which in turn improves the O-O dissociation and subsequent hydrogenation steps. As a result, the nanocage offers a different ORR pathways (O-O dissociation followed by hydrogenation) than the earlier reports (O-O hydrogenation followed by dissociation). This is completely opposite to the previous reports on Pt_3M (M = Ti, V, Ni, Co, Fe, Y, Sc, Rh) alloy based catalysts where the low binding energies of the reaction intermediates (*O and *OH) were credited for the superior catalytic activity. Our potential study indicates that the ORR is thermodynamically favourable at 0.33 V and *OH formation is the rate determining step. The rate determining step (*OH formation) is very much agreement with the kinetic study. Our microkinetic analysis shows that the H_2O formation is favoured over H_2O_2, which again suggests that the nanocage is highly selective for four-electron ORR over two-electron ORR. Hence, we report, platinum nanocage could be very promising catalysts for the efficient and selective reduction of O_2.

3.5. References

1. Jiao Y., Zheng Y., Jaroniecb M., Qiao S. Z. (2015), Design of electrocatalysts for oxygen- and hydrogen-involving energy conversion reactions, Chem. Soc. Rev., 44, 2060-2080. (DOI: 10.1039/C4CS00470A)

2. Vinayan B. P., Nagar R., Rajalakshmi N., Ramaprabhu S. (2012), Novel platinum–cobalt alloy nanoparticles dispersed on nitrogen-doped graphene as a cathode electrocatalyst for PEMFC applications, Adv. Funct. Mater., 22, 3519-3526. (DOI: 10.1002/adfm.201102544)

3. Lubitz W., Tumas W., (2007), Hydrogen: an overview, Chem. Rev., 107, 3900-3903. (DOI: 10.1021/cr050200z)

4. de Bruijn F. A., Dam V. A. T., Janssen G. J. M. (2008), Review: durability and degradation issues of PEM fuel cell components, Fuel Cells, 8, 3-22. (DOI: 10.1002/fuce.200700053)

5. Watanabe M., Tryk D. A., Wakisaka M., Yano H., Uchida H. (2012), Overview of recent developments in oxygen reduction electrocatalysis, Electrochim. Acta, 84, 187-201. (DOI: 10.1016/j.electacta.2012.04.035)

6. Calle-Vallejo F., Koper M. T. M., Bandarenka A. S. (2013), Tailoring the catalytic activity of electrodes with monolayer amounts of foreign metals, Chem. Soc. Rev., 42, 5210-5230. (DOI: 10.1039/C3CS60026B)

7. Wu, J., Yang H. (2013), Platinum-Based Oxygen Reduction Electrocatalysts, Acc. Chem. Res., 46, 1848-1857. (DOI: 10.1021/ar300359w)

8. Antolini E. (2014), Iridium As Catalyst and Cocatalyst for Oxygen Evolution/Reduction in Acidic Polymer Electrolyte Membrane Electrolyzers and Fuel Cells, ACS Catal., 4, 1426-1440. (DOI: 10.1021/cs4011875)

9. Savadogo O., Lee K., Oishi K., Mitsushima S., Kamiya N., Ota K. I. (2004), New palladium alloys catalyst for the oxygen reduction reaction in an acid medium, Electrochem. Commun., 6, 105-109. (DOI: 10.1016/j.elecom.2003.10.020)

10. Wang C. H., Hsu H. C., Wang K. C. (2014), Iridium-decorated Palladium–Platinum core–shell catalysts for oxygen reduction reaction in proton exchange membrane fuel cell, J. Colloid Interface Sci., 427, 91. (DOI: 10.1016/j.jcis.2013.11.068)

11. Xu Y., Ruban A. V., Mavrikakis M. (2004), Adsorption and dissociation of O2 on Pt− Co and Pt− Fe alloys, J. Am. Chem. Soc., 126, 4717-4725. (DOI: 10.1021/ja031701+)

12. Stamenkovic V. R., Fowler B., Mun B. S, Wang G., Ross P. N., Lucas C. A., and Marković N. M. (2007), Science, 315, 493-497. (DOI: 10.1126/science.1135941)

13. Stamenkovic V., Mun B. S., Mayrhofer K. J. J., Ross P. N., Markovic N. M., Rossmeisl J., Greeley J., Nørskov J. K. (2006), Changing the activity of electrocatalysts for oxygen reduction by tuning the surface electronic structure, Angew. Chem., 118, 2963-2967. (DOI: 10.1002/ange.200504386)

14. W Tang. J., Zhang L., Henkelman G. (2011), Catalytic activity of Pd/Cu random alloy nanoparticles for oxygen reduction, J. Phys. Chem. Lett., 2, 1328−1331. (DOI: 10.1021/jz2004717)

15. Holewinski A., Idrobo J., Linic S. (2014), High-performance Ag–Co alloy catalysts for electrochemical oxygen reduction, Nat. Chem., 6, 828–834. (DOI:10.1038/nchem.2032)

16. Wang J. X., Inada H., Wu L., Zhu Y., Choi Y., Liu P., Zhou W. P., Adzic R. R. (2009), Oxygen Reduction on Well-Defined Core−Shell Nanocatalysts:

Particle Size, Facet, and Pt Shell Thickness Effects, J. Am. Chem. Soc., 131, 17298-17302. (DOI: 10.1021/ja9067645)

17. Oezaslan M., Hasché F., Strasser P. (2013), Pt-Based Core–Shell Catalyst Architectures for Oxygen Fuel Cell Electrodes, J. Phys. Chem. Lett., 4, 3273-3291. (DOI: 10.1021/jz4014135)

18. Mazumder V., Chi M., More K. L., Sun S. (2010), Core/shell Pd/FePt nanoparticles as an active and durable catalyst for the oxygen reduction reaction, J. Am. Chem. Soc., 132, 7848-7849. (DOI: 10.1021/ja1024436)

19. J. Greeley, I. E. L. Stephens, A. S. Bondarenko, T. PJohansson, H. A. Hansen, T. F. Jaramillo, J. Rossmeisl, I. Chorkendorff and J. K. Nørskov (2009), Alloys of platinum and early transition metals as oxygen reduction electrocatalysts, Nat. Chem., 1, 552-556. (DOI:10.1038/nchem.367)

20. Stamenkovic V., Mun B. S., Mayrhofer K. J. J., Ross P. N., Markovic N. M., Rossmeisl J., Greeley J., Nørskov J. K. (2006), Cover Picture: Changing the Activity of Electrocatalysts for Oxygen Reduction by Tuning the Surface Electronic Structure, Angew. Chem. Int. Ed., 45, 2897. (DOI: 10.1002/anie.200690063)

21. Jackson A., Viswanathan V., Forman A. J., Larsen A. H., Nørskov J. K., Jaramillo T. F. (2014), Climbing the activity volcano: core–shell Ru@ Pt electrocatalysts for oxygen reduction, ChemElectroChem, 1, 67-71. (DOI: 10.1002/celc.201300117)

22. Kroto H. W., Heath J. R., Obrien S. C., Curl R. F., Smalley R. E. (1985), C60: Buckminsterfullerene, Nature, 318, 162-163. (DOI:10.1038/318162a0)

23. Zhai H., Zhao Y., Li W., Chen Q., Bai H., Hu H., Piazza Z. A., Tian W., Lu H., Wu Y., Mu Y., Wei G., Liu Z., Li J., Li S., Wang L. (2014), Observation of an all-boron fullerene, *Nat. Chem.*, **6**, 727-731. (DOI:10.1038/nchem.1999)

24. Wang X., Xie Y., Guo Q. (2003), Synthesis of high quality inorganic fullerene-like BN hollow spheres via a simple chemical route, Chem. Commun., 2688-2689. (DOI: 10.1039/B308264D)

25. Loiseau A., Willaime F., Demoncy N., Schramchenko N., Hug G., Colliex C., Pascard H. (1998), Boron nitride nanotubes, Carbon, 36, 743-752. (DOI:10.1016/S0008-6223(98)00040-2)

26. Bai J., Virovets A. V., Scheer M. (2003), Synthesis of Inorganic Fullerene-Like Molecules, Science, 300, 781-783. (DOI: 10.1126/science.1081119)

27. Sneed B. T., Brodsky C. N., Kuo C., Lamontagne L. K., Jiang Y., Wang Y., Tao F., Huang W., Tsung C. (2013), Nanoscale-phase-separated Pd–Rh boxes synthesized via metal migration: An archetype for studying lattice strain and composition effects in electrocatalysis, J. Am. Chem. Soc., 135, 14691-14700. (DOI: 10.1021/ja405387q)

28. Xie S., Choi S., Lu N., Roling L. T., Herron J. A., Zhang L., Park J., Wang J., Kim M. J., Xie Z., Mavrikakis M., Xia Y. (2014), Atomic Layer-by-Layer Deposition of Pt on Pd Nanocubes for Catalysts with Enhanced Activity and Durability toward Oxygen Reduction, Nano Lett., 14, 3570-3576. (DOI: 10.1021/nl501205j)

29. Park J., Zhang L., Choi S., Roling L. T., Lu N., Herron J. A., Xie S., Wang J., Kim M. J., Mavrikakis M., Xia Y. (2015), Atomic Layer-by-Layer Deposition of Platinum on Palladium Octahedra for Enhanced Catalysts toward the Oxygen Reduction Reaction, ACS Nano, 9, 2635-2647. (DOI: 10.1021/nn506387w)

30. Zhang L., Roling L. T., Wang X., Vara M., Chi M., Liu J., Choi S., Park J., Herron J. A., Xie Z., Mavrikakis M., Xia Y. (2015), Platinum-based nanocages with subnanometer-thick walls and well-defined, controllable facets, Science, 349, 412-416. (DOI: 10.1126/science.aab0801)

31. Wang X., Figueroa-Cosme L., Yang X., Luo M., Liu J., Xie Z., Xia Y. (2016), Pt-Based Icosahedral Nanocages: Using a Combination of {111} Facets, Twin Defects, and Ultrathin Walls to Greatly Enhance Their Activity toward Oxygen Reduction, Nano Lett., 16, 1467-1471. (DOI: 10.1021/acs.nanolett.5b05140)

32. Mahmoud M. A., O’Neil D., El-Sayed M. A. (2014), Hollow and Solid Metallic Nanoparticles in Sensing and in Nanocatalysis, Chem. Mater., 26, 44-58. (DOI: 10.1021/cm4020892)

33. Fang Z., Wang Y., Liu C., Chen S., Sang W., Wang C., Zeng J. (2015), Rational Design of Metal Nanoframes for Catalysis and Plasmonics, Small, 11, 2593-2605. (DOI: 10.1002/smll.201402799)

34. Popa A., Samia A. C. S. (2014), Effect of metal precursor on the growth and electrochemical sensing properties of Pt–Ag nanoboxes, Chem. Commun., 50**,** 7295-7298. (DOI: 10.1039/C4CC01927J)

35. Chen C., Kang Y., Huo Z., Zhu Z., Huang W., Xin H. L., Snyder J. D., Li D., Herron J. A., Mavrikakis M., Chi M., More K. L., Li Y., Markovic N. M., Somorjai A., Yang G. P., Stamenkovic V. R. (2014), Highly crystalline multimetallic nanoframes with three-dimensional electrocatalytic surfaces, Science, 343, 1339-1343. (DOI: 10.1126/science.1249061)

36. Hong X., Wang D., Cai S., Rong H., Y. Li (2012), Single-Crystalline Octahedral Au–Ag Nanoframes, J. Am. Chem. Soc., 134, 18165-18168. (DOI: 10.1021/ja3076132)

37. Sasaki K., Naohara H., Choi Y., Cai Y., Chen W., Liu P., Adzic R. R. (2012), Highly stable Pt monolayer on PdAu nanoparticle electrocatalysts for the oxygen reduction reaction, Nat. Commun., 3, 1115. (DOI:10.1038/ncomms2124)

38. Sasaki K., Naohara H., Cai Y., Choi Y. M., Liu P., Vukmirovic M. B., Wang J. X., Adzic R. R. (2010), Core-Protected Platinum Monolayer Shell High-Stability Electrocatalysts for Fuel-Cell Cathodes, Angew. Chem., Int. Ed., 49, 8602-8607. (DOI: 10.1002/anie.201004287)

39. Zhang J., Vukmirovic M. B., Xu Y., Mavrikakis M., Adzic R. R. (2005), Controlling the Catalytic Activity of Platinum-Monolayer Electrocatalysts for Oxygen Reduction with Different Substrates, Angew. Chem. Int. Ed., 44, 2132-2135. (DOI: 10.1002/anie.200462335)

40. Yeager E. (1986), Dioxygen electrocatalysis: mechanisms in relation to catalyst structure, J. Mol. Catal., 38, 5. (DOI: 10.1016/0304-5102(86)87045-6)

41. Sanchez-Sanchez C. M., Bard A., (2009), Hydrogen peroxide production in the oxygen reduction reaction at different electrocatalysts as quantified by scanning electrochemical microscopy, J. Anal. Chem., 81, 8094-8100. (DOI: 10.1021/ac901291v)

42. Nørskov J. K., Rossmeisl J., Logadottir A., Lindqvist L., Kitchin J. R., Bligaard T., Jonsson H. (2004), Origin of the Overpotential for Oxygen Reduction at a Fuel-Cell Cathode, J. Phys. Chem. B, 108, 17886-17892. (DOI: 10.1021/jp047349j)

43. Tripkovic V., Skulason E., Siahrostami S., Nørskov J. K., Rossmeisl J. (2010), The oxygen reduction reaction mechanism on Pt(1 1 1) from density functional theory calculations, Electrochimica Acta, 55, 7975-7981. (DOI: 10.1016/j.electacta.2010.02.056)

44. Duan Z., Wang G. (2013), Comparison of Reaction Energetics for Oxygen Reduction Reactions on Pt(100), Pt(111), Pt/Ni(100), and Pt/Ni(111) Surfaces: A First-Principles Study, J. Phys. Chem. C, 117, 6284-6292. (DOI: 10.1021/jp400388v)

45. Tsai H. C., Hsieh Y. C., Yu T., Lee Y. J., Wu Y. H., Merinov B. V., Wu P. W., Chen S. Y., Adzic R. R., Goddard III W. A. (2015), DFT Study of Oxygen Reduction Reaction on Os/Pt Core–Shell Catalysts Validated by Electrochemical Experiment, ACS Catal., 5, 1568-1580. (DOI: 10.1021/cs501020a)

46. Maiyalagan T., Khan F. N. (2009), Electrochemical oxidation of methanol on Pt/V 2 O 5–C composite catalysts, Catal. Commun., 10, 433-436. (DOI: 10.1016/j.catcom.2008.10.011)

47. B. Zhang, D. Wang, Y. Hou, S. Yang, X. H. Yang, J. H. Zhong, J. Liu, H. F. Wang, P. Hu, H. J. Zhao and H. G. Yang, (2013), Facet-Dependent Catalytic Activity of Platinum Nanocrystals for Triiodide Reduction in Dye-Sensitized Solar Cells, *Sci. Rep.*, **3**, 1836. (DOI: 10.1038/srep01836)

48. Hu Y., Zhang H., Wu P., Zhang H., Zhou B., Cai C. (2011), Bimetallic Pt–Au nanocatalysts electrochemically deposited on graphene and their electrocatalytic characteristics towards oxygen reduction and methanol oxidation, Phys. Chem. Chem. Phys., 13, 4083-4094. (DOI: 10.1039/C0CP01998D)

49. Zhang J., Yang H., Fang J., Zou S. (2010), Synthesis and Oxygen Reduction Activity of Shape-Controlled Pt_3Ni Nanopolyhedra, Nano Lett., 10, 638-644. (DOI: 10.1021/nl903717z)

50. Sanchez C. M., Solla-Gullon J., Vidal-Iglesias F. J., Aldaz A., Montiel V., Herrero E. (2010), Imaging Structure Sensitive Catalysis on Different Shape-Controlled Platinum Nanoparticles, J. Am. Chem. Soc., 132, 5622-5624. (DOI: 10.1021/ja100922h)

51. Markovic N. M., Gasteiger H. A., Ross P. N. (1996) Oxygen Reduction on Platinum Low-Index Single-Crystal Surfaces in Alkaline Solution: Rotating Ring Disk $Pt_{(hkl)}$ Studies, J. Phys. Chem., 100, 6715-6721. (DOI: 10.1021/jp9533382)

52. Han B., Viswanathan V., Pitsch H. (2012), First-Principles Based Analysis of the Electrocatalytic Activity of the Unreconstructed Pt(100) Surface for Oxygen Reduction Reaction, J. Phys. Chem. C, 116, 6174-6183. (DOI: 10.1021/jp2075379)

53. Blochl P. E. (1994), Projector augmented-wave method, Phy. Rev. B, 50, 17953. (DOI : 10.1103/PhysRevB.50.17953)

54. Kresse G., Hafner J. (1993), Ab initio molecular dynamics for liquid metals, Phy. Rev. B, 47, 558. (DOI: 10.1103/PhysRevB.47.558)

55. G Kresse., Hafner J. (1994), Ab initio molecular-dynamics simulation of the liquid-metal–amorphous-semiconductor transition in germanium, Phy. Rev. B, 49, 14251-14269. (DOI: 10.1103/PhysRevB.49.14251)

56. Kresse G., Joubert D. (1999), From ultrasoft pseudopotentials to the projector augmented-wave method, Phy. Rev. B, 59, 1758. (DOI: 10.1103/PhysRevB.59.17580)

57. Perdew J. P., Chevary J. A., Vosko S. H., Jackson K. A., Pederson M. R., Singh D. J., Fiolhais C. (1992), Atoms, molecules, solids, and surfaces: Applications of the generalized gradient approximation for exchange and correlation, Phy. Rev. B, 46, 6671. (DOI: 10.1103/PhysRevB.46.6671)

58. Grimme S., Antony J., Ehrlich S., Krieg S. (2010), A consistent and accurate ab initio parametrization of density functional dispersion correction (DFT-D) for the 94 elements H-Pu, J. Chem. Phys., 132, 154104. (DOI: 10.1063/1.3382344)

59. Baroni S., Giannozzi P., Testa A. (1987), Green's-function approach to linear response in solids, Phys. Rev. Lett., 58, 1861. (DOI: 10.1103/PhysRevLett.58.1861)

60. Henkelman G., Jonsson H. **(**2000) A climbing image nudged elastic band method for finding saddle points and minimum energy paths, J. Chem. Phys., 113, 9978-9985. (DOI: 10.1063/1.1329672)

61. C. Kittel, *Introduction to Solid State Physics,* 8th edition; Hoboken, NJ: John Wiley & Sons: Inc, **2005**.

62. Nose S. A. (1984), A unified formulation of the constant temperature molecular dynamics methods, J. Chem. Phys., 81, 511-519. (DOI: 10.1063/1.447334)

63. Duan Z., Wang G. (2011), A first principles study of oxygen reduction reaction on a Pt(111) surface modified by a subsurface transition metal M (M = Ni, Co, or Fe), Phys. Chem. Chem. Phys., 13, 20178-20187. (DOI: 10.1039/C1CP21687B)

64. Li K., Li Y., Wang Y., He F., Jiao M., Tang H., Wu Z. (2015), The oxygen reduction reaction on Pt(111) and Pt(100) surfaces substituted by subsurface Cu: a theoretical perspective, J. Mater. Chem. A, 3, 11444-11452. (DOI: 10.1039/C5TA01017A)

65. Sha Y., Yu T. H., Liu Y., Merinov B. V., Goddard III W. A. (2010), Theoretical Study of Solvent Effects on the Platinum-Catalyzed Oxygen

Reduction Reaction, J. Phys. Chem. Lett., 1, 856-861. (DOI: 10.1021/jz9003153)

66. Keith J. A., Jerkiewicz G., Jacob T. (2010), Theoretical Investigations of the Oxygen Reduction Reaction on Pt(111), ChemPhysChem, 11, 2779-2794. (DOI: 10.1002/cphc.201000286)

67. Puglia C., Nilsson A., Hernniis B., Karis O., Bennich P., Martensson N. (1995), Physisorbed, chemisorbed and dissociated O2 on Pt(111) studied by different core level spectroscopy methods, Sur. Sci., 342, 119-133. (DOI: 10.1016/0039-6028(95)00798-9)

68. P Nolan. D., Lutz B. R., Tanaka P. L., Davis J. E., Mullins C. B. (1998), Translational Energy Selection of Molecular Precursors to Oxygen Adsorption on Pt(111), Phys. Rev. Lett., 81, 3179. (DOI: 10.1103/PhysRevLett.81.3179)

69. Parker D. H., Bartram M. E., Koel B. E. (1989), Study of high coverages of atomic oxygen on the Pt(111) surface, Sur. Sci., 217, 489-510. (DOI: 10.1016/0039-6028(89)90443-3)

70. Steininger H., Lehwald S., Ibach H. (1982), Adsorption of oxygen on Pt(111), Sur. Sci., 123, 1-17. (DOI: 10.1016/0039-6028(82)90124-8)

71. Xiao B. B., Zhu Y. F., Lang X. Y., Wen Z., Jiang Q. (2014), Al13@ Pt42 core-shell cluster for oxygen reduction reaction, Sci. Rep., 4, 5205. (DOI: 10.1038/srep05205)

72. Yue J., Du Z., Shao M. (2015), Mechanisms of Enhanced Electrocatalytic Activity for Oxygen Reduction Reaction on High-Index Platinum n(111)–(111) Surfaces, J. Phys. Chem. Lett., 6, 3346-3351. (DOI: 10.1021/acs.jpclett.5b01345)

73. Yeo Y. Y., Vattuone L., King D. A. (1997), Calorimetric heats for CO and oxygen adsorption and for the catalytic CO oxidation reaction on Pt{111}, J. Chem. Phys., 106, 392. (DOI: 10.1063/1.473203)

74. Karp E. M., Campbell C. T., Studt F., Abild-Pedersen F., Norskov J. K. (2012), Energetics of Oxygen Adatoms, Hydroxyl Species and Water

Dissociation on Pt(111), J. Phys. Chem. C, 116, 25772-25776. (DOI: 10.1021/jp3066794)

75. Thiel P. A., Madey T. E. (1987), The interaction of water with solid surfaces: Fundamental aspects, Sur. Sci., 7, 211-385. (DOI: 10.1016/0167-5729(87)90001-X)

76. Fisher G. B., Gland J. L. (1980), The interaction of water with the Pt(111) surface, Sur. Sci., 94, 446-455. (DOI: 10.1016/0039-6028(80)90018-7)

77. Sha Y., Yu T. H., Merinov B. V., Shirvanian P., Goddard W. A. (2011), Oxygen Hydration Mechanism for the Oxygen Reduction Reaction at Pt and Pd Fuel Cell Catalysts, *J.* Phys. Chem. Lett., 2, 572-576. (DOI: 10.1021/jz101753e)

78. Farberow C. A., Godinez-Garcia A., Peng G. W., Perez-Robles J. F., Solorza-Feria O., Mavrikakis M. (2013), Mechanistic Studies of Oxygen Reduction by Hydrogen on PdAg(110), ACS Catal., 3, 1622-1632. (DOI: 10.1021/cs4002699)

79. R. F. W. Bader, Atoms in Molecules: A Quantum Theory; Oxford University Press: USA, **1994.**

80. Henkelman G., Arnaldsson A., Jonsson H.(2006), A fast and robust algorithm for Bader decomposition of charge density. Comput. Mater. Sci., 36, 354-360. (DOI: 10.1016/j.commatsci.2005.04.010)

81. Sanville E., Kenny S. D., Smith R., Henkelman G. (2007), Improved grid-based algorithm for Bader charge allocation. J. Comput. Chem., 28, 899. (DOI: 10.1002/jcc.20575)

82. Tang W., Sanville E., Henkelman G. (2009), A grid-based Bader analysis algorithm without lattice bias. J. Phys.: Condens. Matter., 21, 084204. (DOI: 10.1088/0953-8984/21/8/084204)

83. P. Strasser, S. Koh, T. Anniyev, J. Greeley, K. More, C. Yu, Z. Liu, S. Kaya, D. Nordlund and H. Ogasawara, M. F. Toney and A. Nilsson, (2010),

Lattice-strain control of the activity in dealloyed core–shell fuel cell catalysts, *Nat. Chem.* 2010, **2**, 454. (DOI: 10.1038/nchem.623)

84. Kattel S., Wang G. (2014), Beneficial compressive strain for oxygen reduction reaction on Pt (111) surface, J. Chem. Phys., 141, 124713. (DOI: 10.1063/1.4896604)

85. Mahata A., Choudhuri I., Pathak B. (2015), A cuboctahedral platinum (Pt79) nanocluster enclosed by well defined facets favours di-sigma adsorption and improves the reaction kinetics for methanol fuel cells, Nanoscale, 7, 13438-13451. (DOI: 10.1039/C5NR01575H)

86. Mehta V., Cooper J. S. (2003), Review and analysis of PEM fuel cell design and manufacturing, J. Power Sources, 114, 32-53. (DOI: 10.1016/S0378-7753(02)00542-6)

Chapter 4

Free-standing Platinum Monolayer as Efficient and Selective Catalyst for Oxygen Reduction Reaction

4.1. Introduction

The oxygen reduction reaction (ORR) has long been a subject of extensive research in developing proton exchange membrane (PEM) fuel cells because the slow reaction kinetics of ORR and the use of cost effective Pt-metal as electrodes (Pt/C) prevent the commercialization of PEM fuel cells *[1-2]*. Therefore, the development of a catalyst with less Pt-content without compromising the performance of ORR is very essential. In this regard, different kinds of catalysts like core-shell nanoparticle *[3-5]*, hollow nano-materials *[6-8]* and metal-free catalyst *[9-10]* have been proposed and found to be efficient for ORR activity.

However, since the discovery of graphene, two-dimensional (2D) materials with atomic layer thickness have attracted widespread attention due to a number of unusual properties and potential applications in next-generation devices like electronics *[11]*, optics *[12]*, magnetics *[13]*, and catalysis *[14]*. Similarly, platinum nanosheets, platinum monolayer-based catalysts on a support material, and platinum monolayer shell with a core-shell nanoclusters have attracted considerable attention *[15-22]*. In fact, metal-based ultrathin catalysts have been recently synthesized, which not only lower the metal-content, but also improve the electro catalytic activity significantly. Duan et al. *[15]* synthesized ultrathin Rh nanosheets, which show excellent catalytic performance for catalytic hydrogenation and hydroformylation reactions. Moreover, Azdic and co-workers synthesized core-shell bimetallic IrNi *[16]* and AuNi *[17]* catalysts with a Pt monolayer shell and reported excellent ORR kinetics. Wang and co-workers *[18]* synthesized free-standing ultrathin Pt−Cu alloy nanosheets of 4−6 atom thickness, which exhibits excellent electrocatalytic activities for the oxidation of ethanol in comparison to commercial Pt black and Pt/C catalysts. Considerable progresses have been made on the noble metal based ultrathin materials, which have been reviewed elsewhere *[19-20]*. Furthermore, Zhang et al. *[21]* theoretically studied the ORR activity of metal monolayers (Pt, Pd, and Au) supported on WC(0001) surfaces and reported that the direct dissociation of O_2 on all three monolayer surfaces are almost impossible due to the large barriers. In another experimental and theoretical study, Yu et al. *[22]* reported core-shell nanoparticle with a monolayer Pt-shell over the Pd core for enhanced ORR activity. Recently, freestanding monolayer of metals (Ag and Au) have been predicted by Yang et al. *[23-24]*. They proposed a hexagonal closed pack structure for the monolayer. However, to the best of our knowledge, no free standing platinum-monolayer has been reported so far. In fact, the metal supported platinum monolayer has been considered as hexagonal closed packed planar structure. However, the structure of the monolayer changes significantly depending upon the hybridization (atomic configuration) of atoms. Graphene, as for example, holds honeycomb planar structure, whereas stanene possess honeycomb buckled structure *[25]*. Therefore, platinum monolayer might possess a unique structural pattern which in turns can facilitate the ORR activity. Therefore, the developments in the field of ultrathin materials inspired us to model an atomically thin platinum monolayer for ORR activity. We report here for the first time that a free-standing platinum monolayer can improve the ORR activity significantly.

Despite extensive experimental reports on ORR activity over the ultrathin materials, the underlying reason behind their excellent catalytic behaviour is yet to be understood. Thereby, the superior catalytic activity of the monolayer is investigated through a systemic study. ORR involves many-electron reduction and it can proceed either through a more efficient four-step, four-electron reduction with the formation of H_2O or via a two-step, two-electron reduction for the formation of H_2O_2. In fuel cells, water formation is very much desirable to maximize the efficiency. Thereby, the product selectivity [H_2O vs. H_2O_2] is very important for the performance of a fuel cell.

Therefore in this chapter, we have modelled a platinum monolayer for improved ORR activity. Furthermore, we have calculated its energetic, dynamical, thermal, and mechanical stabilities for its synthesis and practical usages. The potential applicability of the monolayer as a fuel cell cathode has been verified by studying the ORR activity. The reaction free energies, activation barriers of the possible elementary steps and their dependency with applied voltage have been studied to verify the ORR performance and compared with the previous reports on the bulk

Pt(111) surface and nanostructure based catalysts. Moreover, rational explanation has been offered for the excellent catalytic activity of the catalyst.

4.2. Model and Computational Details

The first-principles calculations are performed using a projector augmented wave (PAW) *[26]* method as implemented in the Vienna Ab initio Simulation Package (VASP) *[27]*. The exchange-correlation potential is described by using the generalized gradient approximation of Perdew-Burke-Ernzerhof (GGA-PBE) *[28]*. Plane wave with a kinetic energy cut off of 470 eV is used to expand the electronic wave functions. The Monkhorst–Pack generated a set of 45 × 25 × 1 k-points which is used to optimize the unit cell and evaluate the density of states of the Pt-ML. A 3 × 2 × 1 set of k-points has been used in all the calculations where supercell is used. The bulk Pt(111) surface is modeled with a (3 × 3) supercell to minimize the lateral interactions between the repeating images. The metal slab is composed of five atomic layers, where the bottom three layers are fixed and the top two layers are relaxed. A 12 Å of vacuum is used along the z-direction to avoid any periodic interactions. The Brillouin zone is sampled using a 3 × 3 × 1 k-point grid for the surface calculations. All the systems are fully optimized, where the convergence criteria for total energy and forces are set at 10^{-4} eV and <0.02 eV/Å, respectively. Spin-polarized calculations are performed for all the molecular species and oxygen adsorbed intermediates. We have included Grimme's D3-type *[29]* of semiempirical method to include the dispersion energy corrections for van der Waals interactions. The climbing nudged elastic band (CI-NEB) method *[30]* is used to locate the transition state. Six intermediate images are used in each CI-NEB pathway. Vibrational frequencies for the initial, transition and final states of the reaction are calculated and the transition states are confirmed by the presence of one imaginary frequency. Zero-point energy (ZPE) is calculated using the following equation:

$$\text{ZPE} = \sum_i 1/2 h v_i \tag{4.1}$$

where h is the Planck constant and υ_i is the frequency of the i^{th} vibrational mode. The reaction free energies (ΔG) are calculated using the following equation:

$$\Delta G = \Delta E + \Delta ZPE - T\Delta S \tag{4.2}$$

where ΔE, ΔZPE and ΔS are the difference in total energies, zero-point energies and entropy between the product/TS and reactant. The forward (k_i) rate constants for all the elementary steps are calculated using the following equation:

$$k_i = \left(\frac{k_B T}{h}\right)\left(\frac{q_{TS}}{q_R}\right) e^{-\Delta G^{\ddagger}/k_B T} \tag{4.3}$$

where k_B is the Boltzmann constant, T is the temperature, h is the Plank constant. Here, q_{TS} and q_R are the vibrational partition functions for the transition state and reactant structures, respectively and $\Delta G^{\ddagger}$ is the Gibbs free energy barrier for the initial and final state of the elementary reaction. The finite system (Pt_7 cluster) calculations are carried out using Becke's three-parameter exchange and the Lee−Yang−Parr correlation functional (B3LYP) as implemented in the Gaussian 09 package *[31]*. LANL2DZ basis sets has been used with effective core potentials (ECPs) *[32]*.

We have modeled the Pt monolayers by cutting along the (110), (111) and (100) planes of bulk fcc platinum, resulting in six-coordinated buckled (Figure 4.1a & b), six-coordinated planar (Figure 4.1c & d) and four-coordinated planar (Figure 4.1e) structures, respectively. The six-coordinated buckled and planar structures have been modeled by considering in both hexagonal and orthorhombic lattices, whereas four-coordinated planar structure possess tetragonal lattice. Therefore, we have studied a total five kind of monolayers as has been shown in Figure 4.1.

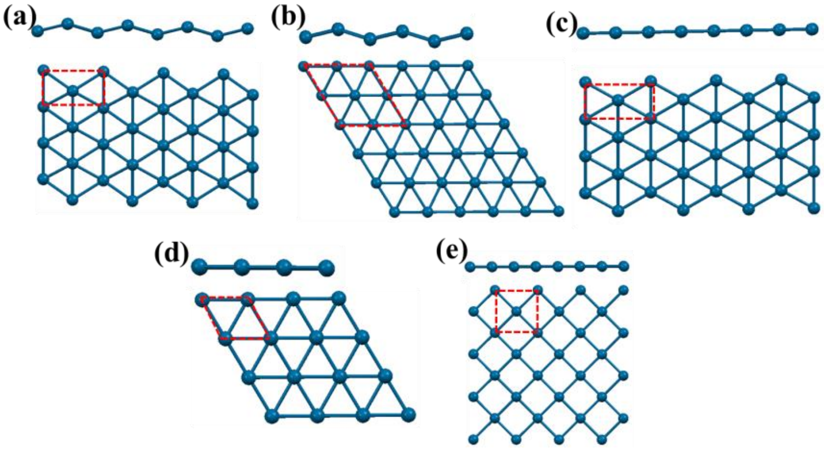

Figure 4.1: Different motifs of 2D platinum monolayer: six-coordinated (a) orthorhombic buckled, (b) hexagonal buckled, (c) orthorhombic planar, (d) hexagonal planar; and four-coordinated (e) planar. Red-colored dashed lines represent the unit cell of the respective structures.

4.3. Results and Discussion

4.3.1 Stability of Pt-ML

The energetic stability of the monolayers is investigated by performing formation *[8]* and cohesive energy *[8]* calculations (Table 4.1). For comparison, the energy values are compared with the single-layered Pt nanocage, nanocluster and bulk Pt(111) surface. Our calculated formation energies of the six-coordinated buckled structures (Figure 4.1a & b), six-coordinated planar structures (Figure 4.1c & d), four-coordinated planar (Figure 4.1e), singled layered nanocage, octahedral nanocluster and bulk Pt(111) surface structures are 0.73, 0.82, 1.32, 0.98, 0.78 and 0.23 eV, respectively. Therefore, the buckled monolayers are easier to synthesis compared to single-layered nanocage and, octahedral nanocluster. Moreover, our calculated cohesive energy of buckled monolayers (-4.95 eV) are very much close to the bulk Pt(111) surface (-5.47 eV). Therefore, the buckled monolayers are energetically stable compared to planar monolayers and other nanostructured based catalyst. This energetic stability could arise due to the buckling nature of the (110) faceted monolayer. Moreover, it is very interesting to note that crystal lattice does not affect the energetic stability of the structures.

Table 4.1: Energetic stabilities of the monolayers. Our calculated values are compared with the previous reports on singled layered nanocage *[8]*, octahedral Pt_{85} nanocluster *[33]* and bulk Pt(111) surface *[8]*

Systems	Formation Energy (eV/atom)	Cohesive Energy (eV/atom)
Six-coordinated buckled (orthorhombic)	0.73	-4.95
Six-coordinated buckled (hexagonal)	0.73	-4.95
Six-coordinated planar (orthorhombic)	0.82	-4.87
Six-coordinated planar (hexagonal)	0.82	-4.87
Four-coordinated planar	1.32	-4.36
Single-layered Pt_{66} nanocage	0.98	-4.71
Octahedral Pt_{85} nanocluster	0.78	-4.91
Bulk Pt(111) surface	0.23	-5.47

The dynamic stabilities of the monolayers are investigated from phonon frequency calculations. To reduce the constraint of the periodic boundary condition, phonon dispersion calculations are carried out in (4 × 4) supercell geometry. The lattice dynamics of the monolayers are examined from their respective phonon dispersion plots (Figure 4.2a & 4.3). The Phonopy code *[34]* is used to calculate phonon properties through density functional perturbation theory (DFPT) *[35]*. Our phonon dispersion plot (Figure 4.2a) shows that the buckled orthorhombic monolayer (Figure 4.1a) shows a very small imaginary frequency of -1.69 cm^{-1}, when the phonon dispersion approaches from Y to Γ. Such a small imaginary frequency value (<10 cm^{-1}) can be ignored *[36-38]* and thus the buckled orthorhombic monolayer can be considered a dynamically stable structure. All the other monolayers (Figure 4.3) have imaginary frequencies from -21 to -73 cm^{-1}. In addition, phonon dispersion is also calculated considering the dielectric effects and Figure 4.4 shows that buckled orthorhombic monolayer has a small imaginary frequency of -2.50 cm^{-1}. Therefore, in spite of the similar kind of energetics stabilities between the two buckled monolayers (hexagonal and orthorhombic), only orthorhombic buckled structure is dynamically stable.

Henceforth, all the studies have been performed on the buckled orthorhombic structures. In analogy with stanene (a monolayer of tin), a monolayer of platinum can be called ‘platene’. Therefore, from here on, the buckled orthorhombic Pt monolayer structure is named as platene (Figure 4.2b-c).

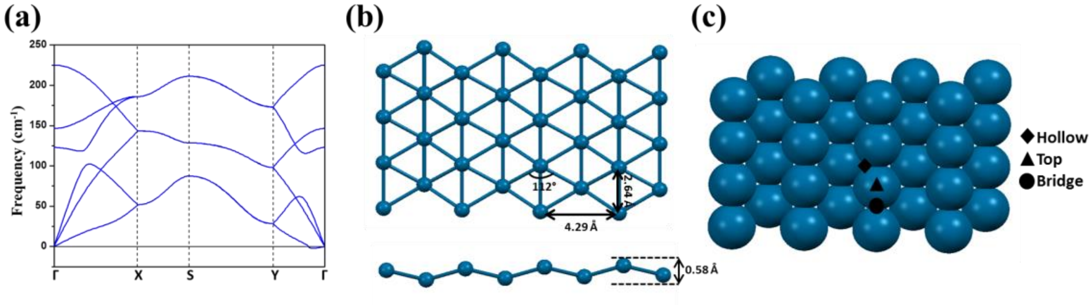

Figure 4.2: (a) Dispersion of phonon modes, (b) Structural parameters and (c) adsorption sites of the buckled orthorhombic monolayer.

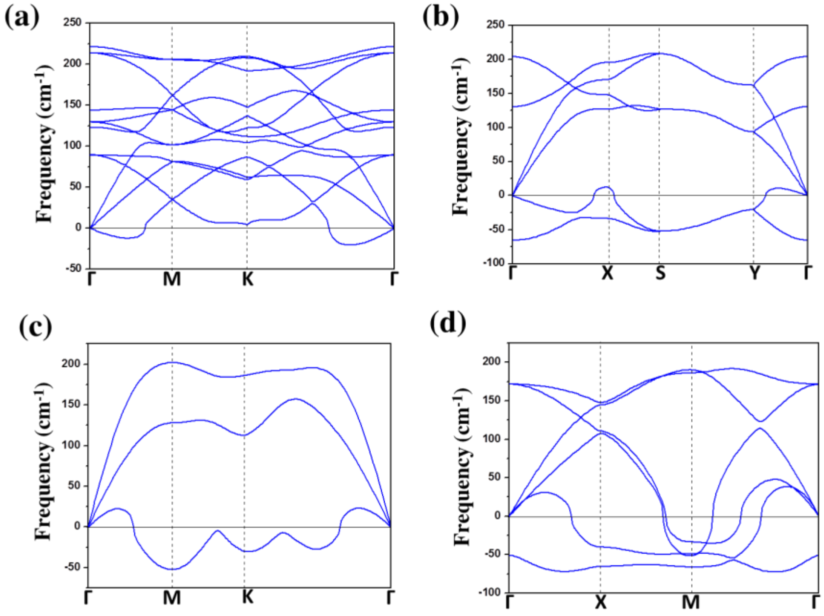

Figure 4.3: Dispersion of phonon modes for six-coordinated (a) hexagonal buckled, (b) orthorhombic planar, (c) hexagonal planar; and four-coordinated (d) planar.

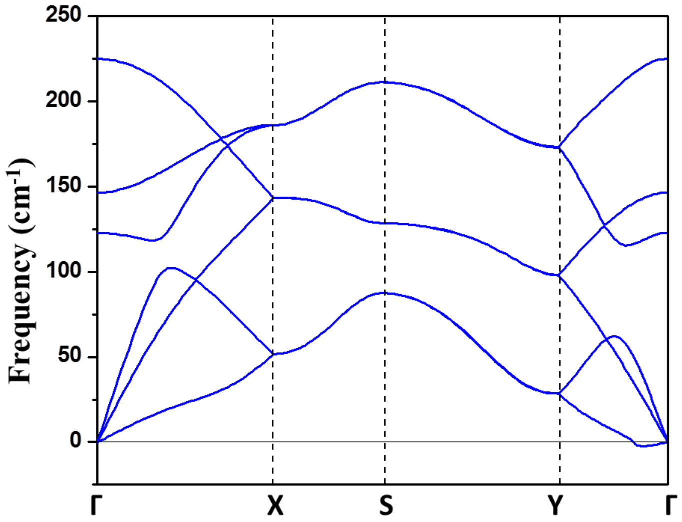

Figure 4.4: Dispersion of phonon modes of the six-coordinated orthorhombic buckled structure under dielectric effects

Low-temperature fuel cells (DMFCs, PEMFCs and AFCs) are operated in the temperature range from 300 to 600 K *[39]*. Therefore, it is necessary to find out the possibility of interconversion of platene to any other conformers in the fuel cell operating temperature. Hence, the thermal stability of platene sheet is verified by performing ab initio molecular dynamics simulations (AIMD) using the Nosé thermostat model *[40]* as implemented in VASP. This is carried out on a (4 × 4) supercell of platene, using an NVT ensemble at 300, 400, 500, and 600 K with a time step of 1 femtosecond (fs) for 15 picoseconds (ps). AIMD calculations are performed on the supercell geometry to reduce the constraint of periodic boundary condition. No structural reconstruction is found at 300 K. The fluctuation of the total energy is smooth throughout the AIMD simulation (Figure 4.5a). Hence, the structure remains stable at room temperature. Furthermore, simulations are carried out using an NVT ensemble at 400, 500 and 600 K and the fluctuation of total energy has been shown in Figure 4.6. The snapshots of atomic configurations of the Pt-ML at the end of MD simulations are shown in the Figure 4.7. We have not found any significant structural reconstructions even after heating at 600 K for 15 ps. Thereby, we predict that platene can withstand temperatures as high as 600 K and the interconversion to any other structures is not possible. These results demonstrate that a high-energy barrier from other local minima energy structures separates the platene structure.

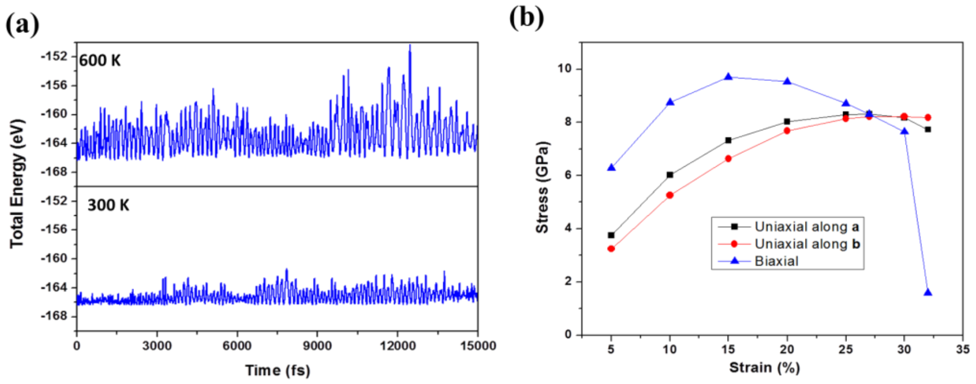

Figure 4.5: (a) AIMD simulations and (b) stress-strain relationship of platene.

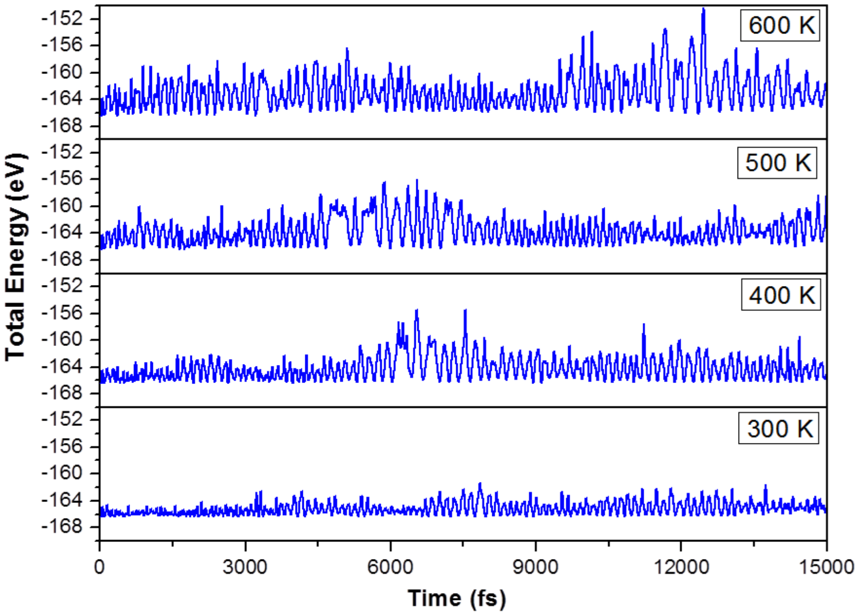

Figure 4.6: AIMD simulations of platene at different temperatures

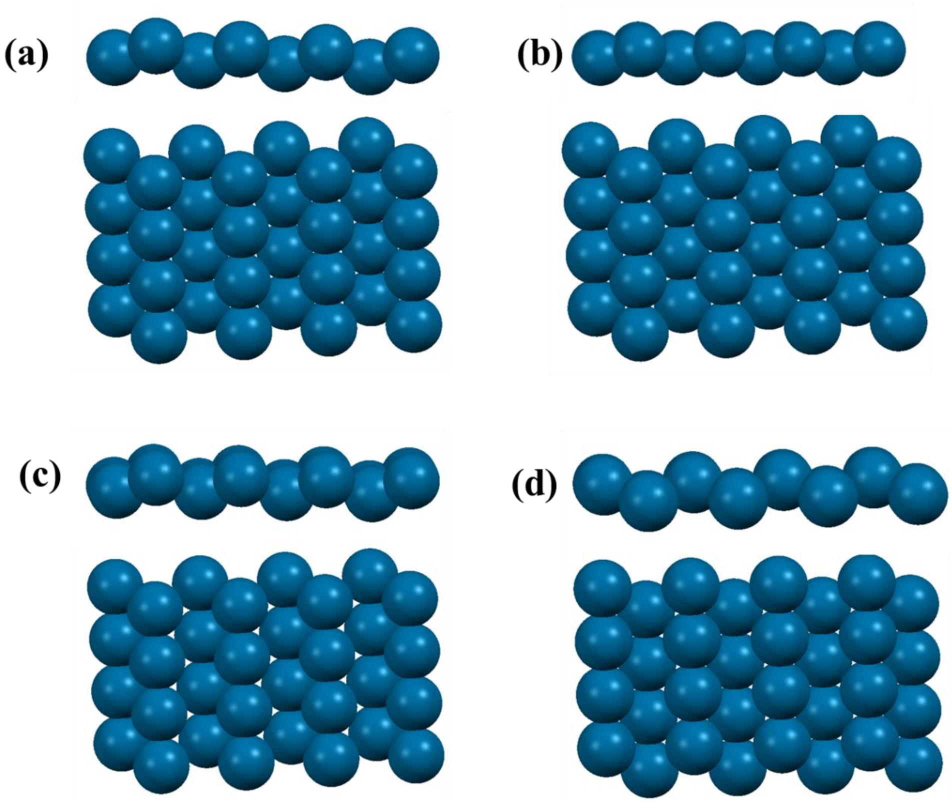

Figure 4.7: Snapshots of the platene after the end of the simulation at different temperatures: (a) 300, (b) 400, (c) 500 and (d) 600 K.

Further, platene may undergo distortion upon the adsorption of reaction species during catalysis. So, it is necessary to evaluate the effect of lattice distortion on structural stability. Thus, the structural stability under strain is very important for their synthesis and applications. Therefore, strains are applied on the (4 × 4) supercell structure along the in-plane uniaxial and biaxial directions to evaluate the mechanical stability of platene and the applied strain (in %) is calculated using the following formula[41]:

$$\% \text{ strain} = \frac{a - a_1}{a} \times 100 \tag{4.4}$$

where 'a' and 'a_1' are the lattice constants of platene sheet before and after the strain, respectively. Atomic positions are relaxed at each strain until the forces on each atom are less than 10^{-2} eV.Å^{-1}. The elastic limit is calculated under tensile stretching. The stress–strain curve (Figure 4.5b) shows that maximum stress occurs at 27%, 30% and 15% for uniaxial along-a, along-b and biaxial directions, respectively. Therefore, the elastic limit of the platene is at 0.15 strain with a maximum stress of 8.82 GPa. Moreover, we have studied the mechanical properties of platene by calculating the change in energy in the strain range of -5% to 5% with an increment of 1% by using the standard Voigt notation.[42-43] The elastic strain energy per unit area can be expressed as[42-43]:

$$U = 1/2C_{11}\varepsilon_{xx}^2 + 1/2C_{22}\varepsilon_{yy}^2 + C_{12}\varepsilon_{xx}\varepsilon_{yy} + 2C_{66}\varepsilon_{xy}^2 \tag{4.5}$$

where C_{11}, C_{22}, C_{12} and C_{66} are the linear elastic constants, whereas ε_{xx}, ε_{yy} and $\varepsilon_{xy}$are the in-plane stress along the x, y and xy directions, respectively. The main criteria for mechanical stability are C11 > C12 and C66 > 0. Our calculated values of C11, C22, C12 and C66 are 164, 120, -30 and 56 GPa.nm, respectively. These are very much comparable with the previously reported values of black phosphorene [*44]* and borophene [*43]*. Furthermore, we have calculated the in-plane Young's modulus (Y) and Poisson's ratio (PR) and can be derived from the elastic constants using the following equations

$$E_x = \frac{C_{11}C_{22} - C_{12}C_{21}}{C_{22}}, \; E_y = \frac{C_{11}C_{22} - C_{12}C_{21}}{C_{11}} \tag{4.6}$$

$$\upsilon_{xy} = \frac{C_{21}}{C_{22}}, \quad \upsilon_{yx} = \frac{C_{12}}{C_{11}} \tag{4.7}$$

Therefore, E_x, E_y and $\upsilon_{xy,}$ υ_{yx} are Young's modulus (Y) and Poisson's ratio (PR) in x and y direction, respectively. The calculated values of Y are 164, 120 GPa.nm, whereas the values of PR are -0.25 and -0.18 in x and y direction, respectively. The value of Y is quite lower than the hexagonal graphene (340 GPa.nm) *[45]* and orthorhombic borophene (398 and 170 GPa.nm) *[43]*. However, our calculated Y is higher than phosphorene (23 and 92.3 GPa.nm along the armchair and zigzag direction, respectively) *[44]* and hexagonal stanene monolayer (24 GPa.nm) *[46]*. The negative PR value has been found due to the buckled configuration of platene. The negative PR value for buckled monolayer has been reported earlier *[42-43, 47-48]*. Our calculated density of states and band structure (Figure 4.8a) of platene show its metallic character.

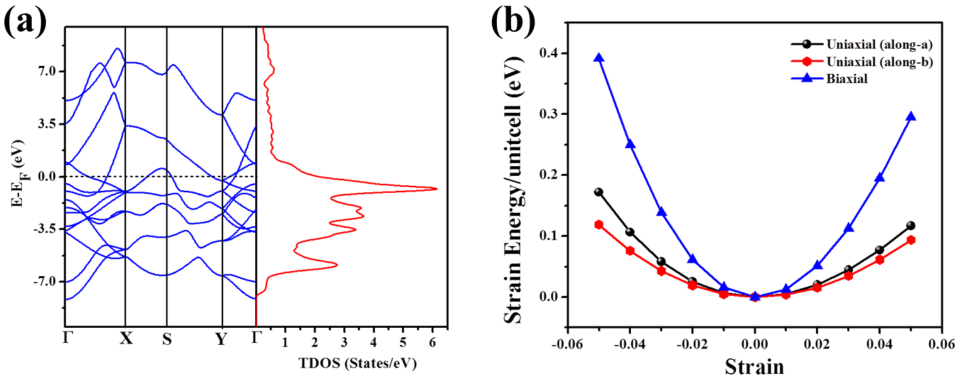

Figure 4.8: (a) Band structure and total density of states (TDOS) and (b) Strain energy under in-plane uniaxial and biaxial strains of platene.

The dissolution of surface atoms of the catalyst is also a very important criterion to describe the electrochemical stability of the catalyst *[49,50]*. It is well accepted that the electrochemical oxidation of Pt ($Pt \rightarrow Pt^{2+} + 2e^-$) is the main phenomenon behind the dissolution *[51-53]*. We have compared the dissolution behavior of platene with respect to the bulk Pt(111) surface. As the surrounding environment i.e. the presence of O, OH and OOH largely influences the dissolution, the calculations are carried out in the presence of these intermediates. Such model has been used for calculating the shift in dissolution potential *[49,51-53]*. Here, the shift (ΔU) in the electrode potential is calculated with respect to the bulk Pt(111) surface using the following equation:

$$\Delta U = U_{\mathrm{Platene}} - U_{\mathrm{Pt(111)}} = (\mu_{\mathrm{Pt-Pt(111)}} - \mu_{\mathrm{Pt-Platene}})/(ne) \qquad (4.8)$$

where $U_{\mathrm{Platene},}$ and $U_{\mathrm{Pt(111)}}$ are the electrode potential of platene, and bulk Pt(111) surface, respectively. $\mu_{\mathrm{Pt-Pt(111)}}$ and $\mu_{\mathrm{Pt-Platene}}$ are the chemical potential of Pt in platene, and bulk Pt(111) surface and n is the number of electron transferred during the dissolution reaction ($Pt \rightarrow Pt^{2+} + 2e^-$).

The shift of electrode potential has been derived as follows:

As mentioned before, dissolution of Pt into the solution proceeds through the following equation.

$$\mathrm{Pt} \rightarrow \mathrm{Pt}^{2+} + 2e^{-} \tag{4.9}$$

When the dissolution of Pt is referenced to the standard hydrogen electrode (SHE) reaction, the equation (4.9) can be written as

$$\mathrm{Pt}^{n+} + n/2\ \mathrm{H}_2 \rightarrow \mathrm{Pt} + n\mathrm{H}^{+} \tag{4.10}$$

The Gibbs free energy (ΔG) for this reaction can be written as

$$\Delta G = -neU \tag{4.11}$$

where U is the electrode potential of Pt vs. SHE. Here, n = 2 for the equation (4.11). Now, considering the platinum in the catalyst and platinum in the solution are in equilibrium, the above equation can be expressed for the monolayer as

$$-neU_{\mathrm{Platene}} = \mu_{\mathrm{Pt-Platene}} + \mu_{\mathrm{nH^+}} - \mu_{\mathrm{Pt^{n+}}} - \mu_{\mathrm{n/2H_2}} \tag{4.12}$$

where $\mu_{\mathrm{Pt-Platene}}$, $\mu_{\mathrm{Pt^{n+}}}$, $\mu_{\mathrm{nH^+}}$ and $\mu_{\mathrm{n/2H_2}}$ are the chemical potentials of platinum metal, dissolved platinum ions, H^+ and H_2, respectively.

Similarly, the electrode potential ($U_{\mathrm{Pt(111)}}$) of platinum in bulk Pt(111) surface can be related with the chemical potentials using the following equation

$$-neU_{\mathrm{Pt(111)}} = \mu_{\mathrm{Pt-Pt(111)}} + \mu_{\mathrm{nH^+}} - \mu_{\mathrm{Pt^{n+}}} - \mu_{\mathrm{n/2H_2}} \tag{4.13}$$

Therefore, the shift of electrode potential (ΔU) of platinum of NCs with respect to the bulk Pt(111) surface can be written as

$$U_{\mathrm{Platene}} - U_{\mathrm{Pt(111)}} = \Delta U = (\mu_{\mathrm{Pt-Pt(111)}} - \mu_{\mathrm{Pt-Platene}})/(ne) \tag{4.14}$$

Now, the chemical potentials of the metal can be defined as

$$\mu_{\mathrm{Pt}} = \frac{\partial A}{\partial N} \approx \frac{\partial E}{\partial N} \tag{4.15}$$

where A, E and N are the total free energy, total energy and changes in number of platinum atoms, respectively. The total free energy can be approximated to total energy because the entropic contributions rules out while calculating the chemical potential difference between the metals.

The dissolution of the platinum has been considered by removing one platinum atom from the surface of the catalysts. Hence, the chemical potential of the equation (4.15) is calculated by considering the defected platene and Pt(111) surface. The chemical potential is obtained by calculating the total energies of the optimized structures (E_{Pt}) and defected structures ($E_{Pt\text{-}def}$).

Therefore, from the equation (4.15), we can get $\mu_{Pt} = (E_{Pt\text{-}def} - E_{Pt})$ (4.16)

The value of N=1 as only one atom is removed for the calculation.

As the surrounding environment i.e. the presence of O, OH and OOH largely influences the dissolution, the calculation is carried out in the presence of these intermediates.

Therefore, $\mu_{Pt} = (E_{Pt\text{-}def\_O/OH/OOH} - E_{Pt\_O/OH/OOH})$ (4.17)

We have calculated the chemical potential of platinum for the platene and bulk Pt(111) surface. The atoms, which are removed for the consideration of dissolution behavior at the different sites of the monolayer, have been shown in Figure 4.9.

Our calculated shift in electrode potential (ΔU) are 0.65, 0.35, 0.29 and 0.18 V for O-, OH-, OOH-adsorbed platene and bare platene, respectively. The positive ΔU value represents that dissolution of Pt atom is less favorable in platene than in bulk Pt(111) surface. The less dissolution tendency of platene can be explained from the structural reconstruction of platene upon adsorption of the intermediates. We find that the Pt atoms of O-adsorbed platene are strongly bonded compared to the O-adsorbed bulk Pt(111) surface. The Pt-Pt bond length in the vicinity of *O is 2.76 and 2.86 Å in platene and bulk Pt(111) surface, respectively. Therefore, the strong Pt-Pt bonding in platene resists from dissolution. Furthermore, the Pt-Pt bond distance in O-adsorbed platene is more close to the bulk fcc platinum (2.77 Å), which again suggests its stability.

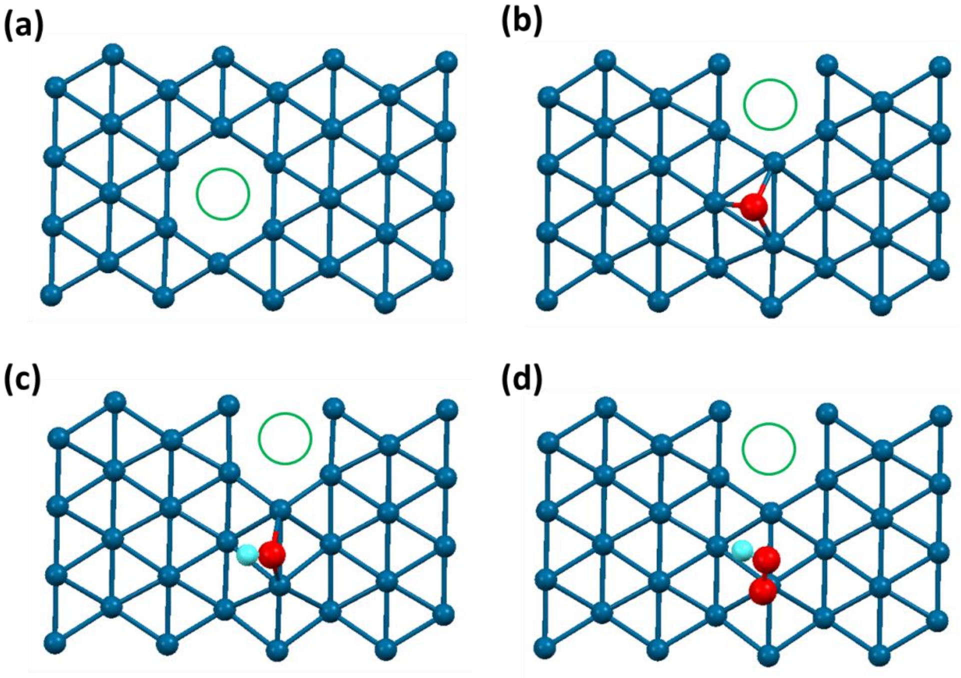

Figure 4.9: Optimized structures of the defected platene: (a) bare platene, (b) O-adsorbed, (c) OH-adsorbed and (d) OOH adsorbed. The green circle represents the defected site.

After carefully investigating the stability of the platene, we have rigorously elucidated the electronic structure to understand the stability of the buckled structure. For comparisons, we have compared with the orthorhombic planar structure. The projected density of states (PDOS) of platene (Figure 4.10a) shows that the π-orbitals (d_{xz} and d_{yz}) are significantly stabilized compared to the planar platinum structure (Figure 4.10b). This is due to the significant interactions between the σ- (d_{x2-y2} and d_{xy}) and π-orbitals (d_{xz} and d_{yz}). This kind of orbital mixing stabilizes the buckling nature in a monolayer sheet *[54]*. In fact, the buckling nature of stanene and silicene is also attributed to the σ-π orbital mixing *[54]*.

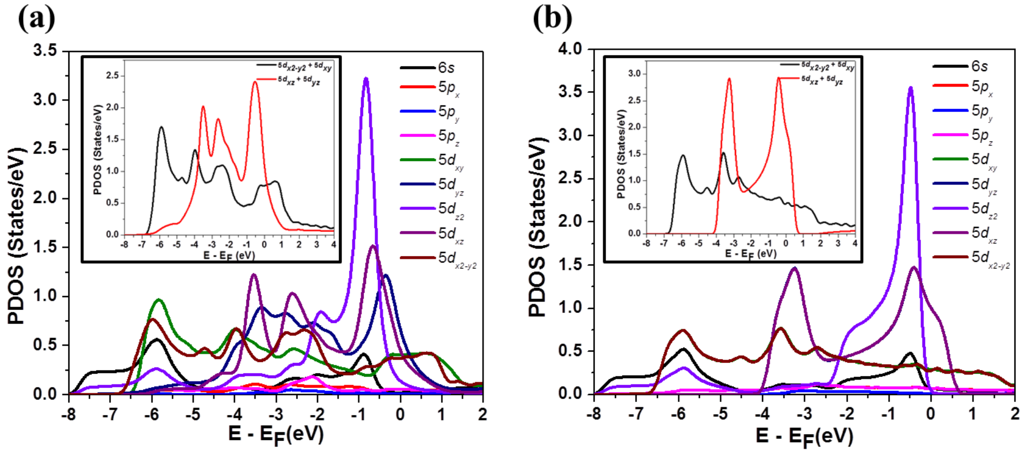

Figure 4.10: Projected density of states (PDOS) of (a) platene and (b) planar structure. The inset pictures show the mixing of σ-π orbtials; black and red line represents the σ- (d_{x2-y2} and d_{xy}) and π-orbitals (d_{xz} and d_{yz}), respectively.

Furthermore, the underlying reason behind the stability of the buckled pattern has been investigated by molecular orbital analysis (Figure 4.11). We have considered a Pt_7 cluster in both planar and buckled structure within the geometry of their respective periodic monolayers. Our calculated molecular orbitals suggest that the orbital compatibility plays an important role towards the exceptional stability of the buckled structure. The concept of orbital compatibility suggests that some orbitals of the system undergo an orientation to gain maximum overlap, which in turn stabilizes the system. The compatibility of orbitals is also well known for the relative stability of polyhedral boranes, carboranes, and metallaboranes *[55-57]*. We find that the d_{z2} orbitals of the out-of-plane Pt atoms tilt themselves (by 30°) toward the d_{yz} orbital of the in-plane Pt atoms to gain the maximum overlap, which in turn stabilizes the buckled structure.

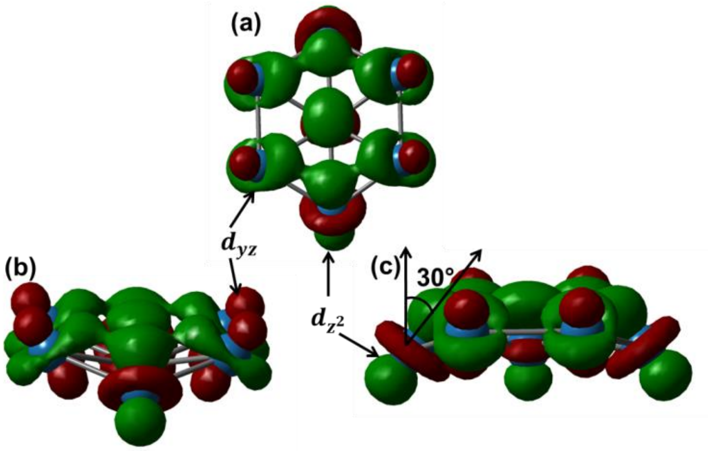

Figure 4.11: Molecular orbitals of buckled Pt_7 cluster along (a) z-, (b) x- and (c) y-direction.

4.3.2 ORR Mechanism

4.3.2.1 Adsorption

Now, the potential applicability of platene towards ORR has been discussed in the following sections. Firstly, the adsorption patterns of all the possible ORR intermediates species ($*O_2$, *O, *OH, *OOH, $*H_2O$ and $*H_2O_2$) are studied over the three possible catalytic sites (Figure 4.2c) on the platene: (i) top, (ii) bridge, and (iii) hollow. We have checked the relative stabilities of the intermediate species adsorbed on all the three possible sites and then the most stable conformer are considered for detailed study. The preferred binding sites along with their respective binding energies are given in Table 4.2. For comparison, we have listed (Table 4.2) reported adsorption energies of the intermediate species on a bulk Pt(111) surface *[8]*. It is worth mentioning that the adsorption energies of $*O_2$ and *O are more or less comparable than that on the bulk Pt(111) surface. In contrary, the end products ($*H_2O$ and $*H_2O_2$) are adsorbed weakly on platene compared to that on the bulk Pt(111) surface. Therefore, platene shows interesting behaviour compared to the bulk Pt(111) surface. The adsorption behaviours of the intermediates have been shown in the Figure 4.12.

Table 4.2: Preferred binding sites, binding energies (eV) of the most stable ORR intermediate species on platene and bulk Pt(111) surface *[8]*. Here t, b, h and f denote top, bridge, hollow, and fcc sites, respectively.

Adsorbed species	**Binding Energy (eV)**	
	Platene	**Bulk Pt(111) surface**
$*O_2$	-0.68 (b)	-0.67 (b)
*O	-4.56 (h)	-4.42 (f)
*OH	-2.09 (b)	-2.37 (t)
*OOH	-0.78 (b)	-1.15 (b)
$*H_2O_2$	-0.10 (b)	-0.30 (b)
$*H_2O$	-0.05 (t)	-0.26 (t)
*H	-2.60 (h)	-2.77 (f)

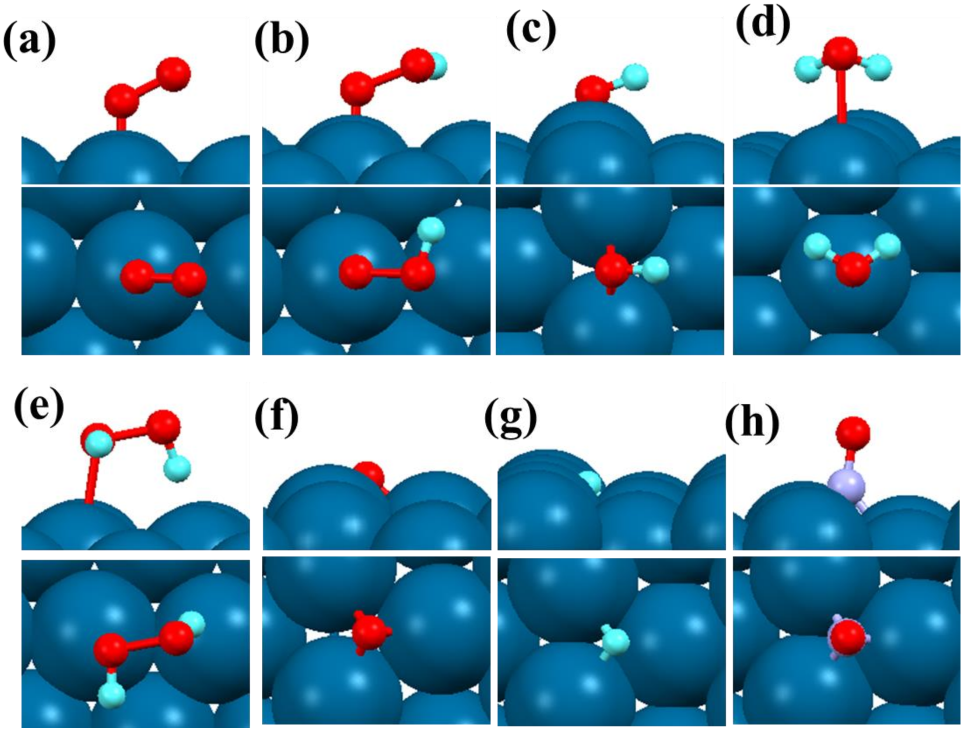

Figure 4.12: Adsorption behaviours of the intermediates: (a) $*O_2$, (b) *OOH, (c) *OH, (d) $*H_2O$, (e) $*H_2O_2$, (f) *O, (g) *H and (f) *CO.

4.3.2.2 Reaction mechanism

Following the O_2 adsorption, the reduction process can proceed via the four-electron ($4e^-$) and two-electron ($2e^-$) reduction pathways for the formation of H_2O and H_2O_2, respectively. On the basis of O_2 bond dissociation, we have proposed two pathways *[8]*: (i) direct and (ii) indirect pathways. In case of direct pathway, O-O bond dissociation is favoured over $*O_2$ hydrogenation, whereas in case of indirect pathway, hydrogenation process is preferred over O-O bond dissociation. Therefore, the product selectivity (H_2O vs. H_2O_2) depends on the direct vs. indirect mechanism. So, we have calculated the reaction free energies and activation barriers for the complete reaction pathway (Scheme 4.1) and our calculated values are compared with the previous reports on the bulk Pt(111) surface and singled-layered nanocage.

O_2 activation:

Direct O-O bond dissociation is one of the very important steps for fuel cell applications as it leads to the formation of H_2O, which reduces the formation of unwanted by-products (H_2O_2). Thereby, direct dissociation favours $4e^-$ reduction over $2e^-$ reduction. Earlier studies show direct O-O bond dissociation (Step 4.1) is not thermodynamically and kinetically favourable over O_2 hydrogenation (Step 4.2) on the periodic Pt, Pd, Ag surfaces *[58-59]*. Thus, there are two competing pathways for $*O_2$ while adsorbed on a catalyst surface. Either the adsorbed O_2 will dissociate into atomic oxygen *O or hydrogenated to *OOH.

$*O_2 \rightarrow *O + *O \quad \Delta G = -0.64, \Delta G^{\ddagger} = 0.21$ eV (Step 4.1)

$*O_2 + *H \rightarrow *OOH \quad \Delta G = -0.44, \Delta G^{\ddagger} = 0.09$ eV (Step 4.2)

$*O_2$ can be adsorbed via two conformers: (i) suproxo and (ii) titled *[5,8,60]*. The calculated $*O_2$ dissociation (Step 4.1) barriers on the platene are 0.97 and 0.21 eV for superoxo and tilted conformers, respectively. Thus, during the activation process, the adsorbed $*O_2$ may rearrange itself from the superoxo to tilted conformer. Similar kind of conformational rearrangements are reported on the bulk Pt(111) surface *[60]* Pt_{79} nanocluster *[33]* and Pt_{66} nanocage *[8]*. The very low barrier for conformational rearrangement certainly favours the O_2 dissociation from the tilted conformer. The previously calculated O-O bond dissociation barriers are 0.53 eV *[56]* and 0.44 eV *[58]* on the bulk Pt(111) surfaces and 0.72 eV and 1.22 eV on the bulk Pd(111) *[63]* and Ag(111) *[54]* surfaces, respectively. Therefore, the direct $^*O_2$ dissociation barrier (0.21 eV) on platene is very much lower than the previous reports on any bulk metal surfaces. It is noteworthy to mention that we have done spin-polarized calculations while oxygen adsorbs on platene surface. We have found that the adsorbed $^*O_2$ (tilted) shows a total magnetic moment of 1.02 μB, whereas adsorbed *O is a nonmagnetic one. Our findings are in good agreement with the previously reported magnetic calculations *[62]*. However, we have not considered the potential energy crossing of the two states.

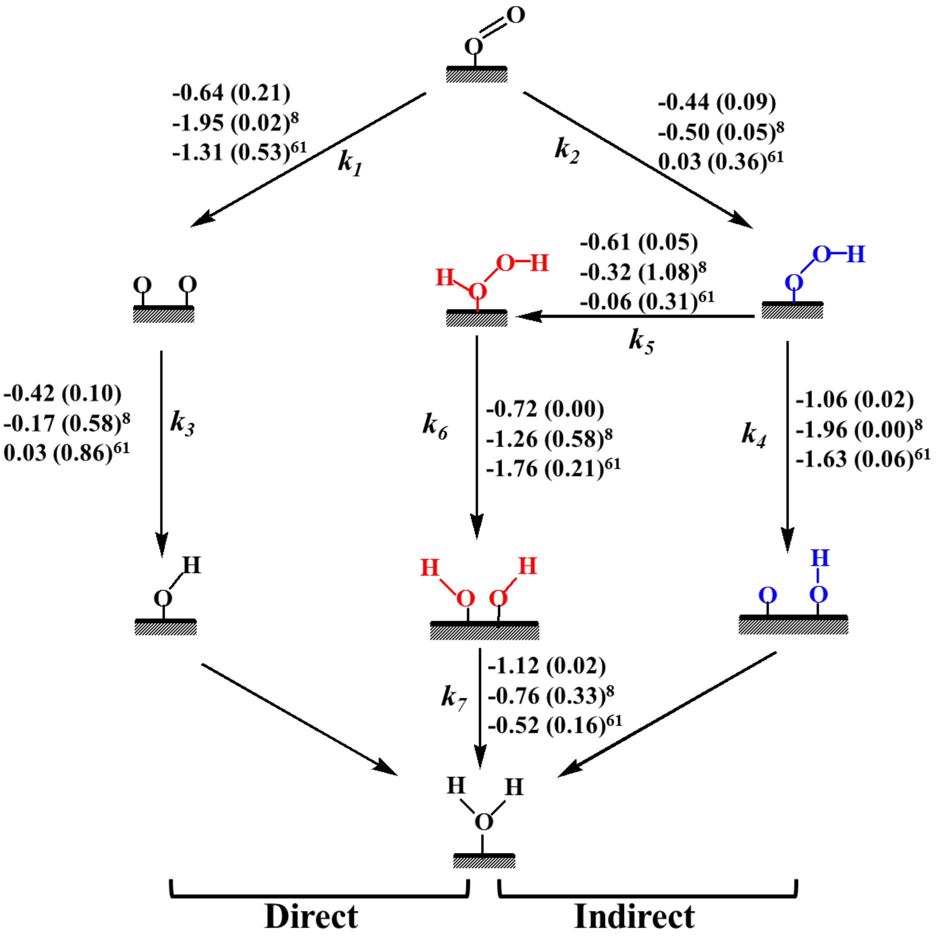

Scheme 4.1: Reaction free energies (eV) and activation barriers (eV, in parenthesis) are presented for all the possible elementary steps of ORR over platene. Our calculated respective values are compared with previous reports on oxygen reduction over single layered nanocage *[8]* and bulk Pt(111) surfaces *[61]*.

Similarly, O_2 hydrogenation (Step 4.2) on platene is also exergonic (-0.44 eV) with an activation barrier of 0.09 eV. The barriers for the same step (Step 4.2) are reported to be 0.25 *[63]*, 0.36 *[61]* and 0.30 eV *[58]* on the bulk Pt(111) surfaces. Therefore, the platene is highly reactive towards O_2 hydrogenation and thus favours indirect over direct O_2 dissociation. This trend is in good agreement with previously reported bulk Pt(111), Pd(111) and Ag(111) surfaces.

*OH formation

The *OH formation is of the most important steps for the ORR and many previous studies reported this is one of the rate determining steps on the bulk Pt(111) surfaces *[58,61,63-64]*.

$*O + *H \rightarrow *OH \quad \Delta G = -0.42, \Delta G^{\ddagger} = 0.10$ eV (Step 4.3)

$*OOH \rightarrow *O + *OH \quad \Delta G = -1.06, \Delta G^{\ddagger} = 0.02$ eV (Step 4.4)

The direct O–O bond dissociation followed by hydrogenation leads to the formation of *OH (Step 4.3). The direct formation of *OH (Step 4.3) on platene is exergonic (-0.42 eV) with a very low activation barrier of 0.10 eV. The very low activation barrier for *OH formation is due to the similarity in adsorption behaviours of *O and *OH. Both the *O and *OH adsorb in the bridge position, which facilitates the *H to migrate to the *O very easily, lowering the *OH formation barrier. In fact, we have calculated the activation barrier of *OH formation while *O is adsorbed at the hollow site and it requires higher activation barrier (0.43 eV) for *OH formation. As the relative stability of *O is very much comparable on the hollow and bridge positions (differ only by 0.20 eV), therefore the surface site occupancy of *O will be very much comparable on platene. This is completely opposite to the adsorption behaviour on the bulk Pt(111) surface, where the *O is not stable at the bridge site (moves to fcc site). Therefore, the buckling nature of (110) faceted platene helps the *O to adsorb in a unique manner (i.e at bridge site) on the platene surface, which subsequently lowers the activation barrier of *OH formation (Figure 4.13). Previous studies reported the activation barriers of 0.74 *[58]* and 0.86 eV *[61]* on the bulk Pt(111) surfaces and 0.72 eV on the bulk Pd(111) surface *[59]*. Thus, the rate-determining step is no longer a rate-determining step when the reaction is catalyzed by the platene catalyst.

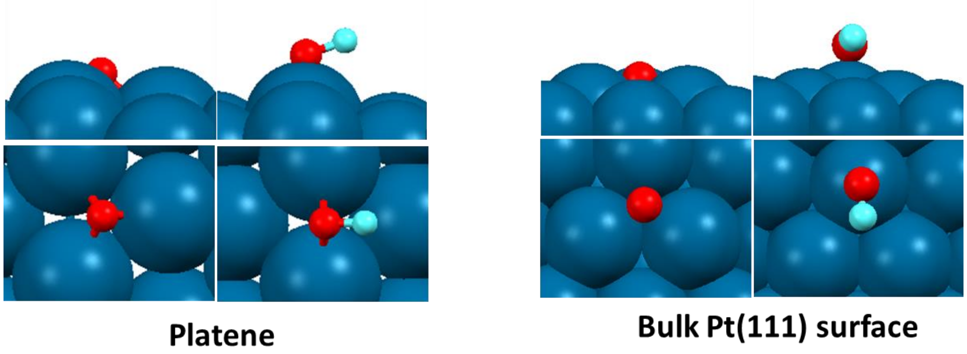

Figure 4.13: Adsorption behaviours of *O and *OH in platene and bulk Pt(111) surface.

Furthermore, *OH formation is possible via indirect pathways (Step 4.4) too, such as via peroxyl formation followed by O–O bond dissociation (Step 4.4). This step requires an activation barrier of 0.02 eV on platene with reaction free energy of -1.06 eV. Sha et al. *[58]* and Li et al. *[61]* reported activation barriers of 0.12 eV and 0.06 eV for the *OOH dissociation (Step 4.4) step over the bulk Pt(111) surfaces.

*H_2O_2 formation and decomposition

The two-electron reduction process leads to the formation of H_2O_2. H_2O_2 can be formed via two successive hydrogenations at O_2 (*O_2 + *H → *OOH, *OOH + *H → *H_2O_2).

$*OOH + *H \rightarrow *H_2O_2$ $\Delta G = -0.61, \Delta G^{\ddagger} = 0.05$ eV (Step 4.5)

$*H_2O_2 \rightarrow *OH + *OH$ $\Delta G = -0.72, \Delta G^{\ddagger} = 0.00$ eV (Step 4.6)

Thus, *OOH can undergo further hydrogenation for the formation of $*H_2O_2$ (Step 4.5). Our calculated activation barrier and reaction free energy for this process are 0.05 and -0.61 eV, respectively. Zhiyao et al. *[58]* reported an activation barrier of 0.19 eV for H_2O_2 (Step 4.5) formation on the bulk Pt(111) surface. This suggests that H_2O_2 formation is favoured on platene compared to that on the bulk Pt(111) surface. However, our calculated rate constant (Table 4.3) values suggest that the ratio of rate constants for *OOH dissociation ($k4$) and *OOH hydrogenation ($k5$) is 4.45. Therefore, the dissociation of *OOH is more favourable than its hydrogenation. The $*H_2O_2$ can again dissociate into *OH (Step 4.6). The step is a barrierless process on platene surface. Therefore, even if there is a possibility of H_2O_2 formation, but then it will dissociate into *OH. Therefore, we find that platene could be a very selective catalyst for water formation and therefore could be a promising catalyst for fuel cell applications.

Table 4.3: Rate constants values for the elementary reactions at different temperatures.

Elementary reactions	300 K	400 K	500 K
$*O_2 \rightarrow *O + *O$ (k_1)	1.87×10^{09}	1.94×10^{10}	8.31×10^{10}
$*O_2 + *H \rightarrow *OOH$ (k_2)	2.23×10^{11}	6.98×10^{11}	1.46×10^{12}
$*O + *H \rightarrow *OH$ (k_3)	9.83×10^{10}	3.51×10^{11}	7.93×10^{11}
$*OOH \rightarrow *O + *OH$ (k_4)	3.11×10^{12}	5.30×10^{12}	7.69×10^{12}
$*H + *OOH \rightarrow *H_2O_2$ (k_5)	6.98×10^{11}	1.61×10^{12}	2.80×10^{12}
$*H_2O_2 \rightarrow *OH + *OH$ (k_6)	5.88×10^{12}	8.00×10^{12}	1.01×10^{13}
$*H + *OH \rightarrow *H_2O$ (k_7)	2.42×10^{12}	4.14×10^{12}	6.00×10^{12}

*H_2O formation

*OH + *H → *H_2O $\Delta G = -1.12$, $\Delta G^{\ddagger} = 0.02$ eV   (Step 4.7)

The adsorbed *OH undergoes protonation for the formation of *H_2O. On platene surface, the activation barrier for this process is 0.02 eV with a reaction free energy of -1.12 eV. Previous studies reported H_2O formation barriers of 0.16 eV *[61]*, 0.09 *[63]* and 0.14 eV *[58]* on the bulk Pt(111) surfaces, which are higher than our calculated barrier of 0.02 eV on the platene surface.

However, the *H_2O formation barrier (0.02 eV) and *OH formation barrier (0.10 eV) is lower than *O_2 dissociation (0.21 eV) barrier on platene surface. This suggests that *O_2 dissociation is the rate determining step on the platene surface. On the other hand, *O_2 dissociation barrier (0.21eV) is significantly higher (0.44-0.53 eV) on the bulk Pt(111) surface than that on platene surface. Moreover, the adsorption energies of *H_2O (-0.05 eV) and *H_2O_2 (-0.10 eV) are very low on platene surface compared to that on the bulk Pt(111) surface (-0.26 for *H_2O and -0.30 eV for *H_2O_2), lessening the possibility of surface poisoning.

Therefore, our results show excellent catalytic activity of platene toward ORR. This includes excellent catalytic activity toward rate-determining steps as well other important steps. We find that *O_2 activation processes (*O_2 → *O + *O and *O_2 + *H → *OOH) and *OH formation (*O + *H → *OH) are significantly improved over platene surface. More importantly, the highest activation barrier for ORR is 0.21 eV on platene surface, which is far lower than any ORR catalysts studied to date.

4.3.3. ORR activity on few-layered platene structures:

For comparisons, we have studied ORR activity on few-layered platene structures. For this, we considered three (odd) and four (even) layers of platene. Here all the atoms are full relaxed to get the exact surface pattern of few-layered platene structures. Interestingly, the (110) surface pattern changes to (100) surface pattern after energy minimization. Besides, they form a planar structure. This is quite logical that highly un-saturated Pt atoms tend to fulfil their valencies and the structure tends to stabilize into a low energy structure. This is very much consistent with the previous reports on the bilayer of buckled stanene and germanene *[65]*.

Nevertheless, we have studied adsorption behaviours of ORR intermediates on tri- and tetra-layers of platene. The calculated adsorption energy values (Table 4.4) are comparable on the three- and four-layered platene structures but the reaction intermediates are strongly adsorbed on the few-layered platene structures compared to that on platene (Table 4.2). Our calculated activation barriers for important ORR steps (Step 4.1, 4.2, 4.3 and 4.7) show that direct O_2 dissociation (Step 4.1) is favourable over layered platene structures compared to that on platene. However, other important steps such as *OH, *H_2O, and *OOH formation are not favourable on the three and four-layered platene structures. Besides, the activation barrier for the rate determining step (*O + *H → *OH) is considerably high over the layered platene structures. Overall ORR activation barriers are higher on the three and four-layered platene structure compared to that on platene. Furthermore, our results on few layers of platene are very much comparable with the previous reports on Pt(100) surface *[61, 66]*. Therefore, platene can be a selective and efficient catalyst over few-layered platene structures.

Table 4.4: Adsorption energies (in eV) of the reaction intermediates on three-layered and four-layered structures.

Species	**Three-layered**	**Four-layered**	**Previous reports on bulk Pt(100) surface**
*O_2	-1.08	-1.07	-1.10 *[61]*, -1.10 *[66]*
*O	-4.45	-4.42	-4.38 *[61]*, -4.03 *[66]*
*OH	-2.88	-2.88	-2.77 *[61]*, -2.78 *[66]*
*OOH	-1.31	-1.28	-1.30 *[61]*, -1.41 *[66]*
*H_2O	-0.25	-0.27	-0.25 *[61]*, -0.27 *[66]*
*H	-2.88	-2.91	-2.71 *[61]*, -2.87 *[66]*

Table 4.5: Reaction free energies (in eV) and activation barriers (in eV, parenthesis) on three-layered and four-layered structures

Elementary steps	**Three-layered**	**Four-layered**	**Previous reports on bulk Pt(100) surface**
$*O_2 \rightarrow *O + *O$	-1.29 (0.11)	-1.25 (0.09)	-1.28 (0.13) *[61]*, -1.20 (0.15) *[66]*
$*O_2 + *H \rightarrow *OOH$	0.55 (0.11)	0.56 (0.26)	0.28 (0.53) *[61]*, 0.26 (0.48) *[66]*
$*O + *H \rightarrow *OH$	-0.25 (0.44)	-0.29 (0.40)	-0.29 (0.42) *[61]*, -0.43 (0.36) *[66]*
$*OH + *H \rightarrow *H_2O$	-0.08 (0.36)	-0.07 (0.41)	0.16 (0.76) *[61]*, 0.06 (0.80) *[66]*

4.3.4. Effect of applied potential:

On the other hand, catalysts are exposed to electrical potential during the course of the reaction. Therefore, the effects of electrode potential on the reaction free energies and reduction mechanisms have been investigated as proposed by Nørskov and co-workers *[67]*. The reaction free energy (ΔG) is calculated as follows:

$$\Delta G = \Delta E + \Delta ZPE - T\Delta S - eU \tag{4.18}$$

where ΔE is the total energy change obtained from the DFT calculations, ΔZPE is the change in zero-point energy, T is 300 K, ΔS is the entropy change, e is the transferred charge for the elementary step and U is the electrode potential with respect to the standard hydrogen electrode.

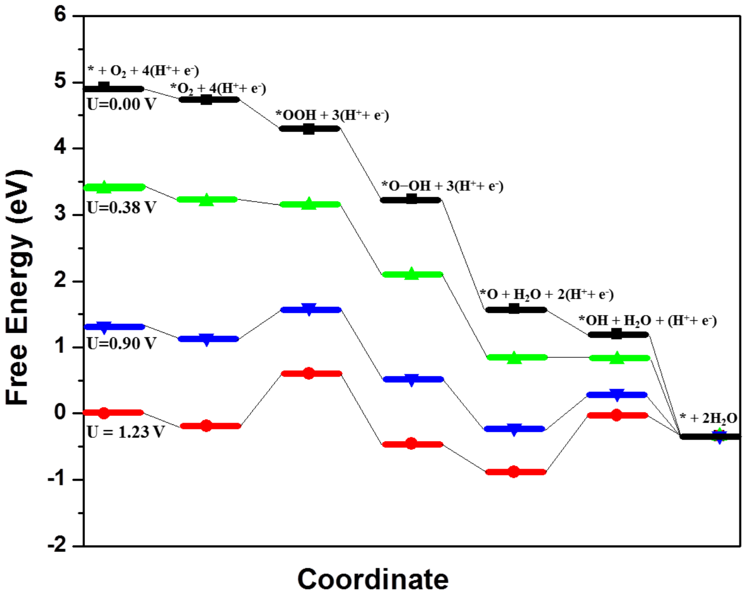

Figure 4.14: Free energy diagrams for ORR mechanism at different potentials

Figure 4.14 shows that all the elementary steps are downhill process at U = 0 V. However, the proton transfer steps are thermodynamically not favourable as we increase the potential. Our calculated reaction free energies show that the highest electrode potential under which all the elementary reactions are exergonic is 0.38 V. Thus, the working potential for platene is 0.38 V and above this potential, some of the elementary reactions are endergonic. The *OH formation (*O + *H → *OH) and *OOH formation steps (*O_2 + H^+ + e → *OOH) are not thermodynamically favourable at higher potentials (>0.38 V). However, the exergonicity of *H_2O formation step is not affected by the applied potential. Furthermore, we have calculated potential-dependent activation barrier [E(U)] according to the following equation:

$$E(U) = E(U^0) + \beta[\mu(*H) - \mu(*) - ½\,\mu(H_2(gas)) + e(U)] \tag{4.19}$$

where E (U^0) is the activation barrier at the equilibrium potential for the adsorption of a proton-electron pair on the surface (*). The quantity [μ(*H) - μ(*) - ½ μ(H_2(gas)], in turn, corresponds to the reaction free energy of hydrogen adsorption on platene surface and defines the equilibrium potential referred to above. β denotes a symmetry factor, which is similar with Brønsted-Evans-

Polanyi coefficient. In our study, the value of β is taken as 0.5. This value of β (0.5) has led to satisfactory results in modelling electrochemical ORR *[63-64]* and CO_2 reduction reaction[65]. This kind of model has been successfully proved in previous literatures for modelling the electrochemical environment of the reactions *[63-66]*. As direct $*O_2$ dissociation (Step 4.1) is not potential dependent, therefore we have calculated the values for *OOH and *OH formation (Step 4.2 & 3). Our calculated potential dependent activation barriers (Table 4.6) show that the activation barriers of these two protonation steps (Step 4.2 & 3) increase with the increase of applied potential. Interestingly, we find that $*O_2$ dissociation step ($*O_2 \rightarrow *O + *O$) remains as a rate determining step below ~0.4 V, whereas the protonation steps ($*O_2 + *H \rightarrow *OOH$, $*O + *H \rightarrow *OH$) becomes rate determining above the ~0.4 V. This is very much consistent with our potential dependent thermodynamic behaviour, where 0.38 V is found to be the maximum potential having all the elementary steps exergonic nature.

Table 4.6: Potential dependent activation barriers for *OOH and *OH formation.

Applied Potential (V)	**Activation Barrier (eV)**	
	$*O_2 + H^+ + e \rightarrow *OOH$	**$*O + H^+ + e \rightarrow *OH$**
0.0	-0.07	0.06
0.2	0.17	0.16
0.4	0.27	0.26
0.6	0.37	0.36
0.8	0.47	0.46
1.0	0.57	0.56

We have further considered the influence of water environment on the ORR process. We have included the solvation effects using the VASPsol code *[72-73]* to calculate the reaction free energies for all the elementary steps. This kind of implicit solvation model has been successfully implemented in previous studies and shows excellent consistency with experiment *[5, 74-75]*. The calculated reaction free energies in the gas phase and in solvent (water) are given in Table 4.7. The results indicate that the elementary steps become more thermodynamically favourable in the water medium. Therefore, the reaction kinetics will improve further in the presence of water.

Table 4.7: Reaction free energies of the elementary steps on platene for (a) gas and (b) solvation medium.

Steps	**Elementary Reactions**	**Platene**	
		ΔG(gas phase)	**ΔG(solvation)**
4.1	$*O_2 \rightarrow *O + *O$ (tilted)	-0.64	-0.67
4.2	$*O_2 + *H \rightarrow *OOH$	-0.44	-0.67
4.3	$*O + *H \rightarrow *OH$	-0.42	-0.59
4.4	$*OOH \rightarrow *O + *OH$	-1.06	-0.96
4.5	$*OOH + *H \rightarrow *H_2O_2$	-0.61	-0.62
4.6	$*H_2O_2 \rightarrow *OH + *OH$	-0.72	-0.78
4.7	$*OH + *H \rightarrow *H_2O$	-1.12	-1.20

Interestingly, we find that (110) faceted Pt-based ultrathin nanosheets have been synthesied and reported to be very effective in catalytic activity. Jia et al. *[76]* synthesized rhombic dodecahedral $PtCu_3$ alloy ultrathin nanosheets, which are exposed with high-energy (110) facets and their electrochemical characterizations showed that the nanosheets exhibit excellent electrocatalytic performance for formic acid oxidation and high antipoisoning activity in comparison with commercial Pt black and $PtCu_3$ alloy nanoparticles with (111) surfaces. Very recently, Chen et al. *[77]* synthesized cubic Pt–Sn alloy nanocrystals with (110) facets composed of 12 nanosheets, showing superior electrocatalytic activity towards methanol oxidation. Therefore, we believe that (110) faceted platinum monolayer is possible to synthesis and will be an excellent catalyst for ORR.

4.4. Conclusion

In conclusion, first-principles calculations are performed to understand the ORR activity on a free-standing Pt-ML, which has been named 'platene'. Platene has an orthorhombic buckled structure with (110) surface, which is different compared to the previously reported hexagonal platinum monolayer synthesized on a metal substrate. Energetic, thermal, dynamic and mechanical stabilities of platene are evaluated from the total energy, AIMD simulation, phonon dispersion and stress-strain relationship, respectively. Molecular dynamics simulations suggest that platene can withstand temperatures as high as 600 K without any structural reconstruction. Phonon dispersion shows that platene is dynamically stable. We find that an orbital mixing between in-plane σ-orbital and out-of-plane π-orbital helps in stabilizing the buckling pattern. Moreover, a significant (by 30°) orbital compatibility of the out-of-plane orbital helps towards the stability of the buckled structure. Reaction free energies and activation barriers are calculated for all the possible elementary steps of ORR on platene and compared with the singled-layered nanocage and previously reported bulk Pt(111) surfaces. After careful investigation on structural parameters of the adsorbed intermediates, we find that a unique adsorption behaviour of *O (at bridge site) on platene makes the *OH formation very much favourable compared to bulk Pt(111) surface. Our potential dependent study indicates that the ORR is thermodynamically favourable at 0.38 V and the *OH ($*O + *H \rightarrow *OH$) and *OOH ($*O_2 + *H \rightarrow *OOH$) formation step becomes thermodynamically unfavourable at higher potentials, which is very much consistent with our calculated potential dependent activation barriers, which show that the $*O_2$ dissociation step ($*O_2 \rightarrow *O + *O$) remains as a rate determining step below ~0.4 V, whereas the protonation steps ($*O_2 + *H \rightarrow *OOH$, $*O + *H \rightarrow *OH$) becomes rate determining above the ~0.4 V. Our kinetics analysis shows that platene is a very selective and efficient catalyst for H_2O formation over H_2O_2, and thus a promising catalyst for the fuel cell applications. Moreover, our solvation calculation shows that the reaction becomes thermodynamically more favorable in water medium and thus the reaction kinetics may further improve in the presence of water. Hence, we report that platene could be very promising catalysts for the efficient and selective reduction of O_2. Moreover, the recent experimental successes on (110) faceted nanosheets and our computational results can motivate experimentalists to synthesis (110) faceted platinum monolayer.

4.5. References

1. Calle-Vallejo F., Koper M. T. M., Bandarenka A. S. (2013), Tailoring the catalytic activity of electrodes with monolayer amounts of foreign metals, Chem. Soc. Rev., 42, 5210-5230. (DOI: 10.1039/C3CS60026B)

2. Watanabe M., Tryk D. A., Wakisaka M., Yano H., Uchida H. (2012), Overview of recent developments in oxygen reduction electrocatalysis, Electrochim. Acta, 84, 187-201. (DOI: 10.1016/j.electacta.2012.04.035)

3. Oezaslan M., Hasché F., Strasser P. (2013), Pt-Based Core–Shell Catalyst Architectures for Oxygen Fuel Cell Electrodes, J. Phys. Chem. Lett., 4, 3273-3291. (DOI: 10.1021/jz4014135)

4. Mazumder V., Chi M., More K. L., Sun S. (2010), Core/shell Pd/FePt nanoparticles as an active and durable catalyst for the oxygen reduction reaction, J. Am. Chem. Soc., 132, 7848-7849. (DOI: 10.1021/ja1024436)

5. Mahata A., Bhauriyal P., Rawat K. S., Pathak B. (2016), Pt3Ti (Ti19@ Pt60)-Based Cuboctahedral Core–Shell Nanocluster Favors a Direct over Indirect Oxygen Reduction Reaction, ACS Energy Lett., 1, 797-805. (DOI: 10.1021/acsenergylett.6b00385)

6. Zhang L., Roling L. T., Wang X., Vara M., Chi M., Liu J., Choi S., Park J., Herron J. A., Xie Z., Mavrikakis M., Xia Y. (2015), Platinum-based nanocages with subnanometer-thick walls and well-defined, controllable facets, Science, 349, 412-416. (DOI: 10.1126/science.aab0801)

7. Wang X., Figueroa-Cosme L., Yang X., Luo M., Liu J., Xie Z., Xia Y. (2016), Pt-Based Icosahedral Nanocages: Using a Combination of {111} Facets, Twin

Defects, and Ultrathin Walls to Greatly Enhance Their Activity toward Oxygen Reduction, Nano Lett., 16, 1467-1471. (DOI: 10.1021/acs.nanolett.5b05140)

8. Mahata A., Rawat K. S., Choudhuri I., Pathak B. (2016), Single-layered platinum nanocage: a highly selective and efficient catalyst for fuel cells, J. Mater. Chem. A, 4, 12756-12767. (DOI: 10.1039/C6TA03245A)

9. Dai L., Xue Y., Qu L., Choi H., Baek J. (2015), Metal-free catalysts for oxygen reduction reaction, Chem. Rev., 115, 4823-4892. (DOI: 10.1021/cr5003563)

10. Zhang P., Xiao B. B., Hou X. L., Zhu Y. F., Jiang Q. (2014), Layered SiC Sheets: A Potential Catalyst for Oxygen Reduction Reaction, Sci. Rep., 4, 3821. (doi:10.1038/srep03821)

11. Osada M., Sasaki T. (2012), Two-Dimensional Dielectric Nanosheets: Novel Nanoelectronics From Nanocrystal Building Blocks, Adv. Mater., 24, 210-228. (DOI: 10.1002/adma.201103241)

12. Perebeinos V. (2015), Metal dichalcogenides: Two dimensions and one photon, *Nat.* Nanotechnol., 10, 485-486. (DOI:10.1038/nnano.2015.104)

13. Zhang X., Zhang J., Zhao J., Pan B., Kong M., Chen J., Xie Y. (2012), Half-metallic ferromagnetism in synthetic Co_9Se_8 nanosheets with atomic thickness, J. Am. Chem. Soc., 134, 11908-11911. (DOI: 10.1021/ja3046603)

14. Song F., Hu X. (2014), Exfoliation of layered double hydroxides for enhanced oxygen evolution catalysis, Nat. Commun., 5, 4477. (DOI: 10.1038/ncomms5477)

15. Duan H., Yan N., Yu R., Chang C., Zhou G., Hu H., Rong H., Niu Z., Mao J., Asakura H., Tanaka T., Dyson P. J., Li J., Li Y. (2014), Ultrathin rhodium nanosheets, Nat. Commun., 5, 3093. (DOI: 0.1038/ncomms4093)

16. Kuttiyiel K. A., Sasaki K., Choi Y., Su D., Liu P., Adzic R. R. (2012), Bimetallic IrNi core platinum monolayer shell electrocatalysts for the oxygen reduction reaction, Energy Environ. Sci., 5, 5297-5304. (DOI: 10.1039/C1EE02067F)

17. Chen G., Kuttiyiel K. A., Su D., Li M., Wang C., Buceta D., Du C., Gao Y., Yin G., Sasaki K., Vukmirovic M. B., Adzic R. R. (2016), Oxygen reduction kinetics on Pt monolayer shell highly affected by the structure of bimetallic AuNi cores, Chem. Mater., 28, 5274-5281. (DOI: 10.1021/acs.chemmater.6b00500)

18. Saleem F., Zhang Z., Xu B., Xu X., He P., Wang X. (2013), Ultrathin Pt–Cu nanosheets and nanocones, J. Am. Chem. Soc., 135, 18304-18307. (DOI: 10.1021/ja4101968)

19. Zhang H. (2015), Ultrathin Two-Dimensional Nanomaterials, ACS Nano., 9, 9451-9469. (DOI: 10.1021/acsnano.5b05040)

20. Ling T., Wang J., Zhang H., Song S., Zhou Y., Zhao J., Du X. (2015), Freestanding ultrathin metallic nanosheets: materials, synthesis, and applications, Adv. Mater., 27, 5396-5402. (DOI: 10.1002/adma.201501403)

21. Zhang X., Lu Z., Yang Z. (2016), A comparison study of oxygen reduction on the supported Pt, Pd, Au monolayer on WC (0001), J. Power Sources., 321, 163-173. (DOI: 0.1016/j.jpowsour.2016.04.135)

22. Zhang Y., Hsieh Y., Volkov V., Su D., An W., Si R., Zhu Y., Liu P., Wang J. X., Adzic R. R. (2014), High Performance Pt Monolayer Catalysts Produced via Core-Catalyzed Coating in Ethanol, ACS Catal., 4,738-742. (DOI: 10.1021/cs401091u)

23. Yang L., Frauenheima T., Ganzb E. (2015), The new dimension of silver, Phys. Chem. Chem. Phys., 17, 19695-19699. (DOI: 10.1039/C5CP03465E)

24. Yang L., Dornfeld M., Frauenheima T., Ganzb E. (2015), Glitter in a 2D monolayer, Phys. Chem. Chem. Phys., 17, 26036-26042. (DOI: 10.1039/C5CP04222D)

25. Zhu F-F., Chen W-J., Xu Y., Gao C-L., Guan D-D., Liu C-H., Qian D., Zhang S-C., Jia J-F. (2015), Epitaxial growth of two-dimensional stanene, Nat. Mater., 14, 1020-1025. (DOI: 10.1038/nmat4384)

26. Blochl P. E. (1994), Projector augmented-wave method, Phy. Rev. B, 50, 17953. (DOI: 10.1103/PhysRevB.50.17953)

27. Kresse G., Hafner J. (1993), Ab initio molecular dynamics for liquid metals, Phy. Rev. B, 47, 558. (DOI: 10.1103/PhysRevB.47.558)

28. G Kresse., Hafner J. (1994), Ab initio molecular-dynamics simulation of the liquid-metal–amorphous-semiconductor transition in germanium, Phy. Rev. B, 49, 14251-14269. (DOI: 10.1103/PhysRevB.49.14251)

29. Kresse G., Joubert D. (1999), From ultrasoft pseudopotentials to the projector augmented-wave method, Phy. Rev. B, 59, 1758. (DOI: 10.1103/PhysRevB.59.17580)

30. Perdew J. P., Chevary J. A., Vosko S. H., Jackson K. A., Pederson M. R., Singh D. J., Fiolhais C. (1992), Atoms, molecules, solids, and surfaces: Applications of the generalized gradient approximation for exchange and correlation, Phy. Rev. B, 46, 6671. (DOI: 10.1103/PhysRevB.46.6671)

31. Grimme S., Antony J., Ehrlich S., Krieg S. (2010), A consistent and accurate ab initio parametrization of density functional dispersion correction (DFT-D) for the 94 elements H-Pu, J. Chem. Phys., 132, 154104. (DOI: 10.1063/1.3382344)

32. Henkelman G., Jonsson H. (2000) A climbing image nudged elastic band method for finding saddle points and minimum energy paths, J. Chem. Phys., 113, 9978-9985. (DOI: 10.1063/1.1329672)

33. Mahata A., Rawat K. S., Choudhuri I., Pathak B. (2016), Cuboctahedral vs. octahedral platinum nanoclusters: insights into the shape-dependent catalytic activity for fuel cell applications, Catal. Sci. Technol., 6, 7913-7923. (DOI: 10.1039/C6CY01709F)

34. Togo A., Oba F., Tanaka I. (2008), First-principles calculations of the ferroelastic transition between rutile-type and $CaCl_2$-type SiO_2 at high pressures,

Phys. Rev. B: Condens. Matter., 78, 134106. (DOI: 10.1103/PhysRevB.78.134106)

35. Baroni S., Giannozzi P., Testa A. (1987), Green's-function approach to linear response in solids, Phys. Rev. Lett., 58, 1861. (DOI: 10.1103/PhysRevLett.58.1861)

36. Zhang Z., Liu X., Yakobson B. I., Guo W. (2012), Two-dimensional tetragonal TiC monolayer sheet and nanoribbons, J. Am. Chem. Soc., 134, 19326-19329. (DOI: 10.1021/ja308576g)

37. Zhou J., Huang J., Sumpter B. G., Kent P. R. C., Xie Y., Terrones H., Smith S. C. (2014), Theoretical predictions of freestanding honeycomb sheets of cadmium chalcogenides, J. Phys. Chem. C., 118, 16236-16245. (DOI: 10.1021/jp504299e)

38. Choudhuri I., Kumar S., Mahata A., Rawat K. S., Pathak B. (2016),Transition-metal embedded carbon nitride monolayers: high-temperature ferromagnetism and half-metallicity, Nanoscale, 8, 14117-14126. (DOI: 10.1039/C6NR03282F)

39. Mahata A., Choudhuri I., Pathak B. (2015), A cuboctahedral platinum (Pt_{79}) nanocluster enclosed by well defined facets favours di-sigma adsorption and improves the reaction kinetics for methanol fuel cells, Nanoscale, 7, 13438-13451. (DOI: 10.1039/C5NR01575H)

40. Nose S. A. (1984), A unified formulation of the constant temperature molecular dynamics methods, J. Chem. Phys., 81, 511-519. (DOI: 10.1063/1.447334)

41. Zhang J., Gong X., Xu B., Xia Y., Yin J., Liu Z. (2014), Half-metallicity in graphitic C3N4 nanoribbons: An ab initio study, Phys. Status Solidi B., 251, 1386-1392. (DOI: 10.1002/pssb.201451110)

42. Zhang S., Zhou J., Wang Q., Chen X., Kawazoe Y., Jena P. (2015), Penta-graphene: A new carbon allotrope, Proc. Natl. Acad. Sci. U. S. A., 112, 2372-2377. (DOI: 10.1073/pnas.1416591112)

43. Mannix A. J., Zhou X., Kiraly B., Wood J. D., Alducin D., Myers B. D., Liu X., Fisher B. L., Santiago U., Guest J. R., Yacaman M. J., Ponce A., Oganov A. R., Hersam M. C., Guisinger N. P. (2015), Synthesis of borophenes: Anisotropic, two-dimensional boron polymorphs, Science., 350, 1513-1516. (DOI: 10.1126/science.aad1080)

44. Wang L., Kutana A., Zoua X., Yakobson B. I. (2015), Electro-mechanical anisotropy of phosphorene, Nanoscale., 7, 9746-9751. (DOI: 10.1039/C5NR00355E)

45. Lee C., Wei X., Kysar J. W., Hone J. (2008), Measurement of the elastic properties and intrinsic strength of monolayer graphene, Science., 321, 385-388. (DOI: 10.1126/science.1157996)

46. Tao L., Yangy C., Wu L., Han L., Song Y., Wang S., Lu P. (2016), Tension-induced mechanical properties of stanine, Modern Phys. Lett. B., 30, 1650146. (DOI: 10.1142/S0217984916501463)

47. Wei Q., Peng X. (2014), Superior mechanical flexibility of phosphorene and few-layer black phosphorus, App. Phys. Lett., 104, 251915. (DOI: 10.1063/1.4885215)

48. Wang H., Li Q., Gao Y., Miao F., Zhou X. F., Wan X. G. (2016), Strain effects on borophene: ideal strength, negative Possion's ratio and phonon instability, New J. Phys., 18, 073016. (DOI: 1367-2630/18/7/073016)

49. Escano M. C. S. (2015), First-principles calculations of the dissolution and coalescence properties of Pt nanoparticle ORR catalysts: The effect of nanoparticle shape, Nano Res., **8**, 1689-1697. (DOI: 10.1007/s12274-014-0670-1

50. Jeon T., Kim S., Pinna N., Sharma A., Park J., Lee S., Lee H. C., Kang S. W., Lee H. K., Lee H. H. (2016), Selective dissolution of surface nickel close to platinum in PtNi nanocatalyst toward oxygen reduction reaction, Chem. Mater., 28, 1879. (DOI: 10.1021/acs.chemmater.6b00103)

51. Ma Y., Balbuena P. B. (2008), Surface properties and dissolution trends of Pt3M alloys in the presence of adsorbates, J. Phys. Chem. C, 112, 14520-14528. (DOI: 10.1021/jp8046888)

52. Greeley J., Nørskov J. K. (2007), Electrochemical dissolution of surface alloys in acids: Thermodynamic trends from first-principles calculations, Electrochimica Acta, 52, 5829-5836. (DOI: 10.1016/j.electacta.2007.02.082)

53. Caballero G., Balbuena P. B. (2010), Dissolution-Resistant Core−Shell Materials for Acid Medium Oxygen Reduction Electrocatalysts, J. Phys. Chem. Lett**., 1,** 724-728. (DOI: 10.1021/jz1000165)

54. Xu Y., Yan B., Zhang H., Wang J., Xu G., Tang P., Duan W., Zhang S. (2013), Large-gap quantum spin hall insulators in tin films, Phys. Rev. Lett., 111, 136804. (DOI: 10.1103/PhysRevLett.111.136804)

55. Pathak B., Pandian S., Hosmane N., Jemmis E. D. (2006), Reversal of stability on metalation of pentagonal-bipyramidal (1-MB6H72-, 1-M-2-CB5H71-, and 1-M-2,4-C2B4H7) and icosahedral (1-MB11H122-, 1-M-2-CB10H121-, and 1-M-2,4-C2B9H12) boranes (M = Al, Ga, In, and Tl): Energetics of condensation and relationship to binuclear metallocenes, J. Am. Chem. Soc., 128, 10915-10922. (DOI: 10.1021/ja061399f)

56. Shameema O., Jemmis E. D. (2009), Relative stability of closo-closo, closo-nido, and nido-nido macropolyhedral boranes: The role of orbital compatibility, Chem. Asian J., 4, 1346 – 1353. (DOI: 10.1002/asia.200900153)

57. Shameema O., Jemmis E. D. **(**2008), Orbital compatibility in the condensation of polyhedral boranes, Angew. Chem. Int. Ed., 47, 5561 –5564. (DOI: 10.1002/ange.200801295)

58. Sha Y., Yu T. H., Merinov B. V., Shirvanian P., Goddard W. A. (2011), Oxygen hydration mechanism for the oxygen reduction reaction at Pt and Pd fuel cell catalysts, *J.* Phys. Chem. Lett., 2, 572-576. (DOI: 10.1021/jz101753e)

59. Farberow C. A., Godinez-Garcia A., Peng G. W., Perez-Robles J. F., Solorza-Feria O., Mavrikakis M. (2013), Mechanistic studies of oxygen reduction by hydrogen on PdAg(110), ACS Catal., 3, 1622-1632. (DOI: 10.1021/cs4002699)

60. Keith J. A., Jerkiewicz G., Jacob T. (2010), Theoretical investigations of the oxygen reduction reaction on Pt(111), ChemPhysChem, 11, 2779-2794. (DOI: 10.1002/cphc.201000286)

61. Li K., Li Y., Wang Y., He F., Jiao M., Tang H., Wu Z. (2015), The oxygen reduction reaction on Pt(111) and Pt(100) surfaces substituted by subsurface Cu: a theoretical perspective, J. Mater. Chem. A, 3, 11444-11452. (DOI: 10.1039/C5TA01017A)

62. Qi L., Qian X., Li J. (2008), Near neutrality of an oxygen molecule adsorbed on a Pt (111) surface, Phys. Rev. Lett., 101, 146101. (DOI: 10.1103/PhysRevLett.101.146101)

63. Duan Z., Wang G. (2011), A first principles study of oxygen reduction reaction on a Pt(111) surface modified by a subsurface transition metal M (M = Ni, Co, or Fe), Phys. Chem. Chem. Phys., 13, 20178-20187. (DOI: 10.1039/C1CP21687B)

64. Sha Y., Yu T. H., Liu Y., Merinov B. V., Goddard III W. A. (2010), Theoretical study of solvent effects on the platinum-catalyzed oxygen reduction reaction, J. Phys. Chem. Lett., 1, 856-861. (DOI: 10.1021/jz9003153)

65. Huang C., J Zhou., Wu H., Deng K., Jena P., Kan E. (2016), Quantum phase transition in germanene and stanene bilayer: From normal metal to topological insulator, J. Phys. Chem. Lett., 7, 1919-1924. (DOI: 10.1021/acs.jpclett.6b00651)

66. Duan Z., Wang G. (2013), Comparison of reaction energetics for oxygen reduction reactions on Pt(100), Pt(111), Pt/Ni(100), and Pt/Ni(111) Surfaces: A first-principles study, J. Phys. Chem. C, 117, 6284-6292. (DOI: 10.1021/jp400388v)

67. Nørskov J. K., Rossmeisl J., Logadottir A., Lindqvist L., Kitchin J. R., Bligaard T., Jonsson H. (2004), Origin of the overpotential for oxygen reduction at a fuel-cell cathode, J. Phys. Chem. B, 108, 17886-17892. (DOI: 10.1021/jp047349j)

68. Tripkovic V., Skulason E., Siahrostami S., Nørskov J. K., Rossmeisl J. (2010), The oxygen reduction reaction mechanism on Pt(1 1 1) from density functional theory calculations, Electrochimica Acta, 55, 7975-7981. (DOI: 10.1016/j.electacta.2010.02.056)

69. Li Y., Zhang S., Yu J., Wang Q., Sun Q., Jena P. (2015), A new C=C embedded porphyrin sheet with superior oxygen reduction performance, Nano Res., 8, 2901. (DOI: 10.1007/s12274-015-0795-x)

70. Nie X., Esopi M. R., Janik M. J., Asthagiri A. (2013), Selectivity of CO2 reduction on copper electrodes: the role of the kinetics of elementary steps, Angew. Chem. Int. Ed., 52, 2459-2462. (DOI: 10.1002/anie.201208320)

71. Clayborne A., Chun H., Rankin R. B., Greeley J. (2015), Elucidation of pathways for NO electroreduction on Pt(111) from first principles, Angew. Chem. Int. Ed., 54, 8255-8258. (DOI: 10.1002/anie.201502104)

72. Mathew K., Sundararaman R., Letchworth-Weaver K., Arias T. A. (2014), Implicit solvation model for density-functional study of nanocrystal surfaces and reaction pathways, J. Chem. Phys., 140, 084106. (DOI: 10.1063/1.4865107)

73. Fishman M., Zhuang H. L., Mathew K., Dirschka W., Hennig R. G. (2013),Accuracy of exchange-correlation functionals and effect of solvation on the surface energy of copper, Phys. Rev. B: Condens. Matter Mater. Phys., 87, 245402. (DOI: 10.1103/PhysRevB.87.245402)

74. Mahata A., Rai R. K., Choudhuri I., Singh S. K., Pathak B. (2014), Direct vs. indirect pathway for nitrobenzene reduction reaction on a Ni catalyst surface: a density functional study, Phys. Chem. Chem. Phys., 16, 26365-26374. (DOI: 10.1039/C4CP04355C)

75. Goodpaster J. D., Bell A. T., Head-Gordon M. (2016), Identification of possible pathways for C–C bond formation during electrochemical reduction of CO2: new theoretical insights from an improved electrochemical model, J. Phys. Chem. Lett., 7, 1471-1477. (DOI: 10.1021/acs.jpclett.6b00358)

76. Jia Y., Jiang Y., Zhang J., Zhang L., Chen Q., Xie Z., Zheng L. (2014), Unique excavated rhombic dodecahedral $PtCu_3$ alloy Nanocrystals constructed with ultrathin nanosheets of high-energy {110} facets, J. Am. Chem. Soc., 136, 3748-3751. (DOI: 10.1021/ja413209q)

77. Chen Q., Yang Y., Cao Z., Kuang Q., Du G., Jiang Y., Xie Z., Zheng L. (2016), Excavated cubic platinum–tin alloy nanocrystals constructed from ultrathin nanosheets with enhanced electrocatalytic activity, Angew. Chem., 128, 9167–9171. (DOI: 10.1002/ange.201602592)

Chapter 5

Cuboctahedral vs. Octahedral Platinum Nanoclusters: Insights into the Shape-dependent Catalytic Activity for Fuel Cell

5.1. Introduction

Proton exchange membrane (PEM) fuel cells are one of the most promising devices for clean energy due to their high efficiency, low operating temperature and zero emission *[1-4]*. ORR is the key reaction at the cathode, which controls the performance of a fuel cell. However, the slow reaction kinetics associated with the ORR remains one of the major limitations for commercialization of low-temperature fuel cells *[5-6]*. Besides, the high Pt loading in a state-of-the-art ORR electrocatalyst is also a topic of major concern *[7]*. These can be addressed either by reducing the Pt-loading of the catalyst or by changing the morphology of the platinum catalyst. In order to lower the Pt-loading, alloying Pt with other transition metals has been emerged as a good alternative for efficiency and stability of the catalyst. Such alloying with other metals leads to the formation of bi-metallic *[8-10]*, mixed alloy *[11-12]* and core-shell structures *[13-15]*. However, due to the dissolution of surface atoms and leaching of the active metal *[16]*, the durability of these catalysts is far from the scenario of commercialization. On the other hand, the catalytic activity of the Pt-based catalysts can be improved by changing the morphology; designing nanoparticles with desirable shapes. Apart from the different metal-based catalysts, the shape of the metal nanoparticle plays a very important role to maximize the specific activity of the catalyst *[17]*. Therefore, the shape-controlled synthesis of a nanocrystal with exposed active surface sites is a topic of current interest.

El-Sayad and co-workers *[18]* have given the breakthrough by synthesizing a series of shape-controlled colloidal platinum nanoparticles in the shapes of tetrahedral, cubic, irregular-prismatic, icosahedral and cuboctahedral structures. Later on, extensive studies have been performed for the synthesis of shape-controlled well-defined platinum nanocatalysts *[19-24]*. Sun and co-workers *[19]* have developed a very facile shape-controlled synthesis technique for platinum nanoparticles and they established a major effect on the ORR of the PEM fuel cell. Using the scanning electrochemical microscopy, Carlos et al. *[20]* reported that the hexagonal platinum nanoparticle with (111) and (100) facets exhibits an enhanced ORR activity while comparing with the spherical and cubic nanoparticles. The shape-controlled synthesis of the Pt_3Ni

nanoctahedra terminated with (111) facets improves the ORR activity by five-fold compared to the similar sized Pt_3Ni nanocube terminated with (100) facets *[21]*. Over the past few years, considerable progresses have been made on the area of shape-controlled synthesis as well as shape-dependent activity of platinum nanoparticles for ORR activity *[25-29]*. The shape of the catalyst is also very important for improving the product selectivity as reported for many organic reactions such as benzene hydrogenation *[30]*, pyrrole hydrogenation *[31]*, butene isomerization *[32]*, glucose oxidation *[33]*, formic acid oxidation *[34]*, and CO oxidation *[35]* reactions.

Despite the extensive experimental studies on the shape-dependent activity, there is a lack of understanding about the dissimilar catalytic activities of different shaped NCs toward a particular reaction. To the best of our knowledge, there are no reports on the ORR reduction on a well-defined NC-based catalyst. Therefore, it is necessary to model NCs of different shapes surrounded by well-defined facets to understand their catalytic activities toward ORR. Here, we have modeled two NCs of similar size in the shapes of cuboctahedral (Pt_{79}) and octahedral (Pt_{85}) geometries and surrounded by well-defined facets. The cuboctahedral and octahedral NCs (Figure 5.1) are considered for our study as these shapes are often realized experimentally *[36, 37]*. Besides, Pt(111) and Pt(100) are the highly exposed surfaces in the experimentally synthesized Pt-nanoclusters *[38, 39]*.

ORR involves many-electron reduction reaction and it can proceed either through a more efficient four-step, four-electron reduction with the formation of H_2O or via a two-step, two-electron reduction for the formation of H_2O_2 *[40]*. However, the four-electron reduction ($4e^-$) is preferred over two-electron ($2e^-$) reduction in order to maximize the efficiency. Besides, H_2O_2 formation affects the durability of the membrane of a PEM fuel cell *[41]*. Thereby, the product selectivity (H_2O vs. H_2O_2) is very important for the performance of a fuel cell. Therefore, a systematic study based on the reaction free energy and activation barriers of all the possible elementary steps is done to understand the shape dependent catalytic properties of the NCs. For comparisons, our results are compared with the available theoretical and experimental data on the bulk Pt(111) surface. Kinetic analysis is performed to gain more insights into the rate of reaction and product selectivity (H_2O vs. H_2O_2). Therefore, in the present investigation, we have demonstrated an atomic level understanding toward the shape-dependent catalyst durability, catalytic activity, and product selectivity of the platinum nanocatalysts toward ORR. This study will certainly provide a significant insight into the designing of an efficient catalyst for fuel cell applications.

5.2. Model and Computational Details

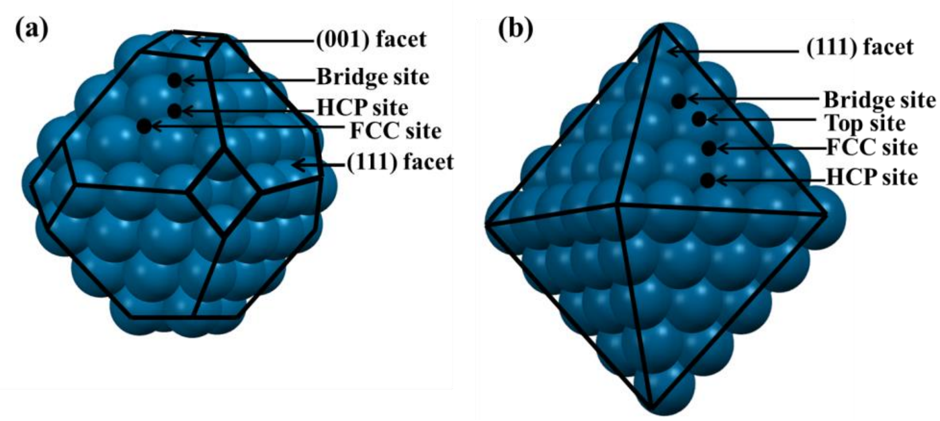

Figure 5.1: (a) Cuboctahedral NC (Pt_{79}) with eight (111) and six (001) facets, and (b) Octahedral NC (Pt_{85}) with eight (111) facets.

Cuboctahedral and octahedral Pt NCs are synthesized with majorly exposed (111), (002) and/or (200) facets *[38, 39]*. Therefore, we have modeled two NCs of ~1.5 nm in the shape of cuboctahedral (Pt_{79}) and octahedral (Pt_{85}) geometry. The cuboctahedral Pt_{79} NC (Figure 5.1a) is modeled with eight (111) and six (001) facets, whereas the octahedral Pt_{85} NC (Figure 5.1b) is modeled with eight (111) facets. Previous experimental and theoretical reports show that Pt(111) surface shows better ORR activity than Pt(100) or any other Pt-surfaces *[9,42-49]*. In fact the specific activity of Pt(111) surface reported to be two times higher than the Pt(100) surface *[9]*. Further, the sequence of ORR activity on Pt surface reported to be in the following order: (100) < (110) < (111) *[42, 46-47]*. More importantly, the ORR activity is highest even on the (111) facet of Pt alloy based catalysts *[43-45]*. Therefore, inspired by all these findings, we have chosen the (111) facet for studying ORR reaction mechanism.

The first-principles calculations are performed using a projector augmented wave (PAW) *[50]* method as implemented in the Vienna Ab initio Simulation Package (VASP) *[51-53]*. The exchange-correlation potential is described by using the generalized gradient approximation of Perdew-Burke-Ernzerhof (GGA-PBE) *[54]*. Plane wave with a kinetic energy cut off of 470 eV is used to expand the electronic wave functions. A 25 × 25 × 25 $Å^3$ cubic supercell is used to optimize the metal clusters to rule out the possibility of interactions between the periodically repeated metal clusters. The Brillouin zone is sampled with a Gamma point (1×1×1) for clusters. The total energy of the Pt_{79} and Pt_{85} cluster are improved by 0.001 and 0.002 eV, respectively if the k-point mesh set to 2 × 2 × 2. Therefore, we have used Gamma point for all the calculations to save the computational cost. All the atoms are relaxed for the full structural relaxation. The bulk Pt(111) is modeled with a (2 × 2) supercell to minimize the lateral interactions between the repeating images. The metal slab is composed of five atomic layers, where the bottom three layers are fixed and the top two layers are relaxed. A 12 Å of vacuum is used along the z-direction to avoid any periodic interactions. The Brillouin zone is sampled using a 3 × 3 × 1 k-point grid for the surface calculations. All the systems are fully optimized, where the convergence criteria for total energy and forces are set at 10^{-4} eV and <0.02 eV/Å, respectively. Spin-polarized calculations are performed for all the molecular species and oxygen adsorbed intermediates. We have included Grimme's D3-type *[55]* of semiempirical method to include the dispersion energy corrections for van der Waals interactions. The climbing nudged elastic band (CI-NEB) method *[56]* is used to locate the transition state. Six intermediate images are used in each CI-NEB pathway. Vibrational frequencies for the initial, transition and final states of the reaction are calculated and the transition states are confirmed by the presence of one imaginary frequency. Zero-point energy (ZPE) is calculated using the following equation:

$$\mathrm{ZPE} = \sum_i 1/2 h\upsilon_i \tag{5.1}$$

where h is the Planck's constant and υ_i is the frequency of the i^{th} vibrational mode. In this work, we employ same methodologies for the energies (free energy and adsorption energy) and activation barrier calculations as in reference *[48-49]*.

5.3. Results and Discussion

We have divided this section into three parts. In the first part, we have investigated the energetic stability, thermal stability, dissolution nature, and coalescence behavior of the NCs. Then, the adsorption behaviors of the ORR intermediates on the (111) facet of the NCs are studied and compared with previous theoretical and experimental reports over the bulk Pt(111) surfaces. The catalytic activities are compared with the previously reported bulk Pt(111) based catalysts, as there are no reports (on full ORR mechanism) on a well-defined platinum NC. Furthermore, all possible ORR mechanisms are studied followed by an attempt which is made to find out the role of the shape towards the ORR activity. Finally, kinetic analysis has been performed to explore the efficiency and selectivity of the NCs toward four-electron vs. two-electron reduction.

5.3.1 Stability of the NCs:

The stability of the NCs is very important for their synthesis and practical usages. Cohesive and formation energy calculations are performed to evaluate the thermodynamic stability of the NCs. For comparisons, we have calculated cohesive energies for the bulk Pt(111) and face centered cubic (fcc) Pt. The calculated cohesive energies are -4.87, -4.91, -5.47 and -5.71 eV/atom for the cuboctahedral, octahedral, bulk Pt(111) and fcc platinum structures, respectively. Our calculated cohesive energy value of the bulk platinum is very much in agreement with the experimental value of -5.84 eV/atom *[57]*. Further, the formation energies *[58-61]* are calculated and the calculated formation energies are 0.82, 0.78 and 0.23 eV/atom for the cuboctahedral, octahedral and bulk Pt(111) respectively. The negative cohesive energy values indicate that the NCs are thermodynamically stable and the formation energy values predict that the NCs are separated by low energy differences.

The thermal stability of the NCs is verified by carrying out Ab Initio Molecular Dynamics Simulations (AIMD) using canonical ensemble at 300-500 K with a time step of 1 femtosecond. Temperature control is achieved by nóse thermostat model *[62]*. First, the structure is heated at 300 K with a time step of 1 femtosecond (fs) for 20 picoseconds (ps). In case of cuboctahedral NC, no structure reconstruction is found after the simulation, whereas the edge atoms are moving inwards for the octahedral NC. We have carefully investigated the structure of the NCs during the AIMD simulation at 300 K. We find that the diameter of the cuboctahedral (11.31 Å) decreases to 11.16 Å and the diameter of the octahedral (14.85 Å) NC decreases to 14.54 Å. The fluctuation of the total energy of cuboctahedral NC is smooth throughout the AIMD simulations (Figure 5.2a). Hence, the structure remains stable at room temperature. In contrary, the fluctuation of total energy is very high for octahedral NC (Figure 5.2c). Therefore, the total energy fluctuation can be related to the changes in the diameter of the NCs. Further, simulations using an NVT ensemble at 400 and 500 K with a time step of 1 fs are carried for 20 ps. We have plotted the root mean square displacement (RMSD) as a function of time step (Figure 5.2b and 5.2d) for all the cases. Our RMSD plots show that atomic displacements of cuboctahedral are negligible throughout the temperature ranges (300-500 K). The snapshots of atomic configurations of NCs at the end of MD simulations are shown in Figure 5.3. We did not find any structural reconstruction of cuboctahedral NC even after heating at 500 K for 20 ps. These results demonstrate that the NCs are separated by high-energy barriers from other local minima structures and they are stable in the fuel cell operating temperatures.

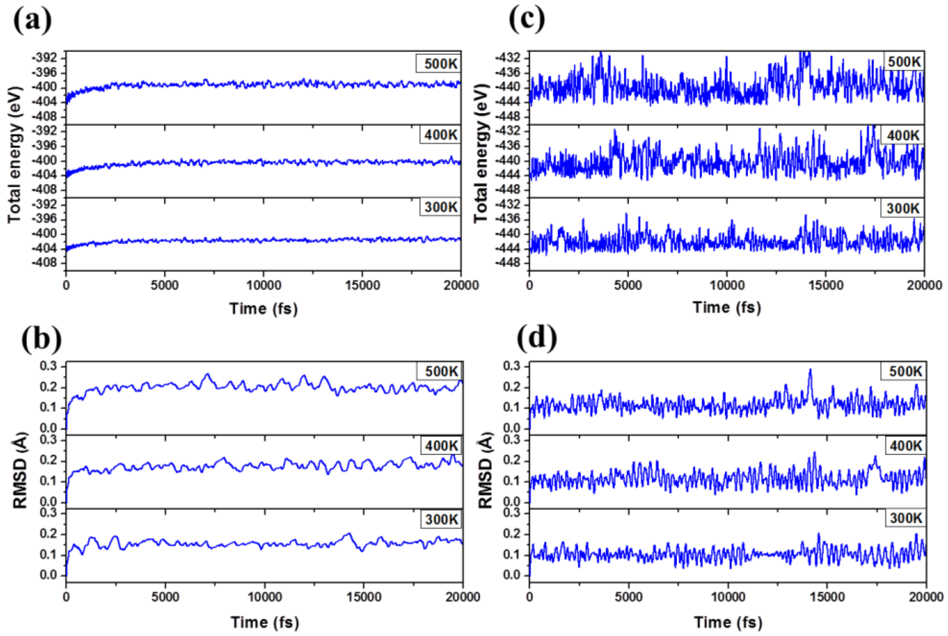

Figure 5.2: Molecular dynamics simulation analysis at different temperatures as a function of time step: (a-b) Cuboctahedral NC and (c-d) Octahedral NC.

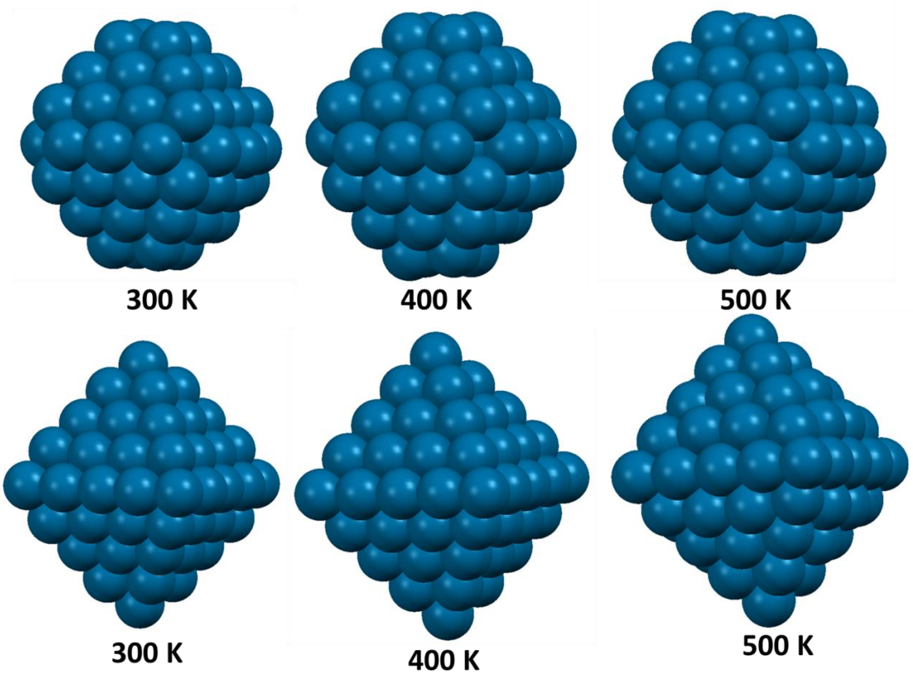

Figure 5.3: Snapshots of the NCs after the simulation at different temperatures.

Apart from the energetic and thermal stability of the NC, the dissolution of surface atoms of the nanoparticle is also a very important criterion to describe the electrochemical stability of the catalyst *[63-64]*. Catalysts of different shapes are different in terms of the extent of unsaturation and hence toward dissolution. Therefore, nanoparticles with different shapes possess different extent of resistant toward dissolution in a fuel cell. It is well accepted that the electrochemical oxidation of Pt ($Pt \rightarrow Pt^{2+} + 2e^-$) is the main phenomenon behind the dissolution *[65-67]*. We have compared the dissolution behavior of the NCs with respect to the bulk Pt(111). As the surrounding environment i.e. the presence of oxygen largely influences the dissolution, the calculations are carried out in the presence of O-atom. Such model has been used for calculating the shift in dissolution potential *[63, 65-67]*. Here, the shift (ΔU) in the electrode potential is calculated with respect to bulk Pt(111) using the following equation

$$\Delta U = U_{NC} - U_{Pt(111)} = (\mu_{Pt-Pt(111)} - \mu_{Pt-NC})/(ne) \tag{5.2}$$

where U_{NC}, $U_{Pt(111)}$, μ_{Pt-NC}, $\mu_{Pt-Pt(111)}$ and n are the electrode potential of the NC, electrode potential of the bulk Pt(111), chemical potential of platinum metal of the NC, chemical potential of platinum metal of the bulk Pt(111) and number of electron transferred during the dissolution reaction ($Pt \rightarrow Pt^{2+} + 2e^-$), respectively. The negative ΔU value for NC represents that the dissolution of the NC is faster than the bulk Pt(111). The detailed discussion for deriving the dissolution potential limit has been provided below. Dissolution of Pt into the solution proceeds through the following equation

$$Pt \rightarrow Pt^{2+} + 2e^- \tag{5.3}$$

When the dissolution of Pt is referenced to the standard hydrogen electrode (SHE) reaction, the equation (5.3) can be written as

$$Pt^{n+} + n/2\, H_2 \rightarrow Pt + nH^+ \tag{5.4}$$

The Gibbs free energy (ΔG) for this reaction can be written as

$$\Delta G = -neU \tag{5.5}$$

where, U is the electrode potential of Pt vs. SHE. Here, n = 2 for the equation (5.5). Now, considering the platinum in the catalyst and platinum in the solution are in equilibrium, the above equation can be expressed for the NCs as

$$-neU_{NC} = \mu_{Pt-NC} + \mu_{nH^+} - \mu_{Pt^{n+}} - \mu_{n/2H_2} \quad (5.6)$$

where μ_{Pt-NC}, $\mu_{Pt-NC^{n+}}$, μ_{nH^+} and $\mu_{n/2H_2}$ are the chemical potentials of platinum metal, dissolved platinum ions, H^+ and H_2, respectively.

Similarly, the electrode potential ($U_{Pt(111)}$) of platinum in bulk Pt(111) can be related with the chemical potentials using the following equation

$$-neU_{Pt(111)} = \mu_{Pt-Pt(111)} + \mu_{nH^+} - \mu_{Pt^{n+}} - \mu_{n/2H_2} \quad (5.7)$$

Therefore, the shift of electrode potential (ΔU) of platinum of NCs with respect to the bulk Pt(111) can be written as

$$U_{NC} - U_{Pt(111)} = \Delta U = (\mu_{Pt-Pt(111)} - \mu_{Pt-NC})/(ne) \quad (5.8)$$

Now, the chemical potentials of the metal can be defined as

$$\mu_{Pt} = \frac{\partial A}{\partial N} \approx \frac{\partial E}{\partial N} \quad (5.9)$$

where A, E and N are the total free energy, total energy and changes in number of platinum atoms, respectively. The total free energy can be approximated to total energy because the entropic contributions rules out while calculating the chemical potential difference between the metals.

The dissolution of the platinum has been considered by removing one platinum atom from the surface of the catalysts. Hence, the chemical potential of the equation (5.9) is calculated by considering the defected NCs and bulk Pt(111). The chemical potential is obtained by calculating the total energies of the optimized structures (E_{Pt}) and defected structures ($E_{Pt\text{-}def}$).

Therefore, from the equation (5.9), we can get $\mu_{Pt} = (E_{Pt\text{-}def} - E_{Pt})$

The value of N=1 as only one atom is removed for the calculation.

As the surrounding environment i.e. the presence of oxygen largely influences the dissolution, the calculation is carried out in the presence of O-atom.

Therefore, $\mu_{Pt} = (E_{Pt\text{-}def\_O} - E_{Pt\_O})$ (5.10)

We have calculated the chemical potential of platinum for the facet, edge and vertex atoms on both the NCs and for the bulk Pt(111).

The atoms, which are removed for the consideration of dissolution behavior at the different sites of the NCs and for bulk Pt(111), have been shown in Figure 5.4 to 5.6.

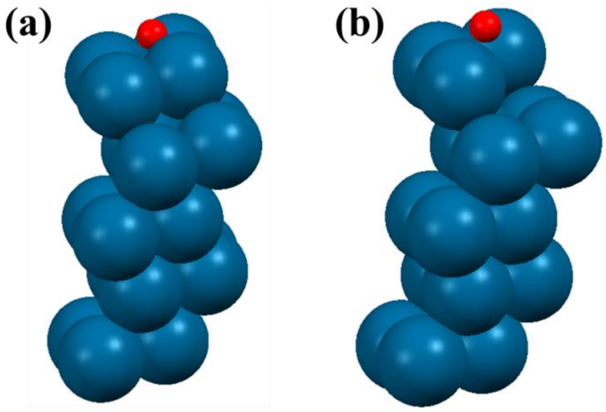

Figure 5.4: The bulk Pt(111) in (a) pure and (b) defected form.

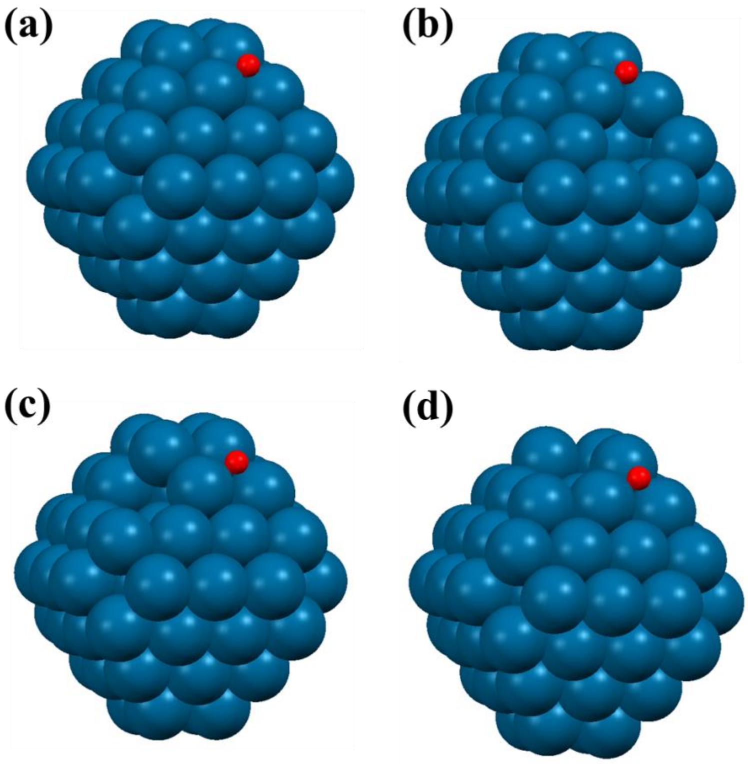

Figure 5.5: The cuboctahedral NC in (a) pure and (b-d) defected forms; (b) at the facet, (c) at the edge and (d) at the vertex.

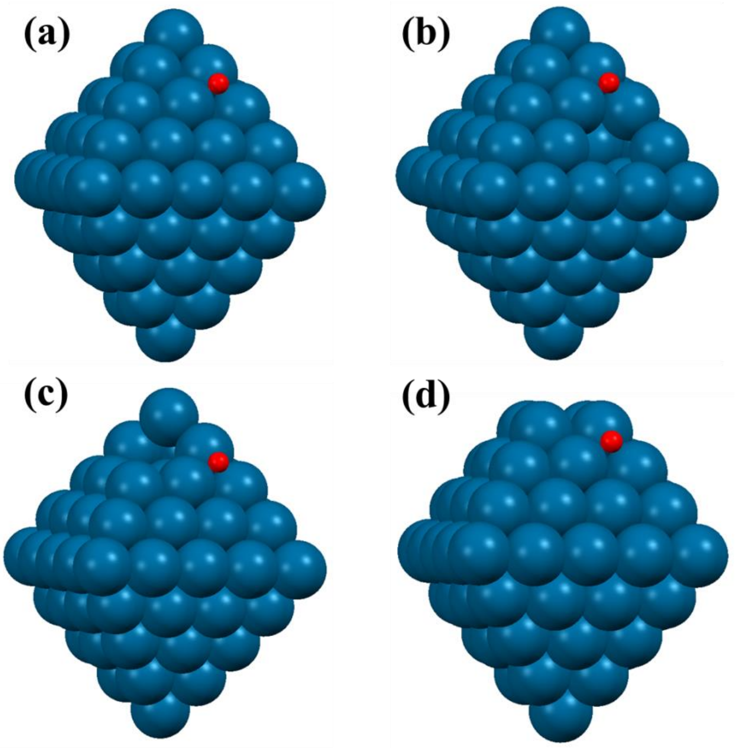

Figure 5.6: The octahedral NC in (a) pure and (b-d) defected forms; (b) at the facet, (c) at the edge and (d) at the vertex.

We have calculated the shift in the electrode potential of the facet, edge and vertex atoms of the NCs (Figure 5.5-5.6). Our results show that the vertex atoms are most prone to dissolution, followed by edge and facet atoms for both the NCs (Figure 5.7). Vertex atoms possess highest unsaturation that causes them to dissolve fast. We find that the facet atoms of the octahedral NC are more stable than that of the cuboctahedral one from dissolution. Interestingly, edge and vertex atoms of the cuboctahedral NC are more stable than the edge and vertex atoms of the octahedral NC. Moreover, we have calculated the dissolution potential in the presence of *OH and *OOH. Our results (Figure 5.8 & 5.9) show that the extent of dissolution is highest in the oxygen environment and least in the OOH environment. This is due to the strong adsorption nature of *O, which destabilizes the NC more than when *OOH is adsorbed. However, the trend of the shift of dissolution potential is similar for vertex, edge and facet sites irrespective of the reaction environment. Therefore, the electrochemical stability of the cuboctahedral structure is better than the octahedral one. Hiroaki et al. *[68]* concluded that the dissolution of the nanoparticle starts from the terrace atoms instead of edge atoms of a cubic platinum nanoparticle. Recently, Ruttala et al. *[69]* found that the Pt-cuboctahedra is more stable than the Pt-nanocube due to the higher dissolution rate of the (100) facet than the (111) facet. Therefore, our results are very much in consistent with previous reports.

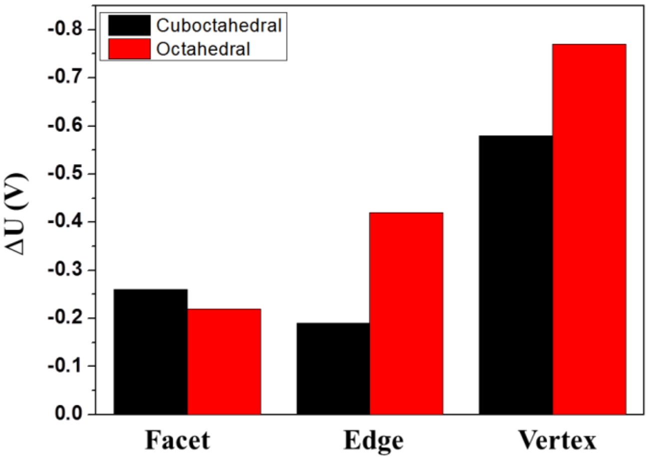

Figure 5.7: The shift in electrode potential of the atoms of the NCs at different sites (facet, edge and vertex) with respect to the bulk Pt(111) in the O environment.

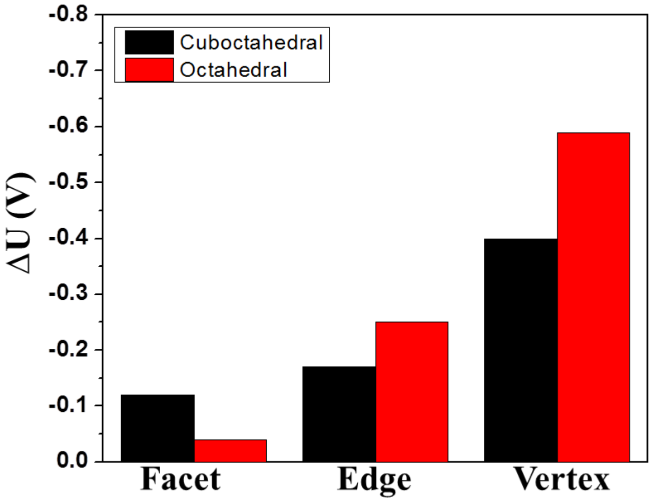

Figure 5.8: The shift in electrode potential of the atoms of the NCs at different sites (facet, edge and vertex) with respect to the bulk Pt(111) in the OH environment.

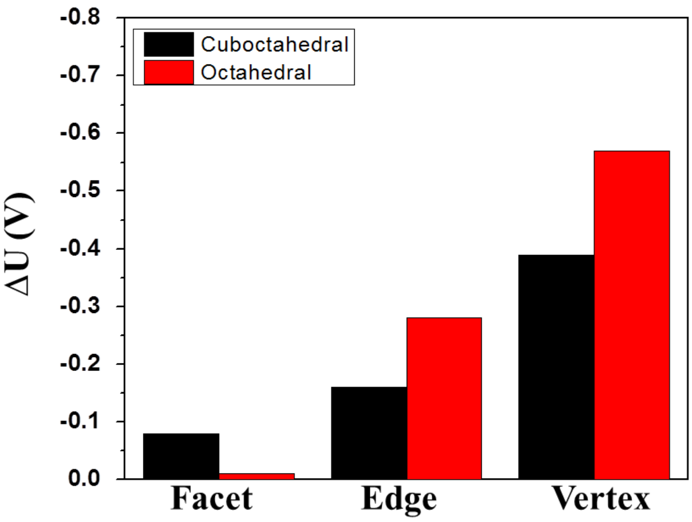

Figure 5.9: The shift in electrode potential of the atoms of the NCs at different sites (facet, edge and vertex) with respect to the bulk Pt(111) in the OOH environment.

5.3.2 ORR Mechanism

5.3.2.1 Adsorption

Four different catalytic sites (Figure 5.1) are present on the Pt(111) facet of the NCs: (i) top, (ii) bridge, (iii) face centered cubic (fcc) and (iv) hexagonal close packed (hcp). The most preferred binding sites of the intermediate species and their respective binding energies are given in Table 5.1. For comparison, we have calculated adsorption energies of the intermediate species on the bulk Pt(111). We find that the preferred binding sites are same for all the adsorbates on the NCs and bulk Pt(111). It is interesting to find that the $*O_2$ and *O bind very strongly on the (111) facet of the NCs than on the bulk Pt(111), whereas the hydrogenated intermediates (*OH and *OOH) and products ($*H_2O$ and $*H_2O_2$) have comparable binding energy on the NCs and bulk Pt(111). Moreover, $*O_2$, *O and *OH bind very strongly on the cuboctahral NC surface than on the octahedral NC. However, the adsorption energy of $*H_2O$ and $*H_2O_2$ are comparable on both the NCs. The adsorption behaviors of the intermediates have been shown in Figure 5.10.

Table 5.1: Preferred binding sites, binding energies (eV) of the most stable ORR intermediate species on the (111) facet of the NCs and bulk Pt(111) surface. Here t, b, and f denote top, bridge, and fcc sites, respectively.

Adsorbed Species	**Octahedral (Pt_{85})**	**Cuboctaheral (Pt_{79})**	**Pt(111)**
$*O_2$	-1.43 (b)	-1.56 (b)	-0.79 (b)
*O	-4.90 (f)	-5.19 (f)	-4.54 (f)
*OH	-2.38 (t)	-2.49 (t)	-2.40 (t)
*OOH	-1.38 (b)	-1.40 (b)	-1.22 (b)
$*H_2O_2$	-0.31 (b)	-0.34 (b)	-0.34 (b)
$*H_2O$	-0.21 (t)	-0.23 (t)	-0.26 (t)
*H	-2.76 (f)	-2.80 (f)	-2.80 (f)

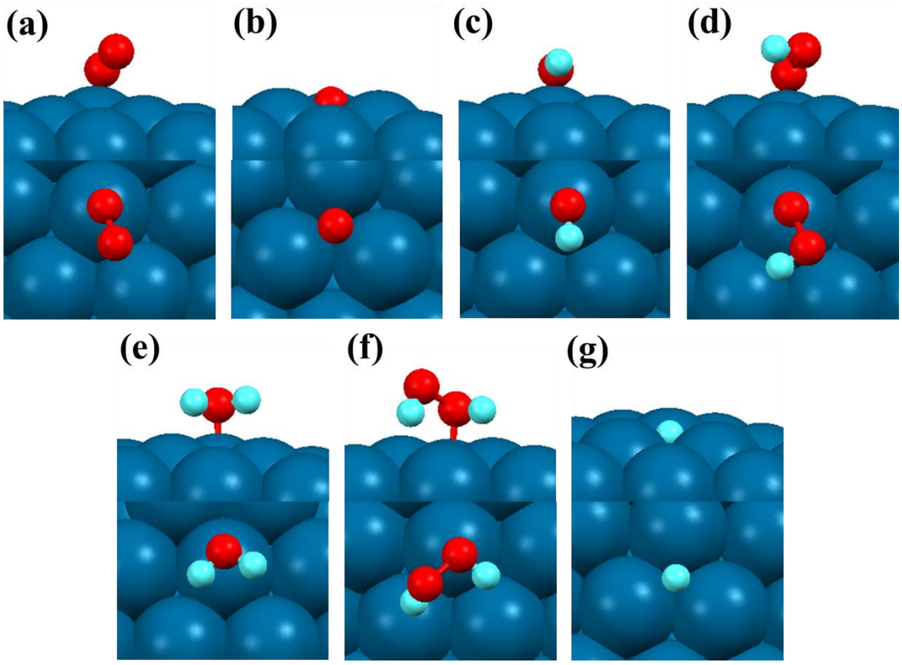

Figure 5.10: Adsorption sites of the most stable adsorbates on the (111) facet of the cuboctahedral NC; (a) $*O_2$, (b) *O, (c) *OH, (d) *OOH, (e) $*H_2O$, (f) $*H_2O_2$ and (g) *H. The most preferred adsorption sites are same on the (111) facet of the octahedral NC.

5.3.2.2 Reaction Mechanism

During ORR, H_2O and H_2O_2 are the two end products, which are formed via four-electron ($4e^-$) and two-electron ($2e^-$) reduction reactions, respectively. We have considered two important pathways for O_2 dissociation: (i) direct and (ii) indirect pathways *[48-49]*. In case of direct pathway, O-O bond dissociation is favored over hydrogenation, whereas in case of indirect pathway, hydrogenation is preferred over O-O bond dissociation *[48-49]*. Further, the product selectivity (H_2O vs. H_2O_2) can be related to the direct vs. indirect mechanism.

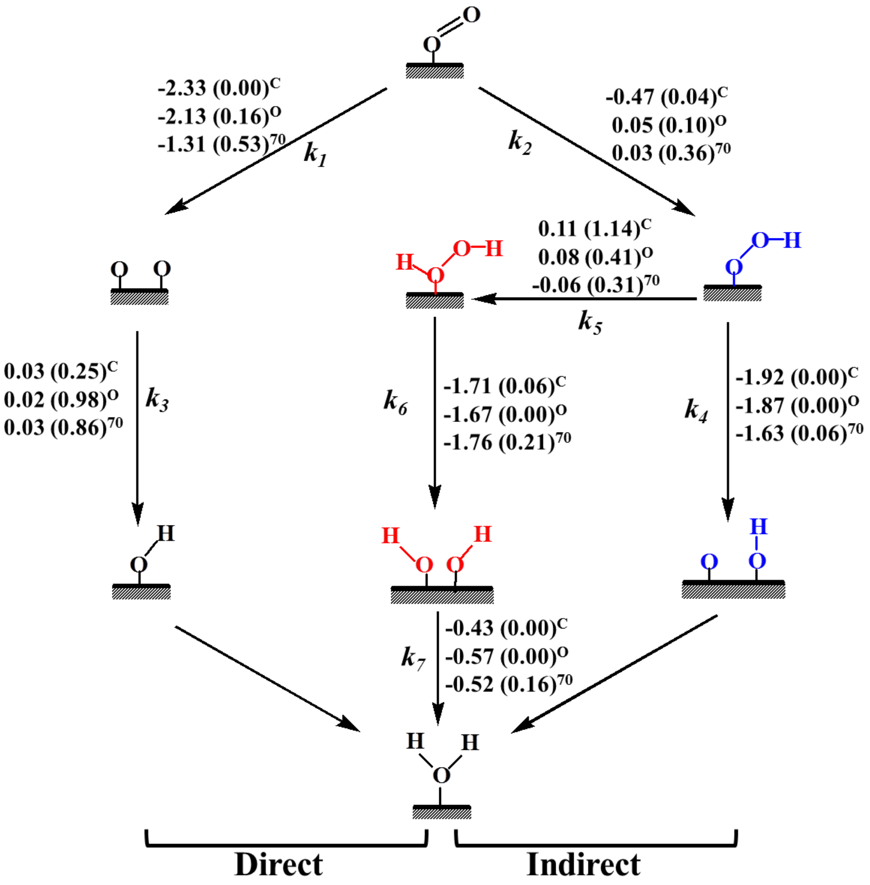

Scheme 5.1: Reaction free energies (eV) and activation barriers (eV, in parenthesis) are presented for all the possible elementary steps of ORR over (111) facet of the NCs, where C and O represent for the cuboctahedral and octahedral NCs, respectively. Our calculated respective values are compared with the previous reports on the bulk Pt(111) *[70]*.

O_2 activation:

Direct O-O bond dissociation via $4e^-$ reduction is a very important step for the fuel cell applications as it leads to the formation of H_2O. Moreover, direct dissociation reduces the possibility of unwanted by-products formation. Previous studies on bulk metal surfaces (Pt, Pd and Ag) show that direct O-O bond dissociation (step 5.1) is not kinetically favored over hydrogenation (step 5.2) *[71-72]*. Thus, the $*O_2$ can be dissociated into atomic oxygen (*O) or can be hydrogenated to *OOH.

Table 5.2: Reaction free energies (ΔG in eV) and activation barriers ($\Delta G^\ddagger$ in eV) for the all-possible elementary reactions on the (111) facet of the cuboctahedral and octahedral NCs.

Steps	**Elementary Reactions**	**Cuboctahedral**		**Octahedral**	
		ΔG	$\mathbf{\Delta G^\ddagger}$	**ΔG**	$\mathbf{\Delta G^\ddagger}$
5.1	$*O_2 \rightarrow *O + *O$	-2.33	0.00	-2.13	0.16
5.2	$*O_2 + *H \rightarrow *OOH$	-0.47	0.04	0.05	0.10
5.3	$*O + *H \rightarrow *OH$	0.03	0.25	0.02	0.98
5.4	$*OOH \rightarrow *O + *OH$	-1.92	0.00	-1.87	0.00
5.5	$*OOH + *H \rightarrow *H_2O_2$	0.11	1.14	0.08	0.41
5.6	$*H_2O_2 \rightarrow *OH + *OH$	-1.71	0.06	-1.67	0.00
5.7	$*OH + *H \rightarrow *H_2O$	-0.43	0.00	-0.57	0.00

The direct $*O_2$ bond dissociation is a barrierless process with reaction free energy of -2.33 eV on the (111) facet of the cuboctahedral NC. However, the activation barrier is 0.16 eV with a reaction free energy of -2.13 eV on the (111) facet of the octahedral NC. Paul et al. *[73]* also reported that the O-O bond dissociation is a barrierless process over the Pt_{79} NC. The previously calculated O-O bond dissociation barriers are 0.53 eV *[58]*, 0.45 eV *[73]* and 0.44 eV *[59]* on the bulk Pt(111); 0.72 eV and 1.22 eV on the bulk Pd(111) *[59]* and Ag(111) *[73]* surfaces, respectively. Therefore, the NCs show superior activity towards direct O_2 dissociation over the bulk surfaces. Moreover, the octahedral NC requires 0.16 eV of more energy for the direct

O-O dissociation than the cuboctahedral NC. Therefore, the shape of the catalyst influences the activation of O-O bond. In fact, the *O-O bond distances in the cuboctahedral and octahedral NCs are 1.29 and 1.27 Å, which indicate that the activation of $*O_2$ is favored on the cuboctahedral (111) facet. The vibrational frequencies of the *O-O bond while adsorbed on the cuboctahedral and octahedral facets are 1200 and 1266 cm^{-1}, respectively, which also support our finding.

Similarly, O_2 hydrogenation (step 5.2) on the cuboctahedral NC is exergonic (-0.47 eV) with an activation barrier of 0.04 eV, whereas the O_2 hydrogenation is an uphill process (0.05 eV) with an activation barrier of 0.10 eV on the octahedral NC. The previous reported barriers for O_2 hydrogenation (step 5.2) are 0.25 *[75]*, 0.36 *[70]* and 0.30 eV *[71]* on the bulk Pt(111).

Interestingly, we find that the direct O_2 bond dissociation is slightly favorable (thermodynamically and kinetically) on the (111) facet of the cuboctahedral NC over the O_2 hydrogenation step. However, the octahedral NC shows a different catalytic trend, though both the steps (steps 5.1-5.2) are very much comparable. Previous studies reported that O_2 hydrogenation is more favorable over direct O_2 bond dissociation on the Pt(111), Pd(111) and Ag(111) surfaces. Therefore, the octahedral NC shows a similar trend in ORR activity like other bulk (111) surfaces. Moreover, the octahedral NC favors *OOH formation, which increases the possibility of H_2O_2 formation.

***OH formation:**

The *OH formation is another important step for ORR and this step is reported to be a rate determining step of ORR on bulk Pt(111) *[70-71,74]*. The direct O-O bond dissociation leads to the formation of *O, which subsequently undergoes hydrogenation for the formation of *OH (step 5.3). The formation of *OH (step 5.3) on the octahedral NC is slightly endergonic (0.02 eV) with an activation barrier of 0.98 eV. However, the *OH formation step requires a lower activation barrier (0.25 eV) on the cuboctahedral NC. Previous studies reported activation barriers of 0.74 *[71]* and 0.86 eV *[70]* on the bulk Pt(111) and 0.72 eV on the Pd(111) surfaces *[72]*. Therefore, the *OH formation is very much favorable on the cuboctahedral NC surface than on the octahedral

NC and bulk Pt(111) surfaces. The lower barrier for the *OH formation on the cuboctahedral NC surface is might be due to the strong adsorption of *OH on the cuboctahedral NC surface (-2.49 eV) than on the octahedral NC surface (-2.38 eV). Moreover, we have carefully investigated the energetics and structural parameters of the transition state to provide the clear understanding behind the distinct nature of *OH formation on the NCs. The Pt-Pt distance is similar (2.67 Å) in both the bare NCs. However, the structural parameters are different in their respective *OH formation transition states (TS). On the cuboctahedral NC, the transition state structure for *OH formation is close to the product structure, whereas the corresponding structure is close to the reactant on the octahedral NC. As *O adsorbs strongly compared to *OH, therefore the extent of deformation on the (111) facet of the NCs are different in their respective transition states. The Pt-Pt bond distances are 2.77 and 2.93 Å on the cuboctahedral and octahedral NC, respectively. Therefore, octahedral NC is under highly strained (9.7%), which makes the TS less stable compared to the transition state on the cuboctahedral NC (3.7% strained). Moreover, we have calculated the strain energy of the NCs in their respective TS geometry. The strain energy of the TS is calculated by evaluating the energy difference between the optimized NC and the single-point energy of the NC within the geometry of the transition states. Our calculated strain energies are 0.73 and 0.26 eV for the octahedral and cuboctahedral NC, respectively. Therefore, the product like transition state makes the *OH formation favorable on the cuboctahedral NC. This may be due to the presence of two different facets (111) and (100) in the cuboctahedral NC.

We have also calculated the activation barriers for *OH formation (*O + *H → *OH) step at the edge site. The calculated activation barriers for the *OH formation are 1.24 and 0.63 eV on the cuboctahedral and octahedral NCs, respectively. Thereby, *OH formation is favourable on the (111) facet than at the edge site of cuboctahedral NC and the trend is opposite on the octahedral NC. The anomaly can be explained from the adsorption energy of the *O and *OH on the NCs. Octahedral NC binds *O in almost similar way on the edge (-4.80 eV) and facet (-4.90 eV) sites, whereas cuboctahedral NC binds weakly (by 0.30 eV) at the edge site compared to facet site. Therefore, the charge transfer from the cuboctahedral NC towards *O will be less at the edge site, which hinders the protonation step.

The site dependent catalytic activity has been reported previously. Gao et al. *[76]* showed some interesting findings on site specific reactivity of Pd nanoparticles for CO_2 reduction and hydrogen evaluation reaction (HER) and reported that the corner, edge, and terrace sites are active for HER, whereas edge sites are active for CO_2 reduction. Using DFT and microkinetic modeling, Cai et al. *[77]* investigated the site specific reactivity on furfural conversion over platinum (Pt) catalysts and reported that the reaction pathways in furfural conversion (hydrogenation or decarbonylation) largely depend strongly on the reactive sites of the catalysts. Furthermore, Lyu et al. *[78]* also reported that the hydrodehalogenation of nitrobenzene highly dependent on the type of reaction sites, whereas the hydrogenation pathways show almost similar activity on different reaction sites.

Furthermore, *OH formation is possible via indirect pathways (step 5.4) too; such as via peroxyl formation followed by O-O bond dissociation (step 5.4). This step is a barrierless process on both the NCs with reaction free energies of -1.92 and -1.87 eV for the cuboctahedral and octahedral NCs, respectively. Yao *et al. [71]* and Kai *et al. [70]* reported activation barriers of 0.12 eV and 0.06 eV, respectively for the *OOH dissociation (step 5.4) step over the bulk Pt(111). Therefore, the *OOH dissociation in general is a favorable process over the NCs and bulk surfaces.

$*H_2O_2$ Formation and Decomposition:

The $2e^-$ reduction process leads to the formation of H_2O_2. H_2O_2 can be formed (step 5.5) via two successive hydrogenations on O_2 ($*O_2 + *H \rightarrow *OOH$, $*OOH + *H \rightarrow *H_2O_2$). Our calculated activation barrier and reaction free energy for H_2O_2 formation are 0.41 and 0.08 eV, respectively over the octahedral NC surface. In fact, the cuboctahedral NC requires far higher activation energy than the octahedral NC for the formation of H_2O_2. Zhiyao *et al. [75]* reported an activation barrier of 0.19 eV for the H_2O_2 formation (step 5.5) on the bulk Pt(111). This suggests that H_2O_2 formation is favorable on bulk Pt(111), whereas it is not favorable on the cuboctahedral NC surface.

The dissociation of $*H_2O_2$ into *OH (step 5.6) is very much comparable on both the NCs. The activation barriers for $*H_2O_2$ dissociation step (step 5.6) is a barrierless process on the octahedral NC, whereas it shows an activation barrier of 0.06 on the cuboctahedral NC.

$*H_2O$ formation:

The adsorbed *OH undergoes further hydrogenation (step 5.7) towards the formation of $*H_2O$. This is calculated to be a barrierless process on the NCs surface. The previous studies reported H_2O formation barriers of 0.16 eV *[72]*, and 0.14 eV *[71]* on the bulk Pt(111), which are higher than our calculated barriers on the NCs surface. However, the $*H_2O$ formation is favorable over *OH formation on the surface of the NCs. This suggests that the *OH formation is the rate determining step on the NCs and $*H_2O$ formation will not influence the reaction kinetics on the NC facet. We find that the $*O_2$ dissociation ($*O_2 \rightarrow *O + *O$) and *OH formation ($*O + *H \rightarrow *OH$) steps are significantly improved over the cuboctahedral NC surface than on the octahedral NC surface. Therefore, our results show that the shape of the NCs has a significant role on the ORR activity. Moreover, the shape is not only influencing the rate-determining step (step 5.3) but also other important steps. So if we compare the catalytic activity of the cuboctahedral and octahedral NCs toward ORR then we find that the cuboctahedral NC is highly selective for four-electron reduction over two-electron reduction. Thus, we predict that the cuboctahedral NC could be a promising catalyst for fuel cell applications.

5.3.3. Origin of the Reactivity

We have calculated the surface energies of the NCs to understand the excellent catalytic activities of the NCs with respect to the bulk Pt(111). The calculated surface energies for the cuboctahedral NC, octahedral NC and bulk Pt(111) are 0.176, 0.172, and 0.114 eV/$\AA^2$, respectively. The presence of low coordinated sites is the reason for high surface energy of the NCs. Thus, our results indicate that the NCs are highly reactive compared to the bulk Pt(111) and the cuboctahedral NC is the most active one, which is very much consistent with our ORR activity study.

Furthermore, we have calculated the strain energy on the facet of the NCs to understand the excellent catalytic activity of the cuboctahedral NC. The calculated strain energies for the cuboctahedral and octahedral NCs are -4.58 and -6.55 eV, respectively. Therefore, the cuboctahedral NC is more reactive than that of octahedral NC. We have carefully investigated the geometrical parameters of the NCs to find out the origin of such reactivity. The average Pt-Pt bond distances of the facet atoms are 2.66 Å for both the cuboctahedral and octahedral NCs compared to 2.77 Å in the bulk Pt(111). Surprisingly, the Pt-Pt bond distances of the edge atoms are 2.64 and 2.62 Å for the cuboctahedral and octahedral NCs, respectively. However, the Pt-Pt bond distance of the (100) facet of the cuboctahedral NC is 2.71 Å. Therefore, due to the presence of two different facets in the cubocatahedral structure, the surface is under strain, which in turn improves the catalytic activity.

We have further calculated the % of strain on the cuboctahedral and octahedral NCs and our results show that the cuboctahedral NC is under less compressive strain (more tensile strain) than the octahedral NC. Besides, the d-band center of the (111) facet of both the NCs is calculated. The d-band center of the cuboctahedral and octahedral NCs are -2.50 and -2.61, respectively. It has been previously reported that the expansion in the lattice parameters (under tensile strain) shifts the d-band center toward Fermi, which strengthens the binding strength of the adsorbate on the surface *[79-81]*. Interestingly, our calculations also show that the less compressive strained cuboctahedral NC shifts the d-band center toward Fermi and binds the reaction intermediates (*O and *OH) strongly. Therefore, the dissociation of $*O_2$ and formation of *OH become favorable on the cuboctahedral NC due to the stabilization of the products (*O and *OH).

Therefore, our detailed investigation concludes that the presence of small traces of (100) facet in the cuboctahedral NC induces compressive strain in the system, which in turn improves the activity; thus improves the adsorption of the intermediates (*O and *OH). As a result, cuboctahedral and octahedral NCs favour two different reaction mechanisms. Cuboctahedral NC prefers direct as well as indirect pathways for ORR mechanism. In contrary, octahedral NC favours indirect over direct pathway and thus increases the possibility of hydrogen peroxide formation (H_2O_2). Therefore we find that cuboctahedral NC improves the ORR activity and selectivity compared to the octahedral NC.

5.3.4. Kinetic Analysis

We have done a detailed kinetic analysis based on our preliminary DFT results to understand the product selectivity between four-electron (H_2O formation) vs. two-electron (H_2O_2 formation) reduction reactions. The forward (k_i) rate constants for all the elementary steps are calculated using the following equation:

$$k_i = \left(\frac{k_B T}{h}\right)\left(\frac{q_{TS}}{q_R}\right)e^{-\Delta G^{\ddagger}/k_B T} \tag{5.11}$$

where k_B is the Boltzmann constant, T is the temperature, h is the Plank constant. Here, q_{TS} and q_R are the vibrational partition functions for the transition state and reactant structures, respectively and $\Delta G^{\ddagger}$ is the Gibbs free energy barrier for the initial and final state of the elementary reaction. The vibrational partition functions (q) are calculated as follows

$$q = \sum_i \frac{1}{1-e^{-h\nu_i/k_B T}} \tag{5.12}$$

where υ_i are the vibrational frequencies.

Table 5.3: Rate constants (s^{-1}) of the elementary reactions at different temperatures on the cuboctahedral NC (CNC) and octahedral NC (ONC). Here k_i stands for the forward rate constant of the ith step.

Elementary reactions	**300 K**		**500 K**	
	CNC	**ONC**	**CNC**	**ONC**
$*O_2 \xrightarrow{k_1} *O+*O$	8.66×10^{12}	1.10×10^{10}	1.24×10^{13}	2.34×10^{11}
$*O_2+*H \xrightarrow{k_2} *OOH$	1.36×10^{12}	1.61×10^{11}	4.31×10^{12}	1.20×10^{12}
$*O+*H \xrightarrow{k_3} *OH$	1.32×10^{08}	1.30×10^{-04}	1.15×10^{10}	9.27×10^{02}
$*OOH \xrightarrow{k_4} *O+*OH$	7.92×10^{12}	7.54×10^{12}	1.22×10^{13}	1.26×10^{13}
$*H+*OOH \xrightarrow{k_5} *H_2O_2$	5.39×10^{-07}	8.17×10^{05}	3.82×10^{01}	8.27×10^{08}
$*H_2O_2 \xrightarrow{k_6} *OH + *OH$	8.73×10^{11}	6.65×10^{12}	3.62×10^{12}	1.11×10^{13}
$*H+*OH \xrightarrow{k_7} *H_2O$	1.67×10^{13}	1.65×10^{13}	2.06×10^{13}	1.99×10^{13}

The rate constants (Table 5.3) are calculated in the temperature range of 300 K and 500 K as the fuel cell operates in this temperate range *[82, 83]*. The rate constants improve significantly as we increase the temperature. At 300 K, the ratios of rate constants (k_1/k_2) between $*O_2$ dissociation and $*O_2$ hydrogenation steps are 6.36 and 0.07 on the cuboctahedral and octahedral NCs, respectively. Hence, *O formation is favorable over *OOH formation ($*O_2 \rightarrow *O + *O$ and $*O_2 + *H \rightarrow *OOH$) on the cuboctahedral surface, whereas both the steps are very much competing on the octahedral surface. However, it is very important to understand whether the shape of the NC affects the *OOH dissociation ($*OOH \overset{k_4}{\rightarrow} *O + *OH$) and hydrogenation ($*OOH + *H \overset{k_5}{\rightarrow} *H_2O_2$) steps or not? We find that the ratios of rate constants (k_4/k_5) of these two steps are 1.46×10^{19} and 9.22×10^{06} for the cuboctahedral and octahedral NCs, respectively; implying that the *OOH dissociation is very much favorable over *OOH hydrogenation on the cuboctahedral NC surface. Therefore, even if the reaction proceeds through the *OOH intermediate, it will further dissociate into *O and *OH ($*OOH \rightarrow *O + *OH$) on the cuboctahedral NC surface. Hence, our kinetic analysis suggests that cuboctahedral NC is highly selective and efficient towards $4e^-$ reduction (H_2O formation) over $2e^-$ reduction (H_2O_2 formation) reaction. More importantly, the rate-determining step ($*O+*H\rightarrow*OH$) is no longer a rate determining step (Table 5.3) when the reaction is catalyzed by the cuboctahderal NC.

Interestingly, the superior catalytic activity of the cuboctahedral NC over octahedral NC has been reported earlier. Wu et al. *[84]* investigated a series of Pt_3Ni NCs with fraction of exposed (111) and (100) facets and reported that the truncated-octahedral or cuboctahedral NCs with highly exposed (111) facets increase the ORR mass activity by 1.8 times than that of the octahedral NCs. Carlos et al. *[20]* also concluded that the hexagonal Pt nanoparticle with (100) and (111) exposed facets displays the highest ORR activity in relative to the sphere (no preferential facets), tetrahedral/octahedral with (111) facets and cubic with (100) facets. Furthermore, the cuboctahedral NCs show better catalytic activity toward other reactions too. Gillian et al. *[85]* reported that the cuboctahedral palladium NC shows superior catalytic activity compared to the octahedral NC for Suzuki-Miyaura cross coupling reactions, where they attributed the presence of the (100) facet for showing better catalytic activity. Recently, Xia and co-workers *[86]* investigated the formic acid oxidation on different Pd polyhedrons enclosed by different proportion of (100) and (111) facets and concluded that the Pd nanocubes with slight ‘truncations’ at the corners to be the best catalysts. Wang et al. *[87]* reported that a 7 nm platinum nanoparticle consisting of (111) and (200) facets or only (100) facet transfers nearly four-electron (3.6) during ORR, whereas 3 and 5 nm nanoparticles with majorly (111) facet transfer less electron (0.7). Our calculation also shows that cuboctahedral NC favours four-electron reduction, whereas octahedral NC favours two-electron reduction. Moreover, Kim et al. *[88]* reported that octahedral Pd nanoparticles favour higher H_2O_2 selectivity during ORR, which is consistent with our results. However, many experimental reports conclude that cuboctahedral NC shows higher ORR activity while compared to octahedral NC. Therefore, the overall ORR activity of the NC is in good agreement with previous experimental reports *[20, 84-88]*. Therefore, it is believed that the presence of the (100) facets along with the (111) facets (i.e. cuboctahedral, truncated-octahedral and hexagonal shape) shows superior catalytic activity than the purely (111) and (100) faceted NCs (i.e. octahedral and cubic shapes). Interestingly, our results are very much in consistent with previous experimental findings and this could be again due to the presence of two types of facets in the cuboctahedral NC. Therefore, our study not only provides an in-depth understanding behind the shape-dependent catalytic activity but also illustrates the experimental finding in the atomic level.

5.4. Conclusion

First-principle calculations are performed to understand the shape-dependent catalytic activities of the platinum NCs toward ORR activity. The cuboctahedral and octahedral platinum NCs enclosed by well-defined facets have been chosen for our study due to their high symmetry and experimental realization. Molecular dynamics simulation suggests that cuboctahedral NC is thermally more stable than octahedral NC and the cuboctahedral NC can withstand temperatures as high as 500 K without any structural reconstruction. Dissolution potential behaviors of the NCs show that cuboctahedral NC is electrochemically stable compared to the octahedral one. Reaction free energies and activation barriers are calculated for all the possible elementary steps of ORR on the (111) facet of the NCs. Our results reveal that the direct O-O bond dissociation is thermodynamically favorable over the NCs surface, which is totally opposite to previous theoretical on the bulk metal (Pt, Pd, Ag) surfaces, where indirect O-O bond dissociation is favorable over direct O-O bond dissociation. Furthermore, the rate-determining step is no longer a rate-determining step when the reaction is catalyzed by the cuboctahedral NC. Our kinetics analysis shows that the $4e^-$ reduction (H_2O formation) is very favorable than the $2e^-$ reduction (H_2O_2 formation) when the NCs. Hence, the efficiency and product selectivity (H_2O vs. H_2O_2) increased significantly when the reaction is catalyzed by the NCs. However, the efficiency and product selectivity reach maximum when the reaction is catalyzed by the cuboctahedral NC. After a detailed investigation on the surface energy and compressive strain, we find that, due to the presence of (111) and (100) facets, the cuboctahedral NC shifts the d-band center position toward Fermi, which allows the NC to interact strongly with the intermediates, which in turn stabilizes the intermediates. As a result, cuboctahedral and octahedral NCs favour two different reaction mechanisms. Cuboctahedral NC prefers direct as well as indirect pathways for ORR mechanism. In contrary, octahedral NC favours indirect over direct pathway and thus increases the possibility of H_2O_2 formation. Therefore we find that cuboctahedral NC improves the ORR activity and selectivity compared to the octahedral NC. Interestingly, earlier experimental reports show that the presence of (100) facets along with the (111) facets (i.e. cuboctahedral, truncated-octahedral and hexagonal) shows superior catalytic activity than the purely (111) and (100) faceted NCs (i.e octahedral and cube), which is in well agreement with our findings. Therefore, our study provides atomistic insights into the shape-dependent catalytic activity of the platinum NCs toward ORR. We believe that our study will certainly help the experimentalists to understand the shape dependent catalytic activity of the NCs, which in turn will guide them for designing more efficient and selective catalyst for fuel cell applications.

5.5. References

1. Jiao Y., Zheng Y., Jaroniecb M., Qiao S. Z. (2015), Design of electrocatalysts for oxygen- and hydrogen-involving energy conversion reactions, Chem. Soc. Rev., 44, 2060-2080. (DOI: 10.1039/C4CS00470A)

2. Vinayan B. P., Nagar R., Rajalakshmi N., Ramaprabhu S. (2012), Novel platinum–cobalt alloy nanoparticles dispersed on nitrogen-doped graphene as a cathode electrocatalyst for PEMFC applications, Adv. Funct. Mater., 22, 3519-3526. (DOI: 10.1002/adfm.201102544)

3. Lubitz W., Tumas W., (2007), Hydrogen: an overview, Chem. Rev., 107, 3900-3903. (DOI: 10.1021/cr050200z)

4. de Bruijn F. A., Dam V. A. T., Janssen G. J. M. (2008), Review: durability and degradation issues of PEM fuel cell components, Fuel Cells, 8, 3-22. (DOI: 10.1002/fuce.200700053)

5. Watanabe M., Tryk D. A., Wakisaka M., Yano H., Uchida H. (2012), Overview of recent developments in oxygen reduction electrocatalysis, Electrochim. Acta, 84, 187-201. (DOI: 10.1016/j.electacta.2012.04.035)

6. Calle-Vallejo F., Koper M. T. M., Bandarenka A. S. (2013), Tailoring the catalytic activity of electrodes with monolayer amounts of foreign metals, Chem. Soc. Rev., 42, 5210-5230. (DOI: 10.1039/C3CS60026B)

7. Wang X. X., Tan Z. H., Zeng M., Wang J. N. (2014), Carbon nanocages: A new support material for Pt catalyst with remarkably high durability, Sci. Rep., 4, 4437. (DOI: 10.1038/srep04437)

8. Xu Y., Ruban A. V., Mavrikakis M. (2004), Adsorption and dissociation of O2 on Pt− Co and Pt− Fe alloys, J. Am. Chem. Soc., 126, 4717-4725. (DOI: 10.1021/ja031701+)

9. Stamenkovic V. R., Fowler B., Mun B. S, Wang G., Ross P. N., Lucas C. A., and Marković N. M. (2007), Science, 315, 493-497. (DOI: 10.1126/science.1135941)

10. Stamenkovic V., Mun B. S., Mayrhofer K. J. J., Ross P. N., Markovic N. M., Rossmeisl J., Greeley J., Nørskov J. K. (2006), Changing the activity of electrocatalysts for oxygen reduction by tuning the surface electronic structure, Angew. Chem., 118, 2963-2967. (DOI: 10.1002/ange.200504386)

11. W Tang. J., Zhang L., Henkelman G. (2011), Catalytic activity of Pd/Cu random alloy nanoparticles for oxygen reduction, J. Phys. Chem. Lett., 2, 1328−1331. (DOI: 10.1021/jz2004717)

12. Holewinski A., Idrobo J., Linic S. (2014), High-performance Ag–Co alloy catalysts for electrochemical oxygen reduction, Nat. Chem., 6, 828–834. (DOI:10.1038/nchem.2032)

13. Wang J. X., Inada H., Wu L., Zhu Y., Choi Y., Liu P., Zhou W. P., Adzic R. R. (2009), Oxygen Reduction on Well-Defined Core−Shell Nanocatalysts: Particle Size, Facet, and Pt Shell Thickness Effects, J. Am. Chem. Soc., 131, 17298-17302. (DOI: 10.1021/ja9067645)

14. Oezaslan M., Hasché F., Strasser P. (2013), Pt-Based Core–Shell Catalyst Architectures for Oxygen Fuel Cell Electrodes, J. Phys. Chem. Lett., 4, 3273-3291. (DOI: 10.1021/jz4014135)

15. Mazumder V., Chi M., More K. L., Sun S. (2010), Core/shell Pd/FePt nanoparticles as an active and durable catalyst for the oxygen reduction reaction, J. Am. Chem. Soc., 132, 7848-7849. (DOI: 10.1021/ja1024436)

16. Pachon L. D., Rothenberg G. (2008), Transition-metal nanoparticles: synthesis, stability and the leaching issue, App. Organometal. Chem., 22, 288-299. (DOI: 10.1002/aoc.1382)

17. Wang Y., Zhao N., Fang B., Li H., Bi X. T., Wang H. (2015), Carbon-Supported Pt-Based Alloy Electrocatalysts for the Oxygen Reduction Reaction in Polymer Electrolyte Membrane Fuel Cells: Particle Size, Shape, and Composition Manipulation and Their Impact to Activity, Chem. Rev., 115, 3433-3467. (DOI: 10.1021/cr500519c)

18. Ahmadi T. S., Wang Z. L., Green T. C., Henglein A., El-Sayed M. A. (1996), Shape-controlled synthesis of colloidal platinum nanoparticles, Science., **272**, 1924.

19. Wang C., Daimon H., Onodera T., Koda T., Sun S. (2008), A General Approach to the Size- and Shape-Controlled Synthesis of Platinum Nanoparticles and Their Catalytic Reduction of Oxygen, Angew. Chem. Int. Ed., 47, 3588-3591. (DOI: 10.1002/anie.200800073)

20. Sanchez C. M., Solla-Gullon J., Vidal-Iglesias F. J., Aldaz A., Montiel V., Herrero E. (2010), Imaging Structure Sensitive Catalysis on Different Shape-Controlled Platinum Nanoparticles, J. Am. Chem. Soc., 132, 5622-5624. (DOI: 10.1021/ja100922h)

21. Zhang J., Yang H., Fang J., Zou S. (2010), Synthesis and Oxygen Reduction Activity of Shape-Controlled Pt3Ni Nanopolyhedra, Nano Lett., 10, 638-644. (DOI: 10.1021/nl903717z)

22. Lim B., Jiang M., Tao J., Camargo P. H. C., Zhu Y., Xia Y. (2009), Shape-Controlled Synthesis of Pd Nanocrystals in Aqueous Solutions, Adv. Funct. Mater., 19, 189-200. (DOI: 10.1002/adfm.200801439)

23. Xia B. Y., Wu H. B., Wang X., Lou X. W. (2013), Index Facets and Enhanced Electrocatalytic Properties, Angew. Chem. Int. Ed., 52, 12337-12340. (DOI: 10.1002/anie.201307518)

24. Tang Y., Cheng W. (2013), Nanoparticle-Modified Electrode with Size- and Shape-Dependent Electrocatalytic Activities, Langmuir, 29, 3125-3132. (DOI: 10.1021/la304616k)

25. Cuenya B. R. 2013, Metal Nanoparticle Catalysts Beginning to Shape-up, Acc. Chem. Res., 46, 1682-1691. (DOI: 10.1021/ar300226p)

26. Wu, J., Yang H. (2013), Platinum-Based Oxygen Reduction Electrocatalysts, Acc. Chem. Res., 46, 1848-1857. (DOI: 10.1021/ar300359w)

27. Tang Y., Cheng W. (2015), Key parameters governing metallic nanoparticle electrocatalysis, *Nanoscale*, **7**, 16151-16164. (DOI: 10.1039/C5NR02298C)

28. Vines F., Gomes J. R. B., Illas F. (2014), Understanding the reactivity of metallic nanoparticles: beyond the extended surface model for catalysis, Chem. Soc. Rev., 43, 4922-4939. (DOI: 10.1039/C3CS60421G)

29. Narayanan R., El-Sayed M. A. (2005), Catalysis with Transition Metal Nanoparticles in Colloidal Solution: Nanoparticle Shape Dependence and Stability, J. Phys. Chem. B., 109, 12663-12672. (DOI: 10.1021/jp051066p)

30. Bratlie K. M., Lee H., Komvopoulos K., Yang P., Somorjai G. A. (2007), Platinum Nanoparticle Shape Effects on Benzene Hydrogenation Selectivity, Nano Lett., 7, 3097-3101. (DOI: 10.1021/nl0716000)

31. Tsung C. K., Kuhn J. N., Huang W., Aliaga C., Hung L. I., Somorjai G. A., Yang P. (2009), Sub-10 nm Platinum Nanocrystals with Size and Shape Control: Catalytic Study for Ethylene and Pyrrole Hydrogenation, J. Am. Chem.Soc., 131, 5816-5822. (DOI: 10.1021/ja809936n)

32. Lee I., Delbecq F., Morales R., Albiter M. A., Zaera F. (2009), Tuning selectivity in catalysis by controlling particle shape, Nat.Mater., 8, 132-138. (DOI:10.1038/nmat2371)

33. Wang J., Gong J., Xiong Y., Yang J., Y Gao., Liu Y., Lu X., Tang Z. (2011), Shape-dependent electrocatalytic activity of monodispersed gold nanocrystals toward glucose oxidation , Chem. Commun, 47, 6894-6896. (DOI: 10.1039/C1CC11784J)

34. Zhang X., Yin H., Wang J., Chang L., Gao Y., Liu W., Tang Z. (2013), Shape-dependent electrocatalytic activity of monodispersed palladium nanocrystals toward formic acid oxidation, Nanoscale., 5, 8392-8397. (DOI: 10.1039/C3NR03100D)

35. Wang R., He H., Liu L. C., Dai H. X., Zhao Z. (2012), Shape-dependent catalytic activity of palladium nanocrystals for the oxidation of carbon monoxide, Catal. Sci. Technol., 2, 575-580. (DOI: 10.1039/C2CY00417H)

36. Nie Y., Li L., Wei Z. (2015), Recent advancements in Pt and Pt-free catalysts for oxygen reduction reaction, Chem. Soc. Rev., 44, 2168-2201. (DOI: 10.1039/C4CS00484A)

37. Rabis A., Rodriguez P., Schmidt T. J. (2012), Electrocatalysis for Polymer Electrolyte Fuel Cells: Recent Achievements and Future Challenges, ACS Catal., 2, 864-890. (DOI: 10.1021/cs3000864)

38. Hu Y., Zhang H., Wu P., Zhang H., Zhou B., Cai C. (2011), Bimetallic Pt–Au nanocatalysts electrochemically deposited on graphene and their electrocatalytic characteristics towards oxygen reduction and methanol oxidation, Phys. Chem. Chem. Phys., 13, 4083-4094. (DOI: 10.1039/C0CP01998D)

39. Maiyalagan T., Khan F. N. (2009), Electrochemical oxidation of methanol on Pt/V 2 O 5–C composite catalysts, Catal. Commun., 10, 433-436. (DOI: 10.1016/j.catcom.2008.10.011)

40. Yeager E. (1986), Dioxygen electrocatalysis: mechanisms in relation to catalyst structure, J. Mol. Catal., 38, 5. (DOI: 10.1016/0304-5102(86)87045-6)

41. Sanchez-Sanchez C. M., Bard A., (2009), Hydrogen peroxide production in the oxygen reduction reaction at different electrocatalysts as quantified by scanning electrochemical microscopy, J. Anal. Chem., 81, 8094-8100. (DOI: 10.1021/ac901291v)

42. Markovic N. M., Gasteiger H. A., Ross P. N. (1996) Oxygen Reduction on Platinum Low-Index Single-Crystal Surfaces in Alkaline Solution: Rotating Ring Disk $Pt_{(hkl)}$ Studies, J. Phys. Chem., 100, 6715-6721. (DOI: 10.1021/jp9533382)

43. Tian N., Zhou Z. Y., Sun S. G., Ding Y., Wang Z. L. (2007), Synthesis of Tetrahexahedral Platinum Nanocrystals with High-Index Facets and High Electro-Oxidation Activity, Science, 316, 732-735. (DOI: 10.1126/science.1140484)

44. Susut C., Chapman G. B., Samjeske G., Osawa M., Tong Y. Y. J. (2008), An unexpected enhancement in methanol electro-oxidation on an ensemble of

Pt(111) nanofacets: a case of nanoscale single crystal ensemble electrocatalysis, Phys. Chem. Chem. Phys., 10, 3712-3721. (DOI: 10.1039/B802708K)

45. Solla-Gullon J. Vidal-Iglesias F. J., Lopez-Cudero A., Garnier E., Feliu J. M., Aldaz A. (2008), Shape-dependent electrocatalysis: methanol and formic acid electrooxidation on preferentially oriented Pt nanoparticles, Phys. Chem. Chem. Phys., 10, 3689-3698. (DOI: 10.1039/B802703J)

46. Duan Z., Wang G. (2013), Comparison of Reaction Energetics for Oxygen Reduction Reactions on Pt(100), Pt(111), Pt/Ni(100), and Pt/Ni(111) Surfaces: A First-Principles Study, J. Phys. Chem. C, 117, 6284-6292. (DOI: 10.1021/jp400388v)

47. Han B., Viswanathan V., Pitsch H. (2012), First-Principles Based Analysis of the Electrocatalytic Activity of the Unreconstructed Pt(100) Surface for Oxygen Reduction Reaction, J. Phys. Chem. C, 116, 6174-6183. (DOI: 10.1021/jp2075379)

48. Mahata A., Rawat K. S., Choudhuri I., Pathak B. (2016), Single-layered platinum nanocage: a highly selective and efficient catalyst for fuel cells, J. Mater. Chem. A, 4, 12756-12767. (DOI: 10.1039/C6TA03245A)

49. Mahata A., Rawat K. S., Choudhuri I., Pathak B., (2016), Octahedral Ni-nanocluster (Ni85) for Efficient and Selective Reduction of Nitric Oxide (NO) to Nitrogen (N_2), *Scientific Reports*, **6**, 25590. (DOI: 10.1038/srep25590)

50. Blochl P. E. (1994), Projector augmented-wave method, Phy. Rev. B, 50, 17953. (DOI : 10.1103/PhysRevB.50.17953)

51. Kresse G., Hafner J. (1993), Ab initio molecular dynamics for liquid metals, Phy. Rev. B, 47, 558. (DOI: 10.1103/PhysRevB.47.558)

52. G Kresse., Hafner J. (1994), Ab initio molecular-dynamics simulation of the liquid-metal–amorphous-semiconductor transition in germanium, Phy. Rev. B, 49, 14251-14269. (DOI: 10.1103/PhysRevB.49.14251)

53. Kresse G., Joubert D. (1999), From ultrasoft pseudopotentials to the projector augmented-wave method, Phy. Rev. B, 59, 1758. (DOI: 10.1103/PhysRevB.59.17580)

54. Perdew J. P., Chevary J. A., Vosko S. H., Jackson K. A., Pederson M. R., Singh D. J., Fiolhais C. (1992), Atoms, molecules, solids, and surfaces: Applications of the generalized gradient approximation for exchange and correlation, Phy. Rev. B, 46, 6671. (DOI: 10.1103/PhysRevB.46.6671)

55. Grimme S., Antony J., Ehrlich S., Krieg S. (2010), A consistent and accurate ab initio parametrization of density functional dispersion correction (DFT-D) for the 94 elements H-Pu, J. Chem. Phys., 132, 154104. (DOI: 10.1063/1.3382344)

56. Henkelman G., Jonsson H. (2000) A climbing image nudged elastic band method for finding saddle points and minimum energy paths, J. Chem. Phys., 113, 9978-9985. (DOI: 10.1063/1.1329672)

57. Kittel, C. (2005), *Introduction to Solid State Physics,* 8th edition. Hoboken, NJ: John Wiley & Sons, Inc,.

58. Choudhuri I., Patra N., Mahata A., Ahuja R., Pathak B. (2015), B–N@Graphene: Highly Sensitive and Selective Gas Sensor, J. Phys. Chem. C, 119, 24827-24836. (DOI: 10.1021/acs.jpcc.5b07359)

59. Garg P., Kumar S., Choudhuri I., A Mahata., Pathak B. (2016), Hexagonal Planar CdS Monolayer Sheet for Visible Light Photocatalysis, J. Phys. Chem. C;, 120, 7052-7060. (DOI: 10.1021/acs.jpcc.6b01622)

60. Choudhuri I., Kumar S., Mahata A., Rawat K. S., Pathak B. (2016),Transition-metal embedded carbon nitride monolayers: high-temperature ferromagnetism and half-metallicity, Nanoscale, 8, 14117-14126. (DOI: 10.1039/C6NR03282F)

61. Shi Z., Zhang Z., Kutana A., Yakobson B. I. (2015), Predicting Two-Dimensional Silicon Carbide Monolayers, ACS Nano, 9, 9802-9809. (DOI: 10.1021/acsnano.5b02753)

62. Nose S. A. (1984), A unified formulation of the constant temperature molecular dynamics methods, J. Chem. Phys., 81, 511-519. (DOI: 10.1063/1.447334)

63. Escano M. C. S. (2015), First-principles calculations of the dissolution and coalescence properties of Pt nanoparticle ORR catalysts: The effect of nanoparticle shape, Nano Res., **8**, 1689-1697. (DOI: 10.1007/s12274-014-0670-1)

64. Jeon T., Kim S., Pinna N., Sharma A., Park J., Lee S., Lee H. C., Kang S. W., Lee H. K., Lee H. H. (2016), Selective Dissolution of Surface Nickel Close to Platinum in PtNi Nanocatalyst toward Oxygen Reduction Reaction, Chem. Mater., 28, 1879. (DOI: 10.1021/acs.chemmater.6b00103)

65. Ma Y., Balbuena P. B. (2008), Surface Properties and Dissolution Trends of Pt3M Alloys in the Presence of Adsorbates, J. Phys. Chem. C, 112, 14520-14528. (DOI: 10.1021/jp8046888)

66. Greeley J., Nørskov J. K. (2007), Electrochemical dissolution of surface alloys in acids: Thermodynamic trends from first-principles calculations, Electrochimica Acta, 52, 5829-5836. (DOI: 10.1016/j.electacta.2007.02.082)

67. Caballero G., Balbuena P. B. (2010), Dissolution-Resistant Core−Shell Materials for Acid Medium Oxygen Reduction Electrocatalysts, J. Phys. Chem. Lett**., 1,** 724-728. (DOI: 10.1021/jz1000165)

68. H. Kikuchi, W. Ouchida, M. Nakamura, C. Goto, M. Yamada, H. Nagahiro. *Electrochem. Commun.* 2010. **12**, 544-547. (DOI: 10.1016/j.elecom.2010.01.039)

69. Devivaraprasad R., Kar T., Chakraborty A., Singh R. K., Neergat M. (2016), Reconstruction and dissolution of shape-controlled Pt nanoparticles in acidic electrolytes, Phys. Chem. Chem. Phys., 18, 11220-11231. (DOI: 10.1039/C5CP07832F)

70. Li K., Li Y., Wang Y., He F., Jiao M., Tang H., Wu Z. (2015), The oxygen reduction reaction on Pt(111) and Pt(100) surfaces substituted by subsurface

Cu: a theoretical perspective, J. Mater. Chem. A, 3, 11444-11452. (DOI: 10.1039/C5TA01017A)

71. Sha Y., Yu T. H., Merinov B. V., Shirvanian P., Goddard W. A. (2011), Oxygen Hydration Mechanism for the Oxygen Reduction Reaction at Pt and Pd Fuel Cell Catalysts, *J.* Phys. Chem. Lett., 2, 572-576. (DOI: 10.1021/jz101753e)

72. Farberow C. A., Godinez-Garcia A., Peng G. W., Perez-Robles J. F., Solorza-Feria O., Mavrikakis M. (2013), Mechanistic Studies of Oxygen Reduction by Hydrogen on PdAg(110), ACS Catal., 3, 1622-1632. (DOI: 10.1021/cs4002699)

73. Jennings. C. P., Aleksandrov H. A., Neymanbd K. M., Johnston R. L. (2014), A DFT study of oxygen dissociation on platinum based nanoparticles, Nanoscale, 6, 1153-1165. (DOI: 10.1039/C3NR04750D)

74. Sha Y., Yu T. H., Liu Y., Merinov B. V., Goddard III W. A. (2010), Theoretical Study of Solvent Effects on the Platinum-Catalyzed Oxygen Reduction Reaction, J. Phys. Chem. Lett., 1, 856-861. (DOI: 10.1021/jz9003153)

75. Duan Z., Wang G. (2011), A first principles study of oxygen reduction reaction on a Pt(111) surface modified by a subsurface transition metal M (M = Ni, Co, or Fe), Phys. Chem. Chem. Phys., 13, 20178-20187. (DOI: 10.1039/C1CP21687B)

76. Gao D., Zhou H., Wang J., Miao S., Yang F., Wang G., Wang J., Bao X. (2015), Size-Dependent Electrocatalytic Reduction of CO_2 over Pd Nanoparticles, J. Am. Chem. Soc., 137, 4288-4291. (DOI: 10.1021/jacs.5b00046)

77. Cai Q., Wang J., Wang Y., Mei D. (2015), Mechanistic insights into the structure-dependent selectivity of catalytic furfural conversion on platinum catalysts, AIChE J., 61, 3812-3824. (DOI: 10.1002/aic.14902)

78. Lyu J., Wang J., Lu C., Ma L., Zhang Q., He X., Li X. (2014), Size-Dependent Halogenated Nitrobenzene Hydrogenation Selectivity of Pd Nanoparticles, J. Phys. Chem. C, 118, 2594-2601. (DOI: 10.1021/jp411442f)

79. Mavrikakis M., Hammer B., Nørskov J. K. (1998), Effect of Strain on the Reactivity of Metal Surfaces, Phys. Rev. Lett., 81, 2819. (DOI: 10.1103/PhysRevLett.81.2819)

80. Kitchin J. R., Nørskov J. K., Barteau M. A., Chen J. G. (2004), Role of Strain and Ligand Effects in the Modification of the Electronic and Chemical Properties of Bimetallic Surfaces, Phys. Rev. Lett., 93, 156801. (DOI: 10.1103/PhysRevLett.93.156801)

81. Kattel S., Wang G. (2014), Beneficial compressive strain for oxygen reduction reaction on Pt (111) surface, J. Chem. Phys., 141, 124713. (DOI: 10.1063/1.4896604)

82. Mahata A., Choudhuri I., Pathak B. (2015), A cuboctahedral platinum (Pt_{79}) nanocluster enclosed by well-defined facets favours di-sigma adsorption and improves the reaction kinetics for methanol fuel cells, Nanoscale, 7, 13438-13451. (DOI: 10.1039/C5NR01575H)

83. Mehta V., Cooper J. S. (2003), Review and analysis of PEM fuel cell design and manufacturing, J. Power Sources, 114, 32-53. (DOI: 10.1016/S0378-7753(02)00542-6)

84. Wu J., Zhang J., Peng Z., Yang, S., Wagner F. T., Yang H. (2010), Truncated Octahedral Pt_3Ni Oxygen Reduction Reaction Electrocatalysts, J. Am. Chem. Soc., 132, 4984-4985. (DOI: 10.1021/ja100571h)

85. Collins G., Schmidt M., Dwyer C., Holmes J. D., McGlacken G. P. (2014), The Origin of Shape Sensitivity in Palladium-Catalyzed Suzuki–Miyaura Cross Coupling Reactions, Angew. Chem. Int. Ed., 53, 4142-4145. (DOI: 10.1002/anie.201400483)

86. Jin M., Zhang H., Xieb Z., Xia Y. (2012), Palladium nanocrystals enclosed by {100} and {111} facets in controlled proportions and their catalytic

activities for formic acid oxidation, Energy Environ. Sci., 5, 6352-6357. (DOI: 10.1039/C2EE02866B)

87. Wang C., Daimon H., Onodera T., Koda T., Sun S. (2008), A General Approach to the Size- and Shape-Controlled Synthesis of Platinum Nanoparticles and Their Catalytic Reduction of Oxygen, Angew. Chem. Int. Ed., 47, 3588-3591. (DOI: 10.1002/anie.200800073)

88. Kim S., Lee D., Lee K. (2014), Shape-dependent catalytic activity of palladium nanoparticles for the direct synthesis of hydrogen peroxide from hydrogen and oxygen, *J*. Mol. Cat. A: Chemical, 391, 48-54. (DOI: 10.1016/j.molcata.2014.03.026)

Chapter 6

Cuboctahedral Platinum (Pt_{79}) Nanocluster Enclosed by Well Defined Facets Favours the Di-sigma Adsorption and Improves the Reaction Kinetics for Methanol Fuel Cell

6.1 Introduction

The ever-increasing demand of energy and the problems associated with fossil fuel burning is the primary reason of searching for various alternative energy sources. Fuel cells are efficient and non-polluting energy sources due to their high energy densities and wide operating range of temperature compared to other conventional systems *[1-5]*. Direct methanol fuel cells (DMFCs) are very promising over any other kind of fuel cells due to their low operating temperature, ease of handling and high energy density and wide variety of portable applications *[6-8]*. The adsorption and catalytic dehydrogenation of methanol on the catalyst surface is a crucial step in DMFC. The chemisorption and decomposition of methanol on electrode's surfaces have been widely studied in recent years. However, the dehydrogenation mechanism of methanol over electrode's surface is not fully understood. As there are three different types of bond (C-H, O-H and C-O) present in methanol, the complexity of the dehydrogenation process arises whether the bond scission occurs via C-H, O-H or C-O bonds. To understand the underlying reaction mechanism of methanol decomposition on catalyst's surface, extensive studies (experimental and theoretical) have been carried out by various research groups *[9-22]*. These experimental and theoretical studies on methanol decomposition concludes that the C-O bond scission is not a favourable one but the sequence of O-H and C-H bond activations steps are very crucial and could be the rate determining steps to improve the efficiency of the methanol fuel cell. Apart from the initial dehydrogenation through C-H or O-H bonds, the surface morphology and size of the metal nanoparticles also plays an important role in the bond scission process which in turn governs the catalytic activity of the metal catalyst. In this context, metal nanoclusters surrounded by multiple numbers of well-defined facets show its potential in comparison to their bulk metal surfaces. Metal nanoclusters enclosed by multiple numbers of facets are very noble types of catalyst and found to be very promising in different electro-oxidation reaction *[21, 23]* due to the presence of high surface unsaturation. Such unsaturation serves as a highly active site for activating chemical bonds which in turn controls the catalytic activity. Many theoretical studies are done on small size metal nanocluster *[18, 24]* to understand the catalytic activity of the nanocluster. However, the size of the nanocluster is very important to its catalytic reactivity due to their finite-size effects *[25-30]*. These low-coordinated sites have higher d-band energies, which actually increase the reactivity of these sites *[31-32]*. But, to the best of our knowledge, there are no reports on methanol decomposition on the well-defined facets of platinum nanocluster. The role of different types of binding sites and modes of the substrate-adsorbent is yet to be known. Therefore, to understand the activity of the nano-sized catalyst and the whole decomposition process over such nanocluster's surfaces, it is necessary to model nanocluster surrounded by different type of facets. The nanocluster with cuboctahedral shape is one of the stable forms due to its high symmetry. Hence we have modelled a ~1 nm size cubocahedral platinum nanocluster enclosed by well-defined low index facets to understand the methanol decomposition pathway. Some questions and comparisons will arise whether the adsorption behaviour and reaction energy of the nanocluster's surfaces is similar to the bulk surfaces or not? Similarly, whether the rate determining steps and the reaction mechanism are similar as in the bulk surfaces or not? In this study, an attempt has been made to address these questions by comparing with previously reported results. The highly unsaturated binding sites such as edge vs. bridge site of the nanocluster surface is considered for the methanol decomposition to get the maximum catalytic activity.

The (111), (002) and/or (200) planes are mainly observed in the XRD patterns of experimentally synthesized Pt nanocluster *[33-37]*. As the (200)/(002) has the same pattern as in (100)/(001), we have considered cubooctahedral Pt_{79} cluster with (111) and (001) facet to model the real experimental situation. Here cuboctahedral Pt_{79} cluster is modelled with eight (111) and six (001) facets (Figure 1a) to improve the catalytic activity of the surfaces. We have considered various active sites on the (111) facet of the nanocluster for our methanol dehydrogenation study as platinum (111) surface is the most exposed and stable surface. The edge position (Figure 6.1), formed by the intersection of the (111) facets, is considered to be one of the highly unsaturated active site of the cluster. Two more highly active catalytic sites such as bridge and three fold hollow sites (Figure 6.1) are also considered on the (111) facet of the nanocluster. Here we have considered methanol dehydrogenation proceeds via adsorption of the various intermediates on the (111) facet of the nanocluster via C- and O- centre.

Therefore, the complete dehydrogenation pathway is studied considering three kind of adsorption (*) to the edge, bridge and hollow site (Figure 6.1) of the (111) facet. All the intermediates adsorbed at the edge position are mentioned as vertical adsorption via C- or O-centre. Similarly, the intermediates adsorbed at the bridge site of the (111) facet of the nanocluster mentioned as parallel adsorption via di-sigma manner [Figure 6.1b]. Some other adsorbents are minima at the three-fold hollow site of the (111) facet. The binding preferences on the edge, bridge or the hollow site of the (111) facet are accessed based on their relative stabilities.

6.2 Computational Methods and Models

The first-principles calculations are performed using projected augmented wave (PAW) method *[38]*, as implemented in the Vienna ab initio simulation package (VASP) *[39-41]*. The exchange-correlation interaction is treated in the level of the GGA using Perdew-Burke-Ernzerhof (GGA-PBE) *[42]*. A 22×22×22 $Å^3$ cubic supercell is used to optimize the structures of the metal clusters to rule out the possibility of interaction of periodically repeated metal clusters. The Brillouin zone is sampled using gamma k-point (1×1×1). We have increased the k-points to 2×2×2 for the Pt_{79} cluster and total energy improved by 0.002 eV. As the box size is quite high therefore we continue our calculation with gamma point only. All the atoms are relaxed for the full structural relaxation. The climbing nudged elastic band (CI-NEB) method *[43]* is used to locate the transition states. Six intermediate images are used in each CI-NEB pathway. Vibrational frequencies for the initial, transition and final states of the reactions are calculated and transition states are confirmed by the presence of one imaginary frequency. Zero-point energy (ZPE) is calculated as ZPE $=\sum_i 1/2h\upsilon_i$ where h is Planck's constant and υ_i is the frequency of the i^{th} vibrational mode. The adsorption energies (E_{ad}) for all possible adsorbates are calculated using the following equation.

$$E_{ad} = E_{cluster\text{-}molecule} - (E_{cluster} + E_{molecule}) \tag{6.1}$$

where $E_{cluster-molecule}$, $E_{cluster}$ and $E_{molecule}$ are the energies of the adsorbed species on cluster, the platinum cluster and the corresponding molecular species. The reaction energy (enthalpy) is calculated using the total energy difference between the products and the reactants. Thus negative reaction energy suggests the exothermic nature of the reaction whereas positive reaction energy suggests the endothermic nature of the reaction. Activation barrier are calculated by the energy difference between the transition and the initial state. The reaction energy and activation barrier is calculated with zero point energy (ZPE) correction and entropy contribution but we have tabulated without ZPE and entropy contribution so that vis-à-vis comparison can be made with previous theoretical studies. However, the ZPE and entropy corrected activation barrier has been also provided separately. The ZPE correction and entropy contribution is included for activation free energy calculation for temperature dependent rate constant.

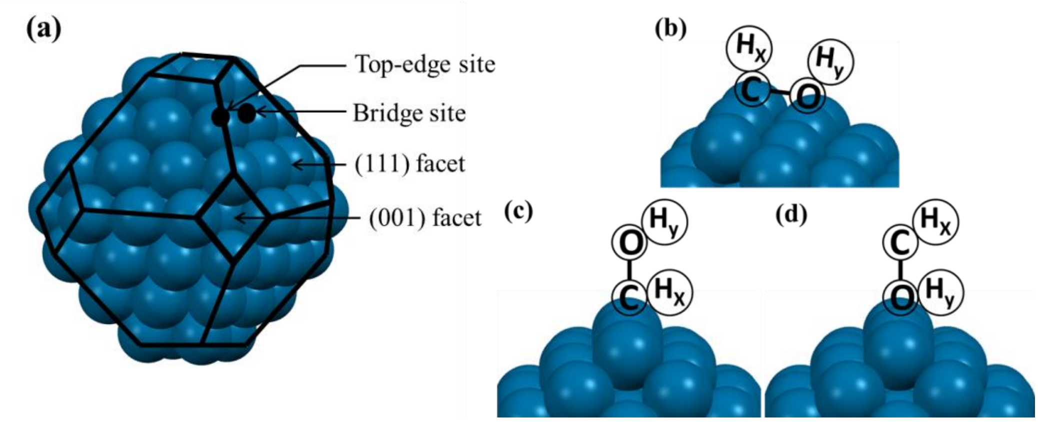

Figure 6.1. (a) Cuboctahedral Pt_{79} nanocluster enclosed by fourteen facets. Intermediates adsorb in a (b) di-sigma fashion and at the top edge site via (c) C- and (d) O-centre

6.3 Results and Discussion

The results and discussion part is divided into four sections for the successive dehydrogenation of four methanol hydrogens. The various intermediates involved for the first (CH_2OH, CH_3O), second (CHOH, CH_2O), third (CHO, COH) and fourth methanol dehydrogenation (CO) steps are discussed as following.

In the beginning of each step, we have discussed the adsorption type, relative stabilities, and adsorption energy of all the intermediates involved for their respective dehydrogenation steps. The intermediates are studied at the three active sites (edge, bridge and hollow) adsorbed through C- and O-atoms. The reaction energy and C-/O-H bond activation barriers for each of those processes are calculated and discussed in their respective sections to understand their reaction thermodynamics. At the end of each section, our calculated results are compared with the available experimental and theoretical data to understand and compare the catalytic activity of our model system.

From here on, methanol, methoxy, hydroxymethyl, hydroxymethelene, formaldehyde, formyl, hydroxymethylidyne, carbon monoxide represented as $*CH_3OH$, $*CH_3O$, $*CH_2OH$, $*CHOH$, $*CH_2O$, $*CHO$, $*COH$, and $*CO$ when adsorbed through C-atom and $*OHCH_3$, $*OCH_3$, $*OHCH_2$, $*OHCH$, $*OCH_2$, $*OCH$, $*OHC$, $*OC$ when adsorbed through O-atom. Similar convention used for the bridge structures ($*CH_3OH$, $*CH_3O$ etc.) as used for the intermediates adsorbed through C-centre at edge position.

6.3.1 First Dehydrogenation Step

Here we have studied the first dehydrogenation mechanism of the methanol which will lead to the formation of hydroxymethyl ($*CH_2OH$) or methoxy ($*CH_3O$) intermediates. So in the beginning, we have discussed about the adsorption behaviour, adsorption energy and relative energetics of all the intermediates (methanol, hydroxymethyl, and methoxy) involved in the first dehydrogenation step and then discussed about their reaction thermodynamics and activation barrier for each of these (C-H/O-H) bond dissociation process on the nanocluster's surface.

6.3.1.1 Adsorption Type and Energetics

Methanol ($*CH_3OH$): The dehydrogenation process of methanol starts with its adsorption on the nanocluster's (111) surface. The methanol molecule calculated to be a minima at the top edge position adsorbed as $*CH_3OH$ (Figure 6.2a) and $*OHCH_3$ (Figure 6.2b) with adsorption energy of -0.24, -0.38 eV respectively. The other structure (Figure 6.2c) calculated to be a minimum is the one adsorbed at the bridge site with adsorption energy of -0.19 eV. Their relative energetic study shows that $*OHCH_3$ is the most stable structure when adsorbed through O-centre and stable by 0.18 and 0.19 eV than the CH_3OH adsorbed at the edge and bridge position respectively. The Pt-C and Pt-O distances at the top edge position adsorbed as $*CH_3OH$ and $*OHCH_3$ structures are 3.24 Å and 2.52 Å respectively but at the bridge position, $*CH_3OH$ adsorbed via di-sigma manner where methanol interacts weakly with the nanocluster surface through the C-H bond. In the bridge structure, the Pt-H, Pt-C and Pt-O bond distances are 2.83 Å, 3.32 Å and 3.59 Å respectively (Figure 6.2c). Such structural parameters reflect that the methanol molecule interacting weakly with the nanocluster's surface. Interestingly, our relative energetic study shows methanol adsorbed at the top edge site (through C-atom) and bridge site are equally stable though methanol interacts weakly with the nanocluster while adsorbed at the bridge position.

Shustorovich *[44]* reported that saturated molecules prefer to bind at the top position of the metal surface, thus agreeing well with our results. The C-O-H bond angle of the methanol changes from 107.72° to 109.34° after adsorption through O-atom, indicating that there is an interaction between the methanol oxygen and platinum of the nanocluster. Slab model surface calculations showed that methanol adsorption is most favourable when it binds through O-atom on the top edge site of Pt(111) surface. Mavrikakis et al. showed that methanol weakly adsorbs through O-atom with adsorption energy of -0.33 eV *[22]*.

In our calculation, the optimized Pt-O bond distance is of 2.52 Å which is in close agreement with the Pt-O bond distance of 2.59Å *[19]* reported previously. The cluster model calculation by Ishikawa and Goddard et al. reported that methanol binds weakly to the top site of platinum through O-atom with binding energy of -0.66 eV *[18]* and -0.64 eV *[24]* respectively. Higher adsorption value is due to the different size of clusters (Pt_{10} and Pt_8) used for their model study. Experimentally, methanol reported to be adsorbed weakly at the top site of Pt(111) through O-atom *[8-9,27]* with binding energy of ~-0.40-0.50 eV *[9,13]*. Our calculated results also suggest that methanol binds weakly to the cluster and among the different binding sites of the cluster, methanol binds most strongly at the top edge site through O-atom with adsorption energy of -0.38 eV, thus supporting the trend of previous experimental and theoretical results.

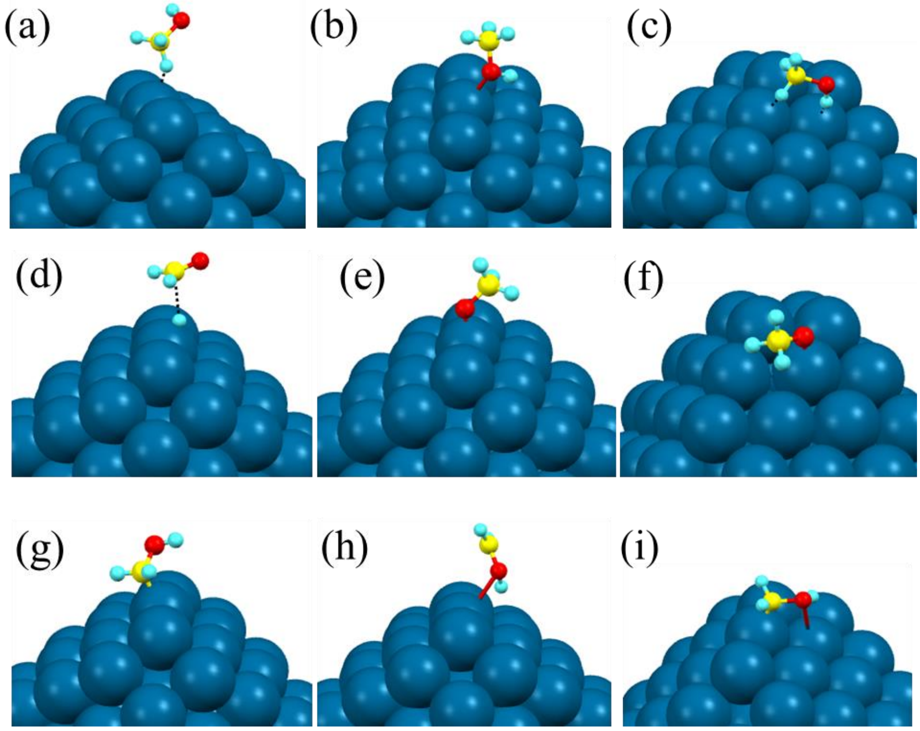

Figure 6.2: Adsorbed methanol at edge via (a) C-atom and (b) O-atom; (c) bridge position. Methoxy at edge via (d) C-atom and (e) O-atom; (f) bridge position. Hydroxymethyl at edge via (g) C-atom and (h) O-atom; (i) bridge position.

Methoxy (*CH_3O): Methoxy is an important intermediate during methanol dehydrogenation process. *OCH_3 is formed through the O-H bond scission of *$OHCH_3$ with adsorption energy of -2.47 eV. In the adsorbed *OCH_3 structure (Figure 6.2e), the Pt-O bond distance (1.97 Å) is shorter than the Pt-O (2.52 Å) bond distance in methanol. The CH_3O structure calculated to be a minima where one of the C-H bond strongly interacting with the nanocluster with C-H bond length of 2.15 Å (Figure 6.2d). *CH_3O binds at the bridge-site in a di-sigma manner with adsorption energy of -2.25 eV. In this di-sigma manner, one hydrogen atom of –CH_3 oriented to the nanocluster, forming Pt-H, Pt-C and Pt-O bond distances of 2.09 Å, 2.99 Å and 2.01 Å respectively (Figure 6.2f). Therefore, we find the adsorption energy is higher by 0.22 eV at the top edge position than at the bridge position, which is also reflected from the Pt-O bond distances at the edge (1.97 Å) and the bridge (2.01 Å) position respectively. Relative energetic study shows, $*OCH_3$ at the top edge site is energetically more stable by 0.30 eV than $*CH_3O$ at the bridge site. Both bond distances and relative energetics suggest about the favourable binding of $*OCH_3$ over $*CH_3O$. Interestingly, both at the bridge and edge position, methyl group interact weakly with the nanocluster. In slab model calculation, Mavrikakis et al. *[17]* showed that methoxy binds through oxygen at the top position with Pt-O distance of 2.03 Å and adsorption energy of -1.54 eV while Desai et al. *[19]* reported that methoxy binds through oxygen at the bridge position with average Pt-O distances of 2.51 Å and adsorption energy of -1.66 eV. Recently, Kramer et al. *[45]* also suggested about the top-site binding of methoxy through oxygen atom with the adsorption energy of -1.59 eV. Goddard et al. also suggested the binding of methoxy at the top site with adsorption energy of -1.07 eV *[24]* on Pt_8 cluster. Ishikawa et al. *[18]* obtained site preference for methoxy in a three-fold hollow site with the binding energy of -2.07 eV in their cluster model study. Though there are many studies on the favourable binding site of the methoxy group but most of them reported that methoxy binds through the O-atom, which agrees well with our calculated results.

Hydroxymethyl ($*CH_2OH$): We find $*CH_2OH$ binds at the top edge position with adsorption energy of -2.76 eV and Pt-C bond distance of 2.08 Å (Figure 6.2g). It even binds weakly as $*OHCH_2$, where O-atom bridging between the two platinum centres with Pt-O bond distances of 3.70 Å and 3.10 Å (Figure 6.2h) and adsorption energy of -1.07 eV. Longer Pt-O bond distances show their reluctance of binding through the O-atom. At the top edge position, $*CH_2OH$ (Figure 6.2i) structure is more stable by 1.55 eV than $*OHCH_2$, suggesting its preference of binding through C-atom. Our findings are well in agreement with the extended Huckel calculation by Hoffman et al. *[46]* that unsaturated radical species such as carbon in hydroxymethyl will certainly form a covalent bond with the metal of the cluster’s surface. The $*CH_2OH$ adsorption on Pt(111) surface reported by various groups and their calculated adsorption energy values are -1.98 eV *[17]*, -2.17 eV *[19]*, and -2.08 eV *[45]* while adsorbed at the top Pt site through C-atom. Cluster model calculations reported higher adsorption energy of -2.51 eV *[18]* and -2.85 eV *[24]* for the similar type of geometries. Therefore, previous studies on slab and cluster models support our findings and our calculated value of adsorption energy agrees well with the cluster model study.

6.3.1.2 Reaction Energy and Activation Barriers

In this part, methanol dehydrogenation energetics related to the formation of methoxy and hydroxymethyl has been discussed. We have calculated the reaction energy and activation barrier for the following possible elementary steps based on their adsorption behaviour.

$*CH_3OH \rightarrow *CH_2OH + *H$ (Step 6.1)

$*OHCH_3 \rightarrow *OHCH_2 + *H$ (Step 6.1a)

$*CH_3OH \rightarrow *CH_3O + *H$ (Step 6.2)

$*OHCH_3 \rightarrow *OCH_3 + *H$ (Step 6.2a)

Table 6.1: Reaction energy (eV) and activation barrier (eV) for the following elementary steps (Step 6.1-2 and Step 6.1a-2a) while adsorbed vertically through C- and O-atom and parallely at the bridge site.

Elementary Reactions	**Edge**				**^{1}Bridge**	
	^{1}C-bonded		**^{2}O-bonded**			
	Reaction Energy	**Activation Barrier**	**Reaction Energy**	**Activation Barrier**	**Reaction Energy**	**Activation Barrier**
$^{1}CH_3OH \rightarrow CH_2OH+H$ $^{2}OHCH_3 \rightarrow OHCH_2+H$	-0.57	0.31	1.36	1.38	-0.29	0.29
$^{1}CH_3OH \rightarrow CH_3O+H$ $^{2}OHCH_3 \rightarrow OCH_3+H$	0.47	0.64	0.29	0.62	0.41	0.65

C-H bond activation

Edge vs. bridge site:

At the edge position, the C-H bond activation from *CH_3OH to the formation of *CH_2OH calculated to be exothermic by -0.57 eV (step 6.1) and endothermic by 1.36 eV (step 6.1a) if the intermediates (*CH_3OH and *$OHCH_2$) are adsorbed at the top edge position through C and O-centre respectively. The calculated activation barriers are 0.31 eV and 1.38 eV respectively. Therefore, the C-H bond activation is favourable at the edge position when the intermediate is adsorbed through C-centre.

At the bridge position, C-H bond dissociation for the formation of *CH_2OH calculated to be exothermic by -0.29 eV (step 6.1) and the activation barrier is of 0.29 eV. Therefore, the C-H bond activation barrier of methanol at the bridge position (0.29 eV) is lower and very much comparable with the top edge site (0.31 eV) when adsorbed through C-centre.

It is clear from the reaction energies and activation barriers that C-H bond activation is very much favourable at the bridge position while the intermediates are adsorbed in a di-sigma manner. It is also clear that C-H bond activation is very much favourable when methanol adsorbed through C-atom (*CH_3OH) than through O-atom (*$OHCH_3$). Recently Kramer et al. *[45]* reported that the activation barrier for this process is of 0.55 eV when it binds through C-atom. Greeley et al. *[22]* reported the activation barrier of 0.67 eV for the C-H bond activation of methanol when it binds through C-atom. Cluster model study by Ishikawa et al. *[18]* showed the activation barrier of 0.42 eV for C-H activation process when adsorbed through C-atom. Therefore, in all the previous studies the C-H bond activation barrier reported to be lowest when the intermediates are adsorbed though carbon atom but we report the C-H bond activation barrier is the lowest (0.29 eV) when the intermediates are adsorbed in a di-sigma manner.

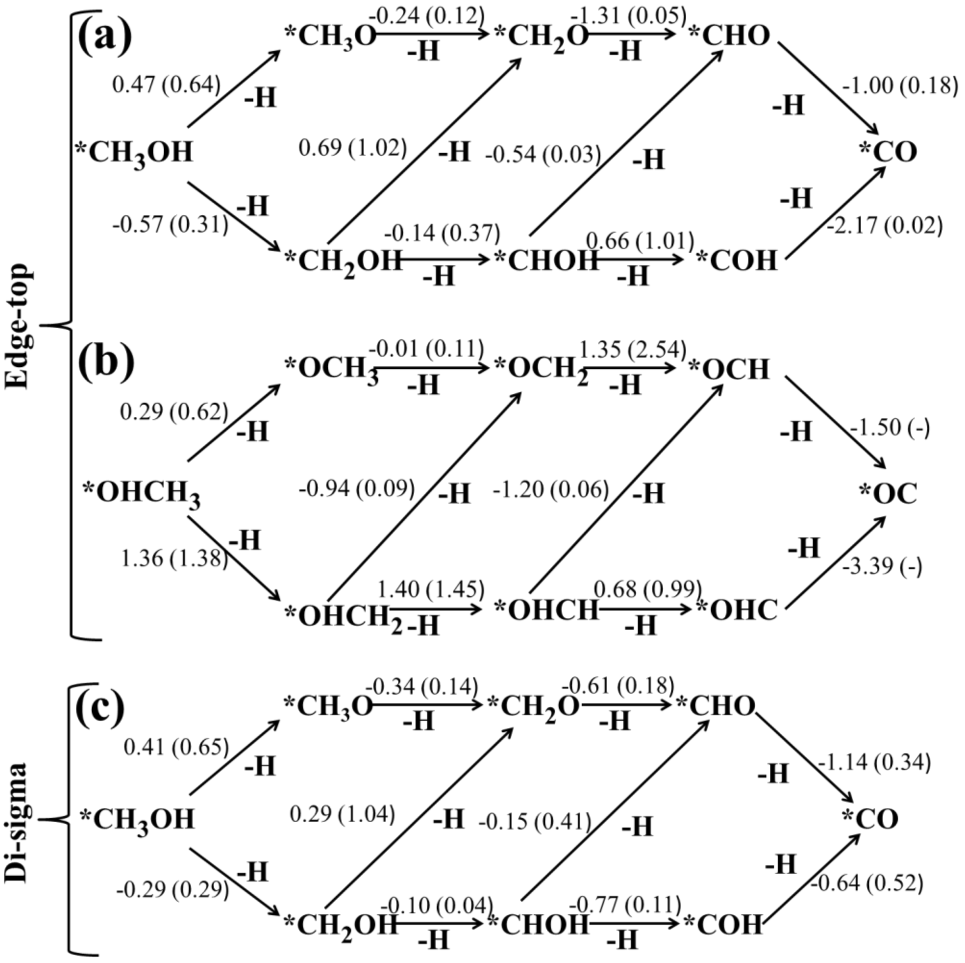

Scheme 6.1: The reaction energies (eV) and activation barriers (eV, values in parenthesis) for the successive methanol dehydrogenation at different binding sites (a) adsorbed through C-atom and (b) O-atom at top edge position and (c) bridge position.

O-H bond activation:

Edge vs. bridge site:

The O-H bond dissociation is endothermic by 0.29 eV (Step 6.2) and 0.47 eV when adsorbed through O- and C-centre respectively (Step 6.2-2a). The activation barriers for these two processes are 0.62 eV and 0.64 eV respectively.

The reaction (Step 6.2) is endothermic by 0.41 eV and the calculated activation barrier is of 0.65 eV while adsorbed in a di-sigma manner. Interestingly, the O-H bond activation barriers are very much comparable whether the intermediates are adsorbed through O- (0.62 eV), C centre (0.64 eV) or in a di-sigma (0.65 eV) manner.

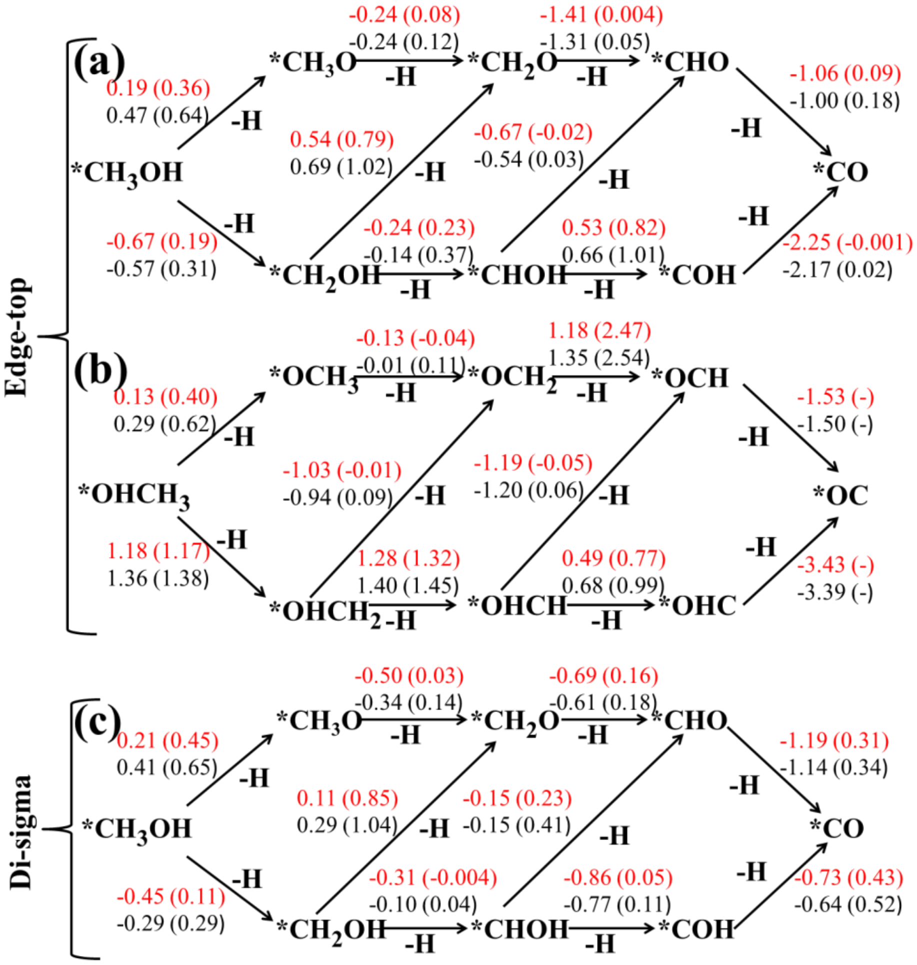

Scheme 6.2: The reaction energies (eV) and activation barriers (eV, values in parenthesis) for the successive methanol dehydrogenation at different binding sites (a) adsorbed through C-atom and (b) O-atom at top edge position and (c) bridge position.[Values in the black colour are without ZPE and entropy correction whereas red colour are including ZPE and entropy correction]

C-H vs. O-H bond activation:

Our reaction thermodynamics and activation barrier study shows C-H bond activation is very much favourable over O-H bond activation at the catalysts surface. Such C-H bond activation preferences over O-H bond activation can be explained from the following findings.

Firstly, the produced *CH_2OH binds more strongly than *CH_3O intermediates at the bridge and edge positions respectively. Secondly, the C-H bond energies are lower than the O-H bond energies. The calculated gas phase reaction energy for the C-H bond activation is 3.98 eV whereas O-H bond activation is 4.23 eV, suggesting that C-H activation is more favourable over O-H activation (Scheme 6.3). In fact the adsorption behaviour of *CH_3OH also suggests its preference for dehydrogenation through C-H bond activation as one of the methanol carbon hydrogen (C-H = 1.13 Å) orients towards the surface of the nanocluster and interacts strongly.

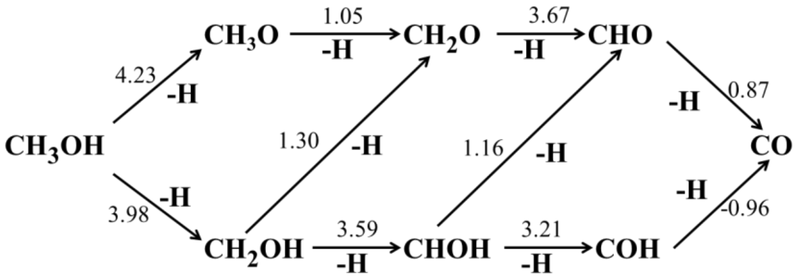

Scheme 6.3: Gas phase energetic (energy in eV) for the complete methanol dehydrogenation pathway.

The preference of C-H bond activation over O-H activation, to form *CH_2OH is reported in the literature using Pt(111) surface and cluster model study. Desai et al. *[19]* showed that C-H bond activation is exothermic by -0.16 eV whereas O-H bond activation is endothermic by 0.66 eV over Pt (111) surfaces. Mavrikakis et al. *[22]* reported the activation barrier of 0.81 eV for O-H bond activation and 0.67 eV for C-H bond activation. Kramer, Cui-Yu and Desai et. al. reported O-H bond activation barrier on Pt (111) surfaces is of 0.81 eV *[45]*, 0.85 eV *[20]*, and 1.47 eV *[19]* respectively. Ishikawa et al. *[18]* in their cluster model study reported that the formation of hydroxymethyl (activation energy 0.42 eV) is more favourable than the methoxy formation (activation energy 0.77 eV).

Therefore, our calculations show the same trend as reported on Pt(111) surfaces and platinum cluster model study that C-H bond activation is more favourable than the O-H bond activation. Here also, we find our calculated activation barrier is the lowest (0.29 eV) while comparing with all the values reported previously. Therefore we assume such Pt cub-octahedral nanocluster could be an excellent catalysis for C-H bond activation.

On the other hand, when intermediates are adsorbed through O-atom, O-H bond activation (barrier = 0.62 eV) is favourable over C-H bond activation (barrier = 1.38 eV) due to the stronger adsorption of $*OCH_3$ (adsorption energy = -2.47 eV) than $*OHCH_2$ (adsorption energy = -1.07 eV). In fact their relative energetic study also shows $*OCH_3$ intermediate is more stable (by 1.04 eV) than $*OHCH_2$.

6.3.2. Second Dehydrogenation Step

In this step, we have studied the second successive dehydrogenation step of methanol which lead to the formation of hydroxymethelene (*CHOH) and formaldehyde ($*CH_2O$) intermediates.

6.3.2.1 Adsorption Type and Energetics:

Hydroxymethelene (*CHOH): We find *CHOH (Figure 6.3a), is stable at the top edge position with adsorption energy of -3.67 eV whereas *OHCH binds weakly at the same site with adsorption energy of -0.25 eV (Figure 6.3b). The Pt-C and Pt-O bond distances are 1.89Å and 2.72Å in case of *CHOH and *OHCH intermediates respectively. *CHOH intermediate calculated to be more stable by 3.03 eV than the *OHCH intermediate. Both adsorption energy and relative energy study shows *CHOH intermediate is the most preferred. *CHOH adsorbed intermediate calculated to be stable at the bridge position too with adsorption energy of -4.86 eV, in a di-sigma manner with Pt-C and Pt-O bond distances of 2.03Å and 2.72Å respectively (Figure 6.3c). The *CHOH structure is 0.15 eV more stable in the bridge position than *CHOH at the top edge position. As *CHOH has a divalent C-atom, it is expected to be stable at the bridge position to fulfil its covalency (become tetravalent), thus favouring the bridged structure.

Slab model study reported that *CHOH binds with equal adsorption energy in the top and bridge position of the Pt(111) surface with adsorption energy of -3.24 eV *[17]*. A recent study *[45]* on Pt(111) surface shows that it prefers to bind at the bridge position with binding energy -3.39 eV. However, study on cluster surface shows that *CHOH is stable at the top position with adsorption energy of -3.79 eV which is in close agreement with our calculated adsorption energy (-3.67 eV) of *CHOH at the top edge position *[18]*. Another cluster model calculation *[24]* shows that it is most preferred at the bridge position with adsorption energy of -3.68 eV but our calculated adsorption value is maximum (4.86 eV) when adsorbed in a di-sigma manner.

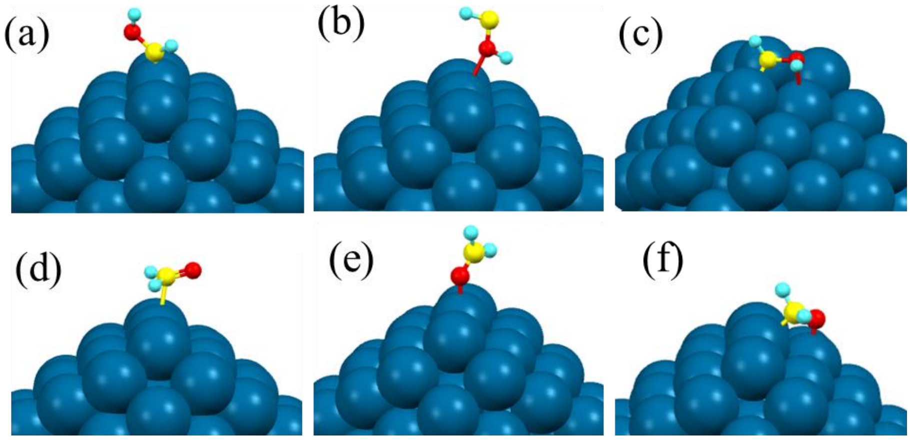

Figure 6.3: Adsorbed hydroxymethelene at edge via (a) C-atom and (b) O-atom; (c) bridge position. Formaldehyde at edge via (d) C-atom and (e) O-atom; (f) bridge position.

Formaldehyde ($*CH_2O$):

We find $*CH_2O$ is also most stable when it adsorbed in a di-sigma manner, at the bridge position (Figure 6.3f) with binding energy of -1.94 eV. Here, the Pt-O and Pt-C bond distances are 2.05Å and 2.11Å respectively. In case of edge position, OCH_2 binds strongly with the nanocluster with adsorption energy of -0.55 eV (Figure 6.3e), whereas $*CH_2O$ binds weakly with adsorption energy -0.17 eV (Figure 6.3d). The Pt-C and Pt-O bond distances are 2.67 Å and 2.18 Å in case of $*CH_2O$ and $*OCH_2$ respectively. The bridge $*CH_2O$ intermediate is energetically most stable by 0.37 eV and 0.10 eV than adsorbed through C and O-centre respectively. Higher adsorption value of $*CH_2O$ at the bridge position (adsorption energy -1.94 eV) than edge position (adsorption energy -0.17 eV) is due to the CO group of formaldehyde interacting more strongly with the surface of the nanocluster. This is more clear from the C-O bond distance of 1.35Å, 1.22Å and 1.23Å for the bridge, top edge $*CH_2O$ and

*OCH intermediates respectively. So such bond elongation at the bridge site justifies about the charge transfer between the C-O group and the platinum nanocluster.

Slab model surface calculation *[19]* on Pt(111) showed that formaldehyde tend to bind at the bridge position in a di-bridge fashion with adsorption energy of -0.50 eV where the Pt-O and Pt-C bond lengths are of 2.12Å and 2.06Å respectively. Others slab model calculation also reported similar kind of binding behaviour with the adsorption energy of -0.43 eV *[45]* and -0.50 eV *[17]*. Cluster model calculation *[24]* also reported about the di-sigma bonding behaviour of formaldehyde with adsorption energy of -0.41 eV. Therefore our result such as di-sigma bonding preference of formaldehyde agrees well with previous reports.

6.3.2.2 Reaction Energies and Activation Barriers

In the second step, the formed methoxy ($*CH_3O$) and hydroxymethyl ($*CH_2OH$) intermediate can further undergo C-H and O-H bond activation. C-H bond activation on methoxy ($*CH_3O$) and hydroxymethyl ($*CH_2OH$) leads to the formation of formaldehyde ($*CH_2O$) and hydroxymethelene (*CHOH) intermediates respectively whereas hydroxymethyl ($*CH_2OH$) can undergo only O-H bond activation to form formaldehyde ($*CH_2O$). The possible elementary steps are shown as following (steps 6.3-5 and 6.3a-5a).

$*CH_2OH \rightarrow *CHOH + *H$ (Step 6.3)

$*OHCH_2 \rightarrow *OHCH + *H$ (Step 6.3a)

$*CH_3O \rightarrow *CH_2O + *H$ (Step 6.4)

$*OCH_3 \rightarrow *OCH_2 + *H$ (Step 6.4a)

$*CH_2OH \rightarrow *CH_2O + *H$ (Step 6.5)

$*OHCH_2 \rightarrow *OCH_2 + *H$ (Step 6.5a)

Table 6.2: Reaction energy (eV) and activation barrier (eV) for the following elementary steps (Step 6.3-5 and Step 6.3a-5a) while adsorbed vertically through C- and O-atom and parallely at the bridge site.

Elementary Reactions	**Edge**				**^{1}Bridge**	
	^{1}C-bonded		**^{2}O-bonded**			
	Reaction Energy	**Activation Barrier**	**Reaction Energy**	**Activation Barrier**	**Reaction Energy**	**Activation Barrier**
$^1CH_2OH \rightarrow CHOH+H$ $^2OHCH_2 \rightarrow OHCH+H$	-0.14	0.37	1.40	1.45	-0.10	0.04
$^1CH_3O \rightarrow CH_2O+H$ $^2OCH_3 \rightarrow OCH_2+H$	-0.24	0.12	-0.01	0.11	-0.34	0.14
$^1CH_2OH \rightarrow CH_2O+H$ $^2OHCH_2 \rightarrow OCH_2+H$	0.69	1.02	-0.94	0.09	0.29	1.04

C-H bond activation

Edge vs. bridge site:

At the edge position, $*CH_2OH$ can undergo C-H bond activation to form *CHOH. The reaction (step 6.3) is calculated to be exothermic by -0.14 eV and endothermic by 1.40 eV when the intermediates are adsorbed through C (step 6.3) and O-centre (step 6.3a) respectively. The calculated activation barriers for the step 6.3 and 6.3a are 0.37 eV and 1.45 eV respectively.

Similarly, $*CH_3O$ can undergo C-H bond activation to form $*CH_2O$ (step 6.4) while adsorbed through C- and O-centre respectively. The reaction energy and activation barriers are calculated to be -0.24 eV and 0.12 eV for C-centre and -0.01 and 0.11 eV for O-centre respectively. Kramer et al. *[45]* reported the activation barrier of 0.19 eV for the $*OCH_2$ formation from $*OCH_3$, agrees well with our results.

On the other hand, at the bridge site, the C-H activation from $*CH_2OH$ (step 6.3) and $*CH_3O$ is exothermic by -0.10 eV and -0.34 eV respectively. The activation barriers for these two steps are 0.04 eV and 0.14 eV respectively. Therefore, the C-H bond activation barrier is the lowest (0.04 eV) when intermediates adsorbed in a di-sigma manner.

Mavrikakis et al. *[22]* found the activation barrier of 0.25 eV for the decomposition of methoxy over Pt(111) surface. Cui-Yu et al. *[20]* found the activation barrier of 0.27 eV for the bridge position. Therefore our calculated activation barrier is far lower than what reported in the literature, shows the excellent catalytic activity of the Pt (111) facet of the nanocluster.

O-H bond activation

Edge vs. bridge site:

The O-H bond activation of $*CH_2OH$ (step 6.5-6.5a) calculated to be endothermic and exothermic by 0.69 eV and -0.94 eV when intermediates are adsorbed through C- and O-centre respectively. The activation barriers for these two steps are 1.02 eV (step 6.5) and 0.09 eV (step 6.5a) respectively. In case of adsorbed hydroxymethyl ($*CH_2OH$), hydroxyl group does not interact with the cluster, thus difficult for O-H bond dissociation, resulting in higher endothermicity (0.69 eV) and activation barrier (1.02 eV).

At the bridge site, the O-H bond activation of $*CH_2OH$ is endothermic by 0.29 eV and activation barrier for this process is of 1.04 eV. Therefore, the $*CH_2O$ formation at the bridge site is not favourable.

C-H vs. O-H bond activation:

It is clear from the activation barriers that at the edge and bridge position, *CHOH formation via C-H bond activation is more preferable than the $*CH_2O$ formation via O-H bond activation. Reaction energy values suggest the same trend. Interestingly, when it binds through oxygen atom, O-H bond activation (formation of $*OCH_2$) becomes more favourable over C-H bond activation (formation of *OHCH). This can be due to the following reasons. Firstly, $*CH_2OH$ adsorbs very strongly (-2.76 eV) than $*OHCH_2$ (-1.07 eV), thus favouring its dehydrogenation. Secondly, the O-H bond distance in the adsorbed $*OHCH_2$ is 1.01 Å, which is longer than in the gas-phase geometry (0.97 Å), showing its tendency to dehydrogenate via O-H bond activation. Therefore, such adsorption fashion favours the O-H bond activation over C-H bond activation. Furthermore, $*OCH_2$ is energetically more stable (by 0.27 eV) over $*CH_2O$.

However, the higher activation barrier of 1.38 eV for the first C-H bond activation of methanol to the formation of $*OHCH_2$ in the first dehydrogenation step (step 6.1a) might not allow further dehydrogenation to the formation of OCH_2 from $OHCH_2$ at this position in spite of its lower activation barrier (0.09 eV).

It is clear from the activation barriers of the first dehydrogenation steps (step 6.1-1a, 6.2-2a) and second dehydrogenation steps (step 6.3-3a, 6.4-4a, 6.5-5a) that $*CH_3OH \rightarrow *CH_2OH \rightarrow *CHOH$ is the most favourable path at the bridge position. But at the edge position, reaction is more favourable through $*CH_3OH \rightarrow *CH_2OH$ followed by $*CH_3O \rightarrow *CH_2O$ which is in agreement with the study of Desai et al. who reported that although methanol prefers to dehydrogenate via C-H bond activation forming hydroxymethyl but in the subsequent step methoxy intermediate prefers to form formaldehyde via C-H bond activation. In contrast, $*OHCH_3 \rightarrow *OCH_3 \rightarrow *OCH_2$ is the most favourable pathway when intermediates are adsorbed through O-atom.

6.3.3. Third Dehydrogenation Step

Here, we have studied the dehydrogenation of the third hydrogen of methanol which lead to the formation of formyl (*CHO) and hydroxymethylidyne (*COH) intermediates from the formaldehyde ($*CH_2O$) and hydroxymethelene (*CHOH) intermediates.

6.3.3.1 Adsorption Type and Energetics

Formyl (*CHO):

*CHO is adsorbed strongly in the edge position (Figure 6.4a) with adsorption energy of -3.03 eV and Pt-C bond distance of 1.96 Å. In contrast, *OCH binds very weakly (Figure 6.4b) with adsorption energy of -0.60 eV at the top edge position. In the bridge position, *CHO intermediate adsorbs in a di-sigma way (Figure 6.4c) with adsorption energy of -3.47 eV. In the bridge position, Pt-C, Pt-O and C-O distances are 2.07Å, 2.15Å and 1.29 Å respectively. Elongation of C-O bond occurs from 1.22 Å to 1.29 Å, suggesting the change of hybridisation on the carbon centre. Surprisingly, *CHO intermediate calculated to be most stable at the edge position by 0.08 eV than the bridge position though the adsorption energy is higher at the bridge position.

Previously Kramer et al. *[45]* reported that formyl binds most preferably through C-atom at the top site of the Pt(111) surfaces, with adsorption energy of -2.29 eV whereas Desai et al. *[19]* reported that formyl prefers to adsorb in a di-sigma manner with the adsorption energy -2.45 eV. Gomes et al. *[47]* found that formyl adsorbed at the bridge site through C-atom with binding energy of -2.61 eV. Previous cluster model study reported the adsorption energy of -2.71 eV *[24]* and -2.84 eV *[18]* for the binding of formyl through C-atom on the top site of the nanocluster surface.

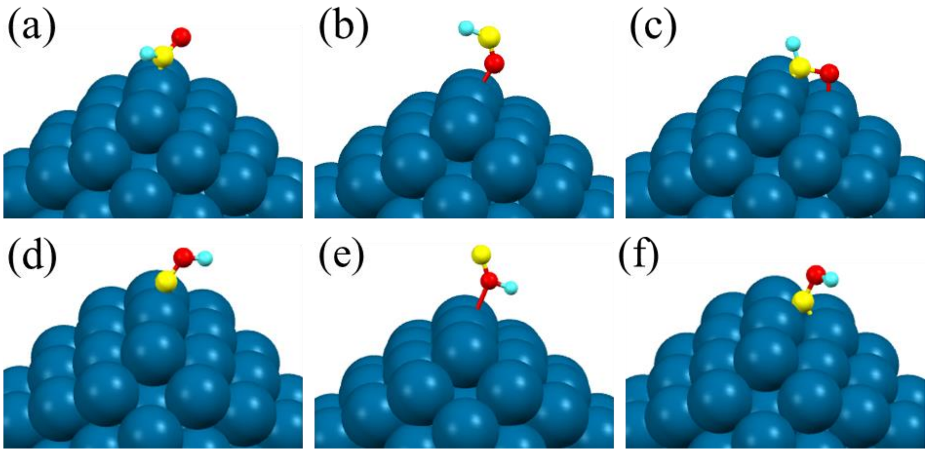

Figure 6.4: Adsorbed formyl at edge via (a) C-atom and (b) O-atom; (c) bridge position. Hydroxymethylidine at edge via (d) C-atom and (e) O-atom; (f) bridge position.

Hydroxymethylidyne (*COH):

In our study, hydroxymethylidyne adsorps at the top site of the edge position with adsorption energy of -3.94 eV and -0.63 eV for *COH (Figure 6.4d) and

*OHC (Figure 6.4e) structures respectively. The Pt-C and Pt-O bond distances in these two structures are 1.78Å and 2.75Å respectively. The structure is not stable at the bridge position. On the other hand, the *COH calculated to be a minima at the hollow site of the Pt(111) facet with adsorption energy of -5.67 eV and Pt-C bond distances of 2.02Å (Figure 6.4f) respectively. Interestingly, the intermediate is most stable at the hollow site (by 1.58 eV) than the edge site.

Slab model calculation by Kramer et al. *[45]* reported that COH preferably binds at the hollow site through C-atom with adsorption energy of -4.70 eV. Cluster model calculation by Goddard et al. *[24]* reported that COH prefers to bind at the hollow site through C-atom with binding energy of -5.25 eV. Another cluster model study by Ishikawa et al. *[18]* found strong adsorption through C-atom with the adsorption energy of -3.05 eV and -4.86 eV at the top and hollow site respectively.

6.3.3.2. Reaction Energies and Activation Barriers

The formed formaldehyde and hydroxymethelene intermediate can further undergo C-H and O-H bond activation. C-H bond activation leads to the formation of formyl and hydroxymethylidyne from formaldehyde and hydroxymethelene respectively whereas only hydroxymethelene can undergo O-H bond activation to form formyl intermediate. The proposed elementary steps are given as following (steps 6.6-8 and 6a-8a).

*CHOH→ *COH+*H (Step 6.6)

*OHCH→ *OHC+*H (Step 6.6a)

*CH$_2$O→ *CHO+*H (Step 6.7)

*OCH$_2$→ *OCH+*H (Step 6.7a)

*CHOH→ *CHO+*H (Step 6.8)

*OHCH→ *OCH+*H (Step 6.8a)

Table 6.3: Reaction energy (eV) and activation barrier (eV) for the following elementary steps (Step 6.6-8 and Step 6.6a-8a) while adsorbed vertically through C- and O-atom and parallely at the bridge site.

Elementary Reactions	**Edge**				**^{1}Bridge**	
	^{1}C-bonded		**^{2}O-bonded**			
	React-ion Energy	**Activation Barrier**	**Reaction Energy**	**Activation Barrier**	**Reaction Energy**	**Activation Barrier**
^{1}CHOH→ COH+H ^{2}OHCH→ OHC+H	0.66	1.01	0.68	0.99	-0.77	0.11
^{1}CH$_2$O→ CHO+H ^{2}OCH$_2$→ OCH+H	-1.31	0.05	1.35	2.54	-0.61	0.18
^{1}CHOH→ CHO+H ^{2}OHCH→ OCH+H	-0.54	0.03	-1.20	0.06	-0.15	0.41

C-H bond activation

Edge vs. bridge site:

*CHOH can undergo C-H bond activation to form *COH (step 6.6) with activation energy barrier of 1.01 eV and 0.99 eV while adsorbed through C- and O-centre respectively (step 6.6-6a). The reaction energies for these process are 0.66 eV (step 6.6) and 0.68 eV (step 6.6a) respectively. Both reaction energy and activation barrier value suggests that this process is not favourable at edge position irrespective of their binding mode. Ishikawa et al. reported the activation barrier of 0.53 eV for this process when the intermediates were bonded through C-atom.

The C-H activation on the *CH$_2$O intermediate (step 6.7) calculated to be exothermic by -1.31 eV with activation barrier of 0.05 eV. In contrast, when *OHC is formed from *OCH$_2$ (step 6.7a), the step becomes endothermic by 1.35 eV with the activation barrier of 2.54 eV. Therefore, the C-H activation on *CH$_2$O is very much favourable when adsorbed through C-atom.

At the bridge position, on the other hand, *CHOH undergoes C-H bond activation to form *COH (step 6.6) with activation barrier of 0.11 eV.

Reaction energy of this step is exothermic by -0.77 eV. $*CH_2O$ can also undergo C-H bond activation to form *CHO and the reaction is exothermic by -0.61 eV with activation barrier of 0.18 eV.

Therefore, the conversion of CHOH→COH is highly unfavourable at the edge position due to the high activation barrier whereas at the bridge position it is very much favourable. It is due to the different adsorption behaviour of the involved intermediates at the bridge position. At the bridge position, *COH adsorbs very strongly at the three-fold hollow site with the adsorption energy -5.67 eV, resulting the lower activation barrier for the process. For the same process, Kramer et al. reported the activation barrier of 0.56 eV.

O-H bond activation

Edge vs. bridge site:

The calculated O-H activation barrier for the formation of *CHO from *CHOH (step 6.8) intermediate is 0.03 eV and *OCH from *OHCH intermediate is 0.06 eV (step 6.8a). The reaction energies for these two process are -0.54 eV (step 6.8) and -1.20 eV (step 6.8a) respectively. Though the adsorption behaviour of *CHOH and *OHCH are different but activation energies are very much comparable for both the cases (step 6.8 and step 6.8a). This could be due to their comparable adsorption energies of the *CHO/*OCH intermediate and the *CHOH/*OHCH intermediate. Ishikawa et al. also reported the activation barrier of 0.44 eV for the same process when adsorbed through C-atom.

Rather at the bridge position, the activation barrier for the formation of *CHO from *CHOH is 0.41 eV and the reaction is exothermic by -0.15 eV. Activation barrier is high due to the strong adsorption behaviour (adsorption energy -4.86 eV) of *CHOH at the bridge position.

C-H vs. O-H bond activation:

It is clear from the calculated reaction energy and activation barrier values that C-H decomposition of $*OCH_2$ or *OHCH is not favoured when it binds through O-atom, due to the lower adsorption energy of the *OCH or *OHC intermediates. But the O-H bond activation step (Step 6.8a) is exothermic which could be due to the similarity in the adsorption behaviour of *OHCH (Figure 6.3b) and *OCH (Figure 6.4b) intermediates. The orientation of Trans *OHCH is similar with *OCH, resulting easy dehydrogenation from O-atom. Therefore its quite unlikely, the formation of *OHCH from *$OHCH_2$ intermediate due to high activation barrier 1.45 eV (step 6.3a), so the successive dehydrogenation steps from there on.

In case of *CHOH when adsorbed at the edge site, there are possibilities of formation of either *COH or *CHO through C-H or O-H bond activation respectively. Generally, the *COH formation is not favourable due to strong adsorption behaviour of *CHOH intermediate. However, this process is quite favourable at the bridge site with activation barrier of 0.11 eV, due to the very strong adsorption (-5.67 eV) behaviour of *COH at the three-fold hollow position. At the edge site, formation of *CHO becomes favourable either via O-H bond activation from *CHOH (step 6.8) or via C-H bond activation from *CH_2O (step 6.7). The C-H bond activation from *CH_2O intermediate calculated to exothermic (-1.31 eV) with low (0.05 eV, step 6.7) activation barrier.

At the bridge position, *CH_3OH→ *CH_2OH→*CHOH is the most favourable pathway up to second dehydrogenation step. The calculated activation barrier of third dehydrogenation step shows that the reaction proceeds via *CH_3OH→ *CH_2OH→ *CHOH→ *COH pathway. At the edge position, reaction proceed through *CH_3OH→*CH_2OH followed by *CH_3O→ *CH_2O→ *CHO.

6.3.4. Fourth Dehydrogenation Step

In this step, dehydrogenation pathways for the formation of carbon monoxide from the formyl and hydroxymethyl intermediates are discussed.

6.3.4.1 Adsorption Type and Energetics:

Carbon monoxide (*CO) and Hydrogen: The adsorption of carbon monoxide has been widely studied experimentally as well theoretically over Pt(111) surfaces. We find, it adsorbs at the top site of the edge position with adsorption energy of -2.21 and 0.04 eV while adsorbed as *CO (Figure 6.5a) and *OC (Figure 6.5b) structure respectively. The Pt-C and Pt-O bond distances in these structures are 1.94 Å and 2.51 Å respectively. In the bridge position, it binds through C-atom at the hollow site with adsorption energy of -2.29 eV where the Pt-C bond distance is of 2.11Å (Figure 6.5c).

On the other hand, hydrogen adsorbs at the bridge, hollow and top side of Pt(111) facet with adsorption energy of -4.50 eV, -4.33 eV and -4.40 eV respectively.

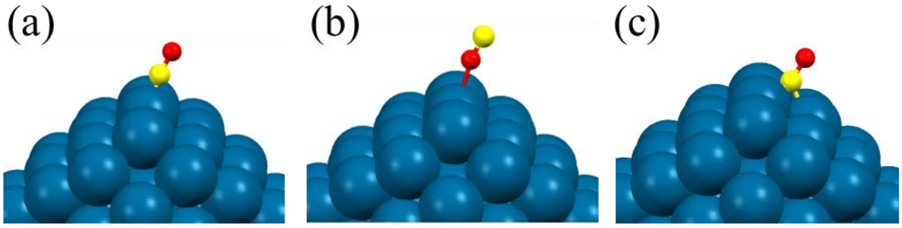

Figure 6.5: Adsorbed carbon-monoxide at edge via (a) C-atom and (b) O-atom; (c) three-fold hollow

6.3.4.2. Reaction Energy and Activation Barriers

Carbon monoxide (*CO) can be formed from formyl (*CHO) intermediate via C-H bond activation or from hydroxymethylidyne (*OCH) via O-H bond activation. The possible elementary steps are given as following (steps 6.9-10 and 6.9a-10a).

*CHO→ *CO + *H (Step 6.9)

*OCH→ *OC + *H (Step 6.9a)

*COH→ *CO + *H (Step 6.10)

*OHC→ *OC + *H (Step 6.10a)

Table 6.4: Reaction energy (eV) and activation barrier (eV) for the following elementary steps (Step 6.9-10 and Step 6.9a-10a) while adsorbed vertically through C- and O-atom and parallely at the bridge site.

Elementary Reactions	**Edge**				**^{1}Bridge**	
	^{1}C-bonded		**^{2}O-bonded**			
	Reaction Energy	**Activation Barrier**	**Reaction Energy**	**Activation Barrier**	**Reaction Energy**	**Activation Barrier**
^{1}CHO→ CO + H ^{2}OCH→ OC + H	-1.00	0.18	-1.50	**-**	-1.14	0.34
^{1}COH→ CO + H ^{2}OHC→ OC + H	-2.17	0.02	-3.39	-	-0.64	0.52

C-H bond activation

Edge vs. bridge site:

The formation of *CO from formyl is exothermic, irrespective of their binding through C- or O-atom. At the edge position, the C-H bond activation of *CHO calculated to be exothermic by -1.00 eV (step 6.9) and the barrier is 0.18 eV whereas reaction is exothermic by -1.50 eV when it binds through O-atom (step 6.9a). We could not locate the TS for the step 6.9a. In the bridge position, step 6.9 is calculated to be exothermic by -1.14 eV with the activation barrier of 0.34 eV.

O-H bond activation

Edge vs. bridge site:

The formation of *CO from COH (step 6.10 and step 6.10a) via O-H bond activation becomes highly exothermic. Step 6.10 is exothermic by -2.17 eV with the activation energy of 0.02 eV whereas step 6.10a is exothermic by -3.39 eV. We could not locate the TS for the step 6.10a. In the bridge position, step 6.10 is exothermic by -0.64 eV with the activation energy of 0.52 eV. The formation of *CO at the edge position is more favourable than at the bridge position due to the little longer O-H bond distance in *COH at the edge position (0.99Å) than at the bridge position (0.98Å).

C-H vs. O-H bond activation:

Our calculated reaction energies and activation barrier study show that at the edge position, the decomposition pathway is more favourable (Scheme 6.1a) as $*CH_3OH \rightarrow *CH_2OH \rightarrow *CHOH \rightarrow *CHO \rightarrow *CO$ and the reaction steps such as $CH_3OH \rightarrow *CH_3O$, $*CH_2OH \rightarrow *CH_2O$ and $CHOH \rightarrow *COH$ are least favourable.

Similarly, at the bridge position the methanol decomposition is most favourable (Scheme 6.1c) as $*CH_3OH \rightarrow *CH_2OH \rightarrow *CHOH \rightarrow *COH \rightarrow *CO$ and the reaction steps such as $CH_3OH \rightarrow *CH_3O$, $*CH_2OH \rightarrow *CH_2O$ and $CHOH \rightarrow *CHO$ are last favourable. Therefore in case of edge and bridge position, the difference in the most favoured pathway is in the first and last two steps. The methanol decomposition pathway is not favourable (Scheme 6.1b) if the intermediates are adsorbed through oxygen centre ($*OHCH_3$).

6.3.5 Temperature vs. Rate Constant

To check the effect of temperature on the methanol decomposition reaction, we have calculated the rate constants of the elementary reactions using the following equation

$$k = \frac{k_b T}{h}\left(\frac{P^0}{RT}\right)^{1-n} \exp\left[-\frac{\Delta G_m{}^{\#}}{RT}\right] \qquad (6.2)$$

where, k and T is the rate constant and reaction temperature and k_b, h, p^0, R, n and ΔG is the Boltzmann's constant, Planck's constant, standard atmospheric pressure and fundamental gas constant, number of reactants and zero-point energy corrected activation barriers respectively.

The methanol decomposition temperature ranges from 323K to 523K, hence the rate constants are calculated at T= 323, 423 and 523K and listed in Table 6.5-9. It is clear from the calculated rate constant values that the first two steps of the methanol decomposition reactions proceeds (Table 6.5-6) very fast when the intermediates are adsorbed parallely in a di-sigma manner. Interestingly, these two steps are reported to be the rate determining steps for the methanol decomposition *[17, 20, 22]* and we find if the intermediates are adsorbed in a di-sigma manner then the kinetics of the rate determining steps can be improved significantly. Skoplyak et al. and Peremans et al. reported experimentally that C=O group of methanol interacts paralley to the surface *[48]* and $-CH_3$ group is also inclined to the surface *[49]*. Taking into account these experimental observations and our calculated DFT results, we believe methanol molecule and the other dissociated intermediates adsorb in a di-sigma manner which in turns lowers the activation barrier thus increases the catalytic efficiency.

On the other hand, reaction proceeds quite favourable (Table 6.7-8) at the edge position too and the reaction kinetics are excellent for the last two dehydrogenation steps of the methanol. Our rate constant study could not find any specific step which is slow, so that can be called as a rate determining step which might be due to excellent catalytic activity of the nanocluster. The methanol decomposition is quite slow while proceeds through O-centre (Table 6.9).

Table 6.5: Rate of the elementary reactions (s^{-1}) at different temperatures of the most favourable pathway at the bridge position when adsorbs as di-sigma manner.

Elementary Reactions	**323K**	**423K**	**523K**
$CH_3OH \rightarrow CH_2OH\text{-}H$	4.12×10^{11}	1.73×10^{12}	4.60×10^{12}
$CH_2OH \rightarrow CHOH\text{-}H$	2.05×10^{13}	3.42×10^{13}	$5.^{13}\times10^{13}$
$CHOH \rightarrow COH\text{-}H$	2.73×10^{12}	7.32×10^{12}	1.47×10^{13}
$COH \rightarrow CO\text{-}H$	3.61×10^{06}	2.36×10^{08}	3.42×10^{09}

Table 6.6: Rate of the elementary reactions (s^{-1}) at different temperatures of the less favourable pathway at the bridge position when adsorbs as di-sigma manner.

Elementary Reactions	**323K**	**423K**	**523K**
$CH_3OH \rightarrow CH_3O\text{-}H$	1.59×10^{06}	1.27×10^{08}	2.07×10^{09}
$CH_3O \rightarrow CH_2O\text{-}H$	5.70×10^{12}	1.31×10^{13}	2.40×10^{13}
$CH_2O \rightarrow CHO\text{-}H$	6.37×10^{10}	4.18×10^{11}	1.46×10^{12}
$CHO \rightarrow CO\text{-}H$	2.65×10^{08}	6.29×10^{09}	4.87×10^{10}

Table 6.7: Rate of the elementary reactions (s^{-1}) at different temperatures of the most favourable pathway at the edge position when binds through C-atom.

Elementary Reactions	**323K**	**423K**	**523K**
$CH_3OH \rightarrow CH_2OH\text{-}H$	1.69×10^{10}	1.50×10^{11}	6.36×10^{11}
$CH_2OH \rightarrow CHOH\text{-}H$	4.99×10^{09}	5.86×10^{10}	2.94×10^{11}
$CHOH \rightarrow CHO\text{-}H$	4.06×10^{13}	5.76×10^{13}	7.82×10^{13}
$CHO \rightarrow CO\text{-}H$	8.25×10^{11}	2.94×10^{12}	7.05×10^{12}

Table 6.8: Rate of the elementary reactions (s^{-1}) at different temperatures of the less favourable pathway at the edge position when binds through C-atom.

Elementary Reactions	**323K**	**423K**	**523K**
$CH_3OH \rightarrow CH_3O\text{-}H$	4.26×10^{07}	1.55×10^{09}	1.57×10^{10}
$CH_3O \rightarrow CH_2O\text{-}H$	1.13×10^{12}	3.72×10^{12}	8.52×10^{12}
$CH_2O \rightarrow CHO\text{-}H$	1.55×10^{13}	2.76×10^{13}	4.33×10^{13}
$CHO \rightarrow CO\text{-}H$	8.25×10^{11}	2.94×10^{12}	7.05×10^{12}

Table 6.9: Rate of the elementary reactions (s^{-1}) at different temperatures at the edge position when binds through O-atom.

Elementary Reactions	**323K**	**423K**	**523K**
$OHCH_3 \rightarrow H\text{-}OCH_3$	1.16×10^{07}	5.73×10^{08}	6.98×10^{09}
$OHCH_3 \rightarrow OHCH_2\text{-}H$	1.00×10^{-05}	3.53×10^{-01}	2.48×10^{02}
$OCH_3 \rightarrow OCH_2\text{-}H$	7.21×10^{13}	8.88×10^{13}	1.11×10^{14}
$OHCH_2 \rightarrow OCH_2\text{-}H$	2.63×10^{13}	4.10×10^{13}	5.92×10^{13}
$OHCH_2 \rightarrow OHCH\text{-}H$	4.42×10^{-08}	5.82×10^{-03}	9.27×10^{00}
$OCH_2 \rightarrow OCH\text{-}H$	4.77×10^{-26}	1.09×10^{-16}	7.18×10^{-11}
$OHCH \rightarrow OCH\text{-}H$	1.30×10^{14}	1.35×10^{14}	1.51×10^{14}
$OHCH \rightarrow OHC\text{-}H$	1.69×10^{01}	1.97×10^{04}	1.69×10^{06}

6.4. Conclusion

DFT calculations have been performed to understand the methanol decomposition pathways on the cuboctahedral platinum nanocluster (Pt_{79}) enclosed by low index facets. Our relative energetic study shows the intermediates adsorbed parallely in a di-sigma manner are the most stable for most of the structures. The calculated reaction energy, activation barriers and temperature dependent reaction constant study shows that methanol decomposition pathway is most favourable at the bridge site while adsorb in a di-sigma manner. Interestingly, the calculated rate constant values show that the first two steps of the methanol decomposition reactions proceeds very fastly when the intermediates are adsorbed parallely in a di-sigma manner. Interestingly, these two steps are reported to be the rate determining steps for the methanol decomposition process and we find the kinetics of the rate determining step can be improved significantly if the intermediates are adsorbed in a di-sigma manner. Our calculated results are compared with previous experimental and theoretical studies and we find our calculated barriers are the lowest when the decomposition is proceeding through a di-sigma manner which is certainly interesting for the methanol dehydrogenation mechanism. To our surprise, methanol experimentally characterized to be adsorbed in a di-sigma manner though no previous theoretical studies consider methanol decomposition mechanism proceeds through a di-sigma manner. Therefore, we believe methanol decomposition might be proceeding through a di-sigma manner.

6.5 References

1. Cheng F., Chen J. (2012), Metal–air batteries: from oxygen reduction electrochemistry to cathode catalysts, Chem. Soc. Rev., 41, 2172−2192. (DOI: 10.1039/C1CS15228A)

2. Steele B. C. H., Heinzel A. (2001), Materials for fuel-cell technologies, Nature, 414, 345−352. (DOI:10.1038/35104620)

3. Yang J., Sudik A., Wolverton C., Siegel D. J. (2010), High capacity hydrogen storage materials: attributes for automotive applications and

techniques for materials discovery, Chem. Soc. Rev., 39, 656−675. (DOI: 10.1039/B802882F)

4. Fabbri E., Pergolesi D., Traversa E. (2010), Materials challenges toward proton-conducting oxide fuel cells: a critical review, Chem. Soc. Rev., 39, 4355−4369. (DOI: 10.1039/B902343G)

5. Wang Y., Chen K. S., Mishler J., Cho S. C., Adroher X. C., (2011), A review of polymer electrolyte membrane fuel cells: Technology, applications, and needs on fundamental research, Appl. Energy, 88, 981−1007. (DOI: 10.1016/j.apenergy.2010.09.030)

6. Oetjen H. F., Schmidt V. M., Stimming U., Trila F. (1996), Performance data of a proton exchange membrane fuel cell using H_2 / CO as fuel gas, J. Electrochem. Soc., 143, 3838−3842. (DOI: 10.1149/1.1837305)

7. Hamnett A. (1997), Mechanism and electrocatalysis in the direct methanol fuel cell, Catal. Today, 38, 445−457. (DOI: 10.1016/S0920-5861(97)00054-0)

8. Reddington E., Sapienza A., Gurau B., Viswanathan R., Sarangapani S., Smotkin E. S., Mallouk T. E. (1998), Combinatorial electrochemistry: a highly parallel, optical screening method for discovery of better electrocatalysts, Science, 280, 1735−1737. (DOI: 10.1126/science.280.5370.1735)

9. Sexton B. A. (1981), Methanol decomposition on platinum (111), Surf. Sci., 102, 271-281. (DOI: 10.1016/0039-6028(81)90321-6)

10. Ehlers D. H., Spitzer A., Luth H. (1985), The adsorption of methanol on Pt(111), an IR reflection and UV photoemission study, Surf. Sci., 160, 57-69. (DOI: 10.1016/0039-6028(85)91026-X)

11. Gibson K. D., Dubois L. H. (1990), Step effects in the thermal decomposition of methanol on Pt(111), Surf. Sci., 233, 59-64. (DOI: 10.1016/0039-6028(90)90175-8)

12. Diekhohner L., Butler D. A., Baurichter A., Luntz A. C. (1998), Parallel pathways in methanol decomposition on Pt(111), Surf. Sci., 409, 384-391. (DOI: 10.1016/S0039-6028(98)00298-2)

13. Peck J. W., Mahon D. I., Beck D. E., Bansenaur B., Koel B. E. (1998), TPD, HREELS and UPS study of the adsorption and reaction of methyl nitrite (CH_3ONO) on Pt(111), Surf. Sci., 410, 214-227. (DOI: 10.1016/S0039-6028(98)00284-2)

14. Henderson M. A., Mitchell G. E., White J. M. (1987), The decomposition of formaldehyde on Pt(111): A TPD and hreels study, Surf. Sci., 188, 206-218. (DOI: 10.1016/S0039-6028(87)80152-8)

15. Levis R. J., Jiang Z. C., Winograd N., Akhter S., White K. M. (1988), Methyl formation from methanol decomposition on Pd{111} and Pt{111}, Catal. Lett., 1, 385-389. (DOI:10.1007/BF00766168)

16. Wang J., Masel R. I. (1991), Carbon-oxygen bond scission during methanol decomposition on (1.times.1)platinum(110), J. Am. Chem. Soc., 113, 5850-5856. (DOI: 10.1021/ja00015a045)

17. Greeley J., Mavrikakis M. (2002), A first-principles study of methanol decomposition on Pt(111), J. Am. Chem. Soc., 124, 7193-7201. (DOI: 10.1021/ja017818k)

18. Ishikawa Y., Liao M. S., Cabrera C. R. (2000), Oxidation of methanol on platinum, ruthenium and mixed Pt–M metals (M=Ru, Sn): a theoretical study. Sur. Sci., 463, 66–80. (DOI: 10.1016/S0039-6028(00)00600-2)

19. Desai S. K., Neurock M., Kourtakis K. (2002), A periodic density functional theory study of the dehydrogenation of methanol over Pt(111), J. Phy. Chem. B, 106, 2559–2568. (DOI: 10.1021/jp0132984)

20. Niu C. Y., Jiao J., Xing B., Wang G. C., Bu X. H. (2010), Reaction mechanism of methanol decomposition on Pt-based model catalysts: A theoretical study, J. Comp. Chem., 31, 2023–2037. (DOI: 10.1002/jcc.21487)

21. Tian N., Zhou Z., Sun S., Ding Y., Wang Z. L. (2007), Synthesis of tetrahexahedral platinum nanocrystals with high-index facets and high electro-oxidation activity, Science, 316, 732-735. (DOI: 10.1126/science.1140484)

22. Greeley J., Mavrikakis M. (2004), Competitive paths for methanol decomposition on Pt(111), J. Am. Chem. Soc., 126, 3910-3919. (DOI: 10.1021/ja037700z)

23. Tian N., Zhou Z., Sun S. (2008), Platinum metal catalysts of high-index surfaces: from single-crystal planes to electrochemically shape-controlled nanoparticles, Phys. Chem. C, 112, 19801–19817. (DOI: 10.1021/jp804051e)

24. Kua J., Goddard W. A. (1999), Oxidation of methanol on 2nd and 3rd row group VIII transition metals (Pt, Ir, Os, Pd, Rh, and Ru): Application to direct methanol fuel cells, J. Am. Chem. Soc., 121, 10928-10941. (DOI: 10.1021/ja9844074)

25. Dobrin S. (2012), CO oxidation on Pt nanoclusters, size and coverage effects: a density functional theory study, Phys. Chem. Chem. Phys., 14, 12122-12129. (DOI: 10.1039/C2CP41286A)

26. Yudanov I. V., Genest A., Rösch, N. (2011), DFT studies of palladium model catalysts: structure and size effects, J. Cluster Sci., 22, 433-448. (DOI: 10.1007/s10876-011-0392-4)

27. Yudanov I. V., Genest A., Schauermann S., Freund H. J., Rösch N. (2012), Size dependence of the adsorption energy of CO on metal nanoparticles: A DFT search for the minimum value, Nano Lett., 12, 2134-2139. (DOI: 10.1021/nl300515z)

28. Li L., Larsen A. H., Romero N. A., Morozov V. A., Glinsvad C., Pedersen F. A., Greeley J., Jacobsen K. W., Nørskov J. K. (2013), Investigation of catalytic finite-size-effects of platinum metal clusters, J. Phys. Chem. Lett., 4, 222-226. (DOI: 10.1021/jz3018286)

29. Lopez N., Janssens T. V. W., Clausen B. S., Xu Y., Mavrikakis M., Bligaard T., Nørskov J. K. (2004), On the origin of the catalytic activity of gold nanoparticles for low-temperature CO oxidation, J. Catal., 223, 232-235. (DOI: 10.1016/j.jcat.2004.01.001)

30. Molina L. M., Hammer B. (2005), Some recent theoretical advances in the understanding of the catalytic activity of Au, Appl. Catal. A, 291, 21-31. (DOI: 10.1016/j.apcata.2005.01.050)

31. Greeley J., Nørskov J. K., Mavrikakis M. (2002), Electronic structure and catalysis on metal surfaces, Annu. Rev. Phys. Chem., 53, 319-348. (DOI: 10.1146/annurev.physchem.53.100301.131630)

32. Hammer B., Nørskov J. K. (1995), Electronic factors determining the reactivity of metal surfaces, Surf. Sci., 343, 211-220. (DOI: 10.1016/0039-6028(96)80007-0)

33. Zhang B., Wang D., Hou Y., Yang S., Yang X. H., Zhong J. H., Liu J., Wang H. F., Hu P., Zhao H. J., Yang H. G. (2013), Facet-dependent catalytic activity of platinum nanocrystals for triiodide reduction in dye-sensitized solar cells, Sci. Rep., 3, 1836. (DOI: 10.1038/srep01836)

34. Hu Y., Zhang H., Wu P., Zhang H., Zhou B., Cai C. (2011), Bimetallic Pt–Au nanocatalysts electrochemically deposited on graphene and their electrocatalytic characteristics towards oxygen reduction and methanol oxidation, Phys. Chem. Chem. Phys., 13, 4083-4094. (DOI: 10.1039/C0CP01998D)

35. Maiyalagan T., Khan F. N. (2009), Electrochemical oxidation of methanol on Pt/V_2O_5–C composite catalysts, Catal. Comm., 10, 433-436. (DOI: 10.1016/j.catcom.2008.10.011)

36. Ha H., Kim I. Y., Hwang S., Ruoff R. S. (2011), One-pot synthesis of platinum nanoparticles embedded on reduced graphene oxide for oxygen reduction in methanol fuel cells, Electrochem. Solid State Lett. 14, B70-B73. (DOI: 10.1149/1.3584092)

37. Xiong L., Manthiram A. (2005), Effect of atomic ordering on the catalytic activity of carbon supported PtM (M = Fe, Co, Ni, and Cu) alloys for oxygen reduction in PEMFCs, J. Electrochem. Soc., 152, A697-A703. (DOI: 10.1149/1.1862256)

38. Blochl P. E. (1994), Projector augmented-wave method, Phy. Rev. B, 50, 17953. (DOI : 10.1103/PhysRevB.50.17953)

39. Kresse G., Hafner J. (1993), Ab initio molecular dynamics for liquid metals, Phy. Rev. B, 47, 558. (DOI: 10.1103/PhysRevB.47.558)

40. G Kresse., Hafner J. (1994), Ab initio molecular-dynamics simulation of the liquid-metal–amorphous-semiconductor transition in germanium, Phy. Rev. B, 49, 14251-14269. (DOI: 10.1103/PhysRevB.49.14251)

41. Kresse G., Joubert D. (1999), From ultrasoft pseudopotentials to the projector augmented-wave method, Phy. Rev. B, 59, 1758. (DOI: 10.1103/PhysRevB.59.17580)

42. Perdew J. P., Chevary J. A., Vosko S. H., Jackson K. A., Pederson M. R., Singh D. J., Fiolhais C. (1992), Atoms, molecules, solids, and surfaces: Applications of the generalized gradient approximation for exchange and correlation, Phy. Rev. B, 46, 6671. (DOI: 10.1103/PhysRevB.46.6671)

43. Henkelman G., Jonsson H. (2000) A climbing image nudged elastic band method for finding saddle points and minimum energy paths, J. Chem. Phys., 113, 9978-9985. (DOI: 10.1063/1.1329672)

44. Shustorovich E. (1990), The bond-order conservation approach to chemisorption and heterogeneous catalysis: applications and implications, Adv. Catal., 37, 101-163. (DOI: 10.1016/S0360-0564(08)60364-8)

45. Kramer Z. C., Gu X., Zhou D. D. Y., Li W., Skodje, R. T. (2014), Following molecules through reactive networks: surface catalyzed decomposition of methanol on Pd(111), Pt(111), and Ni(111), J. Phys. Chem. C, 118, 12364-12383. (DOI: 10.1021/jp503056u)

46. Zheng C., Apeloig Y., Hoffmann R. (1988), Bonding and coupling of C1 fragments on metal surfaces, J. Am. Chem. Soc., 110, 749-774. (DOI: 10.1021/ja00211a015)

47. Gomes J. R. B., Gomes J. A. N. F. (2000), Adsorption of the formyl species on transition metal surfaces, J. Electroanal. Chem., 483, 180-187. (DOI: 10.1016/S0022-0728(00)00014-0)

48. Skoplyak O., Menning C. A., Barteau M. A., Chen J. G. (2007), Experimental and theoretical study of reactivity trends for methanol on Co∕Pt(111)Co∕Pt(111) and Ni∕Pt(111)Ni∕Pt(111) bimetallic surfaces, J. Chem. Phys., 127, 114707. (DOI: 10.1063/1.2768520)

49. Peremans A., Maseri J., Darville J., Gilles J. M. (1990), Interaction of methanol with a polycrystalline platinum surface studied by infrared reflection absorption spectroscopy, Sur. Sci., 227, 73-78. (DOI: 10.1016/0039-6028(90)90393-M)

Chapter 7

Scope for Future Work

7.1. Scope for future work

The present doctoral thesis describes about the atomic scale designing of NC-based electrodes for low-temperature fuel cells. Further understanding on the site and size-specific reactivity of the NCs is required in order to design more efficient and selective catalyst for ORR. The ORR activity can be further explored using high-index NCs as catalyst. The remarkable ORR efficiency of platinum nanosheet can be further investigated on bimetallic nanosheet. Furthermore, a significant scope is there to improve the overpotential of ORR on NC-based catalyst. In addition, further investigation is required to check the possibility of di-sigma adsorption of MOR reaction intermediates on periodic step surface model.